

**Final Report
COVER PAGE**

Federal Agency to which Report is submitted: DOE EERE – Wind & Water Power Program

Recipient: Columbia Power Technologies, INC [798823188]

Award Number: DE-EE0002658

Project Title: Benchmark Modeling of the Near-Field and Far-Field Wave Effects of Wave Energy Arrays

Project Period: January 1, 2010 to August 31, 2012

Principle Investigator: Ken Rhinefrank VP R&D
(541)760-1833
krhinefrank@columbiapwr.com

Report Submitted by: Brad Lamb President & COO
(434)817-8799
blamb@columbiapwr.com

Date of Report: January 26, 2013

Covering Period: January 1, 2010 to August 31, 2012

Working Partners:

Oregon State University

PI	Merrick Haller	(541) 737-9141	hallerm@enr.orst.edu
PI	Tuba Ozkan-Haller		
RA	Aaron Porter		
.	Cameron McNatt		

Columbia Power

SME Pukha Lenee-Bluhm

ershigs Inc. Eric Schumacher (360) 254-8208 eschumacher@ershigs.com

Cost-Sharing Partners: NA

DOE Project Team: DOE HQ Program Manager – Jose Zayas
DOE Field Contract Officer – Pamela Brodie
DOE Field Contract Specialist – Laura Merrick
DOE Field Project Officer – Tim Ramsey
DOE/NAVARRO Project Monitor – Erik Mauer

Signature of Submitting Official:

(electronic signature is acceptable)

Table of Contents

1. Project Objectives	1
2. Project Scope	1
3. Accomplishments (Task Deliverables)	1
3.1. Introduction	1
3.2. Wave Energy Converter Performance in an Array	2
3.2.1. Introduction.....	2
3.2.2. Experimental Setup.....	2
3.2.3. Data Analysis Methodology	12
3.2.4. Results and Discussion	16
3.2.5. WEC Conclusions	28
3.3. Executive Summary: Laboratory Observations and Numerical Modeling of the Effects of an Array of Wave Energy Converters (Appendix 12)	29
3.4. Executive Summary: Wave Field Patterns Generated by Wave Energy Converters (Appendix 13)	30
4. Key Cost/Performance Drivers Identified	31
4.1. Array design	31
4.2. Scaled array experimental design.....	32
4.3. Array spacing	34
5. Recommendations for Future Work.....	34
5.1. Methods for reducing the physical space between WECS	34
5.2. Baseline modeling tool for array design.....	34
5.3. Experimental solutions	35
5.4. Advanced array design tools	36
5.5. Assessment of environmental influence	36
6. Project Summary.....	38
7. Products.....	39
7.1.1. Experimental data	39
7.2. Papers written	39

Invited presentations acknowledging DOE support	39
8. Participants and Other Collaborating Organizations	40
9. Impact	41
10. Changes / Problems.....	41
11. Budgetary Information.....	42
12. Appendix: Laboratory Observations and Numerical Modeling of the Effects of an Array of Wave Energy Converters	43
12.1. Introduction	43
12.2. Experiment and Analysis.....	43
12.3. Results	43
12.4. Experimental Data Set Conclusions	43
12.5. Numerical Modeling.....	43
12.6. Model/Data Results	43
12.7. Numerical Model Conclusions	43
12.8. WAMIT/SWAN WEC Model Comparison	43
12.9. WAMIT/SWAN Results.....	43
12.10. WAMIT/SWAN Conclusions.....	43
12.11. Discussion.....	43
12.12. Conclusions	43
12.13. Bibliography	43
12.14. Appendix	43
13. Appendix: Wave Field Patterns Generated by Wave Energy Converters	43
13.1. Introduction	43
13.2. Background.....	43
13.3. Methods	43
13.4. Results	43
13.5. Discussion.....	43
13.6. Conclusion	43

1. Project Objectives

This project will perform benchmark laboratory experiments and numerical modeling of the near-field and far-field impacts of wave scattering from an array of wave energy devices. We will develop a predictive understanding of the effects of an array of wave energy converters on the wave conditions and the potential for any wave field modifications to change nearshore current and sediment transport patterns

2. Project Scope

This project addresses Topic Area 2: “Marine and Hydrokinetic Site-specific Environmental Studies/Information” under FOA Number DE-FOA-0000069 and is an industry-led partnership that will perform environmental testing studies regarding the installation of arrays of wave energy conversion devices. The study will perform benchmark laboratory experiments using an array of 1:33 scale wave energy conversion devices. The experiments will quantify the wave scattering effects of these arrays and be used to develop and test numerical models for wave-structure interaction and far-field hydrodynamic effects.

3. Accomplishments (Task Deliverables)

3.1. Introduction

As the wave energy conversion industry matures towards commercial viability, multi-megawatt WEC plants will certainly consist of tens or hundreds of individual WECs. It is essential to the industry that we understand the array effects on both the power performance of the array, as well as any potential effects on the surrounding environment.

Columbia Power Technologies (ColPwr) and Oregon State University (OSU) jointly conducted a series of experiments in the Tsunami Wave Basin (TWB) at the O.H. Hinsdale Wave Research Laboratory (HWRL). Experimental trials were run between November 2010 and February 2011. WECs modeled at 33rd scale, representing Columbia Power’s Manta series (version 3.1) Wave Energy Converter (WEC), were moored in configurations of one, three and five WEC arrays. The different array configurations were each subjected to a series of regular wave conditions as well as directionally-distributed spectral sea states.

Research interests included, but were not limited to, an investigation into the effects of the WEC arrays on the near- and far-field wave propagation, and the characterization of WEC performance, for individual WECs as well as for WECs in an array. The approach to these topics included experimental data analysis, numerical modeling (both a phase-resolving model and a spectral model), and model/data comparisons.

The investigation of WEC response with respect to power performance is covered in 3.2. The investigation into the effects of WEC arrays on the far-field waves, as well as a discussion of numerical modeling of these effects, is covered in 3.3. The investigation into near-field effects of WEC arrays, and the use of phase-resolving models to predict these effects, is covered in 3.4.

3.2. Wave Energy Converter Performance in an Array

3.2.1. Introduction

The WEC performance is investigated with respect to mechanical shaft power. Power performance will be quantified with respect to incident wave power, and correlated to incident wave conditions. To facilitate an understanding of the array effects, power performance for an array will also be compared to the performance of an equal number of isolated WECs. The single WEC response is covered in much greater detail elsewhere, and here is given primarily as a means to understand the array performance.

3.2.2. Experimental Setup

3.2.2.1. Wave tank

The TWB is 48.8 m long, 26.5 m wide and 2.1 m deep (maximum operating depth of 1.5 m). The wavemaker consists of 29 individually actuated piston-type paddles and is capable of generating regular and irregular waves which can be normally incident, oblique or multi-directional, as well as solitary or tsunami-like waves. Several different wave regimes were generated for the tests:

- a. Head on regular wave amplitude scan
- b. Head on regular wave frequency scan
- c. Off angle (22.5°) regular wave frequency scan
- d. Simulated real seas

The amplitude scan ran from 3 to at most 15 cm in wave height and was tested to estimate the region of wave heights in which the WEC response was linear. The frequency scan covered a range of wave periods representing the vast majority of what would be expected in the open ocean. At tank scale the wave periods ranged from 0.9 to 2.8 s. The simulated real seas were selected to be representative of conditions expected in potential commercial scale deployment sites. The simulated real seas include head on and off angle cases, as well as several different directional spreading cases. Targeted wave spectra all have a Pierson-Moskowitz (PM) shape and directional spreading is defined using the cos-2s formulation. Real seas nominal wave conditions are listed in Table 1. The mean water depth for all trials was approximately 1.37 m (corresponding to 45.2 m at full scale).

A total of 28 instruments (resistance wire wave gauges, an ultrasonic wave gauge and several Acoustic Doppler Velocimeters) were available for hydrodynamic observations (see Figures 1, 2,

and 3). The instrumentation was arranged in such a way as to resolve the directionally spread incident waves, the reflected/diffracted/radiated waves in the near-field of the array, and the modified far-field waves in the lee of the array.

Table 1.Target sea states, with directionality variations. Spreading index of 1e6 indicates no spreading.

Name	Te [s]	Hm0 [cm]	Mean wave heading [deg]	Spreading Index
Hawaii (HI)	1.04	4.55	0	2
Oregon 2 (OR2)	1.22	7.58	0	4
Oregon 1 (OR1)	1.39	4.55	0	10
Ireland (IR)	1.39	10.61	0	1e6
Oregon 3 (OR3)	1.57	7.58	22.5	1e6
Oregon 4 (OR4)	1.91	7.58		
Oregon 5 (OR5)	1.91	13.64		

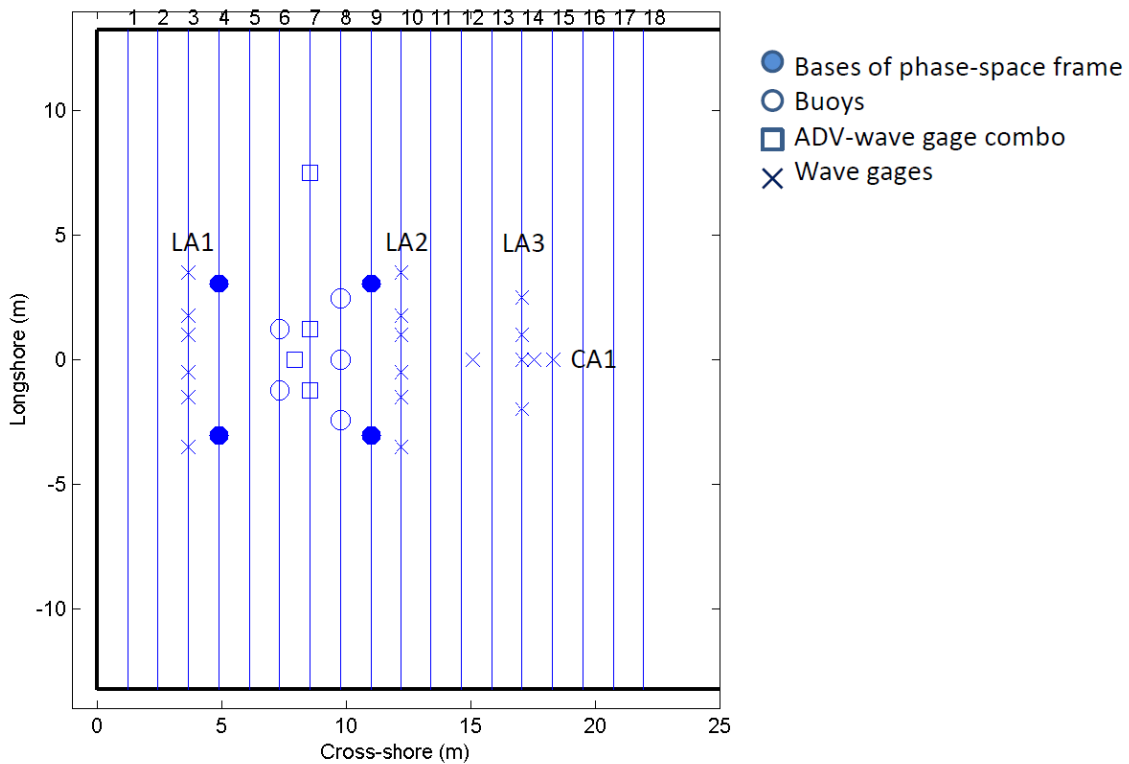


Figure 1. TWB instrumentation setup for wave measurement.

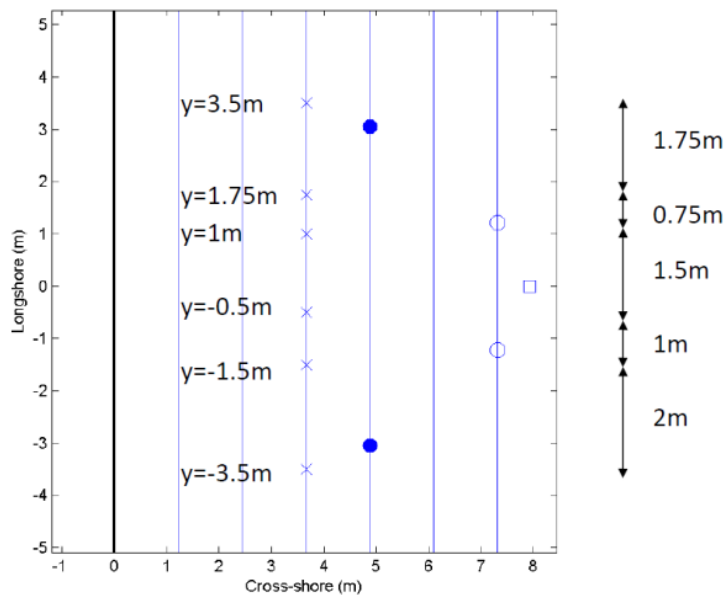


Figure 2. Alongshore array detail - applies to LA1 and LA2.

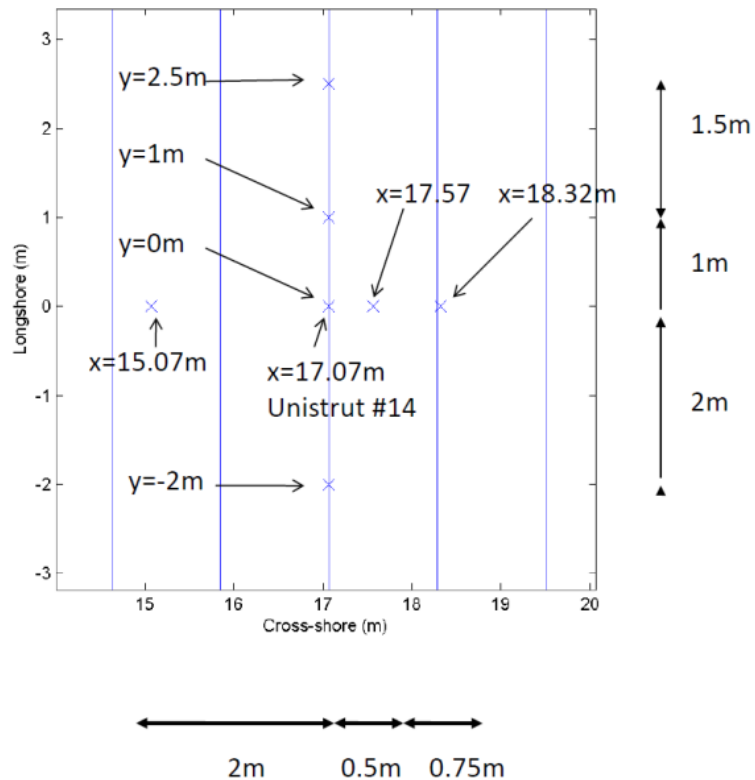


Figure 3. Array detail for LA3 and CA1.

3.2.2.2. Model WECs

A total of five model WECs were fabricated, with tests conducted on arrays of one, three and five WECs. Each WEC consists of three rigid bodies constrained to move in a total of eight degrees of freedom (8 DOFs). The fore and aft floats are free to move in pitch only (w.r.t the central body), thus any possible position of the WEC can be described via 6 DOFs for the central body and 2 DOFs for the pitch positions of each float w.r.t. the central body. The central body is composed of spar, nacelle and damper tank, and is heretofore referred to as the spar. Note that the (unballasted) fore and aft floats are identical, although differ by a rotation of 90° as attached. Figure 4 depicts an assembled model WEC, which was designed to be representative of Manta version 3.1. The mass distribution of the model WECs as designed is given in Table 2.

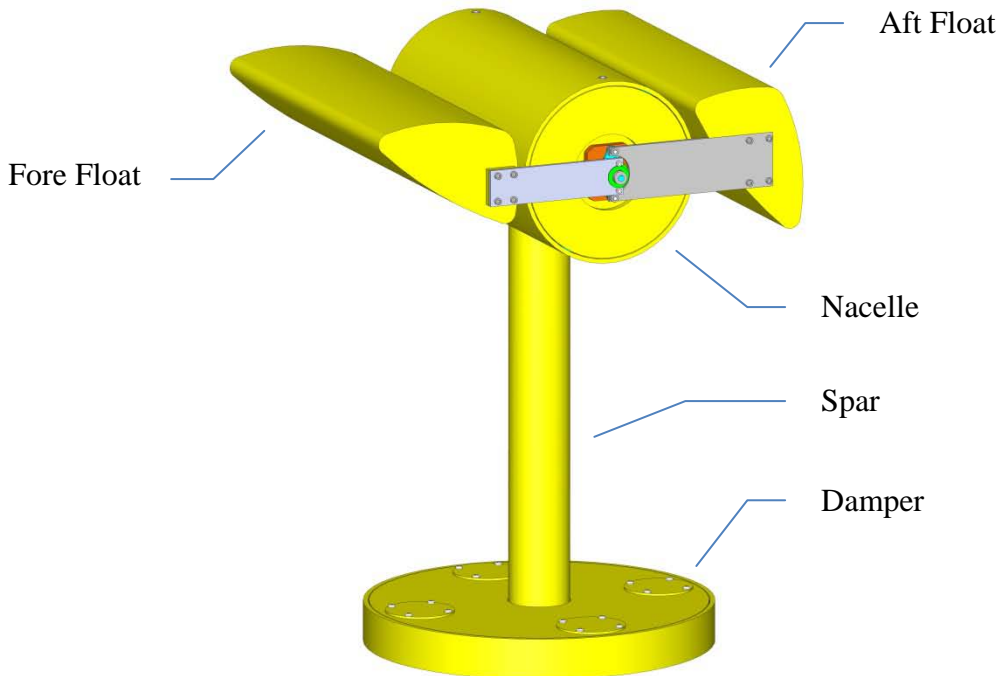


Figure 4. Model WEC assembly.

Each model WEC was outfitted with a pair of model generators – one was actuated by the relative motion between the spar and the fore float, and the other by the relative motion between the spar and the aft float. The generators were modeled using oil-filled rotary dashpots (Kinetrol LA1-DD). Each dashpot was calibrated before deployment by setting the needle valve to achieve the desired torque/speed relationship. A linear damping estimate was calculated as a least squares linear fit of torque to speed (see Figure 5 for sample torque/speed plots). Settings

were determined for damping values that numerical modeling had indicated as ideal over a broad range of sea states (namely, fore damping of 3.55 N m s and aft damping of 2.42 N m s). An over-damped setting for extreme waves testing was also established (fore and aft damping of 8.81 N m s). The damping of each dashpot was checked after the model testing and in many cases was found to have changed significantly. As torque was not measured during the model testing (torque is calculated as the product of damping and rotational velocity) it is imperative that a reasonably accurate estimation of damping as a function of time be determined. A thorough investigation was conducted, concluding that the most plausible model for damping changes was a linear trend from pre- to post-deployment measurements. Thus all data analysis has been carried out pursuant to this model of linear change in damping over time, and the fore and aft damping estimates for each WEC in each trial have been archived.

Table 2. Mass distribution for 33rd scale model WECs. Center of gravity values are referenced from the waterline, which exists at the intersection of axial center of the spar body axis and the water plane.

	Mass [g]	Center of Gravity [cm]	Moment of Inertia about CG [gcm ²]		
Total System	58,147	<i>x,y,z</i>	<i>P_{xx},P_{yx},P_{zx}</i>	<i>P_{xy},P_{yy},P_{zy}</i>	<i>P_{xz},P_{yz},P_{zz}</i>
SPAR	39,900	0.00	48,649,913	2	27
		0.00	2	44,668,629	40
		-53.35	27	40	12,269,318
FWD Float	9,254	23.37	3,261,483	88,438	117,290
		-0.63	88,438	688,825	13,574
		-3.66	117,290	13,574	3,729,845
AFT Float	8,994	-23.00	3,504,810	63,938	68,382
		0.59	63,938	691,134	-3,017
		-6.05	68,382	-3,017	3,697,848

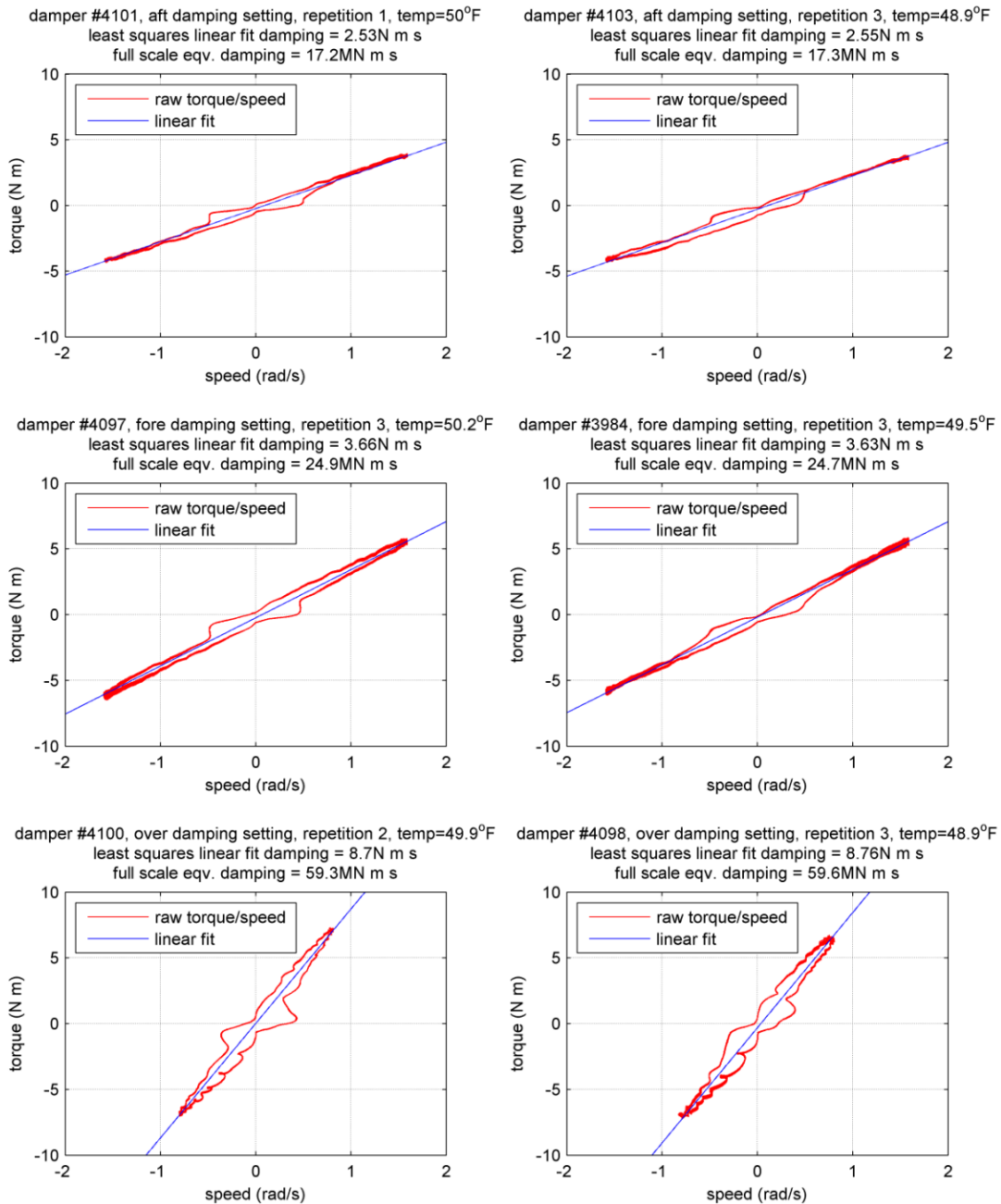


Figure 5. Sample torque/speed plots, with least squares linear fit.

The mooring of each WEC was designed to have roughly the same load-displacement curve as a preliminary design of the commercial scale mooring system. This was accomplished via horizontal elastic lines running between vertical stanchions and the damper tank of a WEC, in a symmetrical three point mooring configuration (see Figure 6). The elastic line was selected to

have a load/displacement curve similar to the commercial scale mooring system. The primary purpose of the mooring system is to keep the WEC on station, and is not expected to have a significant effect on performance. Mooring loads were not measured in the 33rd scale array experiment.

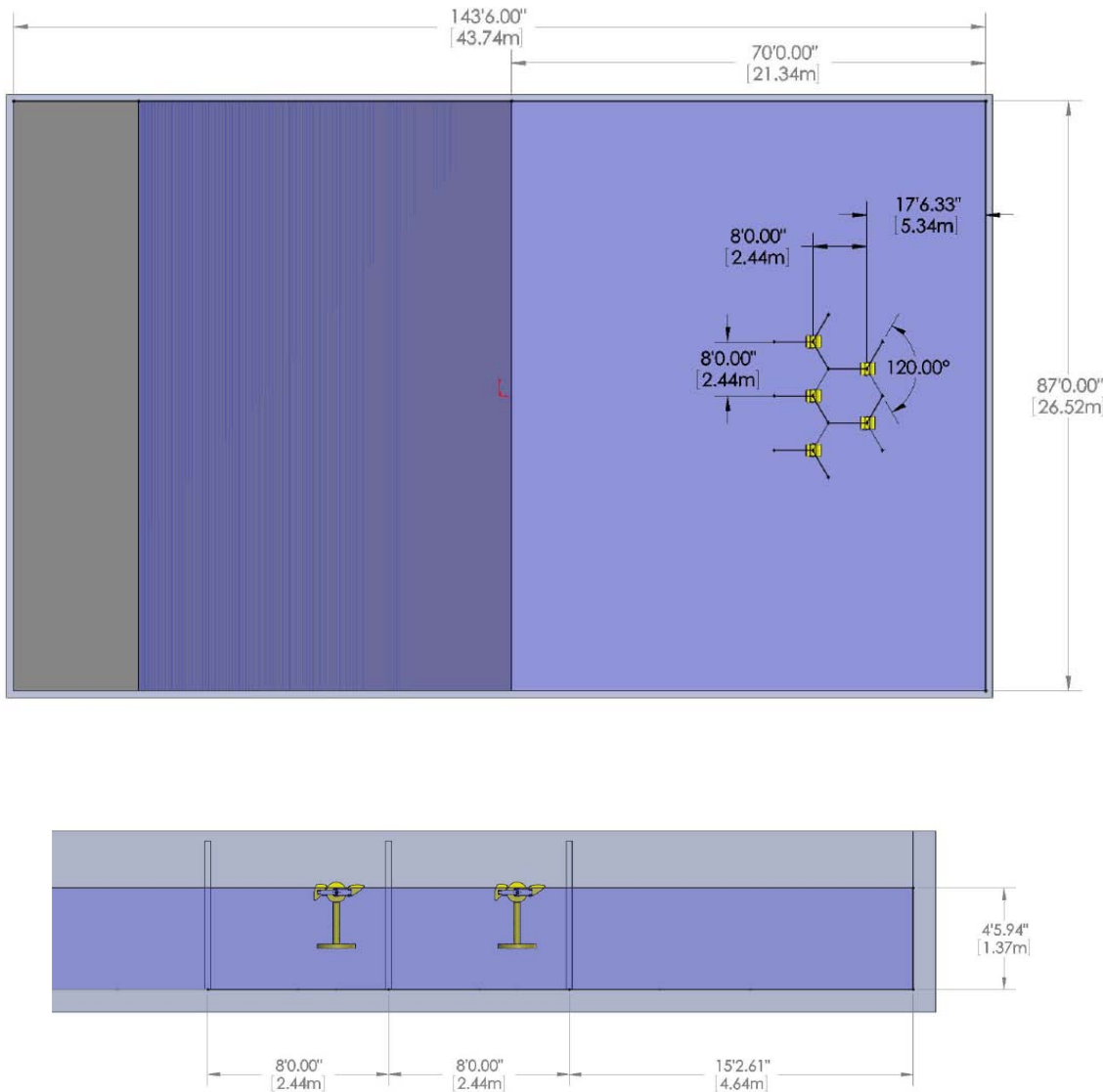


Figure 6. Mooring configuration in the TWB.

3.2.2.3. Array positions and coordinate systems

Tests were conducted for each WEC in isolation, as well as for arrays of three and five WECs. Figure 7 depicts the various array positions. All single WEC tests were in Array Position 1. The

three WEC tests involved WECs 1, 2 and 3 stationed at Array Positions 1, 2 and 3. The five WEC tests used all five Array Positions, but WEC 4 was in Array Position 5 and WEC 5 was in Array Position 4.

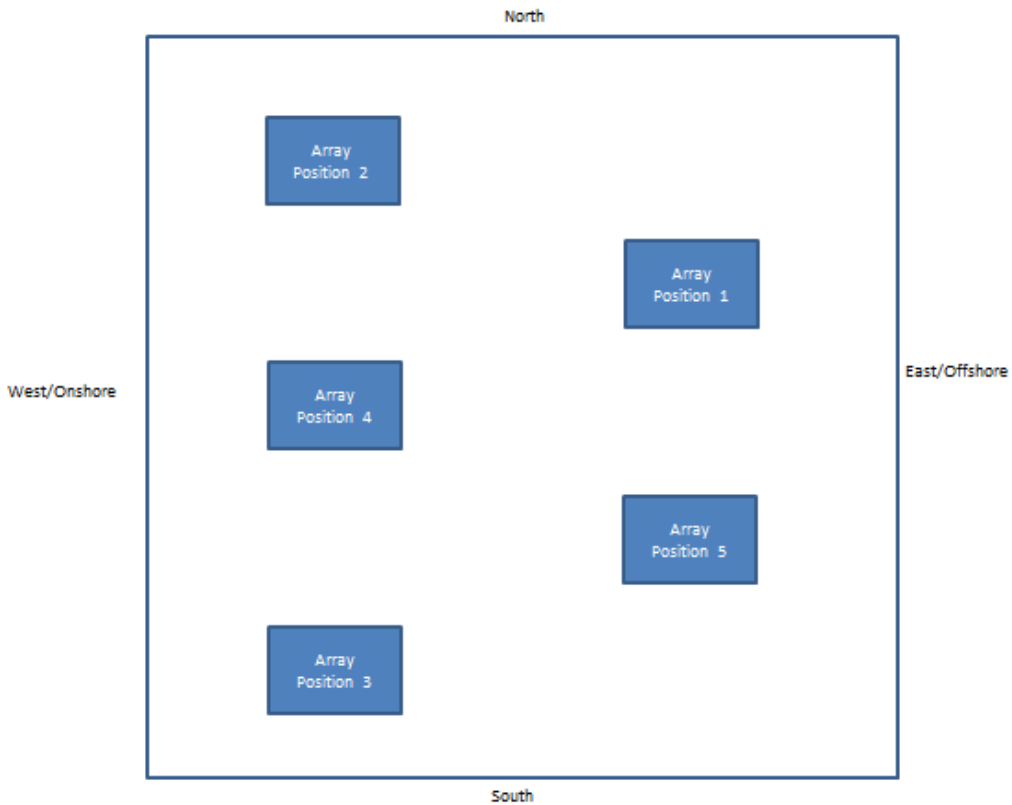


Figure 7. Array positions (note that WECs 4 and 5 are in positions 5 and 4, respectively).

The origin of the TWB coordinate system (used for waves) is on the floor of the tank, in the center of the line of wavemaker paddles, on the onshore side of the paddles (in their neutral position). The x-direction is positive away from the paddles, the z-direction is up (perpendicular to the still water plane), and the y-direction follows from the right-hand rule.

The origin of the PhaseSpace coordinate system (used for WECs) is defined by the PhaseSpace reference LEDs located on a rigid platform above the still water plane (see Figure 8). The x-direction is positive towards the paddles, the y-direction is up (perpendicular to the still water plane), and the z-direction follows from the right-hand rule.



Figure 8. Single WEC and the PhaseSpace reference square.

3.2.2.4. Data Collection

There are two primary data being captured for this experiment: wave elevation and WEC position. This section describes the data collection and the post-processing leading to quality controlled primary data.

3.2.2.4.1. Wave elevation

Wave gauges record water surface elevation and data were collected here at a rate of 50 Hz, and reported in units of volts. A calibration coefficient is necessary to correlate the voltage reading to a water surface elevation. During tank drain and fill operations, the data acquisition system sampled the analog wave gauge signals as well as a pressure-based level indicator. A linear fit was performed between each of the gauge voltage signals and the water depth indicated by the pressure gauge, and the resulting calibration coefficients were recorded. There are four sets of calibration coefficients thus calculated, as there was a drain and fill in 2010 and again in 2011 (a few months apart). It was noted that the drain calibration coefficients differed from their respective fill coefficients by 10 to 20%. As a wave elevation change of 20% corresponds to a wave power change of 44%, the nature of this change was investigated.

Over time, the conductivity in the tank can change, resulting in changing calibration values. To estimate calibration coefficients between the drain and fill, a good understanding about the behavior of conductivity in the tank over time is needed. This was gained by placing an ultrasonic wave gage (uswg), co-located with a wave gage, above the water's surface; the uswg

measurement is more direct as it does not require a calibration coefficient (other than the speed of sound in air). Hence, the uswg provides an absolute measure of water level throughout the experiment (on the other hand, the uswg is noisier when waves are present, which is why not all wave gauges are uswg's). Comparing the readings of the uswg and the nearest wave gauge over time gives an estimate of how the conductivity in the tank changed. It was expected that the calibration coefficient would change very quickly in the first two days after the tank is filled and then the calibration would remain constant over time. This behavior is the result of ionization changes in the standing body of water. The observed calibration changes agreed with these expectations and a MATLAB function was built to compute calibration coefficients for each wave gauge based on the time and date of a given experimental trial. All processed wave data in this experiment uses this method.

3.2.2.4.2. WEC position

The position of each rigid body (up to a maximum of 15 rigid bodies for the five WEC array tests) was tracked at 480 Hz using PhaseSpace technology – a motion capture system employing active LED markers and a network of high speed cameras. Each rigid body was outfitted with 6 LEDs (see Figure 9). The PhaseSpace motion capture system yields position data for each rigid body tracked in a proprietary format (.rpd). PhaseSpace software was used to convert the .rpd formatted data to 6 DOF position in Cartesian coordinates. A zero-phase, 50 Hz low pass filter was applied to the 480 Hz motion data. The resulting signals were subsequently downsampled to 50 Hz and archived.

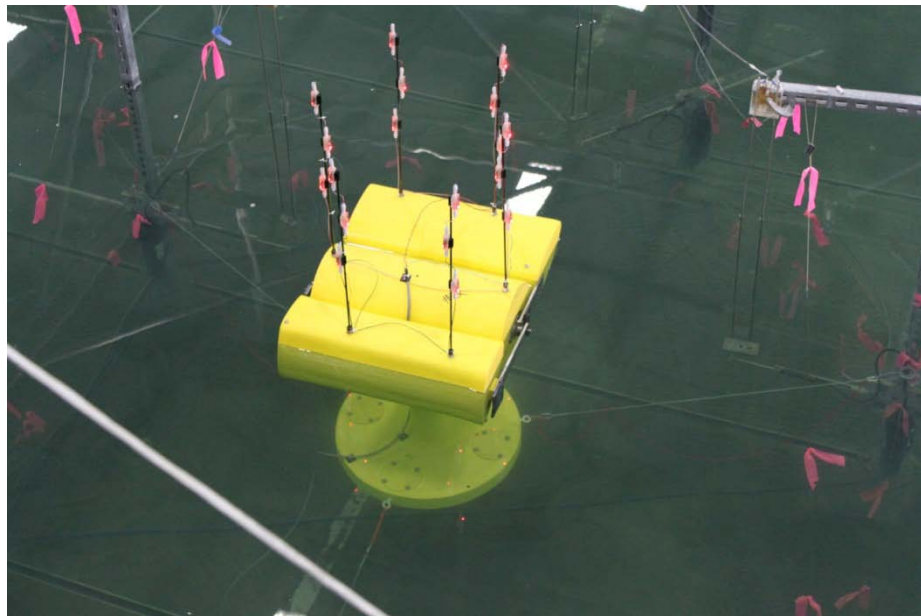


Figure 9. PhaseSpace LED configuration.

Due to the nature of the constraints between the fore float and the spar, and between the aft float and the spar, the total system can be described using only 8 DOF. The required DOFs are three translations and three rotations of the spar center of gravity (cg_{spar}), as well as the pitch positions of the fore and aft floats with respect to the spar. However, the 6 DOF position signals reported by PhaseSpace are for a particular LED (i.e. the reference LED) amongst those being used to track each body. The rotation of any point on a rigid body is identical, but the translation (in a fixed reference frame) of each point on the body may be different. A transformation matrix, based on the instantaneous orientation (i.e. 3 DOF rotations) of the spar, along with the position vector of the center of gravity w.r.t. the reference LED is used to transform the spar LED position signal to a cg_{spar} position signal as

$$\begin{bmatrix} x \\ y \\ z \end{bmatrix}_{cg} = \begin{bmatrix} x \\ y \\ z \end{bmatrix}_{ref} + qpr \cdot \begin{bmatrix} x \\ y \\ z \end{bmatrix}_{cg/ref}$$

where $[x \ y \ z]_{cg}'$ is the position of the cg_{spar} in a fixed reference frame, $[x \ y \ z]_{ref}'$ is the position of the spar reference LED in a global reference frame, qpr is a 3×3 transformation matrix and $[x \ y \ z]_{cg/ref}'$ is the position of the cg_{spar} w.r.t. the spar reference LED in a body fixed reference frame. Because the rotational position is reported as Euler angles of order x-y-z, and pitch is rotation about the z-axis in this axes system, the final two degrees of freedom are calculated quite simply as the pitch motion of a given float minus the pitch motion of the spar.

3.2.3. Data Analysis Methodology

This section describes the analysis performed on the quality controlled primary data leading to a characterization of the incident waves and the WEC response, as well as the correlation between waves and WEC response. The process begins with selecting an appropriate window for analysis within the captured data, and continues with a calculation of some statistical parameters.

3.2.3.1. Analysis windows

The beginning and end of a given experimental record (e.g. time series of water surface elevation) cannot be used in the analysis, as these correspond to the ramp up or ramp down of wave excitation. As such it was important to determine an appropriate window within each signal to use for the data analysis. Essentially, a signal is algorithmically examined and a steady-state portion is identified for analysis. For technical reasons, initiating both wave and WEC measurements with a common trigger was not enacted. Thus these data streams must have analysis windows identified independently. As we are investigating the average conditions during the steady-state portion of the records, a precise alignment of analysis windows is not required.

For water surface elevation records, an analysis window was determined for each wave gauge individually. The central portion of the wave gauge record, where wave heights were within a threshold level of the targeted mean conditions, was used as the analysis window. For the 8 DOF motion of each WEC, a single DOF was used as the indicator signal for analysis of the motion data. The relative rotation of the fore float (a strong, easily excitable response) was selected as this indicator signal, and the analysis window indices determined for this signal were applied to all other DOFs for the given trial and the given WEC.

For the regular wave trials, the signal was first de-means and de-trended using a zero-phase moving-average filter with a window size equal to the target regular wave period. Then, the zero up-crossing indices were identified and the individual waveform amplitudes calculated. To limit the influence of signal noise, the amplitudes were calculated as $\sqrt{2}$ times the RMS value of the signal between zero up-crossings. A threshold value of 50% of the mean of the 10 greatest amplitudes was calculated and the indices bounding the first and last waveforms to exceed this threshold were noted. Finally, as the wavemaker was programmed to ramp up over a period of 20 seconds, the analysis window indices were set 10 seconds in from the indices marking the 50% threshold. For different tests 10, 20, or 50 steady-state waveforms were the targeted experimental conditions, and the analysis window determination algorithm attempts to include as many of these waveforms as possible.

For the real seas trials, windows of a common length are determined, as spectral analysis will be performed and a uniform frequency resolution is required. Trial lengths are either 313 or 540 seconds (corresponding to 30 and 52 minutes at full scale), and analysis windows of 280 or 480 seconds (27 and 46 minutes at full scale) are determined, respectively. These analysis window lengths, along with properly selected post-processing parameters, allow for identical frequency resolution (see 3.2.3.2 for details). To determine the analysis window, the RMS values of non-overlapping 10 s windows (tank scale) of the signal are first calculated. A threshold value of 25% of the mean of the 25 windows of greatest RMS value is calculated, and the mean of the indices at the centers of the first and last 10 second windows with RMS values exceeding this threshold is noted. Finally, an analysis window of appropriate size is centered upon this index.

3.2.3.2. Incident wave conditions

The waves measured by each wave gauge are characterized in an identical manner. There are 7 gauges that are used to characterize the incident wave conditions; this is accomplished by calculating the mean spectra over these 7 gauges, then calculating each of the characteristic wave parameters. The gauges used to characterize incident conditions are numbers 1 to 6, and 10. Referring to Figure 1, these are the six gauges comprising LA1 and the gauge located approximately 7.5 m away from the WEC array in the longshore direction. To minimize the influence of the WEC array on the observations of the incident waves, mean observed wave

conditions during the single WEC trials were used to quantify incident conditions for all trials (see 3.3 for details).

For the regular wave trials, incident wave conditions are characterized by wave height, wave period, and wave direction. The mean wave height is calculated as $2\sqrt{2}$ times the RMS of the signal within the analysis window. The mean wave period is calculated as the mean of the time between adjacent zero up-crossings within the analysis window. The measured, rather than the target, wave parameters are used in all analyses.

For the real seas trials, the incident wave conditions are characterized by the significant wave height, energy period, and omnidirectional wave power. Wave elevation variance density spectra (1D spectra) have been calculated using a discrete Fourier transform (DFT) for each wave gauge and each trial. The DFTs are computed using ensemble averaging and Hamming windows. The analysis employs 28 or 48 degrees of freedom for the 280 and 480 second analysis windows, respectively. Thus the smoothed spectra have a frequency resolution of 0.05 Hz (equivalent to 0.0087 Hz at full scale). The mean of the 1D spectra calculated for the 7 offshore gauges (1 to 6, and 10) is used to characterize the incident wave energy. The significant wave height, energy period and wave power are calculated from this spectrum. The significant wave height, H_{m0} , and energy period, T_e , are calculated as

$$H_{m0} = 4\sqrt{m_0}$$

and

$$T_e = \frac{m_{-1}}{m_0}$$

where m_n represents a spectral moment of the n^{th} order, which is calculated as

$$m_n = \int f^n S(f) df$$

where f is the frequency and $S(f)$ is the wave elevation variance frequency density spectrum. The limits of integration were taken as 0.2 and 5 Hz (equivalent to 0.035 to 0.87 Hz at full scale). The wave energy flux per meter crest length, or wave power, is calculated as

$$J = \rho g \int c_g(f, h) S(f) df$$

where ρ is the density of water (assumed to be 1000 kg/m³ at HWRL), g is the acceleration due to gravity (assumed to be 9.805 m/s²), and $c_g(f, h)$ is the group velocity, which is a function of frequency and water depth, h . A wave power frequency density spectrum, J_f , is calculated as the

element-wise product of group velocity and wave elevation 1D spectrum, scaled by gravity and fluid density, as

$$J_f = \rho g c_g(f) S(f)$$

3.2.3.3. WECs

Having captured WEC motion (i.e. position versus time) with 8 DOFs for each WEC, and determined an appropriate analysis window, the steady-state response of the WEC can now be characterized. The response is normalized by, and correlated to, the incident conditions.

The velocity of the relative rotation of float w.r.t. spar (i.e. generator velocity) is necessary for calculating mechanical power absorbed and is determined as the finite difference of the relative rotation position signal divided by the time step of the 50 Hz signal. It should be noted that the signals were not de-trended for this calculation, but rather used as measured. The instantaneous mechanical power is calculated for each generator (fore and aft) as the element-wise product of the generator speed and the torque. The generator torque is calculated as the product of the estimated linear damping coefficient of the characterized generator and generator speed signal. The mean mechanical power of the fore and aft generators is recorded, as is the mean mechanical power of the total system (i.e. sum of fore and aft mean mechanical power). This same procedure is used to calculate mechanical power in regular waves and real seas.

WEC performance is quantified as the mean mechanical power, normalized by the mean wave power incident across a width equal to the nominal WEC width (54.54 cm). This dimensionless performance parameter, used extensively in the WEC industry, is called the relative capture width (RCW) and can be thought of as the proportion of wave energy (in a crest length equal to the nominal WEC dimension) captured by the device. For 3 and 5 WEC array trials, an RCW is calculated for each WEC individually, as well as the array as a whole. The nominal width used for calculating the array RCW for an N WEC arrays is taken as N times the nominal width of a single WEC. The ratio of the RCW for an array (or a WEC within the array) to that of an isolated WEC in identical conditions quantifies array performance w.r.t. an N individual WECs. This ratio is termed a Q factor.

For the wave propagation modeling undertaken as a part of this research, a model describing wave power absorption by the WECs was required. As expected, the experimental data show that the absorption is strongly correlated to wave frequency. Due to potential nonlinearities in WEC response, it cannot be assumed a priori that the WEC response in real seas is best modeled by the RCW curve garnered from the regular wave frequency sweep. To explore the frequency dependent wave power absorption realized by the WECs in real seas, a spectral approach was taken. DFTs were computed for the speed signals of the model generators, using a methodology

identical to the wave elevation DFTs (i.e. ensemble averaging, Hamming windows, and identical degrees of freedom). By calculating the variance density spectrum of the speed signal of a model WEC generator, and multiply by the linear damping coefficient, a spectrum is yielded which describes the distribution of the mechanical power absorbed over frequency. This is possible because the generator damping is approximately linear. The wave power incident upon the WEC is represented by the wave power frequency density spectrum, J_f , multiplied by the nominal width of the WEC. The mechanical power frequency density spectrum normalized by the wave power frequency density (over the width of the WEC) yields what we will call a spectral RCW curve, which describes the power absorbed as a function of frequency.

3.2.4. Results and Discussion

In this section, the WEC response is correlated with the incident wave conditions. Results in regular and real seas will be discussed. Although response under regular waves illustrates some basic characteristics of the WEC, due to nonlinearities in the WEC/wave system it is the response to real seas that best predicts how the WEC may perform under ocean conditions. First, the results of trials of single WECs in isolation will be discussed, followed by the results of trials of arrays of 3 and 5 WECs. Although limited amplitude scans in regular wave conditions were performed, the bulk of the regular wave trials had incident waves of nominal wave height equal to 6 cm. Furthermore, analysis of the directional characteristics of the directionally spread incident wave conditions has not been undertaken at this time, and as such any assessment of WEC performance in off-angle or directionally spread seas would have insufficient context. This report draws upon the considerable testing done in regular waves with a nominal height of 6 cm and head on real seas with no directional spreading.

For any given wave condition, there were generally multiple trials conducted. Regular wave frequency scans were conducted on all 5 model WECs. Limited real seas trials were conducted on model WECs 3 and 5, with a complete sea state scan conducted on WEC 1. Additionally, for any given combination of wave condition and WEC array, there were typically two repetitions. For regular waves these were truly repetitions, for real seas they were distinct realizations of the same statistical sea state (i.e. different sets of random phases). The responses discussed in the following subsections are presented as the mean response with a 95% confidence interval (CI). The mean and CI is calculated over all trials with the same array configuration (i.e. 1, 3 or 5 WEC array) and incident wave conditions. The confidence interval is computed on the assumption of a Student's t-distribution with $N-1$ degrees of freedom, where N is the number of trials.

3.2.4.1. Single WEC

The RCW response observed for a single WEC in isolation, excited by head on regular waves of nominal wave height equal to 6 cm is given in Figure 10. The RCW at any given period is derived from 2 to 14 trials. The pattern of performance is quite clear and the uncertainty (presented as a 95% CI) is fairly low (on the order of 5 to 10% of expected value). The variability in response may be associated with any number of causes, including but not necessarily limited to differences in: wave gauge calibration error, instrumentation error, as-built model WECs, PTO damping and PTO friction. Clearly, the WEC has a range of frequencies to which the response is quite favorable, but the performance drops off with lower frequency excitation.

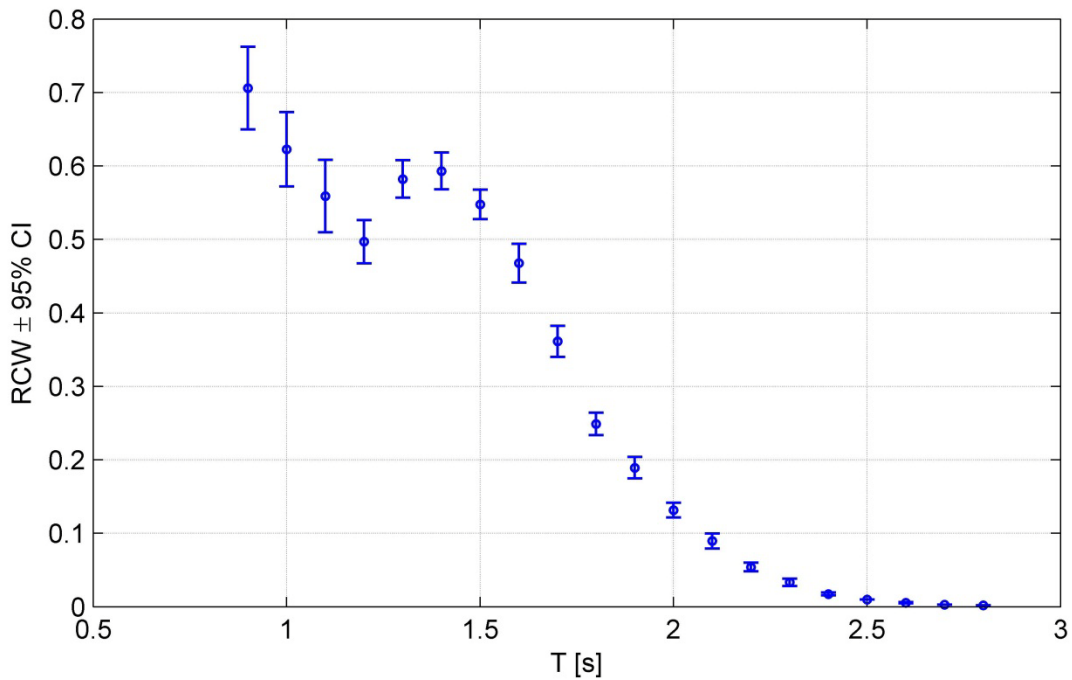


Figure 10. RCW in head on, regular wave conditions.

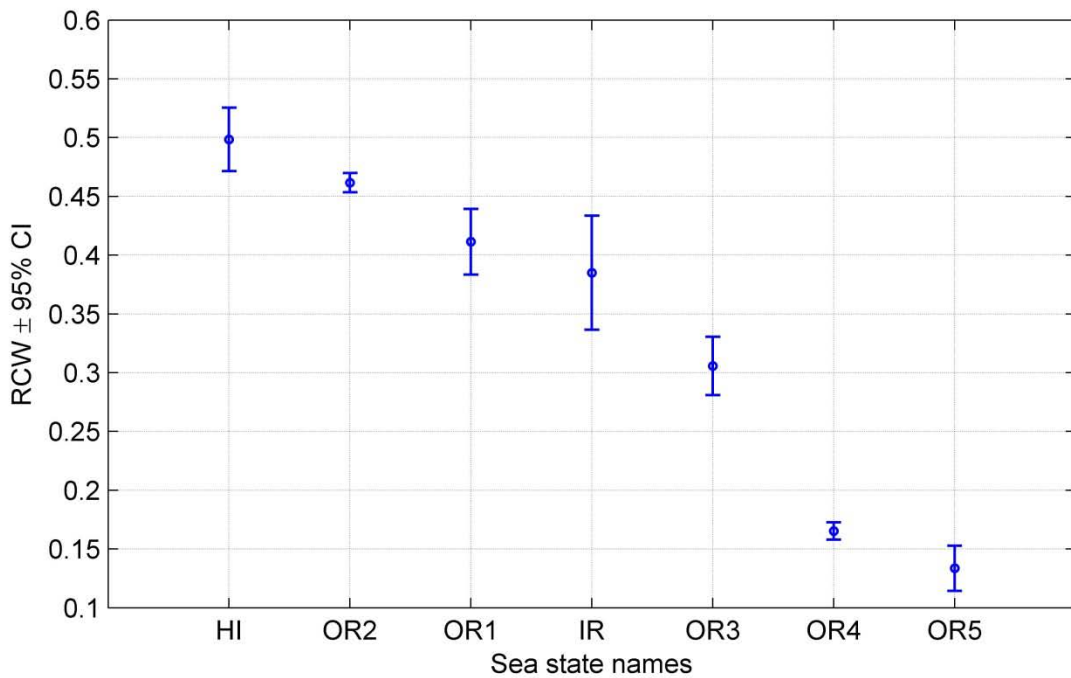


Figure 11. RCW in head on, real seas conditions.

Performance in each of the seven sea states tested are given in Figure 11, with sea states ordered by increasing T_e , followed by increasing Hm_0 . Similar to the regular wave results, it is clear that RCW is reduced in longer period (lower frequency) conditions. Performance is also greater in smaller Hm_0 (for the same T_e); presumably this is due to viscous drag losses (which are proportional to velocity squared). Only one of the model WECs was extensively tested in the full set of real seas conditions listed in Table 1. Two of the remaining four model WECs were tested in a limited number of conditions. The bulk RCW for each sea state is derived from 2 to 6 trials. Although not essential for understanding the results from the perspective of this report (i.e. how array configuration affects performance), keep in mind that the RCW represents a proportion of available wave energy absorbed but not necessarily the magnitude of the energy; although the RCW is lowest for OR5, the absorbed power is in fact greatest for this sea state.

Using spectral analysis, performance as a function of frequency was estimated for real seas cases. Figure 12 depicts the spectral RCW response curves for each sea state individually. The mean response (over all seven sea states) is shown in Figure 13. Note that the RCW response curves shown in Figure 12 extend over a limited range of frequencies. Although the response was calculated up to the Nyquist frequency (25 Hz), it was only deemed significant over the range of frequencies where the incident wave energy was significant. This threshold was set at 0.5% of the incident wave spectrum's peak value of $S(f)$. In the limit as the incident wave

spectrum goes to zero the spectral RCW goes to infinity, as it is in the denominator of the ratio which yields the RCW. When calculating the mean spectral RCW shown in Figure 13, a weighted mean is computed. The weighting function for the ordinate of a given trials spectral RCW was set to zero outside of the range of ‘significance’, and otherwise it was set to the wave elevation variance density at that ordinate. It is assumed that where the input signal was stronger, the output is more significant.

In Figure 14 the RCW derived spectrally from real seas is compared to that derived from a regular wave frequency scan. Note that the response curves are quite similar except for some deviation between roughly 1.3 to 1.7 s. As the response in simulated real seas is expected to be more representative of open ocean conditions than regular waves, it is the spectral RCW that was used to parameterize the wave propagation models discussed in 3.3 and 3.4. Rather than complicate things with multiple RCW curves, it was decided to use the mean spectral RCW curve to represent the WEC response in all conditions.

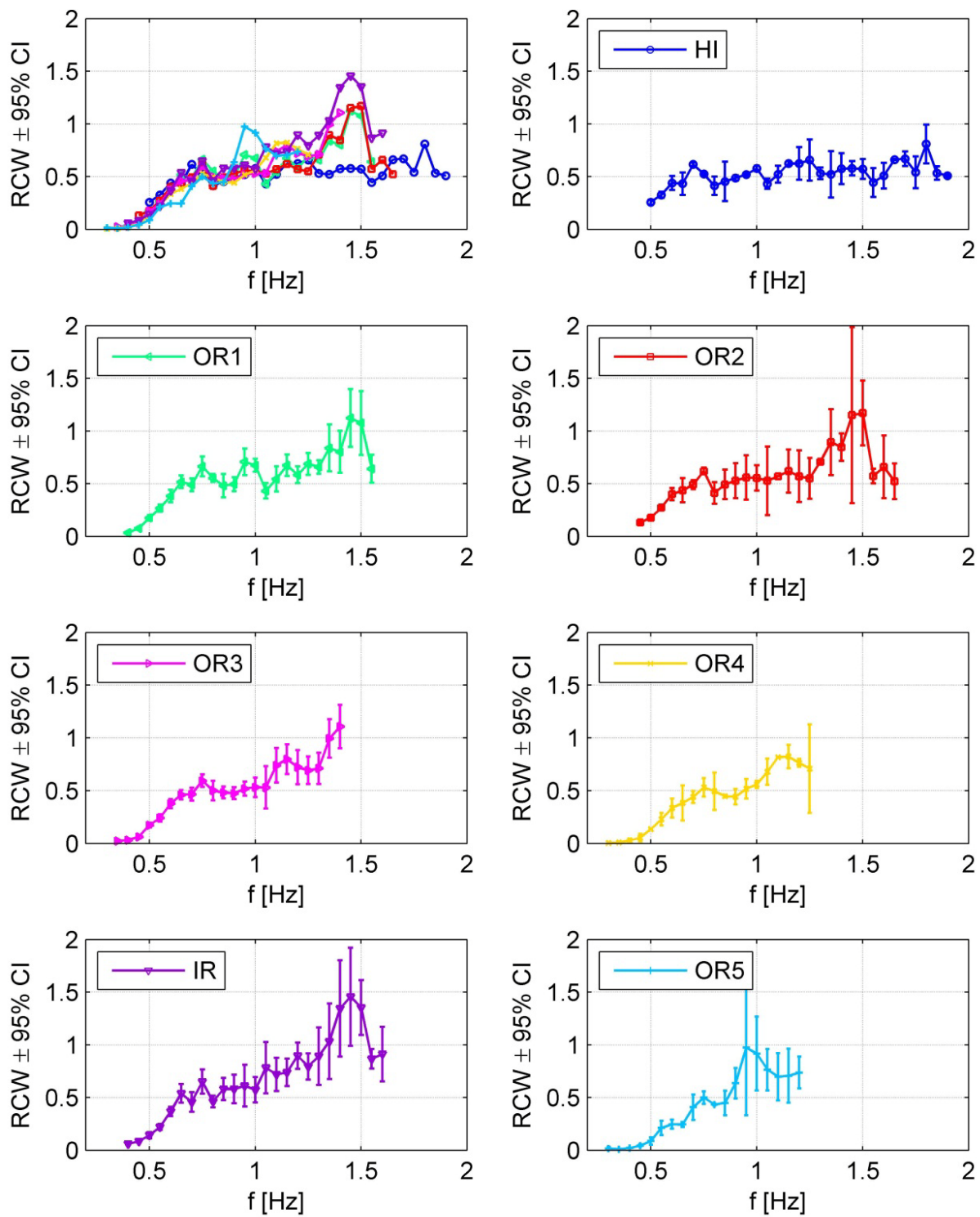


Figure 12. Spectral RCW curves (all curves combined in top left panel).

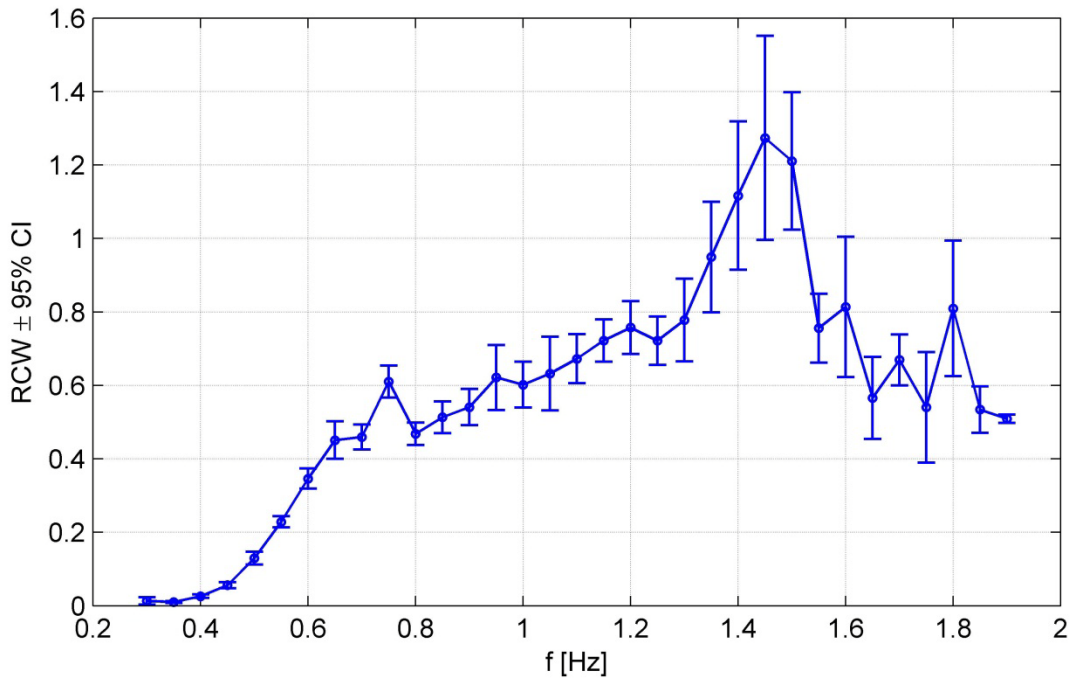


Figure 13. Spectral RCW for single WEC in isolation.

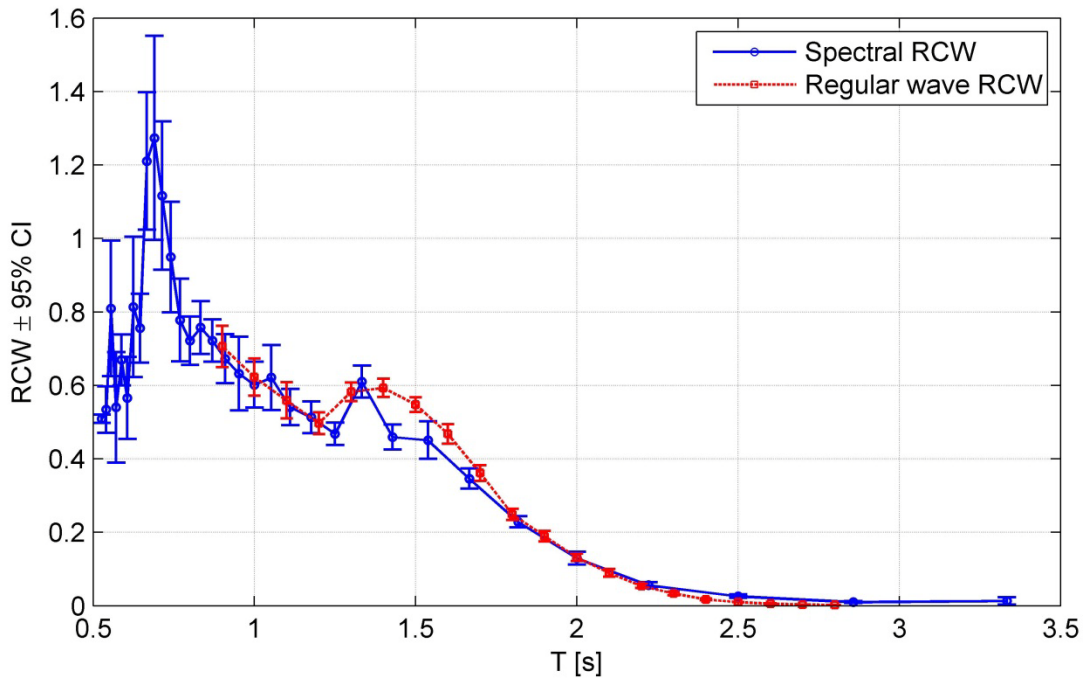


Figure 14. RCW from spectral analysis in real seas compared to RCW from regular wave testing.

3.2.4.2. WEC arrays

The objective at this point is to quantify the response of an array of WECs, and compare this response to that of an equal number of WECs working in isolation. For logistical and economic reasons, it is almost certain that commercial scale WEC installations will involve WECs deployed in large arrays. While it is certainly possible that they will have little impact upon one another, this should not be assumed a priori. This subsection will consider the performance of arrays of 3 and 5 WECs, as well as the performance of each WEC within the array.

The array RCWs derived from regular wave trials are presented in Figure 15, along with the single WEC RCW curve for comparison. The array RCWs are computed as the mean mechanical power of the entire array, normalized by the wave power incident across a crest width equal to N times the nominal width of a single WEC. Although this plot allows the differences in response to be seen, a clearer comparison is had by normalizing the data by the 1 WEC responses, as is shown in Figure 16. These normalized array responses are termed array Q factors, and they describe the relative advantage or disadvantage that the particular array has w.r.t. an equal number of isolated WECs. The CI indicated on the 1 WEC data (whose expected value is identically unity) indicate the uncertainty with which the expected values are known. It is seen that the 3 WEC array has a Q factor of less than unity, and the difference in general is significant. The 5 WEC array, conversely, has a significant performance deficit only at 1.2 and 1.3 s, and a significant advantage for the extreme high and low frequency waves.

Figures 17 and 18 show the Q factors for individual WECs with the 3 and 5 WEC array trials, respectively. In the 3 WEC array, it is arguably WEC 2 whose performance differs most from the isolated WEC. WEC 2 is located behind WEC 1, with WEC 3 abeam but separated by several WEC widths (see Figure 7 for array positions). In the 5 WEC array, WECs 2, 3 and 5 (the three WECs in the back row) could be said to have Q factors significantly below the unity for some of the shorter periods. Conversely, WECs 3 4 and 5 (the three on the south end of the array, where north-south is longshore dimension) are seen to have Q factors significantly above unity for long periods. For an in-depth discussion of near field wave patterns and their potential effects on WEC performance, please see 3.4.

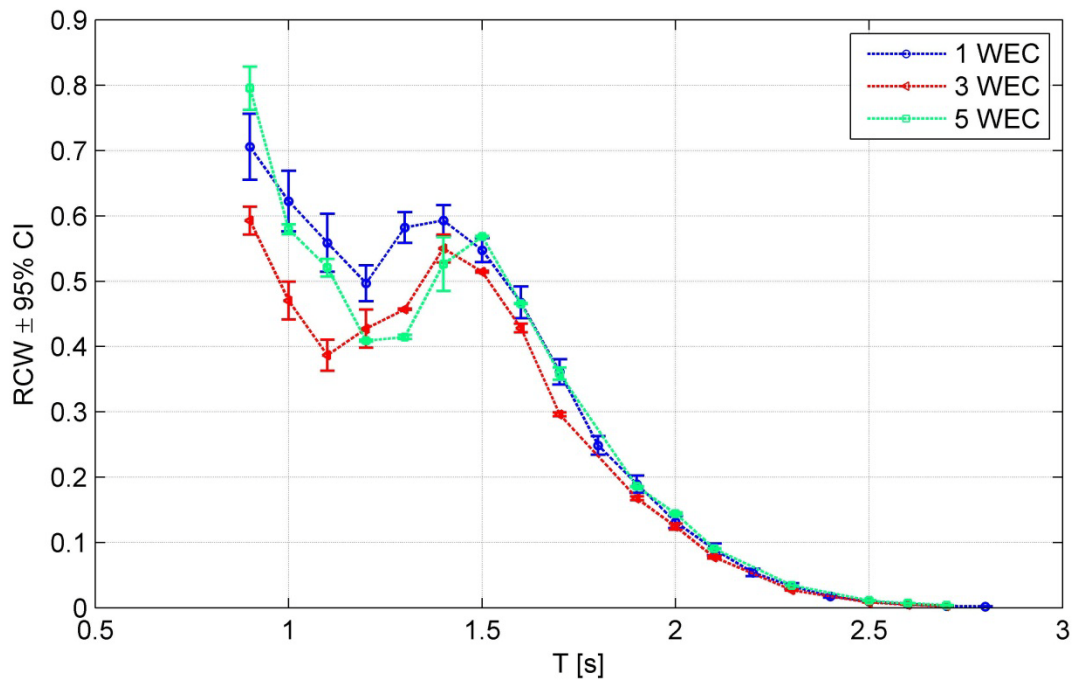


Figure 15. Regular wave RCW for 3 and 5 WEC arrays, compared to single WEC in isolation.

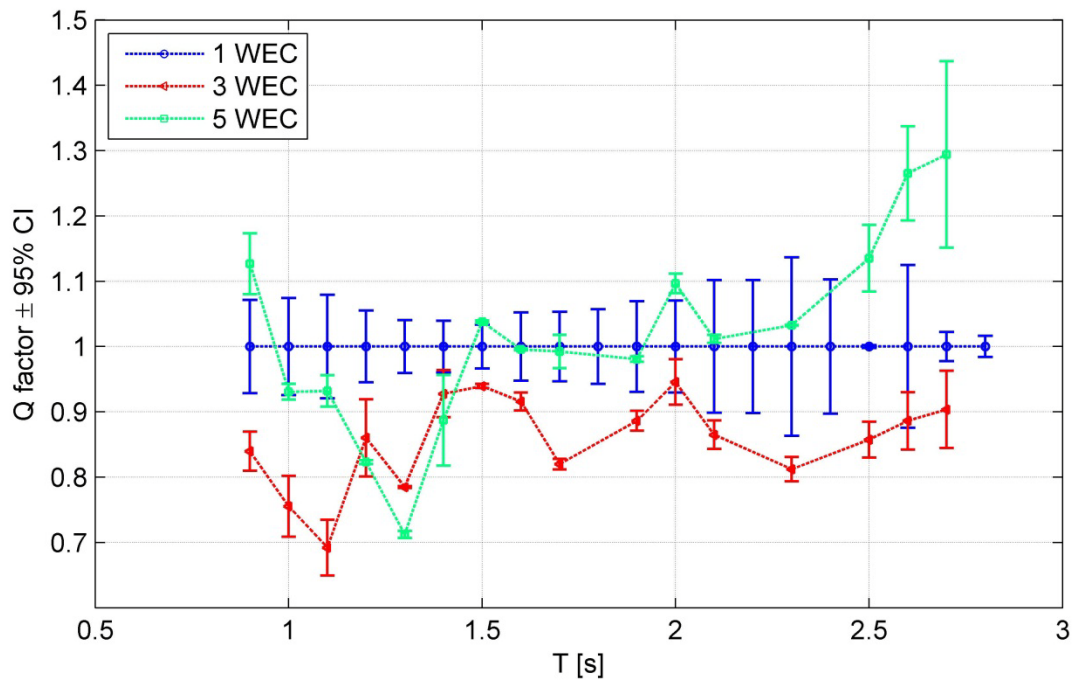


Figure 16. Regular wave Q factors for 3 and 5 WEC arrays, compared to single WEC in isolation.

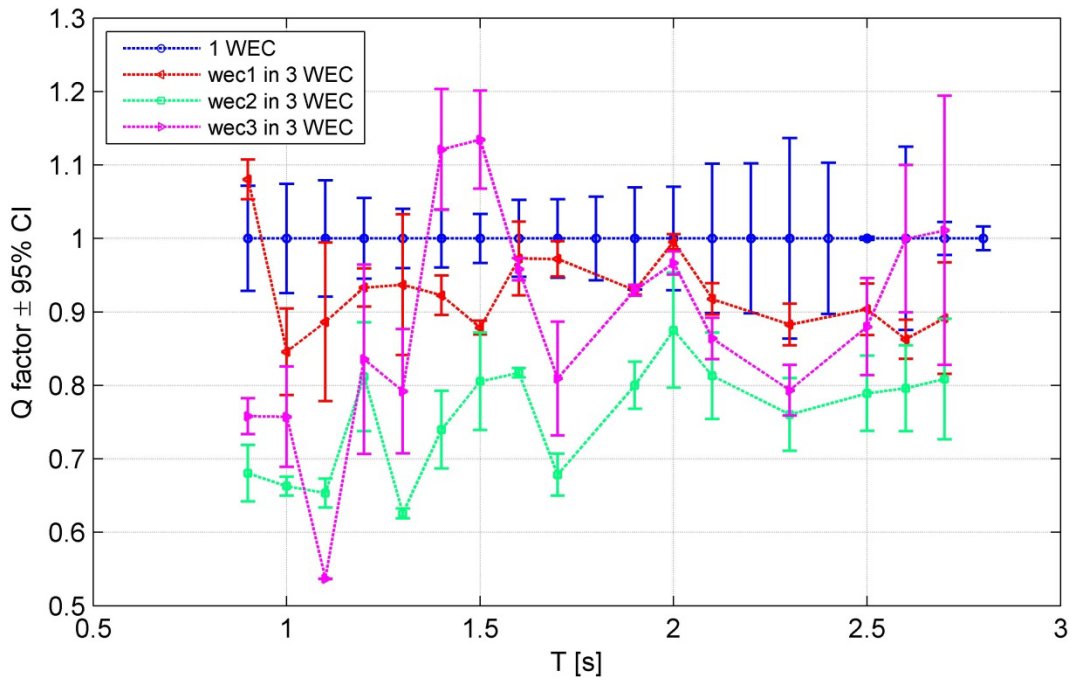


Figure 17. Regular wave Q factors for individual WECs in 3 WEC array, compared to WEC in isolation.

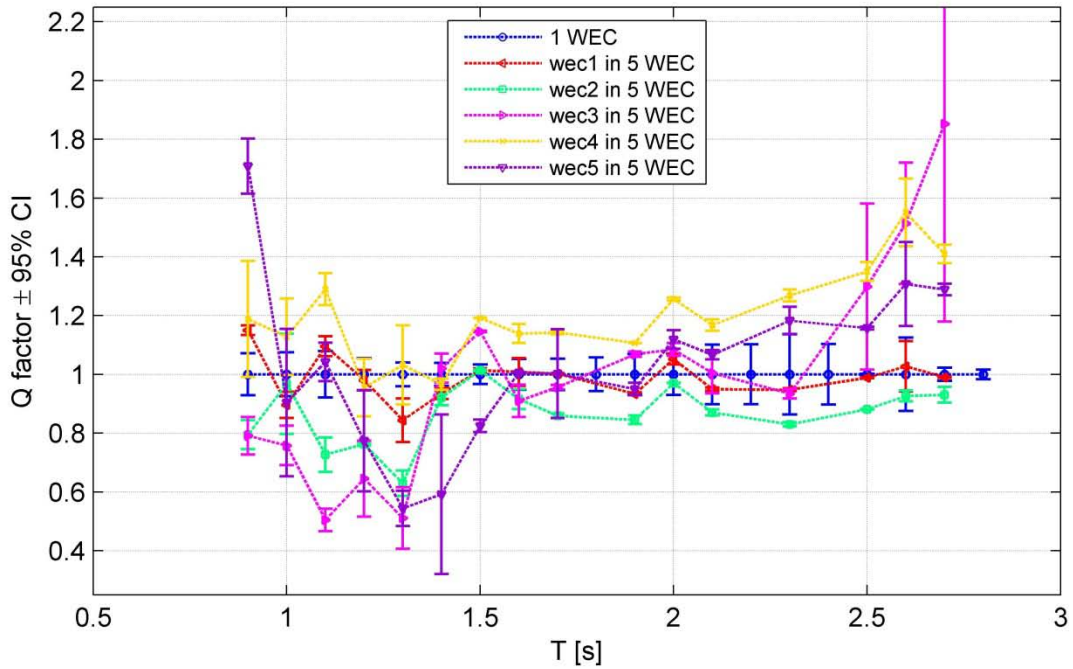


Figure 18. Regular wave Q factors for individual WECs in 5 WEC array, compared to WEC in isolation.

The array RCWs derived from real seas trials are presented in Figure 19, along with the single WEC RCW curve for comparison. The array Q factors are shown in Figure 20. It should be noted that the CIs for the 5 WEC response is non-existent for all but one sea state; this is because only one trial remained for the other six sea states after removing trials from consideration due to PhaseSpace errors. That being said, a pattern is seen that is somewhat similar to the regular wave trials; the 3 WEC array has a Q factor significantly below unity for many of the cases, while the 5 WEC array is generally on par with the 1 WEC trials.

Figures 21 and 22 show the Q factors for individual WECs in the 3 and 5 WEC array trials, respectively. Once again, similarities to regular wave responses are seen in this data. For the 3 WEC array, WEC 2 (behind WEC 1) is once again seen to underperform w.r.t. the other WECs in the array. In the 5 WEC array, WECs 2 3 and 5 (behind WECs 1 and 4) tend to underperform w.r.t. the offshore WECs. That being said, WEC 4 performs significantly better than WEC 1, while both are in the offshore side of the array. As they are symmetrically positioned in the array, this is difficult to understand. Differences in as-built model WECs, errors in damping estimates, or spatially inhomogeneous wave conditions are all possible explanations.

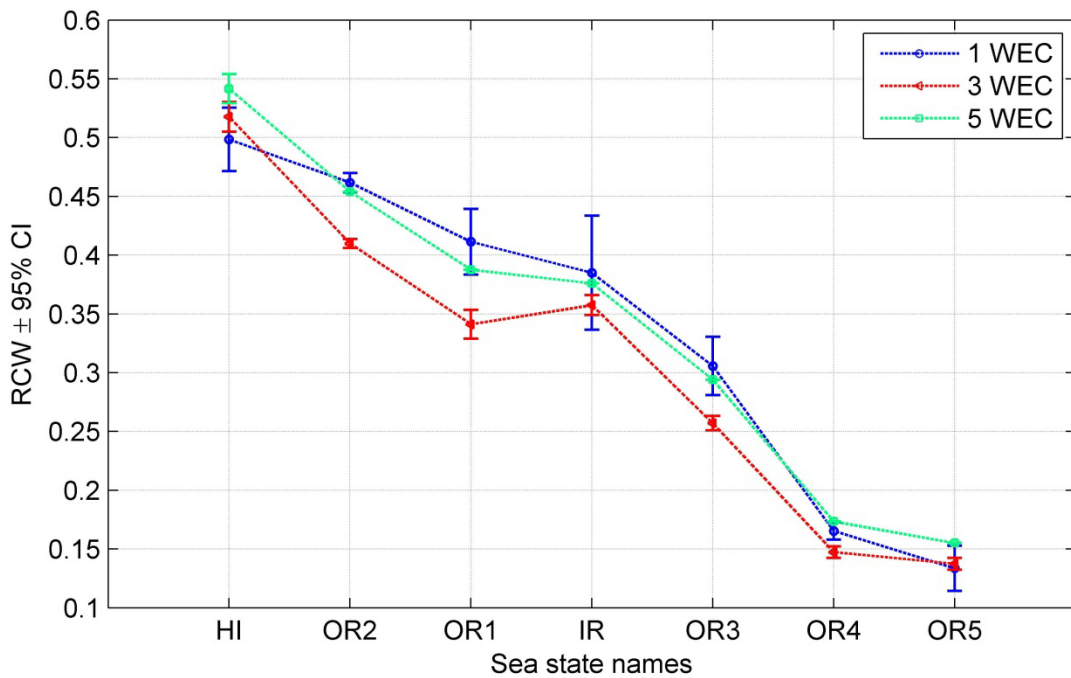


Figure 19. Real seas RCW for 3 and 5 WEC arrays, compared to single WEC in isolation.

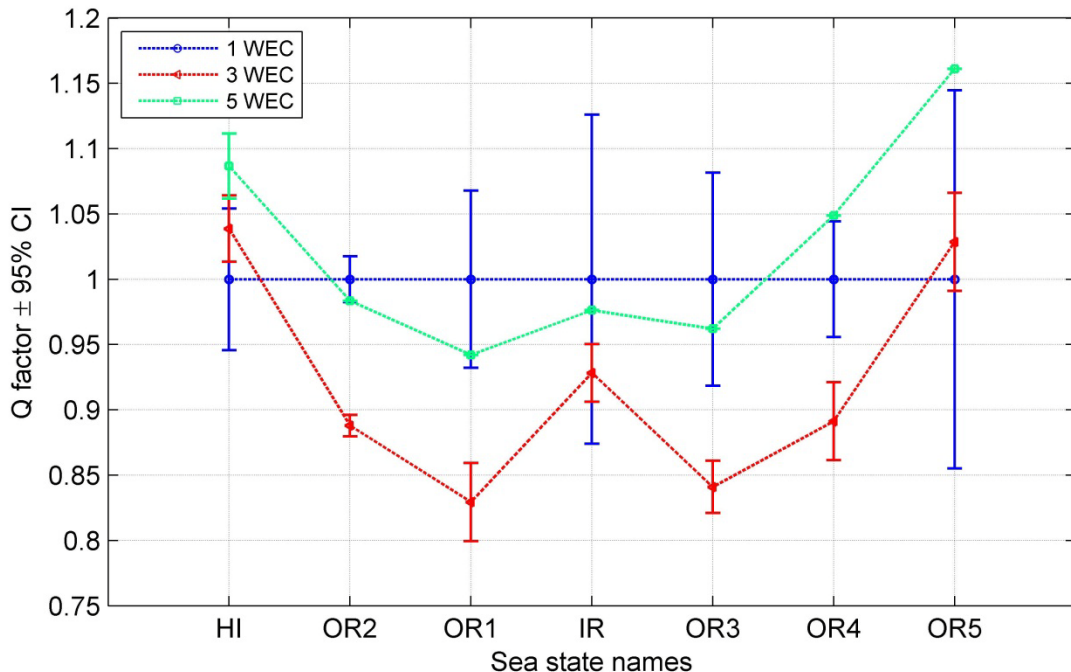


Figure 20. Real seas RCW for 3 and 5 WEC arrays, compared to single WEC in isolation.

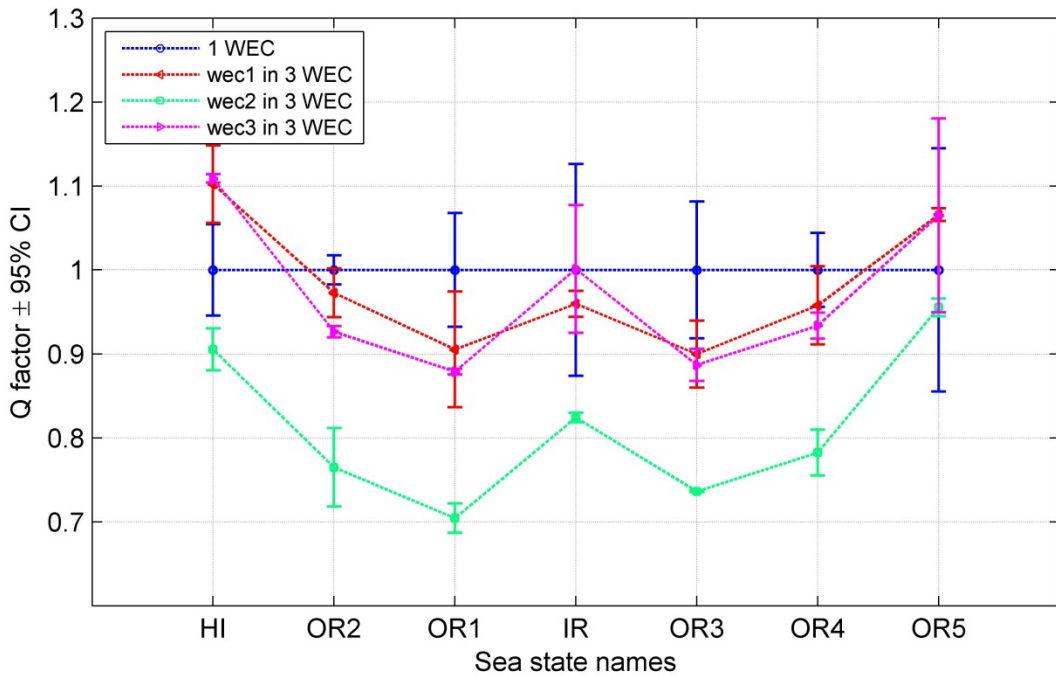


Figure 21 Real seas Q factors for individual WECs in 3 WEC array, compared to single WEC in isolation.

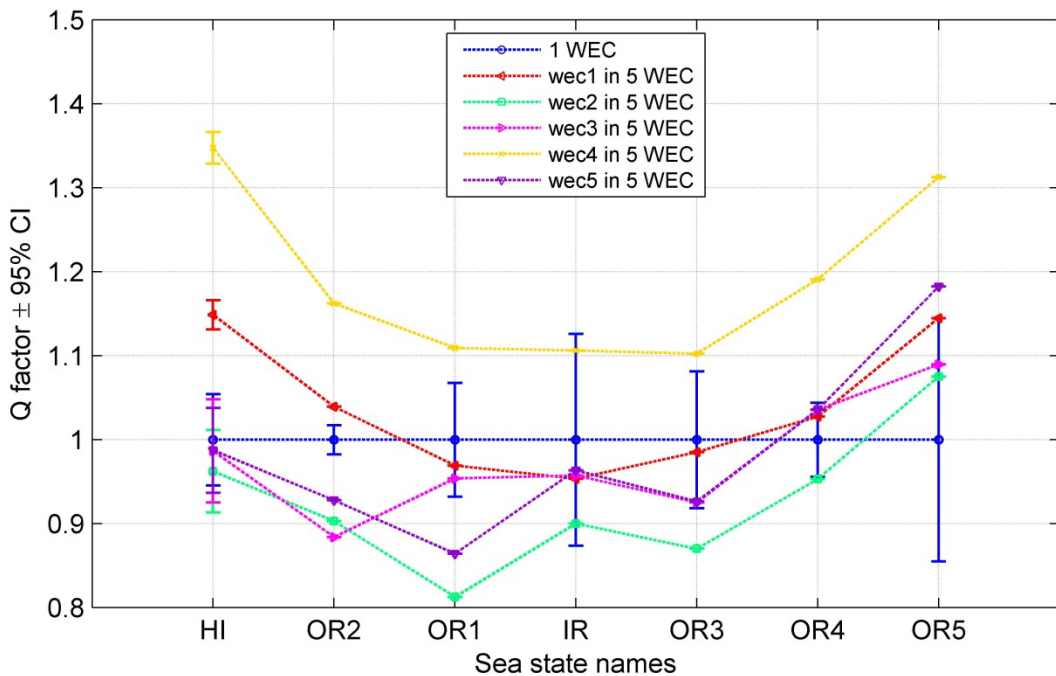


Figure 22 Real seas Q factors for individual WECs in 5 WEC array, compared to single WEC in isolation.

3.2.5. WEC Conclusions

Models at 33rd scale representing ColPwr's Manta series v3.1 WEC were extensively tested in configurations of one, three and five WEC arrays, with both a series of regular wave conditions as well as directionally-distributed spectral sea states. Performance was quantified via RCW for both the individual WECs and for each WEC array as a whole. Over the range of wave frequencies generated, the WEC to WEC spacing was on the order of 0.5 to 6 wave lengths.

Generally speaking, performance is seen to be positively correlated with the incident wave frequency. Conversely, performance is negatively correlated with incident wave height. The mean spectral RCW, calculated over seven real seas conditions, compares favorably, over a significant portion of the frequency spectrum, with the RCW curve derived from regular wave trials. This mean spectral RCW curve is expected to be more representative of a WECs performance in real seas; as such, the spectral RCW was used as the basis for WEC-array parameterization developed for numerical wave propagation modeling.

In addition to RCWs, array performance is quantified via a Q factor: the ratio of performance in an array to expected performance of a single WEC in isolation. The overall trend in performance is just as with single WECs; performance is positively correlated with wave frequency and negatively correlated with wave height. In regular wave conditions, Q factors for the 3 WEC array were typically less than unity, on the order of 0.9. Q factors for the 5 WEC array were below unity around 1.2 to 1.3 s range, but were above unity for waves of 2.5 s and above.

In real seas conditions, array performance once again was seen to trend alongside the individual WEC results. The 3 WEC array has a Q factor of less than unity for most of the sea states (on the order of 0.9), while the 5 WEC array has a Q factor near unity for most cases. In the 5 WEC array, array effects appear to be less prominent than in the 3 WEC array. It is not immediately clear why this should be, but perhaps the effects of any standing wave patterns generated by the WECs are reduced as multiple patterns superimpose.

The laboratory experiments and wave modeling work undertaken in this project also served as the basis for two Masters Theses in Coastal & Ocean Engineering. The Theses are entitled "Laboratory Observations and Numerical Modeling of the Effects of an Array of Wave Energy Converters" by Aaron Porter and "Wave Field Patterns Generated by Wave Energy Converters" by Cameron McNatt. They are presented verbatim in Appendices 12 and 13 and each is summarized below.

3.3. Executive Summary: Laboratory Observations and Numerical Modeling of the Effects of an Array of Wave Energy Converters (Appendix 12)

The results from the WEC-Array experiments showed that the wave shadow is a function of wave period. In addition, the WEC power capture was well correlated with the observed degree of wave shadowing. This is an indication that WEC power capture (as opposed to scattering induced by WECs) is the primary driver of wave shadowing for the tested conditions. Deviations from this behavior were observed for wave periods in the range $T = 1\text{-}1.4$ seconds, especially under regular waves. This is an indication that scattering from the devices is more important for those smaller wave period conditions.

One of the challenges that arose in the data analysis was how best to characterize the incident wave power for a given test condition. This was especially challenging for the 3-WEC and 5-WEC arrays as there was a clearly observed backscattering of wave energy from the larger arrays that affected wave gage measurements. In this work it was determined that the incident conditions measured during the 1-WEC tests would serve as the standard estimate for characterizing the 3-WEC and 5-WEC tests.

The report also provides details on the magnitude of the power deficits for the various WEC-array sizes and the tested wave conditions. A priori we had expected that the power deficits would be difficult to measure, and significant experimental resources were expended on instrumenting the lee of the WEC-array. However, the results have shown that the power deficits (i.e. the wave shadowing induced by the WEC-arrays) were clearly measurable. The net power deficit was shown to scale up approximately linearly as the number of WECs increased from 1 to 3 to 5 in the arrays.

After the WEC-array shadowing analysis was performed on the laboratory data, we designed a WEC-array parameterization for use in the spectral wave transformation model SWAN (this parameterization is generic and could be used in any spectral wave model). The parameterization treats the WEC-array as a sink of wave energy with energy losses (i.e. capture by the WECs) dependent on wave frequency and calibrated to the measured performance of the CPT WECs. The parameterization was then implemented into model simulations of the laboratory experiments. It is important to note that the parameterization was developed based on the measured WEC performance (i.e. the motion capture data) as opposed to the observed wave shadowing. Hence, the model simulations represent an independent test of whether a WEC-array parameterization based only on WEC power absorption characteristics can effectively simulate wave shadowing by WEC-arrays. The simulations were performed for regular wave conditions and real seas conditions for which the mean wave angle was normally incident to the WEC-arrays. The wave modeling results indicated that the wave shadowing induced by WEC-arrays can be effectively simulated using the developed WEC-array parameterization. However, the simulations degrade noticeably for short wave periods where the importance of scattering increases significantly. Scattering at higher frequencies is a technology specific characteristic, thus when assessing WEC power absorption as a function of frequency it is equally important to quantify WEC reflection coefficient and this scattering should not be neglected without complete WEC characterization.

3.4. Executive Summary: Wave Field Patterns Generated by Wave Energy Converters (Appendix 13)

In this study, the WEC wave field is investigated for a single WEC and a five WEC array using model computations and results are compared with experimental data. Both regular waves and spectral seas are considered. Computational results are produced with the linear boundary-element-method (BEM) hydrodynamic software WAMIT for a simplified WEC geometry that is representative of the CPT device. Experimental data comes from the set of WEC-array experiments that took place at Oregon State University over the winter of 2010-11. The experimental measurements help validate the computational modeling, and the computational models serve as an aid to interpreting the experimental data.

Results reveal two universal WEC wave field features - partially standing waves and a wave shadow, both of which are the result of the coherent interaction of the incident waves with the circular waves generated by WECs through the processes of diffraction and radiation (i.e. scattering). The partial standing waves in the offshore are seen qualitatively in the experimental data but could not be exactly reproduced computationally, because the computational model is only a simple representation of the physical model. In the lee of the WEC, the measured alongshore structure of the wave shadow is in good agreement with theoretical expectations as well as computational results. It is believed that the agreement is because the formation of the wave shadow is dominated by energy extraction (i.e. power capture by the devices), which was approximately the same for both the computational and physical models.

The positions and magnitudes of the offshore partially standing waves are very sensitive to wavelength, and WEC geometry, motions and location, and in spectral seas, the variations in significant wave height are relatively smoothed. All of which suggest that it may be difficult to use them advantageously in the design of WEC arrays. The wave shadow is a dominant feature of the WEC wave field for both regular waves and spectral seas. It appears to be fairly generic and to be based on power absorption. In the design of WEC arrays, rather than attempting constructive interference by using standing wave crests, perhaps the best one can do is to avoid destructive interference effects of the wave shadow.

Results from the WAMIT-SWAN comparison showed us that the difference between the predicted shadow and measured shadow was due to scattered short waves caused by additional hydrodynamic interactions of the WEC with the incident wave field. An investigation into the ability of the spectral model SWAN to predict WEC-effects on the wave-field against a phase-resolving model, WAMIT, proved extremely useful in determining scattered waves as the sources of difference between SWAN and observations.

The extensive experimental data set validated not only the SWAN model, but the WAMIT model as well [McNatt, 2012b]. It provided us with great insight for investigating effects of WEC arrays on the wave-field, and the subsequent modeling.

In addition to the WEC-array experiments and associated modeling, the WAMIT SWAN model comparison showed us that with diffraction on, or in directionally spread seas, SWAN is able to make good predictions of the magnitude and shape of the wave shadow in the lee of a single device, except at small wave periods. In directionally spread seas, having diffraction "on" or "off" did not make an observable difference in results. The short wave periods tested showed that SWAN underestimates the wave shadow because of increased scattered short waves. Because of these findings the WAMIT-SWAN comparison gave great insight into what roles the different wave field physics play in wave shadows, and improved our understanding of the empirical data set.

4. Key Cost/Performance Drivers Identified

This project's objectives were to develop an understanding of the affects of WEC arrays on the wave climate in order to develop predictive tools for environmental impact assessment. Our findings regarding the effects on wave climate are covered in depth in section 3. In addition to the project objectives, we came away from this work with some additional findings and "lessons learned" that we describe below in the hope that they might aid in evaluating individual WEC and WEC-array performance in future testing efforts

4.1. Array design

This project experimentally demonstrated how the near-field wave conditions are modified by WEC's within an array, such that individual WEC performance has some dependency on the respective physical placement within the array. These affects are driven by wave frequency, the dominant incident wave direction, and the directional spreading within the wave spectrum, and scaled by WEC spacing within the array. Wave height also has some influence, and, of course, the specific WEC design is a primary aspect, being as there is a wide range of potential WEC designs. This report has also outlined techniques for modeling and generating numerical predictions for specific wave conditions, WEC designs, and WEC-array configurations.

Generalizing these results, the most obvious recommendation for a cost effective array would be to physically optimize the design for the specific range of wave lengths and directional spreading encountered at a potential wave farm site, such that each WEC is physically located outside of the low energy shadow caused by all other WECs. Following this recommendation means avoiding tightly spaced arrays and wave conditions where diffraction and radiated waves are dominant and avoiding the wave shadow is more difficult. Simply modeling such situations and characterizing the wave shadow requires more detailed near-field, phase-resolving models that are computationally intensive. Fortunately, the present effort points the way to avoiding those

conditions, such that a spectral modeling approach with power absorption as the dominant process will be an effective design tool for predicting environmental effects.

4.2. Scaled array experimental design

When we consider laboratory scale projects where the number of WECs is necessarily limited and when we consider a diverse set of wave conditions that bound the range of expected conditions in the real ocean, there are many scenarios where the affect of the WEC-array on the wave climate is small and can be challenging to measure. For this project, the spacing within the WEC-array was arranged to be tight (80 m full-scale equivalent) in order to maximize the array shadowing “signal” and increase the probability of identifying the arrays affects on the wave climate. That is not to say that WEC-arrays only have a minimal effect on the wave climate, it is just that 3-WEC and even 5-WEC arrays are not large. They are certainly not as large as what is being called for in many of the proposed commercial WEC-array designs. So, by necessity, in the laboratory we are working with relatively small signals. Hence, through this effort we have identified some key factors that should be considered in the design of future experiments and testing.

- Quantifying the incident wave conditions in the presence of a WEC-array is challenging. The key challenge is that the WEC-array scatters waves; hence, even the wave field offshore of the array is modified by the presence of the array. So the “true” incident wave conditions are unknown. The cleanest way to solve this issue is to run all wave conditions of interest in an empty tank (i.e. a tank without WECs but *with* wave gauges). This, of course, increases the testing time required and requires the mental fortitude to persevere through testing conditions where your primary interest (WEC performance) is not being considered.
- WEC performance and power capture are strong functions of wave frequency, i.e. WECs are designed to be efficient at capturing energy over only a finite range of frequencies. This range is typically smaller than the natural range of frequencies that exist under ambient conditions. Hence, as a function of frequency, the signal of power capture and the signal of wave scattering and shadowing ranges from significant and measurable to small and challenging to discern. In addition, the wave field effects contain a lot of structure (high spatial variability) in the near-field (in and around the WEC-array) and then smooth out to more broad scale patterns in the far-field. This level of complexity is difficult to capture with a finite number of in situ wave gauges. In our opinion, there does not yet exist a good solution for the near-field problem, which is why experimental efforts attempting to maximize WEC performance through unique array design spacing should be considered qualitative, at best. There are simply too many complicating factors and the directional wave spectrum within the array is essentially un-measurable. On the other hand, measuring the far-field wave effects is definitely achievable. As our results will attest.

- Even in the laboratory, WECs are complicated machines and a set of WECs cannot be carbon copies of each other. Hence, different WECs will demonstrate different performance even under the same incident wave conditions. Hence, the performance of each individual WEC needs to be characterized before the WECs can be evaluated in an array configuration. This adds to the necessary testing time.
- The previous items have described considerations that necessarily add to the testing time required for experimental efforts. Settling time between tests (i.e. waiting for wave motions to decay due to friction in between tests) can be reduced and the wave field can be made “cleaner” if the wave tank facility has the capability for wave absorption, passive and/or active.
- There are three main experimental aspects that wave gauge resources can be assigned to: 1) offshore wave conditions, 2) near-field wave conditions, and 3) the far-field conditions. All of these aspects require an array of wave gages (rather than a single point measurement) because the wave field will have directional characteristics everywhere due to scattering from WEC-arrays. It is highly likely there are not enough resources to measure all three of these aspects effectively. Decisions have to be made.
- Power take off (PTO) design and implementation at small scales introduces compromises in perfectly matching the full scale mass, inertia and torque (or force). This challenge combined with performance variance caused by the PTO adds more uncertainty to the results. Proper scaled PTO selection and design is crucial to ensure sufficient accuracy.
- WEC data measurement needs to be sufficient for measuring position, velocity and torque (force) with a high degree of accuracy in testing of this nature. When testing five or more WECS, an intensive data collection system is required.
- Both data measurement and motion tracking systems may require a power source on WEC and data transfer from WEC to shore. Due to low forces at this scale, the use of wires/cables to transfer power to the WEC or wires that transfer data from the WEC run the risk of affecting the WEC motion.
- Targeted WEC mass and CG are difficult to achieve on small scale WECS due to high mass of the PTO and other hardware needed on the WEC. Lower mass PTO solutions would improve model accuracy.
- Mooring lines used (light weight elastic) stretched out and changed stiffness properties over time. Accurately scaled mooring solutions would improve future WEC tests.
- A Wide basin is needed for array testing (unless the array is simply a line of WECs oriented parallel to wave travel). The one used at HWRL is such a basin, but for 33rd scale modeling was limited to full scale depth of 45 m or less; deployments will likely be in deeper water, a deeper tank is needed.
- As mentioned previously, at laboratory scales the WEC-array effects we seek to measure can be small. Hence, wavemaker performance curves are required at a level of accuracy

not typically required for most coastal process studies. Having performance curves available at a higher level of accuracy (this level of accuracy was not available for our tests) would increase the efficiency of the testing process.

4.3. Array spacing

During design of experiment for this project, it was apparent that no commercial solution is available to construct a tightly spaced WEC array and that present mooring and electrical cable solutions require large spacing between WEC's. Designs, equipment and methods for reducing the physical space between WECS may reduce array costs and improve the utilization of the wave resource.

5. Recommendations for Future Work

The experimental data set collected herein is extensive and there is more to be learned through follow-on efforts. For example, our ongoing research through the auspices of Northwest National Marine Renewable Energy Center involve: 1) investigating the influence of wave directional characteristics on the far-field wave climate, 2) incorporating our WEC-array parameterization into field-scale environmental studies for environmental assessment of potential WEC-array sites, and 3) supporting collaborative efforts in the development of wave/wec interaction models by supplying our data for model/data comparisons. In addition, we summarize the following further recommendations that were derived from our experience developed during the project. These may be useful for future full scale array design efforts or scaled experiments.

5.1. Methods for reducing the physical space between WECS

Designs, equipment and methods for reducing the physical space between WECS may reduce array costs and improve the utilization of the wave resource. Numerous design opportunities could be explored that aim to increase WEC density in an array. These design opportunities likely hinge on improved mooring and cabling solutions.

5.2. Baseline modeling tool for array design

In the short term, WEC array designs should perhaps consider configurations that avoid low energy zones created by wave shadows and place less (or no) emphasis on attempting to gain performance through constructive interference, as our results suggest that any such gains are likely small and certainly highly transient as wave conditions change. A design tool that includes all parameterized inputs of WEC energy absorption, WEC spacing, site bathymetry and site wave conditions and outputs a recommended array design layout and spacing could be used as an initial baseline tool that aids in designing WEC arrays. The physics to build such a tool already are understood, the challenge is that results hinge on the power absorption and wave scattering

performance of individual WEC designs, of which there are many, and the lack of field scale performance data with which to validate the design tools.

5.3. Experimental solutions

Cost effective approaches that improve the experimental tools for scaled WEC testing are needed. The marine industry has reliably and effectively tested ships and structures for decades and those methods have served the need well. However, through the experience of this project and previous WEC testing, those tools do not fully meet the needs for experimentally assessing WEC performance. A number of recommendations from Section 4.2 would require instrumentation or equipment that is not presently commercially available, the following experimental equipment, instrumentation or tools would aid in future array and single WEC testing:

5.3.1.1. Motion tracking solution for multiple bodies

The Optical motion tracking system (PhaseSpace) generally performed admirably, but had problems in particular when tracking 3 to 5 WECs (up to a total of 15 bodies with 90 discrete LED's), resulting at times in poor quality or no data. A system to track multiple bodies in water, accurately and precisely, is essential for array physical testing. WEC's with three moving bodies in arrays with five WECs require that the motion tracking system be capable of tracking at least 15 bodies and perhaps more for larger arrays.

5.3.1.2. Scaled Mooring system

Improved scale mooring hardware should be developed that follows a scaled force displacement curve of the intended full scale mooring that minimizes the effects of viscous drag at smaller scale. Such a system is under development: A programmable mooring controller (PMC) jointly developed under another project by Columbia Power, OSU and NREL is being tested presently (November 2012).

5.3.1.3. Development of low cost and accurate scaled PTO's

PTO's should be highly repeatable from test to test and over an extended period (weeks) of use. PTO mass, inertia and torque (force) should be scalable to assure PTOs are accurately simulated and should have minimal affects from friction, backlash or hysteresis; such PTO's are not commercially available. WEC testing can benefit from small, light weight, low inertia, low friction and high torque motors/generators or actuators.

5.3.1.4. Wireless WEC data/control systems

Light weight experimental packages that provide wireless data transfer to shore and wireless self-powered on WEC data acquisition and controls systems would benefit scaled WEC testing.

5.3.1.5. Accurate Self calibrating wave gauges

Precise wave measurements are essential for tests of this nature. Self calibrating gages allow for improved gage accuracy in conditions where water conductivity and gage readings vary with

time or temperature. OSU's wave lab (HWRL) is presently (November 2012) testing the use of self calibrating gages.

5.4. Advanced array design tools

The end goal of research in projects such as these are to support the development of methods and tools that can accurately and cost effectively evaluate all WEC-wave influences including energy shadow, diffracted and radiated waves from a single WEC and then extend these results to a full-scale array in real seas. In the present work, emphasis was placed on the conditions under which wave absorption was the dominant process and we have developed a tool that works effectively at predicting the far-field wave effects under these conditions. However, assessing the diffraction and radiation effects in WEC-arrays remains a modeling challenge and a challenge to experimentally verify. Methods and tools that accurately and cost effectively evaluate the diffracted and radiated waves from a single WEC could aid in future array experiments and modeling. Such tools would lie in the middle ground between high-resolution, computationally intensive wave/structure interaction models and the large-scale wave transformation and environmental modeling that are required for field-scale, commercial design. These large scale modeling tools are presently inherently limited by their degree of accuracy in parameterizing the near-field wave effects of particular WEC-array designs.

5.5. Assessment of environmental influence

In this test, a 5-WEC array with 80 m mean spacing (in prototype) was shown to have a measurable effect on the wave environment. Also, based on the experimental results, a tool was developed to simulate these wave effects and the tool was verified at lab scale against the experimental data. Presently, one of our ongoing efforts under NNMREC funding is to use this tool to extrapolate these results to larger WEC-arrays (50-100 WECs) placed in potential wave energy development field sites.

Though it was successful, this effort was only intended to address a portion of what is needed to fully characterize the environmental effects of WEC-arrays. In general, a list of what is needed for environmental characterization is as follows:

- a) Baseline study – characterizing the local wave resource and the pre-existing environmental conditions (including natural variability of the system).
- b) WEC design and performance characteristics – size, shape, and motion characteristics of the WECs, power absorption capabilities, and mooring design.

- c) WEC-array parameterization – wave model sub-module capable of describing the near-field wave effects in a bulk fashion (*note: the accuracy of this sub-module is highly dependent on the understanding of the wave resource and item b*)).
- d) Coastal-scale wave transformation model – spectral models such as SWAN (or equivalents) are likely sufficient here for typical point-absorber WEC-array design, but accuracy will only be as good as the accuracy of item c).
- e) Environmental modules – this is a suite of models that simulate the environmental effects, e.g. nearshore currents, sediment transport, shoreline change, or ecological aspects. The wave transformation model outputs and the baseline study (e.g. local sediment characteristics, bathymetry) serve as inputs to these models.

As evident from this list, the assessment of environmental influences of WEC-arrays can be viewed as unidirectional flow chart, Step a leads to Step b leads to Step c etc. etc. Speaking for the industry as a whole, many baseline studies (Step a) have either been completed or are well under way for the high-priority development sites. Work is continuing on Step b, but as it is mostly under the purview of developers, most results are proprietary. Step c is a huge existing knowledge gap and our project concentrated much effort there. Step d and Step e are mostly solved problems, in the sense that useful engineering models already exist (though significant efforts continue to improve their accuracy). What remains is to apply these models to specific sites, but the results will hinge on the preceding steps.

What was unique about our project was that: Step a was prescribed (we were working under controlled conditions), Step b was part of the project scope and the results were fully utilized by our academic-industry partnership, and Step c was also a primary new result of our project. Steps d and e were not part of our project scope; however, the results of Step c are now ready for incorporation into environmental assessment efforts (within the bounds of the conditions for which they have been verified) for sites of interest.

In our opinion, the knowledge gaps that remain in the context of this environmental assessment list are as follows (in ranked order):

1. WEC-array parameterizations for designs where scattering is a dominant process (or perhaps the industry should avoid such designs).
2. The impact of mooring solutions on WEC performance and on environmental effects. It is possible that the mooring configurations for very large scale arrays could be a more dominant driver of environmental effects than the WECs themselves.

3. WEC-array parameterizations for other WEC designs (though in theory, the parameterization we developed can be easily adapted to other designs, as long as their performance characteristics are supplied).
4. How to incorporate the rate of change in the baseline conditions (e.g. due to climate change) into WEC-array design – and what is the design lifespan?

6. Project Summary

Briefly summarizing the results—computational results were produced with the linear boundary-element-method (BEM) hydrodynamic software WAMIT for a simple WEC geometry. Results reveal two universal WEC wave field features - partially standing waves and a wave shadow, both of which are the result of the coherent interaction of the planar incident wave with the circular generated wave, composed of the diffracted and radiated waves. The partial standing waves in the offshore are seen qualitatively in experimental data but could not be exactly reproduced computationally, because the computational model is only a simple representation of the physical model. In the lee of the WEC, the measured longshore structure of the wave shadow is in good agreement with theoretical expectations as well as computational results. It is believed that the agreement is because the formation of the wave shadow is dominated by energy extraction, which was approximately the same for both the computational and physical models.

The positions and magnitudes of the offshore partially standing waves are very sensitive to wavelength, and WEC geometry, motions and location, and in spectral seas, they are smoothed when considering significant wave height. All of which suggest that it may be difficult to use them advantageously in the design of WEC arrays. In the design of WEC arrays, rather than attempting constructive interference by using standing wave crests, perhaps the best one can do is to avoid destructive interference of the wave shadow.

The observed wave measurement and WEC performance data sets allowed for a direct computation of power removed from the wave field for a large suite of incident wave conditions and WEC array sizes. To numerically represent WEC effects in the SWAN spectral wave model (a large scale “area” model) the influence of the WECs upon the wave field was parameterized using the power absorption data from the WECs. It was of interest as to whether this parameterization, which does not account for wave scattering among other physics, could provide a good estimate of far-field effects. Considering the complexity of the problem, the parameterization of WECs by only power absorption turned out to be a reasonable predictor of the effect of WECs on the far field for cases that were not dominated by wave diffraction effects.

7. Products

7.1.1. Experimental data

Data from the set of laboratory experiments is publicly available through NNMREC (link is pending). The data has already been shared with researchers at Sandia National Laboratory, Garrad Hassan, and other collaborators.

7.2. Papers written

Haller, M.C., A. Porter, P. Lenee-Bluhm, K. Rhinefrank, E. Hammagren, T. Özkan-Haller, D. Newborn, Laboratory observations of waves in the vicinity of WEC-arrays, *Proceedings of European Wave and Tidal Energy Conference (EWTEC 2011)* (peer reviewed), Paper No.419, 2011.

Porter, A.K., M.C. Haller, and P. Lenee-Bluhm, Laboratory observations and numerical modeling of the effects of an array of wave energy converters, in *Proceedings of 33rd ICCE 2012*, Santander, Spain, doi:10.9753/icce.v33.management.67, 2012.

Invited presentations acknowledging DOE support

- “Physical Environmental Effects of Wave and Offshore Wind Energy Extraction: A synthesis of recent oceanographic research”, *Oregon Marine Renewable Energy Environmental Science Conference*, November 28-29, 2012.
- “Laboratory observations of waves in the vicinity of WEC-arrays”, *European Wave and Tidal Energy Conference (EWTEC 2011)*, September, 6, 2011.
- *INVITED*: “Wave Energy Sites: Methods of evaluation and related research”, *Taller Internacional Sobre el Estado Actual de la Investigación Científica en Energías Marinas*, Pontificia Universidad Católica de Chile, Santiago, Chile, July 6-7, 2011.
- “*Far-field effects of WEC-arrays*”, *Wave Energy Conversion Array Network (WECAN)5th Annual Meeting*, Imperial College London, May 14, 2012.
- *INVITED*: “Wave Energy Research at Oregon State University”, Civil Engineering Design Seminar, Boğaziçi University, Istanbul, Turkey, March 16, 2012.

8. Participants and Other Collaborating Organizations

Name	Ken Rhinefrank
Project Role	Principal Investigator
Nearest Person Month worked	2 months
Contribution to Project	VP of Research & Development
Funding Support	Columbia Power
Collaborated w/ individual in foreign country	Yes, but in conjunction with a separately funded project
Country(ies) of foreign collaborator	Italy, but in conjunction with a separately funded project
Traveled to foreign country	Yes, but in conjunction with a separately funded project
If traveled to foreign country, duration of stay	5 days

Name	Erik Hammagren
Project Role	R&D Engineer - Mechanical
Nearest Person Month worked	2 months
Contribution to Project	
Funding Support	Columbia Power
Collaborated w/ individual in foreign country	N/A
Country(ies) of foreign collaborator	N/A
Traveled to foreign country	N/A
If traveled to foreign country, duration of stay	N/A

Name	Pukha Lenee-Bluhm
Project Role	R&D Engineer - Data Analyst
Nearest Person Month worked	1 month
Contribution to Project	
Funding Support	Columbia Power
Collaborated w/ individual in foreign country	N/A
Country(ies) of foreign collaborator	N/A
Traveled to foreign country	Canada, Norway unrelated to this project
If traveled to foreign country, duration of stay	3 days, 3 Days

Organizations: Organizations that have been involved:

**NNMREC - Corvallis OR (Oregon
State University)**

Hinsdale Wave Energy Laboratory
Dr. Merrick Haller
Dr. Tuba Ozkan- Haller
Dr. Ted Brekken
Aaron Porter
Cameron McNatt

Ershigs Inc. - Vancouver WA

Hull & ballasting design & modeling
Fabrication shop

9. Impact

.....

10. Changes / Problems

None. Project is complete

11. Budgetary Information

Spending Summary DE-EE0002658		FROM	TO
	Project Period	12/1/2009	8/31/2012
Object Class Categories (SF424a)	Project Expenditures		
	Approved Budget	Cumulative to Date	Delta
a. Personnel	\$23,570	\$33,158	\$-9,588
b.Fringe	\$4,549	\$6,399	\$-1,850
c.Travel	\$450	\$3,616	\$-3,166
d.Equipment	\$78,440	\$59,913	\$18,527
e.Supplies	\$0	\$340	\$-340
f.Contractual	\$477,032	\$471,718	\$5,314
g.Construction	\$0	\$0	\$0
h.Other	\$0	\$3,512	\$-3,512
i.Total Direct Charges	\$584,041	\$578,656	\$5,385
j.Indirect Charges	\$14,113	\$19,498	\$-5,385
k.Totals (i+j)	\$598,154	\$598,154	\$598,154
DOE Share	\$598,154	\$598,154	\$598,154
Recipient Cost Share	\$0	\$0	\$0
Cost Share Percentage	0%	0%	0%

AN ABSTRACT OF THE THESIS OF

Aaron K. Porter for the degree of Master of Science in Civil Engineering presented on August 13, 2012

Title: Laboratory Observations and Numerical Modeling of the Effects of an Array of Wave Energy Converters

Abstract approved:

Merrick C. Haller

This thesis investigates the effects of wave energy converters (WECs) on water waves through the analysis of extensive laboratory experiments, as well as subsequent numerical simulations. Data for the analysis was collected during the WEC-Array Experiments performed at the O.H. Hinsdale Wave Research Laboratory at Oregon State University, under co-operation with Columbia Power Technologies, using five 1:33 scale point-absorbing WECs. The observed wave measurement and WEC performance data sets allowed for a direct computation of power removed from the wave field for a large suite of incident wave conditions and WEC array sizes.

To numerically represent WEC effects the influence of the WECs upon the wave field was parameterized using the power absorption data from the WECs. Because a large driver of the WECs influence on the wave field is absorbed wave power by the WEC, it is reasonable to attempt a parameterization based on this process. It was of interest as to whether this parameterization, which does not account for wave scattering among other physics, could provide a good estimate of far-field effects.

Accurately predicting WEC-array effects in the far-field requires empirical validation. Previous WEC analysis and modeling studies had limited data available for model verification, and additionally had used idealized WEC performance. In the present work we develop a WEC-array parameterization for use in phase-averaged wave models (e.g. SWAN). This parametrization only considers the wave absorption effects of the WECs and the model predictions of far-field effects are compared to observations. Further testing of the SWAN model was performed against a phase-resolving model, WAMIT, to determine the significance of physics the WEC absorption parameterization does not capture, such as scattered waves. Considering the complexity of the problem, the parameterization of WECs by only power absorption is a reasonable predictor of the effect of WECs on the far field.

© Copyright by Aaron K. Porter

August 13, 2012

All Rights Reserved

Laboratory Observations and Numerical Modeling of the Effects of an Array of Wave
Energy Converters

by

Aaron K. Porter

A THESIS

submitted to

Oregon State University

in partial fulfillment of
the requirements for the
degree of

Master of Science

Presented August 13, 2012
Commencement June 2013

Master of Science thesis of Aaron K. Porter presented on August 13, 2012

APPROVED:

Major Professor, representing Civil Engineering

Head of the School of Civil and Construction Engineering

Dean of the Graduate School

I understand that my thesis will become part of the permanent collection of Oregon State University libraries. My signature below authorizes release of my thesis to any reader upon request.

Aaron K. Porter, Author

ACKNOWLEDGMENTS

Sifting through and understanding all of the data produced by the WEC-Array Experiments was no easy task, and could not have been done without the collaborations of Cameron McNatt, Pukha Lenee-Bluhm, and my adviser Mick Haller. The spectacular data sets Pukha put together to characterize WEC device performance, and the countless meetings and data processing help he provided were essential; thank you Pukha. Without Cameron's help, my understanding of the wave field produced by WECs would be much more elementary; his WAMIT model results were one of the lynchpins of this thesis. Thank you Cameron for your insights, critical thinking, and WEC-array wave patterns.

Mick, your involvement and hands-on guidance kept this thesis afloat. Thank you also for involving me in such an interesting project. I cannot think of a more rewarding research endeavor for a thesis, and look forward to future work.

Thank you to my whole family for keeping a keen interest and stake in my research these past two years. Mom, thank you for your unconditional support. Dad, thank you for always telling me, "If it were easy, everyone would do it." Caroline, thank you for being such a supportive sister and encouraging me to go back to school to study what I wanted to study. I love you all.

Thank you to all my friends I gained during the thesis process. George, Kyle, John, Cameron, I would not have made it through without you guys. The late nights we had studying (mostly) in Graf Hall seems to have paid off. Marisa, I may not have met you if not for presenting this research, and for that I am extremely lucky. Your support while I wrote this thesis was invaluable, thank you for keeping me on an even keel, and among other things, I love you greatly.

This research was supported by the U.S. Department of Energy (DE-EE0002658), Sandia National Labs, and Columbia Power Technologies under Research Subagreement NO. 2010-1698, additional support came from Oregon Wave Energy Trust through Award Number OIC-0911-109. I'd also wish to thank the staff of the Hinsdale Wave Research Laboratory for their considerable effort.

TABLE OF CONTENTS

	<u>Page</u>
1 Introduction	1
2 Experiment and Analysis	8
2.1 WEC-Array Experiments	8
2.2 Data Processing	21
3 Results	31
3.1 Monochromatic Wave Shadowing Analysis	35
3.2 Real Seas Shadowing Analysis	38
3.3 Parametrization of the Incident Wave Field	48
3.4 Laboratory Effects	55
4 Experimental Data Set Conclusions	62
5 Numerical Modeling	63
5.1 SWAN Physics	63
5.2 SWAN Model Simulations	65
6 Model/Data Results	73
6.1 Spectral Model and Comparison to Wave Data	73
6.2 Comparison to Mechanical Power Captured	78
7 Numerical Model Conclusions	81
8 WAMIT/SWAN WEC Model Comparison	82
8.1 Model Physics	82
8.2 Comparison Methods	83
9 WAMIT/SWAN Results	86
9.1 Unidirectional Waves	86
9.2 Directional Spreading	89
10 WAMIT/SWAN Conclusions	98
11 Discussion	99
12 Conclusions	100

TABLE OF CONTENTS (Continued)

	<u>Page</u>
Bibliography	102
Appendix	105

LIST OF FIGURES

<u>Figure</u>	<u>Page</u>
1 Typical experimental set-up of the WEC-Array Experiments	9
2 “Manta” 3.1 WEC	9
3 Wave gage locations	10
4 Experimental Layout	11
5 WEC-Array Positions Detail	15
6 2010 Calibration	18
7 Wave Repeatability	23
8 Hamming Window Application	26
9 Ensemble Averaging Sample	27
10 Qualitative relative capture width (RCW) curve	29
11 Wave height reduction due to WEC-arrays	32
12 Spectral Changes due to WECs	33
13 Characteristic wave shadowing	34
14 Power loss calculation diagram.	35
15 Regular wave power results	37
16 Scaling WEC-array power loss ratios, regular waves	39
17 Real Seas bulk power results	42
18 Scaling WEC-array power loss ratios, real seas	43
19 Spectral power deficits in the lee wave field	45
20 Spectral power deficit ratios	46
21 RIW and RCW at peak spectral energy	47
22 Energy flux transects 1	49
23 Energy flux transects 2	50
24 Energy flux transects 1	51
25 First five waves analysis	52
26 Real seas offshore wave height variation	53
27 Incident wave spectra in variable sized arrays	54
28 Spectral coherence of wave gage arrays.	56
29 Empty tank analysis: regular wave longshore transects	57
30 Empty tank analysis: real seas longshore transects	58
31 Empty tank analysis: cross-shore transects	59
32 Reflection coefficients	61
33 External spectra modification in SWAN	71

LIST OF FIGURES (Continued)

<u>Figure</u>		<u>Page</u>
34	Typical SWAN result	74
35	Typical Model2Data energy flux transects	74
36	Incident wave power in SWAN	75
37	Model to empirical data results	77
38	WEC absorption behavior and empirical shadowing	79
39	Comparison of SWAN to mechanical data trends	80
40	Idealized WEC	85
41	Idealized WEC RCW	85
42	WAMIT/SWAN wave shadow, $T = 1\text{sec}$	87
43	WAMIT/SWAN wave shadow, $T = 2\text{sec}$	88
44	WAMIT/SWAN wave shadow, $T_p = 1\text{sec}$	90
45	WAMIT/SWAN wave shadow, $T_p = 1\text{sec}$	91
46	WAMIT/SWAN Cross-shore transects, $T_p = 1\text{sec}$	92
47	WAMIT/SWAN Cross-shore transects, $T_p = 2\text{sec}$	93
48	WAMIT/SWAN directional spreading, $T_p = 2\text{sec}$, $s = 10$	94
49	WAMIT/SWAN directional spreading, $T_p = 2\text{sec}$, $s = 4$	95
50	WAMIT/SWAN cross-shore directional spreading, $T_p = 2\text{sec}$, $s=4$	96
51	WAMIT/SWAN cross-shore directional spreading, $T_p = 2\text{sec}$, $s=10$	97

LIST OF TABLES

<u>Table</u>		<u>Page</u>
1	Tests in the WEC-Array Experiments	13
2	Regular wave trial conditions	13
3	Real seas target wave conditions 1	14
4	Real seas target wave conditions 2	40
5	Regular wave boundary conditions for SWAN	67
6	Real seas boundary conditions for SWAN	68
7	SWAN computational grid	68
8	Incident wave conditions for SWAN/WAMIT comparisons	84

Laboratory Observations and Numerical Modeling of the Effects of an Array of Wave Energy Converters

1 Introduction

As the importance and potential of emerging renewable energy resource technology increases, so does the need for objective research. In this case the resource of interest is the harnessing of ocean waves via wave energy converting buoys. A clear understanding of how wave energy converters (WECs) will affect the ocean environment, ocean waves in particular, is needed before commercial application. Of importance to both private industry and the public is how this new technology will affect our oceans' waves, and in turn the beach.

This thesis presents observations of laboratory data, analyzes the results, simulates select wave cases with the spectral model SWAN, and evaluates the ability of such models to predict the wave field leeward of WEC-arrays. The basis of comparison between model and experiment are longshore transects of wave height and energy flux, total power deficits between seaward and leeward locations of the WEC-array, and changes to the incident wave spectra induced by WEC-arrays. This thesis covers a wide range of information, but has three essential parts. It will make conclusions of how WECs affect the wave field by analysis of experimental data, determine whether spectral modeling can predict the affected wave field by verification against the experimental data set, and evaluate spectral model capabilities against a phase-resolving boundary element method (BEM) model, WAMIT.

Wave energy conversion is currently in it's nascent stage and has various designs, ranging from the point absorbing buoy (WEC of interest), to on-shore installments; each generates power from the oscillating nature of ocean waves. While test berths of WECs are expected to have few devices, and possibly only a single device, it is expected that WEC buoys will be deployed in arrays to employ efficiency in installment and maintenance. This paper explores single buoy and multiple buoy (array) cases.

Ocean waves, the source of power for WECs, are a manifestation of multiple forces including wind, the moon, the sun, and in some cases tectonic motion [Dean & Dalrymple, 1998]. Of interest to this paper and most common are wind waves; perturbations in the still water surface are created by the wind. These perturbations continue to grow in size with exposure time.

For the purposes of this investigation on affected water waves, the assumption of linearity is reasonable. Linear wave theory assumes waves travel through a inviscid and incompressible fluid, and flow is irrotational.

$$\eta(x, t) = a \cos(kx - \sigma t) \quad (1)$$

where η is the sea surface elevation [The SWAN Team, 2011], a is the wave amplitude, k is the wavenumber, x is location in space, σ is the radial frequency ($\sigma = 2\pi f$), and t is time. The wavenumber, k , is related to wavelength by, $L = 2\pi/k$. Wavenumber is related to radial frequency, and water depth by the dispersion relationship:

$$\sigma^2 = gk \tanh(kh) \quad (2)$$

The combination of many waves often results in the ocean surface appearing irregular and random. However, the sea surface η is a summation of sinusoidal wave forms of frequency σ , amplitude a , and phase α , at time t [Dean & Dalrymple, 1998]. Real seas are often described by its spectral content, $S(f, \theta)$ at each frequency (inverse of wave period, T^{-1}) and direction. Different frequencies in the sea will be home to varying amounts of energy. The collection of these energies is called the wave spectra. Normally in the ocean, energetic frequencies range from .05Hz to 0.25Hz, or wave periods between twenty and four seconds, respectively. At the lab scale in this thesis (1:33) that translates to 0.29Hz and 1.43Hz

Eventually the waves approach a coastline where depths decrease. Here the waves undergo transformations such as shoaling and refraction that conserves energy flux, $E_f = EC_g$ [Watts/meter]. Energy flux conservation is defined as:

$$(EC_g)_1 b_1 = (EC_g)_2 b_2 \quad (3)$$

where

$$E = \frac{1}{8} \rho g H^2 \quad (4)$$

and

$$n = \frac{C_g}{C} = \frac{1}{2} \left(1 + \frac{2kh}{\sinh(2kh)} \right) \quad (5)$$

$$C_g = Cn \quad (6)$$

$$E_f = EC_g = ECn \quad (7)$$

where H is wave height; $C = L/T$ (wave celerity); C_g is group velocity, or the velocity at which energy propagates; n is a unit-less factor that asymptotes at 1.0 in shallow water and 0.5 in deep water; and b is the unit crest length of analysis, and varies depending on refraction.

Breaking waves are of great importance to beaches and other shorelines, because this is how energy flux from the waves is dissipated, or transferred to the environment. When waves break, they exert forces. These are always in directed in the cross-shore direction (normal to the shoreline), and if the waves break at an angle to the shoreline there are also

forces in the alongshore direction (parallel to the shoreline). Simply, force balances show that forces in the cross-shore cause undertow and set-up, while forces acting alongshore result in currents flowing parallel to the shore. These two types of current are the basis for sediment transport and help shape the beach environment. Understanding potential changes to these currents is vital to ensuring the environmental well-being of our beaches, shorelines, and aquaculture.

In a commercial wave energy farm, as with any obstruction of waves, the waves will experience diffraction and reflection when interacting with the WEC-array. Diffraction is the process in which energy is spread laterally perpendicular to the dominant direction of wave propagation [Dean & Dalrymple, 1998], that is, energy will leak along the crest of the wave and appear to smooth out the wave heights along a crest. A more technical description of the diffraction process can be found in section 5.1.

When ocean waves are affected by an outside source, the effects are not only seen in the near-field, but as previously discussed, in the far-field as well. It is expected that WECs will in some capacity affect the wave field, whether or not these effects are significant in the far-field is under investigation. These effects could be seen by decreased wave heights due to absorption by the array, diffraction around the array, changes in spectral shapes, or decreased longshore current. Accurately predicting far-field wave effects is still difficult because of limited field deployments of WEC arrays up to this time, and the difficulty in accurately modeling all the physics present needed to predict wave action near WECs.

To date, there is still a knowledge gap between numerical simulations of wave action in the presence of WEC arrays, and observational verification. In order to improve accuracy of numerical simulations we must develop a wave model parametrization for WEC arrays that is verified with both scaled laboratory data, and measured WEC performance data. Specifically of interest are the changes in waves between the unaffected and the affected, in the area in the lee of the array. To model the near and far field effects, SWAN, a third generation phase-averaged spectral model is employed [SWANTeam, 2011]. It can obtain realistic estimates of wave parameters on any scale relevant for wind-generated surface gravity waves, model over real bathymetry, and is able to model objects in the sea (such as jetties and islands) [SWANTeam, 2011].

Previous work to get to this knowledge gap between empirical and numerical simulations has not been trivial. There have been previous attempts at roughly predicting far-field WEC influences by modeling. Additionally there have been several WEC-array experiments, but none had yet closed the gap between model and observations.

Literature Review Wave energy has been of interest to the scientific and engineering community for several decades, with literature dating back to the 1970s [Budal, 1977], but only recently has there been a sharp increase of analysis and experimentation. Previous experiments have been small in scope and varied in the type of WEC used. Ashton et. al.

[Ashton et al., 1999] measured the effects of an array of WECs on the surrounding wave field with a floating oscillating water column device, but data analysis was limited to five wave gages sparsely populated near and within the array with only one being completely in the lee. They found that single point measurements are not suitable to quantify the effect of a WEC on the surrounding wave field, and that more measurement points were needed to provide a more detailed pictured of what was occurring in the wave field.

Running WEC experiments is a difficult task in part because of small response signal sizes in comparison to tank modes [Boyle et al., 2011], which may have been a factor in the experiments by Ashton et al [1999]. Boyle et. al. showed that point measurements of surface elevation are not sufficient in defining the incident wave conditions for many WEC models by extensive empty tank testing and modeling. Nodes and anti-nodes make it difficult to isolate the response signals of the WEC-array, especially signals below 10 percent [Boyle et al., 2011].

Alexandre et al. [2009] ran physical experiments with 1/67th scale heaving point absorbing WECs and tracked the changes made to the spectra in the physical experiment between incident and lee conditions using seven wave gages; three in the lee, three in the offshore, and one longshore of the WECs. The measured relative changes in spectra due to the five by two sized WEC-array were input to a numerical model, SWAN, then the authors ran the model towards a shoreline. They found that group velocity had changed from the incident wave climate, as well as the spectral shape, which had become bi-modal when the WEC was tuned to the peak frequency of the incident spectra.

Preliminary work for this thesis was published in Haller et al. [2011] and among the results was that the shadow was not dependent on incident wave height, but primarily upon wave period and array size. This suggests the nonlinear effects are not of primary concern. This paper also remarked that based on wave height analysis wave absorption, and not scattering was the dominant process inducing the shadow.

None of the experiments listed above considered interactions between WECs in arrays. When interactions between WECs influence the overall performance of the array, this effects of this physical process are called the interaction factor, or q . The interaction factor is equal to 1.0 when the maximum power absorbed in an array is the same as achieved in isolation, with values greater or less than this indicating positive and negative interactions, respectively [Weller et al., 2009]. Weller et. al. obtained experimental measurements of power absorbed by a small two-dimensional array of heaving devices in regular and irregular waves. It was reported that the factor q can be anywhere between 0.8 to 1.1 for regular waves, and 0.8 to 0.9 in irregular waves. These values were intended help form a basis for evaluating numerical models.

Most recently, two major fields in WEC-array modeling have emerged; understanding behavior within and very near WEC arrays, and modeling WEC-array effects in the far-

field. Often, these goals require different modeling and analysis techniques. Phase averaged models, like SWAN, are intended for multi-kilometer domains with varying bathymetry, while phase resolving programs like WAMIT are better suited to model the near-field and are not built for modeling large domains with variable bathymetry.

As previously mentioned this paper primarily uses SWAN to model the wave field, as it is a common tool in wave analysis and has been used in the past to model WEC-array effects [Millar et al., 2007; Smith et al., 2012; Alexandre et al., 2009]. As a spectral model it does not model individual wave forms, instead it tracks spectral energy in space and time as phase averaged quantities. In this sense it cannot model constructive or destructive interference from multiple waves, or interactions between WECs. However, it has previously been shown that although such a model cannot account for WEC interactions, spectral models may be able to reasonably predict the wave field in the lee of a WEC-array [Folley & Whittaker, 2011]. It is not without its limitations though, Monk et. al. [Monk et al., 2011] found that when compared to experimental data SWAN does not laterally spread leeward wave energy passing through a WEC quickly enough.

SWAN was developed to numerically represent the effects of spatial propagation, refraction, shoaling, wave generation, dissipation, and nonlinear wave-wave interactions. In order to accurately represent these effects, SWAN solves the spectral action balance equation:

$$\frac{\partial N}{\partial t} + \frac{\partial c_x N}{\partial x} + \frac{\partial c_y N}{\partial y} + \frac{\partial c_\sigma N}{\partial t} + \frac{\partial c_\theta N}{\partial t} = \frac{S_{tot}}{\sigma} \quad (8)$$

where σ = radian frequency, N is the energy density $E(\sigma, \theta)$ distributed over radian frequencies σ and propagation directions θ . The evolution of the action density, N , is determined in space and time; it is defined as $N = E/\sigma$ and is contained wholly on the left side of the equation. The right side S_{tot} is the sum of physical processes, or the “sources and sinks”, that generate, dissipate, or redistribute wave energy. S_{tot} balances with the kinematics of the wave energy located on the left side of the equation. SWAN has six process that add to S_{tot} :

$$S_{tot} = S_{in} + S_{nl3} + S_{nl4} + S_{ds,w} + S_{ds,b} + S_{ds,br} \quad (9)$$

These terms, in order, represent: wave growth due to wind, nonlinear transfer of wave energy through three-wave and four wave interactions, wave decay due to white-capping, wave decay due to bottom friction, and wave decay due to wave breaking [SWANTeam, 2011].

At the onset of spectral WEC modeling in SWAN, WECs were represented as large objects, where energy is removed from the wave field at equal magnitudes across all frequencies over a large swath of sea. For example, Millar et. al., modeled the effects of the proposed Wave Hub in the U.K. off the north coast of Cornwall by a 4km wide partially transmitting obstacle. This type of obstacle removes portions of energy up to one-hundred

percent, equally across all frequencies; the percent removed is chosen by the user [SWAN-Team, 2011]. A range of transmission coefficients was chosen to represent varying degrees of WEC spacing in the array. The results from that analysis showed a minimal impact to the shoreline, and little cause for concern. However, those authors noted that their analysis does not use transmission coefficients from actual WECs, and that the purpose of the analysis was to determine whether the effects could be practically measured.

Since then, predicting WEC array effects with spectral modeling has evolved, taking into account the frequency dependence of WECs. It started with Alexandre et. al. in 2009 who fused together numerical and physical modeling of WECs to get an idea of how a frequency dependent transmission coefficient alters the wave climate. In contrast with this paper, their interest was in how spectra change as they approach the shore, and not precisely modeling WECs in SWAN.

More recently, two of the authors from the previous Wave Hub paper, addressed the Wave Hub problem again in 2012 [Smith et al., 2012]. Here, the authors modified the SWAN source code to allow for directional and frequency dependent transmission coefficients. The purpose of this paper was not to get the best simulations from SWAN, but rather to asses the differences between WEC arrangements in the wave-farm. To this point, they varied the shape of the relative capture widths (RCW) of the WECs between a narrow band (large amounts of energy absorbed at few frequencies) and a wide band (small amounts of energy absorbed at many frequencies). They found that no matter the arrangement or RCW shape, wave height differences at the shoreline were very small.

The TELEMAC-based Operational Model Addressing Wave Action Computation model, or, TOMAWAC, is spectral wave model similar to that of SWAN. Like SWAN, it solves the wave action density balance equation (eaquation 8). Silverthorne and Folley [Silverthorne & Folley, 2011] used TOMAWAC to model WEC-array effects in order to examine the importance of frequency and directionality responses of the wave climate. The WECs are treated as an additional sink term in equation 9 which are directional and frequency dependent, similar to the process is the 2012 Wave Hub paper by Smith et. al. Unlike Smith et. al., here the authors calculated a RCW curve for an idealized surging WEC based on a linear single degree of freedom system that was a nonlinear function of the ratio between frequency, f , and the device's natural frequency, f_0 . The WEC model had a cosine squared directional dependence, which was consistent with frequency domain modeling of the Oyster oscillating surge wave converter [Silverthorne & Folley, 2011]. They found that modeling the WECs as individual grid points, rather than a single line to represent many WECs, was more realistic. This sub-grid resolution for WEC representation could be important for WEC array design.

Different from spectral models are those models that are not phase averaged, such as MILDwave which solve the mild slope equation, and WAMIT which is a boundary element method (BEM) model. Troch et al [2010] investigated the effects of an overtopping WEC

by modeling in MILDwave. Because MILDwave is phase resolving, the interactions between WECs can be included in model physics. It was found that staggered WEC arrangements result in the highest power consumption, and that lee wave regeneration depends on wave period and directional spreading. Also it was concluded in this paper that wave shadows behind a device have a shorter cross-shore extent with increased wave period and increased directional spreading.

Interactions between WECs are one of the biggest differences between spectral and phase-resolving models. Phase resolving models can attempt to predict the interactions between WECs in the array. Borgarino et. al. assessed the influence of separating distances between generic points absorbing WECs using a custom BEM. It was found that the yearly averaged q factor varied at different wave periods and spacings between positive thirteen percent and negative eighteen percent off of unity, but that over the time period of a year the negative and positive interactions compensate for each other, and positioning is not a major issue. Prior to the Borgarino paper, Cruz et. al. modeled four-WEC array effects with WAMIT and found that for a selection of suboptimal control strategies the q factor equaled between 0.92 and 0.98 [Cruz et al., September 2009].

Model choice really depends on the intent of the model. Large domains (like the entire nearshore domain) are better modeled with spectral models like SWAN, while BEM models such as WAMIT are better suited for localized effects [Folley et al., 2012]. According to Folley et al. [2012] other models such as Mild-slope or Boussinesq models should do moderately well in both environments, but not as well as a spectral model in very large domains .

2 Experiment and Analysis

This section describes the WEC-Array experimental setup and analysis methodology. The physical model is described in detail as well as the data processing needed to obtain useful wave data from instrumentation for each trial. Wave conditions for each trial are discussed and summarized, further details are given in Appendix A. Organization of the processed data set is also described for later use. The processed data set was then used to determine wave shadowing characteristics for every trial by comparing the incident waves set to waves in the lee of WEC-arrays. The (non-trivial) details of how the incident wave conditions were determined when multiple WECs were installed in the tank are given in section 3.3.

2.1 WEC-Array Experiments

The WEC-Array experiments were conducted in the Tsunami Wave Basin at the O.H. Hinsdale Wave Research Laboratory (Oregon State University). The experiments used five 1:33 scale point absorbing wave energy converters (WECs, Columbia Power Technologies “Manta-3.1”). Data was collected between November 18, 2010 and February 15, 2011 (Processed data is available upon request, merrick.haller@oregonstate.edu). The organization and format of the processed data is located in section 2.1.4. Figure 1 shows the experimental set-up from a typical five WEC (devices in yellow) array. The sticks protruding from the devices hold LEDs which were used for optical motion tracking for each 3-bodied device. Also shown are several wave gages with pink flags attached. The water surface appears cloudy due to a chalk-like substance that was used as a contrast agent for the stereo imaging camera system mounted on the ceiling

2.1.1 Experimental Set-up

Wave Energy Converters The lab experiments were performed with a 1/33rd scale version of the “Manta 3.1” WEC, a point-absorber designed to capture energy in both heave and surge. In theory, such a design allows the device to capture twice the wave energy of a point-absorber designed to capture in heave only. The “Manta” has both a fore and aft float which are attached to a heavy spar through a drive shaft, which is shown in Figure 2. As incoming waves pass the WEC, heave and surge motions force the floats to rotate about the top portion of the spar and drive their respective direct drive rotary (DDR) generators. At lab scale the WECs have a diameter of approximately 0.55 meters, at field scale this is equivalent to eighteen meters. Using the motion tracking data, power capture by the WECs was measured and recorded for each trial condition. This mechanical power capture behavior by the WECs are compared to power deficits measured in the wave field.

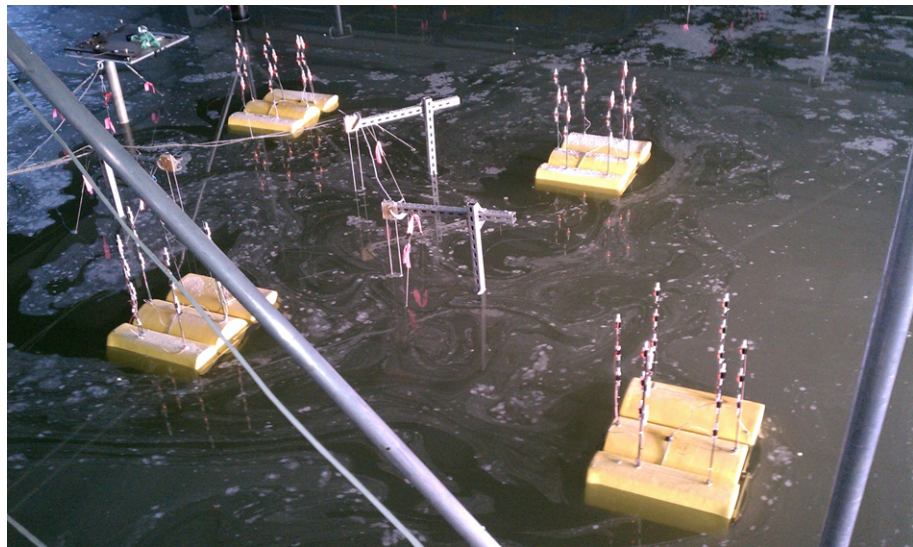


Figure 1: Photograph of the 5-WEC array experimental setup. WECs are yellow with LEDs attached to vertical posts for motion tracking. Also shown with the pink flags attached are several wave gages



Figure 2: The "Manta 3.1" 1:33 scale wave energy converter (Columbia Power Technologies)

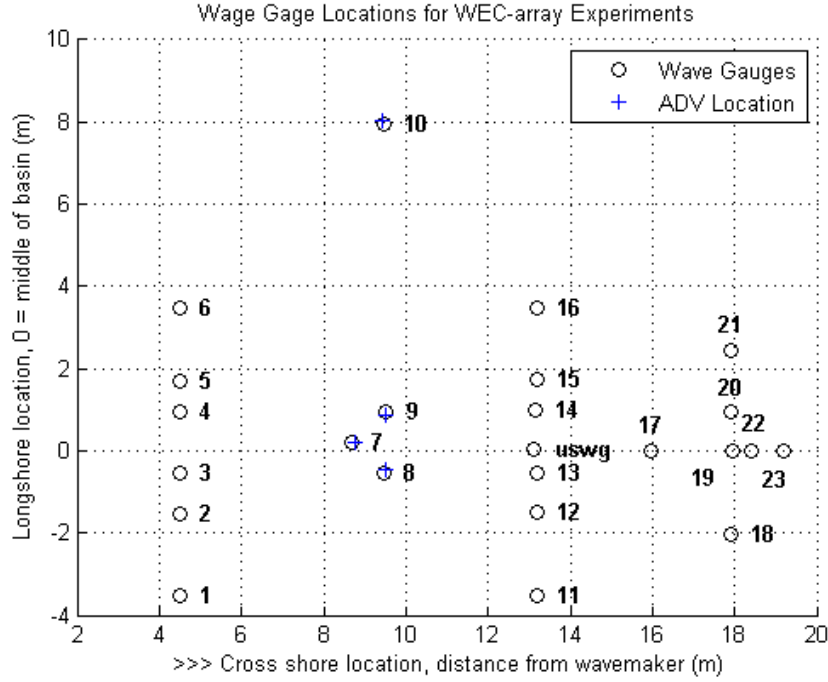


Figure 3: Layout of the wave gages for the WEC-Array Experiments.

Physical Model The internal dimensions of the wave basin are approximately 48.8 m in length by 26.5m with the Directional Tsunami Wavemaker situated at one end. A plan view of the wave basin is shown in Figure 4. This figure also shows the coordinate axes; the origin is located at the wavemaker. The wavemaker consists of twenty-nine, two-meter wide, piston-type wave-boards. These wave boards have a maximum stroke of 2.1 meters, have directional wave capability, and are equipped with active wave absorption. The system has the ability to produce regular, irregular, tsunami, multidirectional, and user defined wave fields. The maximum water level in the basin is 2.1 meters; however, for this experiment water levels ranged from 1.365 meters to 1.372 meters. Opposite the wavemaker, on the far end of the basin, a crushed rock beach of initial grade of approximately 1:12 was installed to mitigate cross-shore wave reflections in the tank.

Instrumentation Twenty-seven in-situ instruments were placed in the wave basin. This included twenty three wave gages, one ultrasonic wave gage, and three acoustic doppler velocimeters (ADVs). Detailed locations are plotted in Figure 3. Wave gages were placed in instrument arrays designed to measure and resolve directionally-spread incident wave fields, wave fields in the lee of the WECs, wave scattering in and around the WECs, far-field effects, and cross-shore reflections near the beach. Theses gages report voltage, which is

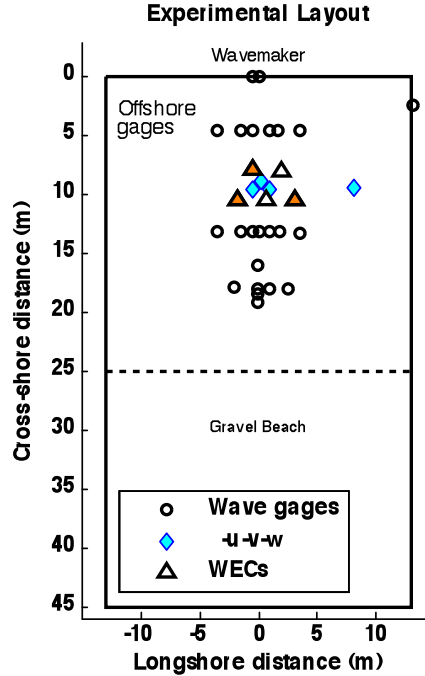


Figure 4: Experimental layout of wave gages, acoustic doppler velocimeters (ADVs), and WECs in 5-WEC array arrangement. Three device arrangement shown in orange.

linearly proportional to water surface elevation, η . To convert data units from voltage to meters, the gages must be calibrated, and produce a calibration coefficient. Each gage was calibrated at each basin fill, and drain. The method for determining calibration coefficients is discussed further in section 2.1.3 and the results plotted in Figure 6. Co-located with select wave gages within the WEC array, and at gage ten, are ADVs which measure fluid velocity in three directions, $u - v - w$. See Figure 4 for locations of the gages in reference to the WEC-array. The WEC location(s) are centered in the basin to reduce side wall effects, eight to ten meters from the wave maker. Each of the WECs was moored to the basin floor in one of five positions. Throughout the experiment the number of WECs in the water at one time varied between one, three, and five; and when in the water, the WECs were always moored in the same position (1-5). To measure WEC movements, in order to calculate power absorbed by the WECs (i.e., velocity squared times damping = power), a commercial LED tracking system was employed. LEDs were attached the WECs via rods protruding from the three WEC body portions (main body, front and back flaps). Through the tracking data, the system was able to measure time-series of position in 3D space. These data were used to calculate object velocity and extracted power. Attached to the ceiling of the facility was a bi-static camera system to include 3D imaging capability through binocular stereo.

Basin Survey Bathymetric surveys of the beach were taken before and after the experiment occurred. Survey data is contained in the WEC-array experiments processed data set. The surveys were taken using LIDAR technology, by Michael Olsen and the OSU Geomatics unit at a resolution of 5 cm with 222,744 total grid points. Because of line-of-sight limitations, three scans are combined to include the entire basin. The LIDAR data set was produced in the TWB coordinate system. For the purposes of this experiment five centimeter spacing was not needed, so the original grid was interpolated to a regular 10cm regular grid.

2.1.2 Wave Conditions

The experiment consisted trials that varied between regular monochromatic waves and irregular (real seas) waves; single and multidirectional waves; and normally incident and off-angled waves. The lab scale waves were developed from a suite of target field scale conditions. Equivalent lab scale wave periods were calculated using Froude scaling, $T_{scale} = \sqrt{L_{scale}}$, where T is time scale and L is the length scale.

Test names and trials are organized by wave-type, and WEC-count (i.e., 3-WEC frequency scan, where frequency scans are constant wave height and variable regular wave period). These tests consist of variable amounts of individual trials, depending on type, and vary between thirteen and one-hundred-ninety-four trials per test. Most tests were run over several days, while some (i.e., Single Buoy Characterization) were ran in several days over the course of 2-3 months. Characterization tests are only different than other tests in that the physical WEC in the water was changed throughout, although the WECs mooring position was always the same. Detailed characteristics of the trials are located in the Appendix.

Regular Waves Regular waves tests consisted of monochromatic waves, with incident angles of normal, and twenty two and one half degrees. At field scale these waves range from periods of 5.2 seconds to 16 seconds, and wave heights of one meter to five meters. Table2 has a summary all of the regular wave conditions tested from both the scans and the characterization. A more detailed description of conditions tested, along with associated trial numbers can be found in the Appendix. Although the wave heights span a range of values, in the following analysis the focus is on target wave heights of six centimeters. The six centimeter waves have the most populated scans between different wave periods.

Regular wave trials generally consist of 50 waves; so the sample times vary depending on nominal wave period. Early on in the experiment, during the single buoy scans, only twelve waves were ran per trial instead of fifty, so these runs are much shorter. However, the single buoy characterization trials all have 50 waves per trial.

Table 1: Tests in the WEC-Array Experiments

The WEC-Array Experiments	
Test Name	No. Trials
Argus Pre-test (empty tank)	13
Single Buoy Amplitude Scan	75
Single Buoy Frequency Scan	82
Single Buoy Real Seas	76
Three Buoy Amplitude Scan	51
Three Buoy Frequency Scan	62
Three Buoy Real Seas	70
Five Buoy Amplitude Scan	53
Five Buoy Frequency Scan	54
Five Buoy Real Seas	60
Single Buoy Characterization	194
Single Buoy Characterization Off Angle	114
Single Buoy Characterization Real Seas	39
Single Buoy Extreme Seas	9
Total	952

Table 2: Regular wave trial conditions

Regular Waves			
H (cm)	Period ¹ (s)	Angle ² (θ)	WEC-array ³
3	1.0-2.8 [11]	0, 22.5	1
6	0.9-2.8 [20]	0, 22.5	1
6	0.9-2.7 [15]	0, 22.5	3, 5
6	1.8-2.8 [3]	22.5	3, 5
9	1.0-2.6 [7]	0, 22.5	1, 3, 5
12	1.3-2.6 [5]	0, 22.5	1, 3, 5
15	1.3-2.6 [5]	0, 22.5	1, 3, 5

¹Wave periods represent max and min of tested range; bracketed number indicates number of periods tested within this range.

²Wave angle with respect to shore normal.

³Number of devices in array.

Table 3: Real seas target wave conditions 1

Real Seas					
Wave height	Peak period	Peak direction	Directional Spreading	Sea State	WEC-Array
$H_{m0}(cm)$	$T_p(sec)$	θ_p	s^1		
4.5	1.2, 1.6	0, 22.5	4, 10, UD	HI – Kaneohe, Oregon 1	1
4.5	1.2, 1.6	0, 22.5	2, 4, 10, UD	HI – Kaneohe, Oregon 1	3, 5
7.6	1.4, 1.8, 2.2	0, 22.5	4, 10, UD	Oregon 2, 3, 4	1
7.6	1.4, 1.8, 2.2	0, 22.5	2, 4, 10, UD	Oregon 2, 3, 4	3, 5
10.6	1.6	0, 22.5	4, 10, UD	IR – M4 Buoy	1
10.6	1.6	0, 22.5	2, 4, 10, UD	IR – M4 Buoy	3, 5
13.6	2.2	0, 22.5	4, 10, UD	Oregon 5	1
13.6	2.2	0, 22.5	2, 4, 10, UD	Oregon 5	3, 5
30	2.6	0	UD	Oregon Storm	1
45.2	2.6	0	2, UD	Extreme Seas ²	1
45.2	2.6	22.5	UD	Extreme Seas ²	1

¹Directional spread parameter, s, for distribution $[0.5 \cos(\theta - \theta_{mean})]^{2s}$

²100 year storm event

Real Seas Also run in during the experiment were the real seas simulations. These trials are intended to simulate sea state conditions at different potential installation sites. Spectra for all trials are Joint North Sea Wave project (JONSWAP) shaped with $\gamma = 1.0$; equivalent to the Pierson-Moskowitz (PM) spectra [Sorensen, 2006].

$$S(f) = \frac{\alpha * g^2}{(2 * \pi)^4 f^5} e^{-1.25(f_p/f)^4 * \gamma} \quad (10)$$

Both unidirectional (UD), and multidirectional incident wave spectra were run from normal and offangle directions. At field scale the typical peak periods of the spectra range from seven to fifteen seconds, and significant wave heights of one and a half meters to four and a half meters. Real seas trials have longer sampling times than regular waves trials so that the random wave spectra can be considered statistically significant. The sample times for real seas tests ranged from 313 seconds to 540 seconds, with the latter applicable to all but the Single Buoy Real Seas Test and a portion of the Single Buoy Characterization Real Seas test. Table 2.1.2 summarized real seas wave conditions tested. A more detailed description of conditions tested, along with associated trial numbers can be found in the Appendix.

WEC-arrays WEC-array arrangement varied throughout the experiment, with any of one, three, or five WECs in the water at one time. There were five possible mooring positions for the WECs, seen in 5. During the trials WECs tended to move slightly around in the basin, so the positions plotted are the average positions as determined by motion tracking

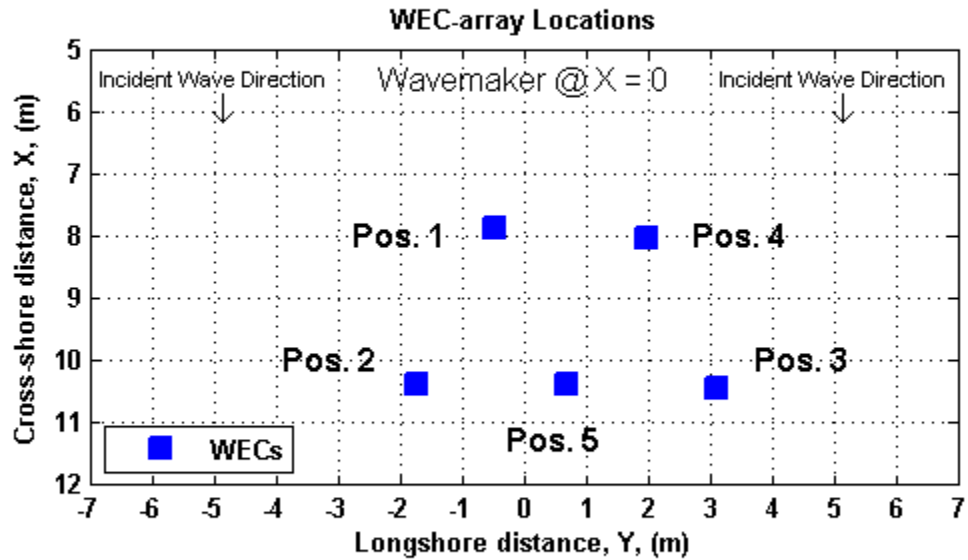


Figure 5: Detailed locations of the five WEC-array positions. Blue squares mark the mean positions of the WECs.

data for select trials. For almost the entirety of the experiment, WECs were moored in only one location (i.e., WEC #3 was only moored in position 3). The lone exception was during single buoy characterization trials, where all WECs, 1-5, were moored to Position 1 for different trials throughout the tests. For all single buoy tests the WECs were moored in Position 1 only; for all of the three buoy tests WECs were moored in Positions 1, 2, and 3; for the five buoy tests WECs were moored according to their WEC number at all five positions.

2.1.3 Quality Control

The first step in processing trial data was to review time series data for all wave gages for every trial in order to check for possible flagged trials. There are twenty-four channels (twenty three wave gages and one ultrasonic wave gage) with sea surface elevation time-series; data from a single trial is best viewed on separate subplots of several gages apiece.

Flagging potential problems was done by hand on a quality control spreadsheet. The quality control sheet contained a matrix of trial numbers and wave gages for each test. Trials that looked odd or contained questionable data were marked as so for reference. The quality control sheets later saved time by reducing the amount of back checking necessary. During the quality control process the ultrasonic wave gage was identified as having extremely noisy data in many of the trials.

It's important to remove the noise (spikes) in the ultrasonic data so that accurate wave heights are recorded. The accuracy of the ultrasonic gage is especially important because it is part of the process that calibrates the conversion from volts to meters for wave gages; the calibration process is discussed in depth in the following section "Wave Gage Calibration". Spikes in wave gage surface elevation time series were identified and then removed using phase-space method developed by Goring and Nikora [2002], and later modified by Nobuhito Mori [2007]. This method assumes that the data set is random, and that the instantaneous acceleration must be less than gravity. Many of the data trials in the current data set however, were not random, but instead contained sets of regular waves. This caused problems in recognizing real spikes against false spike identifiers. A small adjustment to the spike identifying threshold was made to account for the regularity of the sinusoidal waves. The original universal threshold was $\lambda = 2 * \log(n)$ but an adjustment that worked, with visual confirmation, was to multiply this value by $\sqrt{2}$, which decreased the sensitivity of spike identification. This allowed regular wave trials to be better analyzed by the method.

Wave Gage Calibration A calibration value is needed to convert the voltage in each gage to units of meters. From past experience at the HWRL, it has been shown that the electronegativity in the tank changes during the first few days after the basin is filled with water, which results in changing calibration values. Hence, calibration values need to be monitored throughout the experiment. However, the standard method for obtaining calibration coefficients for each gage involves either draining or filling the tank. To estimate calibration between calibration events, a good understanding about the behavior of electronegativity in the tank over time is needed. Here we have used a fixed ultrasonic wave gage (USWG), co-located with one of the regular resistance wave gages, as a fixed reference point; under the assumption that the calibration coefficient of the USWG does not change over time (since it is based on the speed of sound in air). Comparing wave height readings from these two gages gives an estimate of how the electronegativity in the tank changes over time. However, data from the USWG is noisier, so these data need to be used with care so that noise does not overly affect the calibration adjustments.

Two sets of calibration curves were needed, because there were two separate instances of filling the basin, and then draining it. The ratio of the USWG to the local gage in each instance, these are denoted as $2010ratio$, and $2011ratio$ (occurring in Experimental Phases One and Two. The 2010 fill/drain spanned a longer period of time, and in turn has a larger

range between fill and drain calibration coefficients.

To start, we looked at the recorded voltages of the co-located gage during regular wave trials and compared it to voltage from the USWG. Before this was possible, the noise problem in the uswg had to be fixed to obtain accurate Hmean values for each trial. We decided to find trials that did not have any noise problems throughout a portion of the trial that was at least five wave periods long, and that had a standard deviation between wave heights within the trial of 0.003. This standard deviation constraint was chosen since the method for determining steady state portions of the trials was still in its infancy, and at the time, safeguards were thought to be needed to avoid inaccurate data. Trials that passed this are the only those trials used to determine the calibration equation. We assume that the quality of these trials give an accurate representation of the real ratio between the local gage, and the uswg.

Plotting the 2010*ratio* (between H_{mean} of the USWG and the local gage, or *USWGRatio*) for trials that passed the above constraints indicated that just after the drain, the ratio fell sharply, before falling slowly off, as shown in Figure 6. Two curves are used to describe the 2010*ratio*. The first is fit to tests ‘SingleBuoyAmplitudeScan’, ‘SingleBuoyFrequencyScan’, and ‘ThreeBuoyAmplitudeScan’; these are used in the curve fit of the time in which the 2010*ratio* drops off relatively quickly. The 2010*ratio* data from these tests was fit to a power curve of the form: $ratio = a^{\log(b*UTC_{date})+c}$, and the coefficients were determined by reducing the levels of squared absolute error. The resulting curve is seen in Figure 6 and the equation, “CalibrationRatioPowerCurve”. Additionally, a linear fit from the end value of the power curve fit, to the drain calibration value completes the calibration curve for 2010 data.

Phase 2 of the experiment occurred in 2011, in a different fill/drain period, and makes up the second calibration curve. The time period which it occurred in was shorter than the 2010 period, and less change in calibration coefficients were observed between the fill and drain. Because of this a linear fit between the fill and drain calibration coefficients was chosen as the calibration curve. The next step was to convert from units of volts to units of meters. This was done by multiplying the constant uswg calibration (0.174 volts/m) by the ratio between the local gage and the uswg, giving the calibration coefficient of the local gage to convert to meters from volts at any point in time.

Each gage has its own calibration coefficient for the fills and drains, which was measured and calculated by wave basin staff. The ratio curve must be scaled accordingly to each gage’s change in calibration magnitudes, which vary by up to approximately 100%. That is, the curve must be scaled to account for differences in the absolute change of calibration values for each gage, compared to the absolute change of the co-located gage. That ratio, of gage thirteen to any other gage, is approximated by a linear trend by both gages between their fill and drain coefficients. While this method of scaling is not exact, it provides a decent

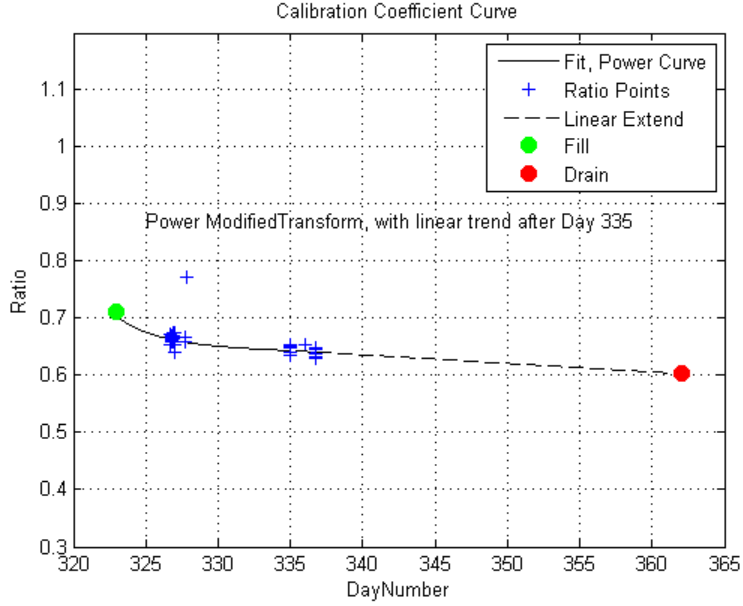


Figure 6: Calibration curve for the 2010 raw wave data. A modified power curve was fit to data points that passed stringent quality control checks.

approximation for the differences between the absolute changes of each of the gages at any day and time. The functions *CalCoeff2010* and *CalCoeff2011* do this. The calibration coefficient for any gage in time is then $0.174 * USWGRatio$, multiplied by the ratio of the approximate change of a selected wave gage at a certain time to the approximate change of the local wave gage at a that same time (*gage2gageRatio*). This method applies to both the 2010ratio and 2011ratio.

$$CalCoeff = 0.174 * USWGRatio * gage2gageRatio \quad (11)$$

The end product, the calibration coefficient *CalCoeff*, is multiplied by the raw data which is in units of volts, and converts the wave data into meters. All processed wave data uses this method, and is therefore reported in meters. The function *CalCoeff* is able to produce any calibration coefficient given a channel number (1-30) and UTC date, and in turn, calibrated wave heights.

2.1.4 Data format and Organization

Wave gage data from the WEC-Array experiment was reported in units of volts, and stored in large text files with the nomenclature "...analog_master.txt". Each trial has its own text file that contains 30 columns of wave data, and approximately fifty lines of metadata. The

thirty data columns are from data collection channels; 24 of which are wave gages used for experimental analysis, one of these is an ultrasonic wave gage. The remaining channels are used by the wave lab staff for various operational reasons. Data was collected at 50Hz in all of the tests.

Processed data for the experiment is organized in Matlab structure files by test name. The processed data files contain data extracted from the raw text files, which are then converted to meters using the function *CalCoeff* as described in equation 11, and truncated to include only data measured during steady state. The raw text files are fairly consistent, but not entirely so; the command inputs had to be modified occasionally between trials and tests to accurately import the necessary information such as the time and date for each trial, the incident conditions, and the wave data. This information, as well as wave characteristics, fill the data structures.

When opening the structure files the user will encounter a four element structure comprised of:

- 'Testfolder', the name of the folder in which the raw data is located, in the experiment data
- 'TrialNumbers'. This vector contains the trial numbers from the test folder of interest (Amplitude Scan, Frequency Scan), in order. All of these trials are included in the TrialData structure. It links each of the trial entries in TrialData to their corresponding trial order in the TestFolder.
- 'TrialData' contains the data from corresponding trials in 'TrialNumbers' from the original test folder of interest .

TrialData is organized by trial number and then by wave gauge, i.e. ProcData.Trial.Wavegage. TrialData opens to many structures, one for each of the TrialNumbers. The user may notice some trials are missing from the data set, these are trials that did not pass an exhaustive quality control analysis. Each of these trial structures contains eight entries: Trial Number, UTCDate (1-360 for each year), TrialDescription, TrialConditions, Trial Tank Temp, Buoy Number (WEC), Rawpoints (# of points in raw DAQ file), and WaveGages. The structure, 'WaveGages', lists each wave gauge for the current trial. There are twenty-three wave gauge structures, listed 1-23, within the WaveGages structure. Regular waves and real seas data have different wave characteristics of interest, so the data that fills the WaveGages structure differs between the two types. Each regular wave test has fourteen entries in it's respective wave gauge structure:

- Channel Number,
- xpos (x-position in basin),
- ypos (y-position in basin)
- Hseries (calculated as crest to trough)

- Tseries, Hmean (of Hseries)
- AmpSeriesRMS (waveform amplitudes calculates as $\sqrt{2} * \text{RMS}(\text{waveform})$)
- HRMS (mean wave height as calculated by RMS)
- Hdev (standard deviation of crest to trough)
- Hmean, Tmean, Tdev (standard deviation)
- Number of waves (between QCindices)
- QCindices (starting and ending points of steady state)
- CalibrationCoefficient

Real seas data contains calculations based on either 280 or 480 seconds of steady state wave data. This size of “window” was chosen so that the frequency resolution is .05, which corresponds to 28 and 48 degrees of freedom, respectively. The eighteen data entries in the real seas data sets are slightly different than regular waves:

- Channel Number
- xpos (x-position in basin)
- ypos (y-position in basin)
- PSD (Power Spectral Density, m^2/Hz)
- Frequencies (associated with PSD)
- Hm0 (four times the square root of the sum of the power spectral density, summed between $\frac{1}{2}$ of the peak frequency to 5Hz)
- Tp (Peak frequency in PSD)
- Te (Energy Period, negative first moment divided by the zeroth moment)
- J (Omnidirectional Wave Power = $\text{density} * 9.81 * \text{sum}(\text{group_velocity} * \text{PSD} * \text{df})$);
- DegreesOfFreedom
- df (Frequency resolution in PSD)
- QCindices (starting and ending points of steady state identifier algorithm)
- NumWaves (Number of waves between QCindices)
- Hseries

- Tseries
- Hmean
- CalibrationCoefficient

As an example, to access the spectral density for each trial one and gage 16, the user simply types *ProcData.TrialData(1).WaveGages(16).PSD*.

Averaged incident wave conditions for the experiment are collected in a separate master file. It covers all regular waves with a target wave height of six centimeters, and all real seas simulations with no directional spreading. Like the processed data, this data is most easily organized into a structure. However, this structure includes both regular wave and real seas data. For more on this see section 3.3.

2.2 Data Processing

2.2.1 Regular Waves

Regular (monochromatic) waves are the simplest and easiest waves to understand, and are a good starting point for understanding how WECs affect waves. In these experiments there were sixteen regular waves tests which spanned the range of wave periods from 0.9 seconds to 2.8 seconds, range in wave height from three centimeters to fifteen centimeters, and have incident directions of shore-normal and 22.5° off normal. This section details how wave height and wave period of these waves are calculated, and also sets a criteria for determining when full wavemaker action is in effect.

Determining Steady State for Regular Waves When the wavemaker begins to make waves there is an initial ramp-up period during which the wavemaker stroke steadily increases from rest to target amplitude. Wave data of interest occurs when the waves recorded are those created by the wavemaker when it is in full action. Since the WEC-array experiments contained a range of wave periods the amount of sample time the wavemaker at full action running varies. Also varying in the data set was the still-water time that was recorded before wavemaker action began. The following accounts for this, finds the wave data of interest, and extracts it from the time series of the whole run.

To figure out how many data points should be included in the “good”, or steady state, wave data, first a database containing the wave period for each run is compiled. The test plan sheets tell how many waves are going to be made under full wavemaker action for each run. Every trial during the experiments was run at a sampling rate of 50 points per second. So for example, during a certain run we know there are 50 waves made at a period of 1.0 seconds and there are 50 data points per second. The data we want to look at is

then approximately $50\text{waves} * 1.0\text{sec/wave} * 50\text{pts/sec} = 2500\text{pts}$, twenty-five hundred data points long.

The gages, however, were not equidistant in the cross-shore from the wavemaker so the waves passing through each gage will reach full height at different points in time. We have defined this initiation point to be when the wave heights measured by the gages have exceeded one half the maximum recorded wave height in the trial, $0.5 * \max(H)$ for each gage. When the $0.5 * \max(H)$ threshold was exceeded the wavemaker action was at least half-ramped up. By inspection it is known that the total ramp-up time was just under 20 seconds, and was not dependent on wave height or frequency. Therefore the 'good' wave data under full wavemaker action must be in action ten seconds (500 data points) past the threshold exceedance. The same methodology was applied to the tail end of the trial to get the chopped time-series of wave data we call *wavedata*.

Wave Characteristics After determining the steady state portion of the wave gage time series, the processed wave data routine can begin. The data was first run through a filter that is the same length as the nominal wave period, which de-means and de-trends the data set. Wave heights are calculated by a zero up-crossing method, and are done so twice; once to determine the steady state boundaries, and again to determine the steady state wave heights. The zero up-crossing method identifies individual waveforms, and their height by noting indices each time the wave form crosses the zero sea surface elevation, in a positive (upwards) direction, $zero_i = \text{find}(\eta < 0 \& \eta_1 \geq 0)$, where $\eta = \text{wavedata}(1 : \text{end} - 2)$ and $\eta_1 = \text{wavedata}(2 : \text{end} - 1)$. Wave periods, T , are the length of time between $zero_i$ indices, and wave heights, H , are the difference between minimum and maximum sea surface elevations, η , between $zero_i$ and $zero_{i+1}$. This method gives vectors for both H and T and the mean of these are the characteristic wave height and period for the trial.

The root mean squared wave height, H_{rms} , is an alternate way of determining wave height. For each wave form, ζ (that is, η between $zero_i$ and $zero_{i+1}$), $H_{rms} = 2 * \text{std}(\zeta)$. Both measures of wave height were reported, and their results are nearly identical. Individual wave heights are needed to complete this routine. The wave height of record in this data set was H_{rms} .

Repeatability An important check in any experiment is repeatability, in this section we check the repeatability of both the wave maker and WEC effects. For a single target wave height (six centimeters), the repeatability of wave data between like trials of four regular wave periods were investigated for 1-WEC, 3-WEC, and 5-WEC array configurations. Figure 7 shows longshore transects of wave height in both the offshore and lee, with associated error bars of one standard deviation for these trials. The error bars are small in the offshore, indicating to us that there was good repeatability in wavemaker ability. Small error bars in the lee tell us the WEC effects on the lee wave field are also repeatable.

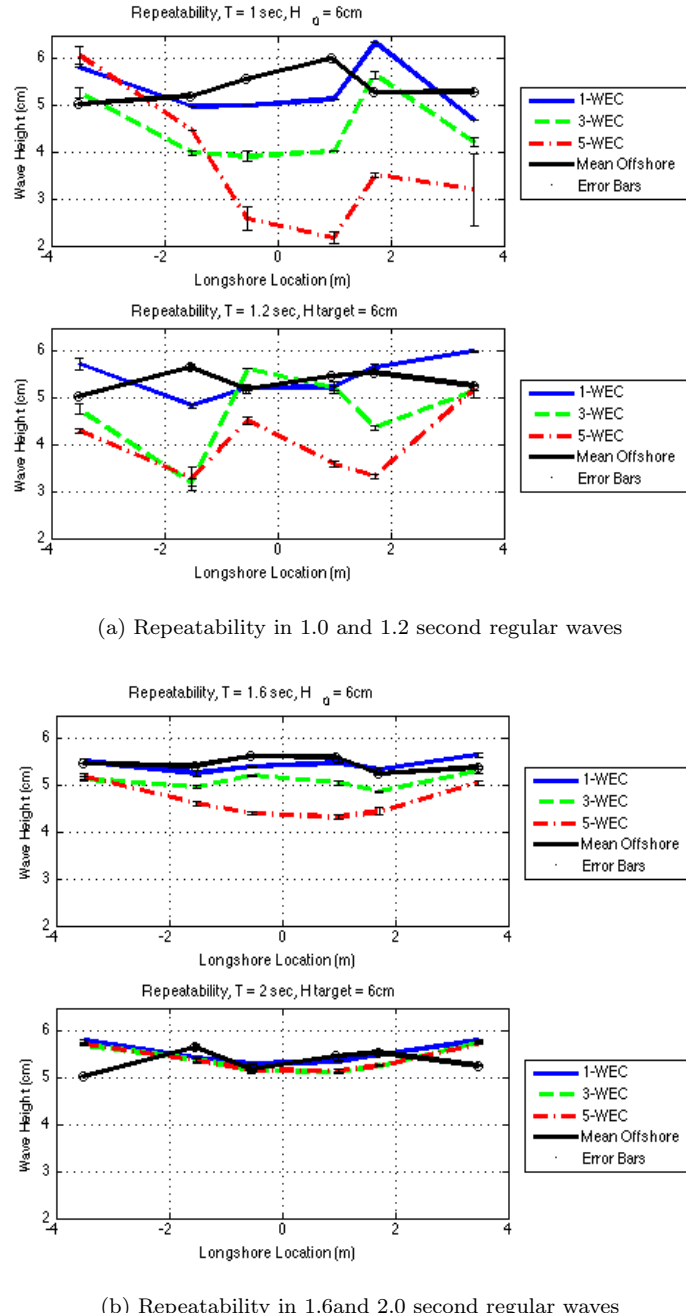


Figure 7: Wave maker and WEC influence repeatability of wave data between like trials of four regular wave periods in single, three, and five device WEC arrays. Error bars of one standard deviation show very good repeatability between like trials. The x-axis is longshore location, the y-axis is wave height.

2.2.2 Real Seas

Data analysis for real seas trials was similar in some ways to the regular waves trials, but since the sea surface elevation characteristics are not discernible to the naked eye, more faith in analysis is required. This section details how full wavemaker action were determined, how the frequency spectra was determined, how significant wave height was calculated, and how energy flux and power were found.

Determining Steady State for Real Seas Determining steady state in a random sea was quite different than from a regular wave situation since the expected wave height of each waveform is unknown and by nature random. The duration of time between the onset of data collection wave not automated (it was a manual process); hence, the need for an automated algorithm to determine the steady state conditions based on data alone. Our method was based on calculating the root mean squared wave height, H_{rmsWin} in a series of ten-second windows throughout the trial, on a gage-by-gage basis. For each trial and gage the “pre-chopped” wave data, $wvdata$, contained $WinNum = \text{length}(wvdata)/(10\text{sec} * 50\text{pts/sec})$, where $WinNum$ is the number of windows. Characteristic wave heights for each ten-second window were calculated, and the cumulative elapsed sample time, t_s at the midpoint of each window was recorded. Windows were sorted by H_{rmsWin} , and a threshold was developed from mean of the top twenty-five windows, $0.2 * \text{mean}(H_{rmsWin}(1 : 25))$. The collection of windows that pass this threshold are sorted chronologically, and the midpoint in time is the mean of the first and last windows $Midpt = \frac{t_{s,1} + t_{s,end}}{2}$. Trial indices are then $Ind_1 = Midpt - \frac{t_{total}}{2} + 1$, and $Ind_2 = Midpt + \frac{t_{total}}{2}$, where t_{total} is the total sample time of the trial which is known in advance.

Spectral Analysis This section details some aspects of spectral analysis, and how the spectral density was calculated for the WEC-Array Experiments. The processed energy spectra was calculated at twenty-eight or forty-eight degrees of freedom (dof) depending on trial length, with constant $df = 0.05$, and ensemble (Bartlett) averaging, with a Hamming Window.

The energy spectrum describes a random sea state by the energy levels at different wave frequencies, where the sum of energy from all frequencies is the total energy in the wave field, and each frequency is a sinusoidal wave form with an component wave amplitude. To characterize random seas trials, common practice is to employ spectral analysis in order to find the energy spectrum, $S(f)$, and in turn calculate the significant wave height, H_s , the peak energy period, T_p , and the energy flux, E_f .

Spectral analysis based on the Fast Fourier Transform (FFT) was developed by Cooley and Tukey [Cooley & Tukey, 1965], which makes the assumption that any piecewise continuous function can be represented over an interval of time as the sum of sines and cosines

[Dean & Dalrymple, 1998]. An additional important assumption that the FFT takes is that the time-series is infinitely long. The fact that this is never true results in an imperfect and noisy FFT full of smearing and energy leakage. These issues are dealt with through windowing and averaging energies of frequencies together, or increasing the degrees of freedom (DOF). The raw frequencies at which energies are calculated are called the Fourier frequencies, f_j , where $f_j = j / (N\Delta t)$ for $j = 0, 1, 2, \dots, N - 1$, where N is the number of data points in the time-series, and Δt is the sampling rate. The energy spectrum at this stage is extremely noisy, with many spikes and troughs; a result of a finite number of waves frequencies made by the wavemaker, the collection rate, and a finite record length.

To deal with problems in the energy spectrum associated finite record length and non-zero end points, windowing methods are applied. Leakage occurs because only energy at frequencies that coincide with a Fourier frequency will project onto a single basis vector; all other frequencies will exhibit non zero projections onto the entire set [Harris, 1978]. Windows are weighting functions applied to time-series data to reduce the spectral leakage associated with finite time-series [Harris, 1978], the problem is that they reduce the total amount of energy in the time series, seen in Figure 8. A correction factor must be used to scale or “boost” the energy spectrum back to its nominal total energy. This scaling factor is calculated by:

$$bst = \sqrt{\frac{var(\eta)}{var(\eta * W)}} \quad (12)$$

where η is the sea surface elevation before the window is applied, and W is the window function of length η . Both the window and the boost are applied to the time-series before any FFT algorithms are done.

Two kinds of energy spectra averaging can be employed to smooth the energy spectra: bin-averaging in the frequency domain, and ensemble (or Bartlett) averaging in the time-domain. This paper uses ensemble averaging. To ensemble average, the time-series is broken up into equal ensembles of length $N_{ens} = N / (dof/2)$, and an FFT is taken of each ensemble. These ensembles are averaged together at each frequency to get the estimated energy spectra, S :

$$S_i = \frac{\left(\left| \frac{FFT(\eta_i * W * bst)}{N_{ens}} \right| \right)^2}{df_{ens}} \quad (13)$$

for $i = 1 : N_{ens}$, and $df_{ens} = s/N_{ens}$. The resulting spectra S_i are averaged together to obtain the ensemble averaged spectra, seen in Figure 9.

Increasing the degrees of freedom results in a more statistically significant spectra, but reduces the frequency resolution. The frequency interval is related to degrees of freedom by $df = s / \frac{2N}{dof}$. As discussed 2.1.2, some of the the single-WEC real seas trials had a shorter sample time, and therefore a smaller N than 3-WEC and 5-WEC trials. We opted to

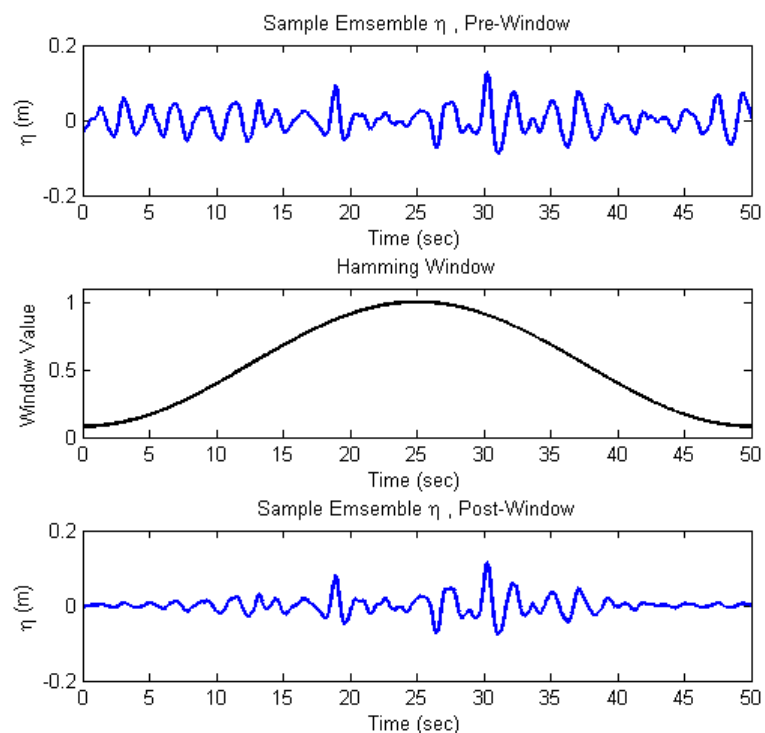


Figure 8: This example of the application of the Hamming window shows energy losses to the time-series, and the need for energy “boosting”.

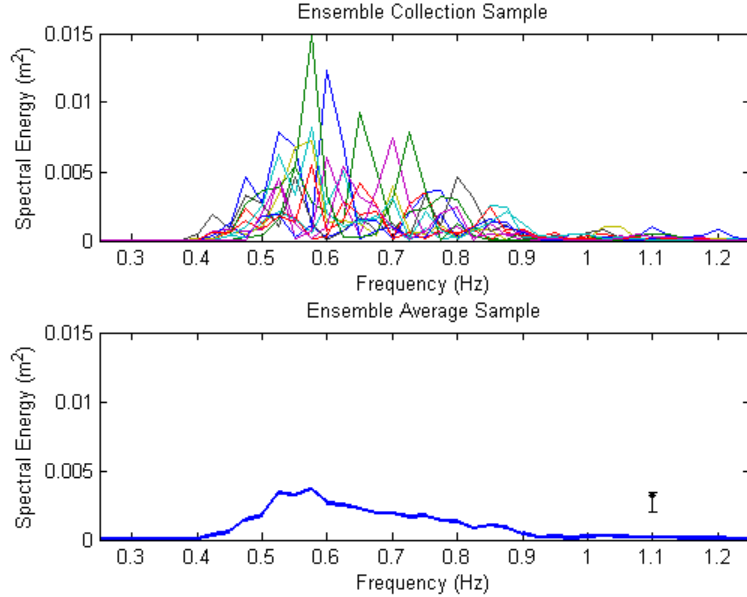


Figure 9: Many ensembles are averaged together from the top panel to get a single representative wave spectra of the entire time series in the bottom panel. Confidence interval plotted to the right.

keep df constant between these two sets of trials, and live with different levels of statistical significance. Although trial lengths of 313 seconds and 540 seconds were run, the best combination of N and df came from using 280 seconds of the shorter trials, and 480 seconds of the longer trials. With df constant, the resulting degrees of freedom were 28, and 48, respectively.

Confidence intervals for the spectra were calculated from the χ^2 distribution, and depend on the degrees of freedom, dof , the confidence level, α , and the spectral value, S . Upper and lower confidence bounds are calculated as:

$$Prob \left[\frac{dof}{q_{\chi^2}[\frac{\alpha}{2}, dof]} S \leq S_{true} < \frac{dof}{q_{\chi^2}[1 - \frac{\alpha}{2}, dof]} S \right] = 1 - \alpha$$

where S is the expected value of the spectral energy calculated by the methods outlined above, and S_{true} is the true spectrum. In the following analysis the confidence level is ninety-five percent. A function *PSDconfSpec* was created to find the upper and lower confidence interval bounds that could be plotted along with processed data spectra using the *errorbar* function in Matlab.

Characteristic Wave Statistics The primary wave parameters for real seas are significant wave height, H_s , and peak period, T_p . Peak period is determined by the inverse of the frequency bin that has the maximum energy of all frequencies in the energy spectrum, $f_{max} = \max(S(f))$ and $T_p = f_{max}^{-1}$. The significant wave height can be measured as the average of the top one third of all wave heights recorded in each time-series, $H_{1/3}$. In the frequency domain, the significant wave height, H_{mo} , is typically calculated from the zeroth moment, $m_o = \sum S * df$, and defined as $H_{mo} = 4 * \sqrt{m_o}$. This thesis characterizes the significant wave height as $H_s = H_{mo}$.

2.2.3 Energy Flux and Power

Total energy flux is the spatial integration of energy flux. Energy flux per unit crest length, Ef , for monochromatic waves was described in equation 7, but the formulation to find energy flux of a spectrum is different. Unlike a monochromatic wave the energy spectrum contains many different frequencies of waves, all with different group velocities. Recall that $Ef = EC_g$; to accurately calculate energy flux in a spectral sea state, each frequency must be considered individually before a summation of energy flux can be made to characterize the data. Common practice is to calculate group velocity $C_{g,i}$ for each frequency, f_i , , multiply this value by the energy at associated frequency bin, S_i , and integrate across all frequencies.

$$Ef = \int \rho g * C_{g,i} * S_i * df \quad (14)$$

For regular waves the energy flux calculation must be multiplied by two because frequency integration for regular waves and real seas data yield different results (i.e., $\text{trapz}(f, S_f) = \frac{H_{mo}^2}{16}, \frac{H^2}{8}$, for real seas and regular waves, respectively), and was checked against numerous hand calculations of known energy flux for regular waves.

For this work we have only calculated energy flux for unidirectional conditions. Energy flux in multi-directional conditions will depend on the accuracy of the directional spectrum estimation, and will be perused at a later date. Net shoreward directed wave power was calculated as the longshore integration of energy flux. Because the six-gage offshore gage array and the six-gage lee gage array are both longshore transects, wave power passing through their respective footprints can be calculated and compared:

$$P = \int Ef * dy \quad (15)$$

which was done by the *trapz* integration method in Matlab. It was expected that the loss power loss between the two gage arrays should be approximately equal to the wave power absorbed by the WEC-array.

It is well known that WECs modify wave power in a frequency dependent fashion. In

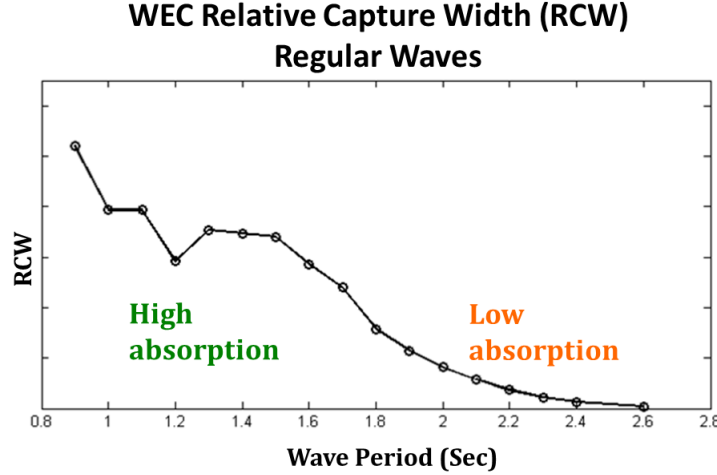


Figure 10: Qualitative relative capture width (RCW) curve for regular wave cases of the “Manta 3.1” wave energy converter

this thesis the frequency dependent relative capture width (RCW), or, the power capture relative to the available wave power within the longshore footprint of the WEC is analyzed. It was of interest to see if the same frequency dependent power absorption recorded by the WEC can be tracked from the offshore gage array to the lee gage array. Since WEC RCW is a ratio between units of power absorbed per unit width [$\frac{\text{Watts}/\text{m}/\text{Hz}}{\text{Watts}/\text{m}/\text{Hz}}$], the wave gage comparison needed to be as well. In finding the energy flux for a single gage, the wave power spectra was also calculated; it is the energy flux before the frequency vector integration

$$S_{waveP} = \rho g * C_{g,i} * S_i * df [\text{Watts}/\text{m}/\text{Hz}] \quad (16)$$

The difference between the incident power and the power measured at the lee gages gives power lost from the wave field (deficit), at each frequency element. The ratio of power deficit to incident power gives relative power loss at each frequency, or the Relative Influence Width (RIW). It is characterized as influence because it is not a direct calculation of capture, but rather parametrizes the influence the WEC has had on the surrounding wave field.

2.2.4 Mechanical Power

Power takeoff from the “Manta” device was actuated by pitch motion of the float with respect to the nacelles (the wing-like objects on either side of the device). The nacelles rotated about the center float driving the linear damping, c . Mechanical power was calculated by

tracking relative position, θ , of the nacelles; for clarification of this geometry see Figure 2. Tracking enabled the calculation of velocity, $\omega = (\theta_{i+1} + \theta_i)/dt$, torque, $\tau = c\omega_i$, and power, $P = \frac{1}{N} \sum_i^N \omega_i \tau_i$.

Performance of the device was characterized by relative capture width (RCW), where $RCW = P/RPA$, and P is equal to mechanical power, and RPA is relative available power, or the amount of wave power available in the footprint of the device. Figure 10 shows qualitatively the RCW curve for the “Manta 3.1” wave energy converter device. The device was designed for higher relative capture in shorter wave periods.

To ensure the consistent comparisons, wave data and mechanical data processing and analysis has to be consistent. Only the following cases were included in RCW calculation: head-on regular waves with a target wave height of six centimeters, and head-on real seas waves with no spreading. Spectral analysis was needed to analyze real seas cases, and the same spectral methods as described in paragraph 2.2.2 were used. RCW for a single regular wave period was the mean of all RCWs for trials with the same nominal wave period. Similarly, for real seas each ordinate of the spectral RCW is calculated from all significant spectra in all repetitions regardless of WEC number. Spectral ordinates were considered significant in if the value was at least 0.5 percent of that spectrum’s maximum spectral density. The number of trials for an ordinate ranges from two to twenty-six trials.

3 Results

Data analysis was extensive, and it was impossible to include all data analysis done on this data set in the following section. What follows are important aspects of the data analysis that follow along a critical path to the conclusions in this thesis. Results from regular waves with a target wave height of six centimeters and real seas trials with no directional spreading are presented. Reductions of wave height and power in the lee gage array due to the presence of WEC arrays are investigated.

The lee gage array (gages 11-16) best captures the wave height reductions in the basin that were due to WEC arrays since it is both the widest gage array shoreward of the WECs and is close enough to the WECs to have a large signal. As was shown in Haller et al. [2011], wave height reductions due to WECs are dependent on wave period. Figure 11 shows reduced wave heights in the lee gage array, it also shows incident wave heights in the offshore array and wave heights lateral of the WEC array in gage ten. It is clear that wave heights in the lee are reduced, and show a shadow like pattern with more reductions typically occurring near the middle of the array. The three WEC array case has some irregularities due to asymmetry in the array configuration.

Because in real seas conditions the WECs modify wave spectra at different magnitudes along the frequency domain, we compared incident wave spectra to the spectra measured in the lee of the array. Changes in spectral shape indicate at which frequencies the WECs are modifying the incident power and by how much. Alexandre et al. [2009] showed that if the WEC is tuned to the peak frequency of the incident spectrum, the leeward shape should be bi-modal compared to the single-mode incident spectra. Figure 12 shows statistically significant differences between incident and lee spectra for three and five WEC arrays, with five WEC arrays having larger differences. Lee spectra were characterized as the average spectra from gages thirteen and fourteen (see Figure 3), which are centrally located in the lee of the WEC array and have the largest wave height deficit. Incident spectra were measured for each sea state. Also shown are the 95% confidence intervals.

Differences between the incident spectra and the lee spectra change depending on the sea state, but one can see that at higher frequencies the differences are generally larger. At frequencies lower than 0.6 Hz there are no significant differences between spectral shape in any of the sea states. Although the shadow signals are smaller at higher frequencies, there was clearly more spectral modification from the WEC in this region. Unlike predictions by Alexandre et al. [2009], the resultant spectra are not bi-modal, but this is because the WEC is not tuned to a single wave period. Still some bi-modal characteristics were seen, especially in the Oregon3 sea state as seen in figure 12.

During the remainder of this thesis the incident wave characteristics for all target wave conditions are specified as the conditions measured during single WEC trials. That is, incident wave data for determining shadow magnitude in three and five device arrays is

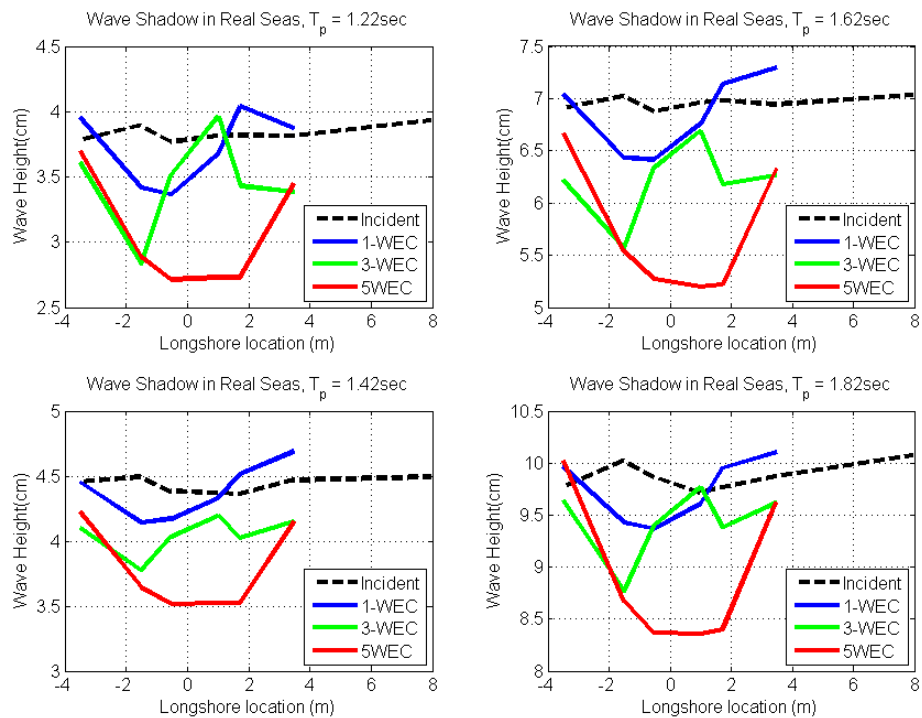


Figure 11: Wave height reductions in the lee gage array due to the presence of different sized WEC-arrays in four real seas sea states. Black is the incident wave condition, blue is the single-WEC case, green is the three device case, and red is from the five device case.

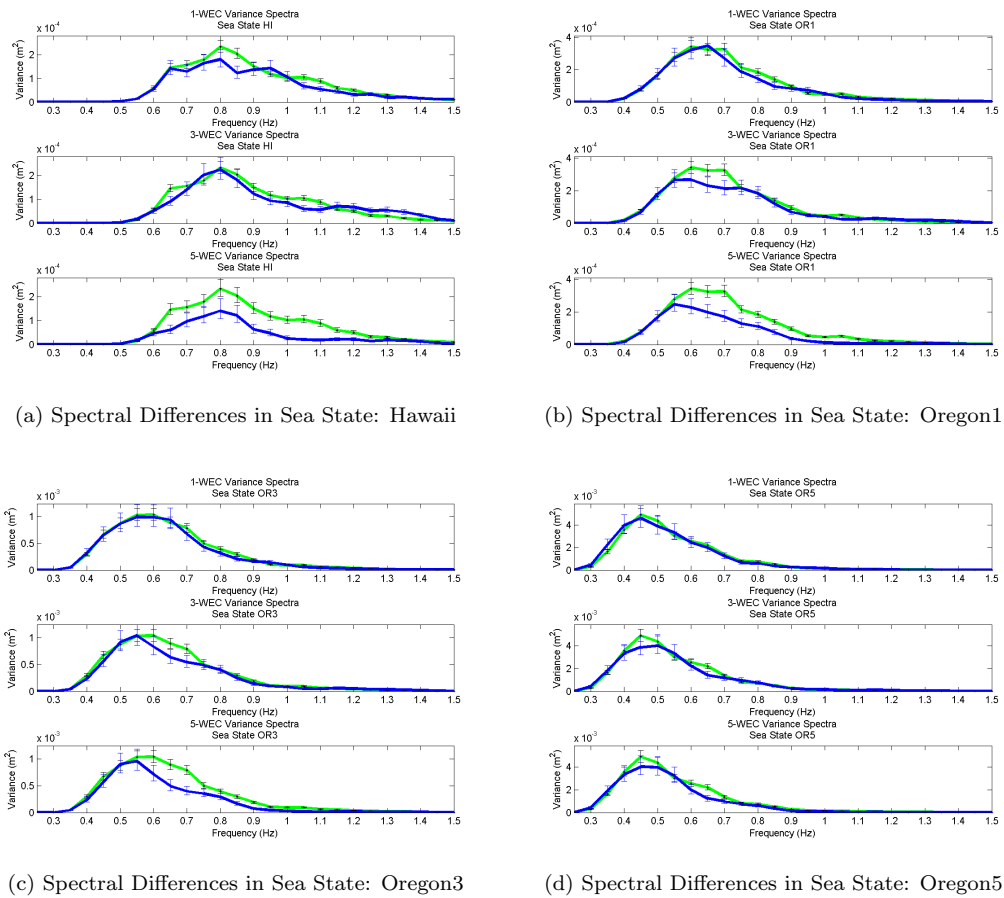


Figure 12: Measured changes to the variance spectra for four select sea states, between incident and the average of gages thirteen and fourteen in the lee of the array.

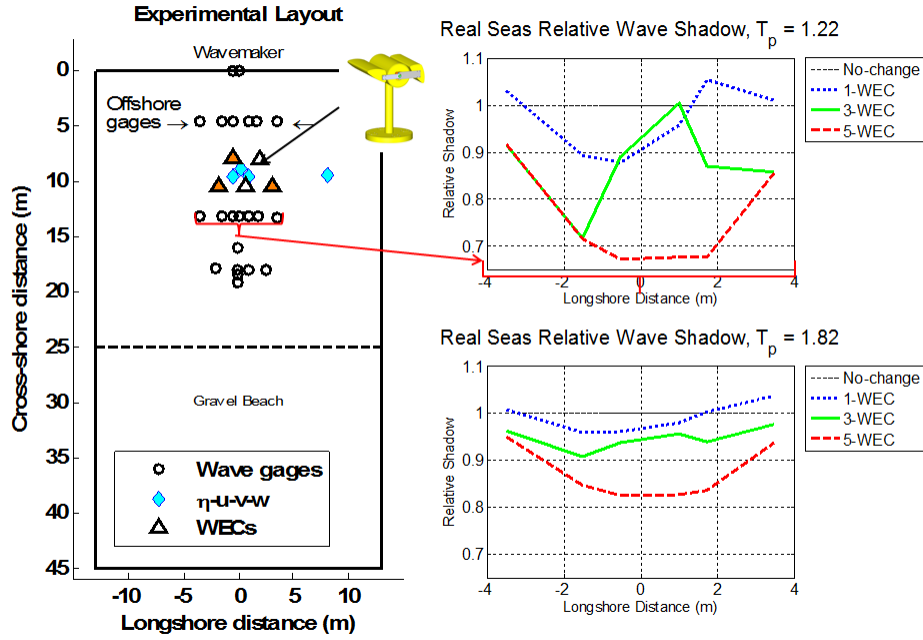


Figure 13: Wave Shadowing in two real seas trials (HI & OR3). The left panel shows where the the array shadow is measured in the experimental set-up. The right panel shows that more shadowing occurs in larger arrays, and in real seas with shorter peak wave periods.

from single device trials that had the same target wave conditions. This was done to reduce the influence of larger WEC arrays on the measured incident wave field. More on this can be found in Section 3.3. Using the wave data we now look at relative wave height reductions, with respect to the incident wave field. Figure 13 shows in the right panel relative wave height reduction plots in the lee of the WEC-array (wave shadowing) as a function of longshore location for two real seas sea states. The y-axis on this plot is relative wave height reduction, which is the ratio of wave heights recorded in the along the lee gage array with respect to the measured incident wave height. The red arrow indicates where the wave shadow calculations for the gages were made in the experimental layout. Black circles are the wave gages, triangles indicate the location(s) of WECs in the array, where orange triangles are the locations of the asymmetrical 3-WEC arrangement, and the blue diamonds locations of co-located current meters.

The total magnitude of shadowing was characterized as the power deficit between the incident wave field and the lee gages. Incident power was specified as the average energy flux from gages one through six and ten, and then multiplying by the length of the lee gage array. Conceptually the power deficit was the power lost between the offshore gages and the

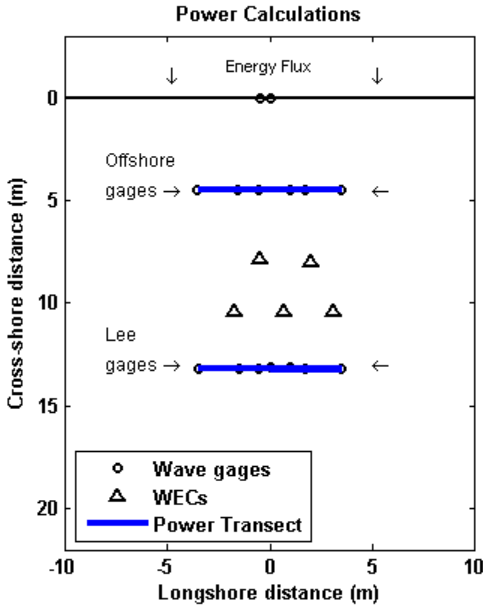


Figure 14: Power lost in the wave field is characterized as the difference between the incident power and the power measured at the lee gage array. Incident (offshore) power is the mean energy flux from gages one through six (the offshore gage array) and ten, multiplied by the width of the lee gage array.

lee gages due to the WEC array, as seen in Figure 14.

3.1 Monochromatic Wave Shadowing Analysis

Trends of wave shadow magnitude in regular wave trials are presented in this section, as are comparisons of these deficits to mechanical power capture measured from the WEC device. Also investigated were wave shadow magnitudes with respect to the incident wave power available, which gives a good estimate to how much influence the WEC-array had on a range of wave conditions. These results help to understand changes to the wave field in the real seas trials, as well as help to constrain future model results.

Energy Flux and Power WECs are designed to extract wave power; hence the power exchange from wave to device should be evident in the measured power loss of the waves in the basin. The WEC-Array Experiment data set has many trials to investigate the magnitude of this physical process, often there is more than one trial per wave condition. When the opportunity arose to average like trials, the wave data from the trials were averaged. Typically two trials were averaged; however, not all conditions contained multiple trials for analysis due to occasional bad data.

Analysis of the observed wave data showed that the power absorption ratio is frequency dependent, which is good considering that the WEC power generation ratio (relative capture width) is also frequency dependent. The relative capture width (RCW) of a WEC operating in isolation at a range of distinct frequencies was known: calculated by Columbia Power Technologies. Therefore a similar parameter should be designated for wave gage data. Relative influence width (RIW) is a proxy for shadow magnitude, and is calculated by the ratio of the relative power available (RPA) to measured power loss, where RPA is the incident energy flux multiplied by the nominal width W of a WEC (.55 meters), and by the number of WECs in the water.

$$RPA = W * Ef * \#WECs \quad (17)$$

$$RIW = \frac{P_{loss}[\text{watts}]}{RPA[\text{watts}]} \quad (18)$$

Measured power deficit and the Relative Power Available (RPA) from the regular wave trials are plotted in Figure 15. The parameters RPA and RIW are defined in equations 17 and 18. Measured RIW is the ratio of the measured power deficit in the waves to the RPA. Relative capture width (RCW) was calculated by Columbia Power Technologies from the measured power capture by an isolated WEC (see section 2.2.4), and corresponds well with the measured wave power.

The top panel of Figure 15 shows relative power available for the WEC-array as a function of wave period. This is the average incident wave power from the incident wave data set, multiplied by the summed longshore width of the WECs in the array for a given array size. For a given wave height RPA increases with wave period. The RPA curve reflects this trend with a leveling off at the higher periods due to a decreased wave height in those trials.

From 0.9 seconds to 1.9 seconds, there are significant amounts of wave power lost, which is mirrored in the RCW curve (lower panel), which was determined from the WEC mechanical power data only. At wave periods above 1.9 seconds the impact of the WEC-power absorption signal is likely not visible in the wave data above normal experimental variation and noise. In the wave periods where power absorption is present, the RIW curves for 3-WEC and 5-WEC are generally higher than the 1-WEC RIW curve, likely due to variability in the signal-to-noise ratio. At wave periods above two seconds, there is a consistent pattern of negative power loss, or power gain. This also is because of low signal to noise ratios. Wave power increases with wave periods given a constant wave height so it follows that errors in wave gage data are amplified in this region as well. It is known that the WEC was not designed to perform as well at these wave periods so it will have a small power capture.

The bottom panel of Figure 15 shows the ratio of power deficit (power deficit in wave data) to relative power available (RPA), this ratio was previously defined as relative influence

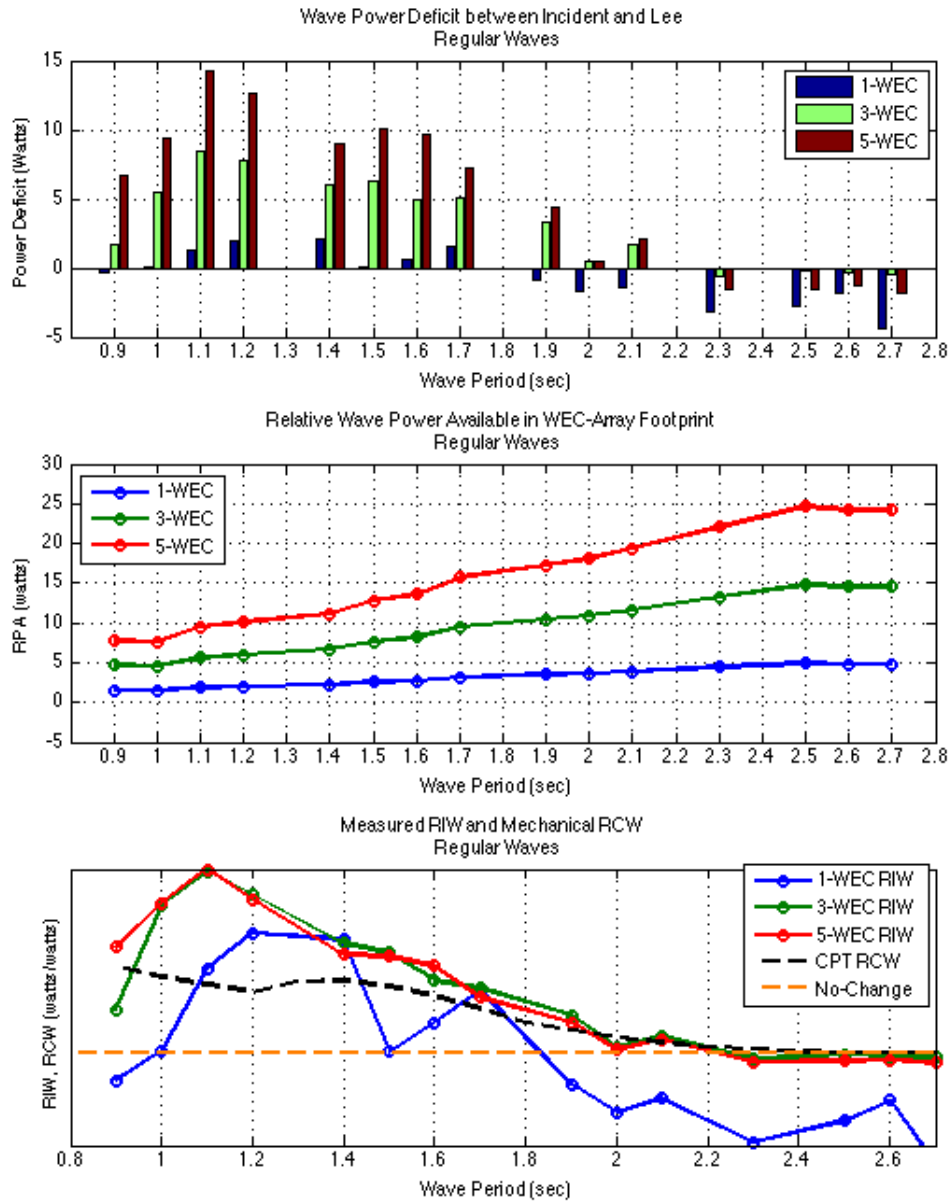


Figure 15: . The top panel shows the measured power loss, and relative power available (RPA) over a range of regular wave periods. The bottom panel displays the relative influence width (RIW) for differently sized WEC-array arrangements over a range of regular wave periods. The RCW curve is property of CPT so y-axis labels are not included.

width (RIW). RIW is plotted as a function of frequency for each array size, and against the mechanical RCW. The calculation for mechanical RCW is described in Section 2.2.4, and represents the performance of the device at different wave periods by the ratio of power absorbed by the device to the wave power available. Mechanical power absorbed (RCW) and power removed from the wave field (RIW) follow the same trends, decreasing in increased wave periods. In places where the magnitudes of the RIW curves are higher than the RCW curve this figure indicates other physics than WEC absorption are adding to the WEC shadow. Other physics must be present because the RCW only represents power removed by the wave field by WEC absorption. At shorter periods the differences between the RIW curves and the RCW are greater. The RIW for single device arrays is more variable because of low signal-to-noise ratio, as described earlier. More trust should be put into the three and five device results since their signals are stronger, and the fact that they are so similar gives even more reason to believe they are truly representing the power deficits in wave field. Because the power-based RIW curves between three and five WEC arrays are so similar, this implies at least moderate linearity of scaling between array sizes.

An additional parametrization of the linearity of power deficit between different WEC-array sizes is an investigation of the ratios of power deficits between different array sizes. If the relationships are completely linear, power absorption from the 3-WEC array, for example, should be three fifths that of the 5-WEC array. Figure 16 shows moderate linearity between 5-WEC and 3-WEC power deficits. The green dots represent the ratio of power deficit in the wave data from 3-WEC to 5-WEC, while the green line is equal to 0.6 which corresponds to perfectly linear scaling between array sizes. When the green dots are above the solid green line, this would indicate non-linear growth between array scaling, that is more power is removed than the nominal gain due to an increase in the number of WECs. Dots below the solid lines represent power deficits less than the nominal gain by the addition of WECs. Ratios of 1-WEC array deficits to 5-WEC deficits are extremely volatile due to the low signal-to-noise ratios in the 1-WEC array data as discussed earlier. Overall, signal-to-noise ratios are worse from left to right due to the amplification of wave gage noise and the decline in the WEC power absorption, which may help explain the very high ratios from 3-WEC to 5-WEC at higher periods. Periods over two seconds have not been included here because of the low signal-to-noise ratio. Within the range of decent signal-to-noise ratios, scaling between the array sizes appears to be moderately linear.

3.2 Real Seas Shadowing Analysis

Real seas analysis builds upon trends learned in regular waves analysis and is important for understanding what kind of effects WEC-arrays will have at in-situ commercial applications. This section details how the seven sea states (Oregon 1-5, Hawaii, and Ireland) are affected by different WEC-array configurations and directional spreading, by looking at power loss,

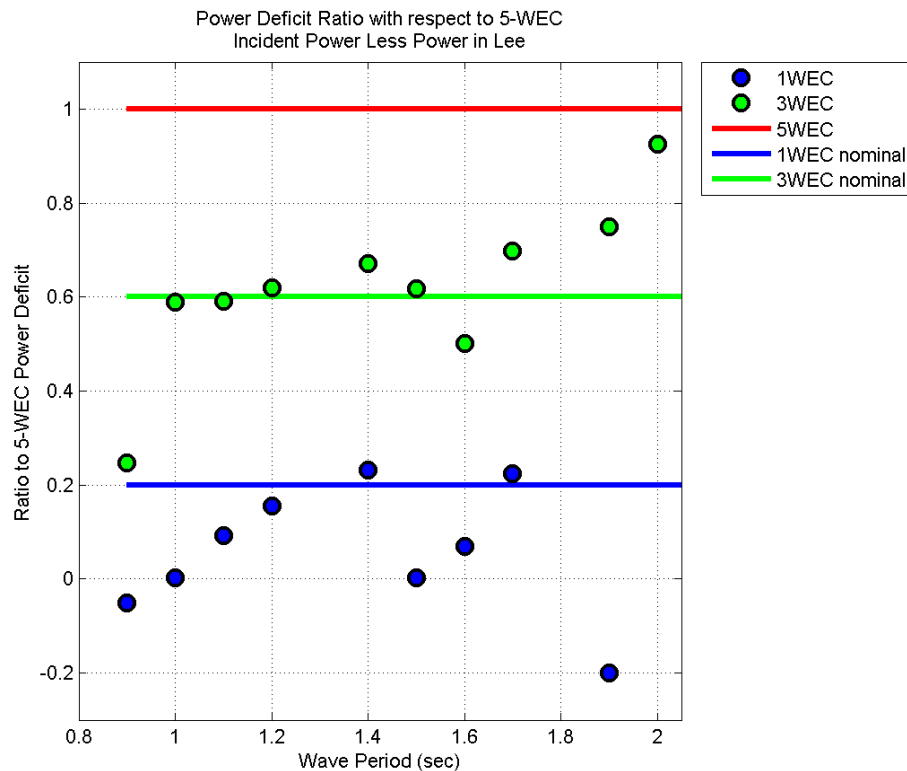


Figure 16: The green dots represent the ratio of power deficit in the wave data from 3-WEC to five WEC, while the green line is equal to 0.6 which corresponds to perfectly linear scaling between array sizes. When the green dots are above the solid green line, this would indicate non-linear growth between array scaling

Table 4: Real seas target wave conditions 2

Real Seas		
Sea State	Wave height	Peak period
	$H_{m0}(\text{cm})$	$T_p(\text{sec})$
HI	4.5	1.22
OR1	4.5	1.62
OR2	7.6	1.42
OR3	7.6	1.82
OR4	7.6	2.22
IR	10.6	1.62
OR5	13.6	2.22

and changes to the spectral shape. The sea states are described in Table 4

Energy Flux and Power This section will present results for linking power measured in the wave field to mechanical WEC power trends, and understanding the correlation between the two for real seas. Power deficits measured in wave spectra are investigated in bulk (summed across all frequencies) and frequency-dependent fashions. Several ratios were calculated to better understand to what degree the wave-field was modified, these were the relative power available (RPA), relative influence width (RIW), and the 5-WEC Power Ratio. A reminder as to what each sea state's characteristics can be found in Table 4.

This analysis will focus solely on unidirectional sea states. Directionally spread cases are not included because accurate calculations of shore-directed energy flux require directional spectra analysis, which have not been attempted yet. To accurately calculate power or energy flux in a spectral sea state, each frequency must be considered individually. The formulation for energy flux is described in equation 14. This section will describe how the bulk and frequency specific parameters of energy flux and power were attained.

Bulk parameters of energy flux and power were attained in a similar fashion to those parameters for regular waves. The incident wave power (as calculated in the incident data set) was compared to the power measured in the lee of the array; bulk power lost was the difference of the two. Relative power available (RPA) was calculated as as the average incident energy flux multiplied by the total footprint of WECs in the array. Bulk RIW was then the ratio of bulk power loss to RPA.

Frequency dependent parameters better inform as to how the WEC affect the wave field piece-by-piece; they can describe how the incident power has been lost on a frequency basis. Because energy flux can be evaluated at each frequency, so can power. Here, the wave power spectrum, which was described in equation 16, in units of [Watts/m/Hz], can be integrated in the longshore to obtain total power at each frequency for the domain of interest. This was

done for both the average incident wave power spectrum [Watts/m/Hz] and the lee gages array spectra [Watts/m/Hz], where both were integrated along the length of the lee gage array [meters] to obtain the wave power spectrum for each [Watts/Hz]. Power loss spectra was then calculated as the element-wise difference between incident wave power spectra [Watts/Hz] and the lee wave power spectra [Watts/Hz]. The relative power available (RPA) spectra [Watts/Hz] was calculated as the average incident wave power spectra [Watts/m/Hz] multiplied by the total longshore footprint [meters] of the WECs in the water [Watts/Hz]. WEC-array footprint width is characterized as the nominal width of of the device (.55m), multiplied by the number of WECs in the water (1, 3, or 5) to get a width in meters. Relative influence width (RIW) was then the ratio of the RPA spectra to the power loss spectra and is expressed in units of {[Watts/Hz]/[Watts/Hz]}, similar to equation 18, but at each frequency. This process was applied to wave data from the average of all unidirectional wave cases for each of the seven sea states.

Bulk power losses are calculated similarly for real seas as they were for regular waves. Bulk power parameters are shown in Figure 17 as a function of sea state. Incident wave power increases left to right, and peak period varies. In all panels the blue colors corresponds to 1-WEC, green to 3-WEC, and red to 5-WEC. The top panel shows that the Hawaii sea state has the smallest power deficit for each WEC arrangement, while Oregon5 has the largest. Some of the 1-WEC power deficits are negative due to low signal-to-noise ratios; as incident power increased so did the noise and in high period cases this overcame the low signal. The middle panel shows that the incident wave power is much greater Oregon5 than Hawaii. Relative influence of the WEC array was calculated as the ratio of power loss to power available. Relative influence width ratio is shown for each sea state in the bottom panel. Note that the WEC-arrays in the Hawaiian sea state had the largest influence, while the RIW for Oregon5 had much less. The RIW for single-WEC data is more variable than the three and five WEC arrays since the signal for single-WEC arrays is much smaller. Results from three and five device arrays give an good idea as to how the array modulated the wave field for each sea state since the signal-to-noise ratio was much higher. Generally, the RIW curve is higher in sea states with short peak periods, and drops in sea states with high periods (OR4, OR5), indicating the WEC has more influence in sea states with shorter peak periods. This was also true in regular waves, as seen in the bottom panel of Figure 15. Because the RIW values for three device arrays and five device arrays are very similar, linear scaling between array sizes may be present.

As with regular waves, a good estimate of the linearity of the power deficit between different WEC-array sizes was done by comparing the deficits of single and three device arrays to that of a five device array. If the relationships are completely linear, power absorption from the 3-WEC array, for example, should be three fifths that of the 5-WEC array. Figure 18 shows moderate linearity between 5-WEC and 3-WEC power deficits. The green dots

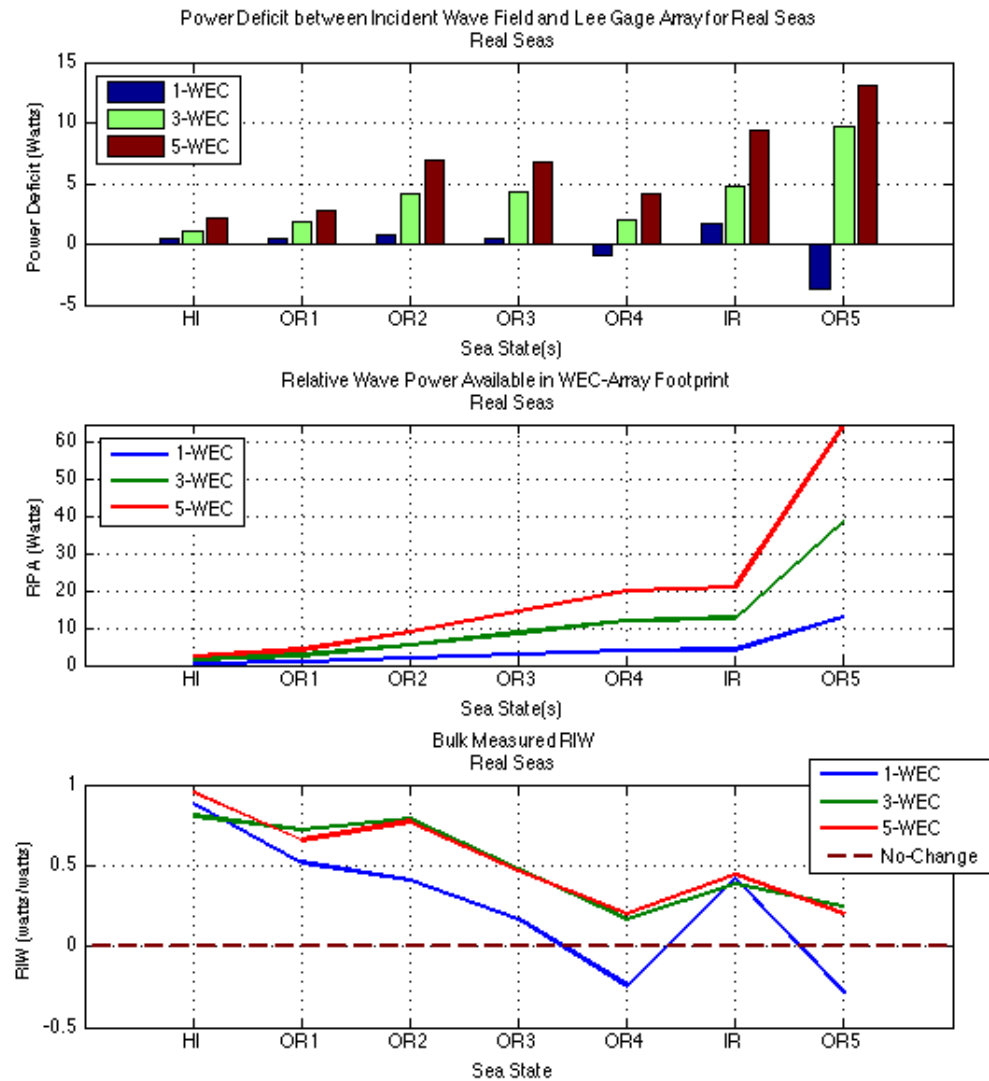


Figure 17: The top panel shows the measured power loss for each of the seven sea states. The middle panel shows wave power available in the footprint of the WEC-array. The bottom panel displays the relative influence width (RIW) for differently sized WEC-array arrangements for each sea state.

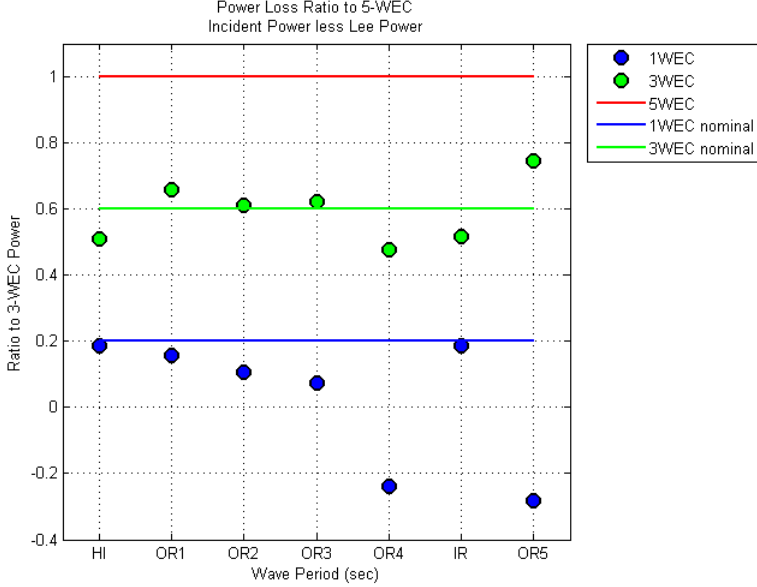


Figure 18: The green dots represent the ratio of power deficit in the wave data from 3-WEC to five WEC, while the green line is equal to 0.6 which corresponds to perfectly linear scaling between array sizes. When the green dots are above the solid green line, this would indicate non-linear growth between array scaling.

represent the ratio of power deficit in the wave data from 3-WEC to 5-WEC, while the green line is equal to 0.6 which corresponds to perfectly linear scaling between array sizes. When the green dots are above the solid green line, this would indicate non-linear growth between array scaling, that is more power is removed than the nominal gain due to an increase in the number of WECs. Dots below the solid lines represent power deficits less than the nominal gain by the addition of WECs. Ratios of the single-WEC power deficit were also moderately linear, except in the sea states Oregon4 and Oregon5 where there appears to be an increase in power. In these sea states the peak period was the highest (2.22 sec), therefore the shadow signal was lower than the noise signal. In sea states and arrays where the the signal-to-noise ratio was higher, this figure shows moderate linearity in scaling of array sizes.

Because the three and five device arrays have very similar bulk RIW curves and power deficits appear to scale moderately linear with size, we next examine how well these RIW curves match the mechanical relative capture width (RCW) curves. In real seas conditions the RCW curves were calculated in the frequency domain for each frequency. To compare the mechanical RCW to power loss measured in the wave field, the RIW spectrum is needed. Figure 19 shows power deficits from a 5-WEC array in the lee wave field as a function of frequency. Because of shadow signal strength considerations, only results from the five device

array are shown here. The top panel shows incident power spectra for seven unidirectional sea states; incident power from OR5 dominates since both the peak wave period and significant wave height were highest. The middle panel shows the element-wise deficit between the lee and incident power spectra, with OR5 having the largest signal. The bottom panel shows the ratio of deficit to incident power (RIW) along the frequency spectrum against the sea state averaged mechanical RCW (ratio of panels one and two). The fourth panel shows the seven point smoothed RIW against the measured RCW, which is easier to read than the unsmoothed one. This figure tells us that power deficits vary across the frequency spectrum in the wave data, similar to the power absorption in the mechanical data. In the high signal portions of incident spectra power deficit ratios were generally larger at higher frequencies, just like in the RCW. The level of power deficit ratios in the wave data varied by sea state. The Oregon5 sea state followed the RCW curve very closely, while sea states Oregon2 and Hawaii had the greatest deviation from the RCW.

A sea state specific RCW to RIW analysis was done to further investigate the correlation of mechanical power absorption to wave data power losses. The relative capture width measured for individual sea states under unidirectional cases only was compared to the RIW of the WEC measured in the wave data. Figure 20 on page 46 shows this comparison plotted on top of incident wave power spectra (blue dashed lines). Incident spectra are included in this plot to show at what frequencies the RIW/RCW comparisons are significant. Only RIW curves from three and five WEC arrays are included since the array signal was large enough in these cases to get a realistic RIW. Generally, the RIW curves for both three and five device arrays follow each other closely and are larger than the RCW curve across the frequency band of interest. In sea states with shorter peak periods (HI, OR2), the RCW and RIW diverge greater than in the sea states with larger peak periods (OR4, OR5). Similar results were observed in the RIW comparison to the average RCW seen in Figure 19 on the next page. Looking specifically at the RCW and RIW values measured at peak frequencies of each sea state is important because this is where the RCW will have the biggest impact on the wave field. Figure 21 on page 47 shows RIW and RCW values at the peak frequencies of each sea state. As frequency increases, so does the gap between RCW and RIW. At the low peak frequency sea states the RIW and RCW are very close, in the middle frequencies RIW values are slightly higher than RCW values, and in the sea state with the highest peak frequency (Hawaii) the RIW values are much higher than both the sea state specific RIW and average RIW.

Variations in the longshore transects of energy flux calculated from real seas trials are plotted in figures 22, 23 and 24 on page 51. This shows energy fluxes at the gages in the offshore (including gage ten) and energy fluxes at the lee gages as a function of longshore location in the wave tank. The red lines are associated with five device arrays, green with three device arrays, and blue with single device arrays. There were clear shadow structures

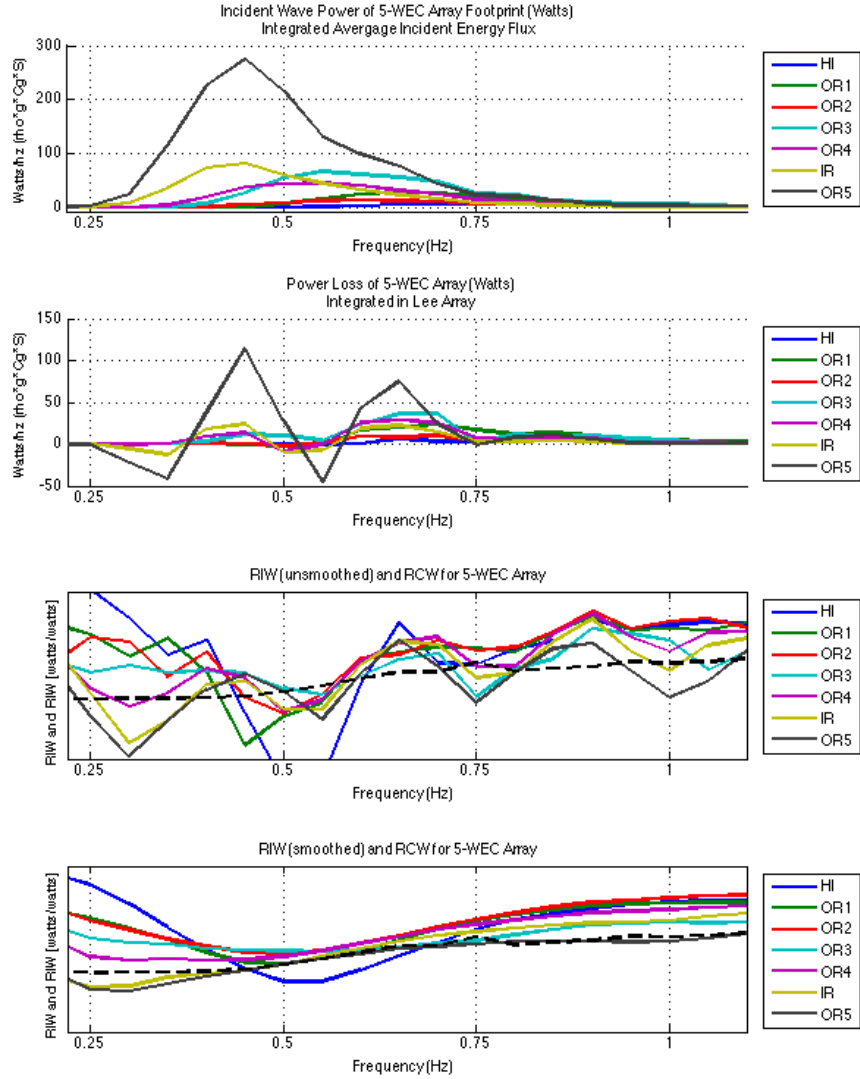


Figure 19: Power deficits in the lee wave field with respect to incident as a function of frequency. The top panel shows incident power spectra for seven unidirectional sea states. The middle panel shows the element-wise deficit between the lee and incident power spectra. The third panel shows the ratio of deficit to incident power (RIW) along the frequency spectrum against the sea state averaged mechanical RCW. And the fourth panel shows the seven point smoothed RIW against the measured RCW. The RCW curve is property of CPT so y-axis labels are not included.

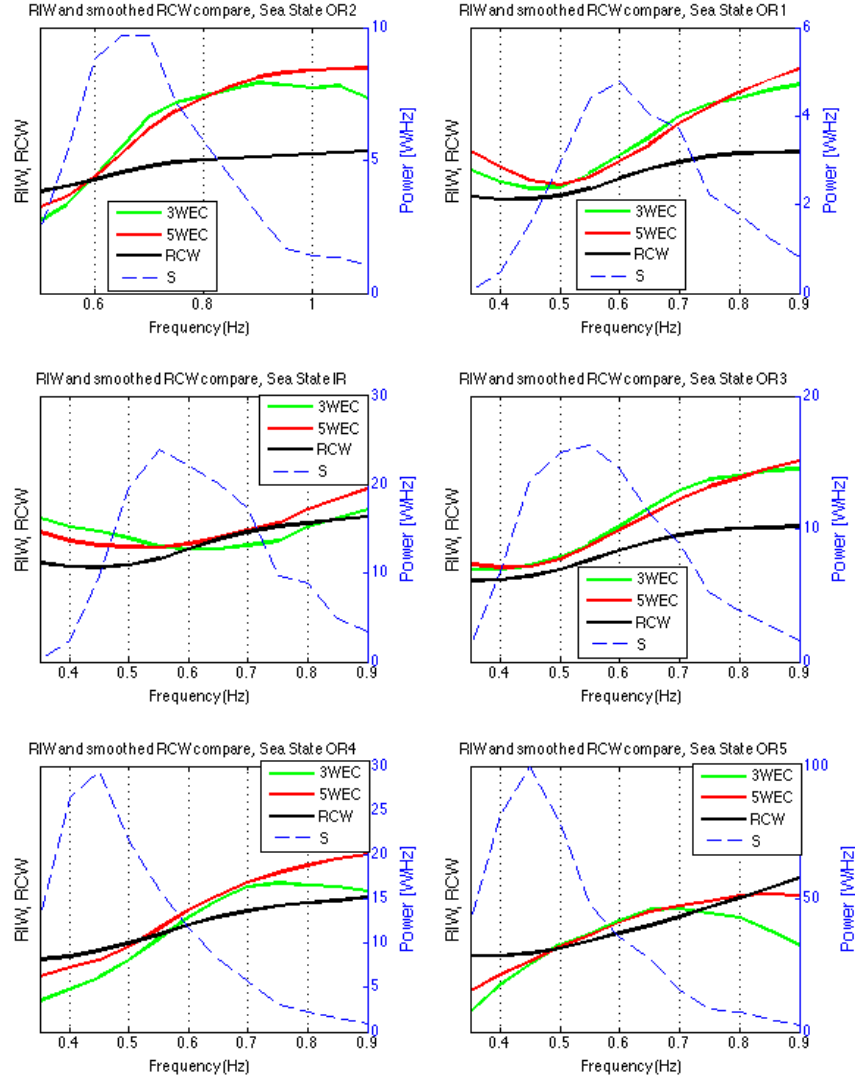


Figure 20: Power deficit ratios in the lee wave field for specific sea states as a function of frequency plotted on top of incident wave power spectra (Blue dashed lines). Green lines are the 3-WEC RIW, red lines are the 5-WEC RIW. Also pictured as the solid black lines are the sea state specific mechanical power RCW. Incident spectra are included in this plot to show at what frequencies the RIW/RCW comparisons are significant. Y-axis labels on the right side correspond to the incident spectra. The RCW curve is property of CPT so y-axis labels are not included for the left side.

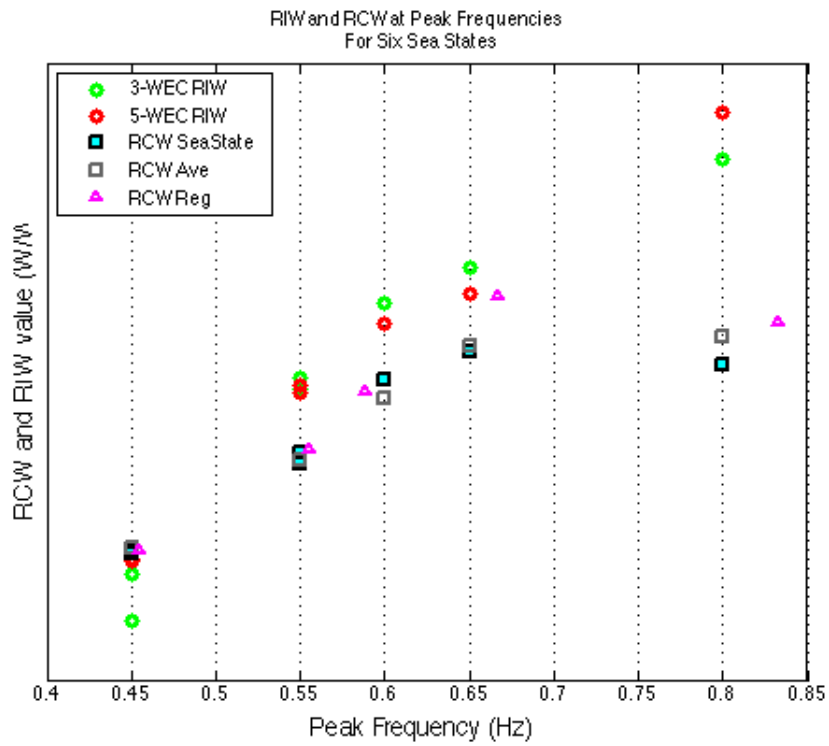


Figure 21: RIW and RCW values at peak frequencies of real seas sea states. The circles represent unsmoothed RIW values measured at the peak frequency of each sea state. Blue squares are the sea state specific RCW values, and the gray squares are the averaged RCW. Regular wave RCW values are plotted for reference as the triangles. The RCW curve is property of CPT so y-axis labels are not included.

present of all three array sizes in nearly all sea states, except for the single device array in the Oregon5 sea state. Of particular interest were the the shapes of the shadow in the three device array. It is easily seen that the shadow shapes have a distinct reflection of the asymmetrical array geometry, with two devices being placed towards the left side, and only one placed on the right side. Typically the shadows are deeper on the left than on the right in cases with three WECs, a direct result of array geometry. One more piece of information to note about the shapes of the three and five WEC shadows was that the shadow magnitudes at the extents of the lee gage array were nearly identical between the two sizes for all sea states. This means that the lee gage array captured the same portion of the longshore shadow for both cases, which was important for comparing power deficits between array sizes. It helps to validate linearity between array size scales.

3.3 Parametrization of the Incident Wave Field

The incident wave field for all shadowing and modeling analysis was determined to be best characterized by the mean wave parameters measured at gages one through six and ten for all like trials in regular waves and real seas. Characterizing the incident wave field was a difficult endeavor because of larger than expected WEC array influences on the offshore gage array. Wave data from single device arrays appears to have the least influence from the WEC arrays in the time, and frequency domains.

As shown in Figure 3, wave gages one through six are closest to the wavemaker, and were intended to characterize the incident wave conditions. As a group they are referred to as the “offshore gage array”. Gage ten, located approximately eight meters (or approximately fourteen WEC diameters) lateral of the WEC-array at nearly the same cross-shore distance as the array, was also intended to capture the incident wave conditions, with limited WEC-array influence. This section details how and why this argument is sound.

3.3.1 WEC-Array Effects on Incident Measurements

To analyze the best way to characterize the incident wave field, several analyses were conducted. To check whether the influences of the WECs on the incident wave field were not steady state, a comparison of power deficit ratios measured from only the first five waves of regular wave trials was compared to deficit ratios of wave data collected along the entirety of the steady state sample time. To investigate the effects of array size, longshore variability of incident wave height and spectra of real seas trials were evaluated for different array sizes. Accurate incident wave conditions were essential so that the relative wave shadow and power deficits from the wave field could be correctly determined.

Similar methods to that of those in Section 3.1 were used to provide an exact comparison, as shown in Figure 25. This figure shows the power deficit ratios from three and one WEC

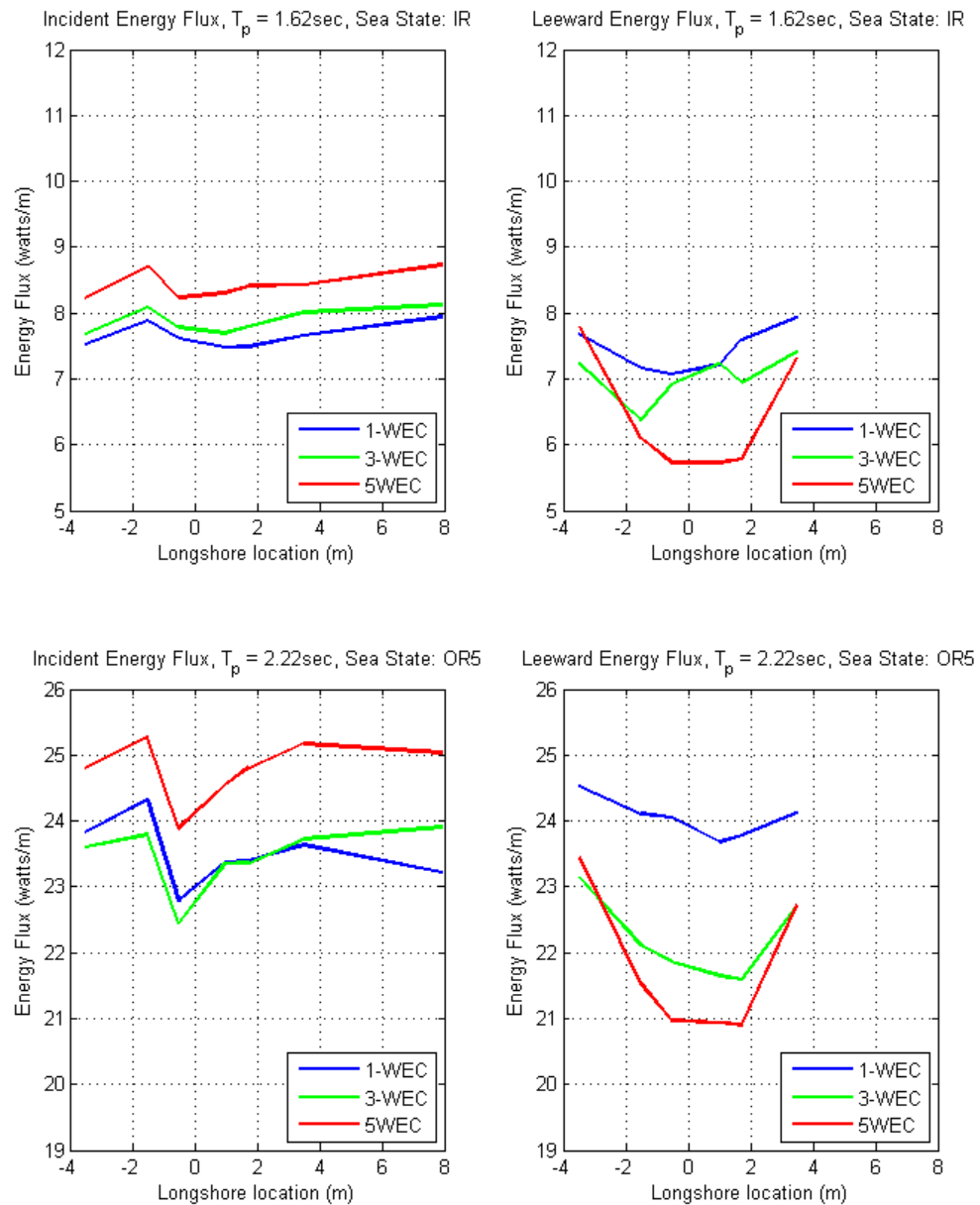


Figure 22: Longshore transects of energy flux in Ireland and OR5 sea states

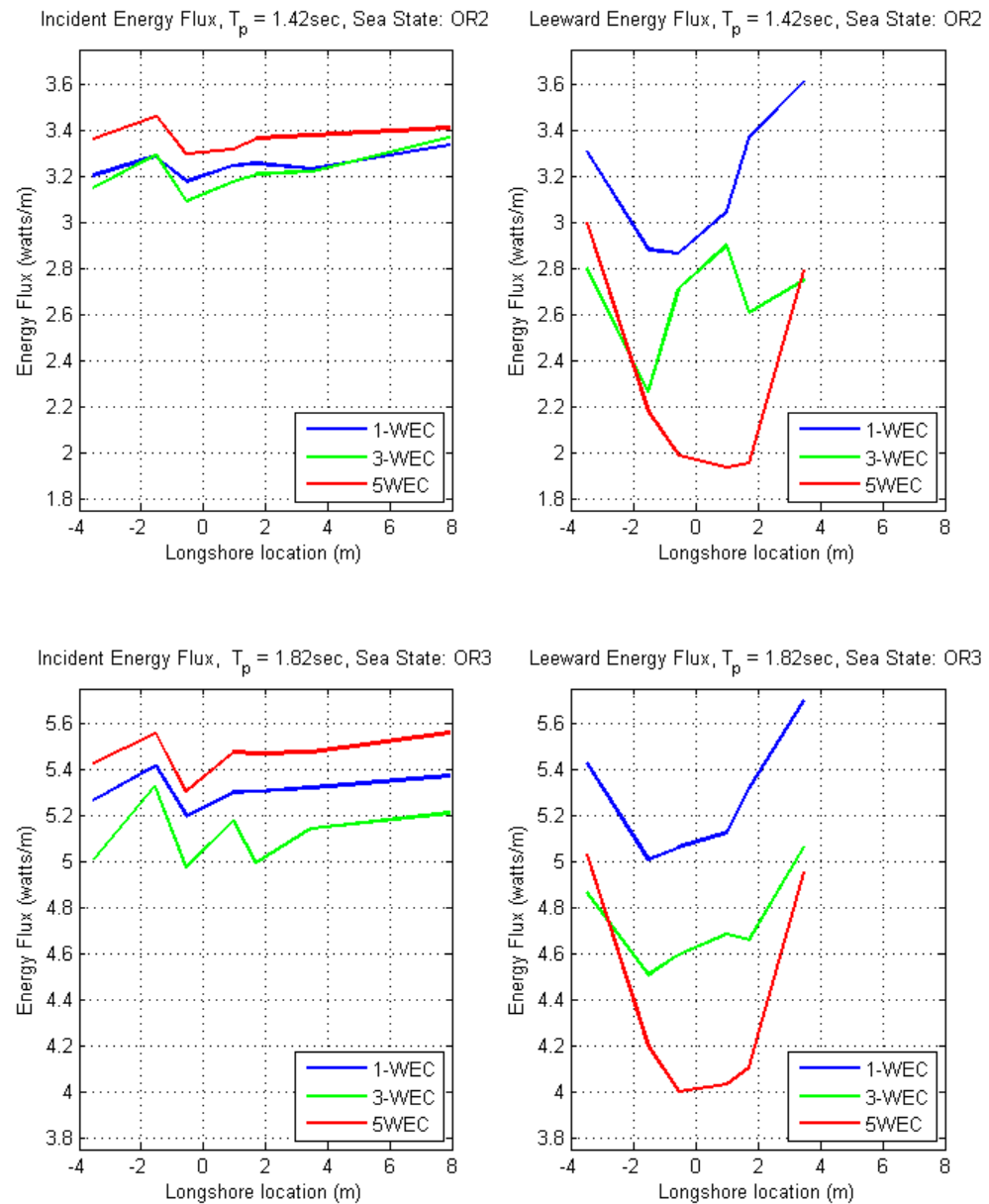


Figure 23: Longshore transects of energy flux in OR2 and OR3 sea states

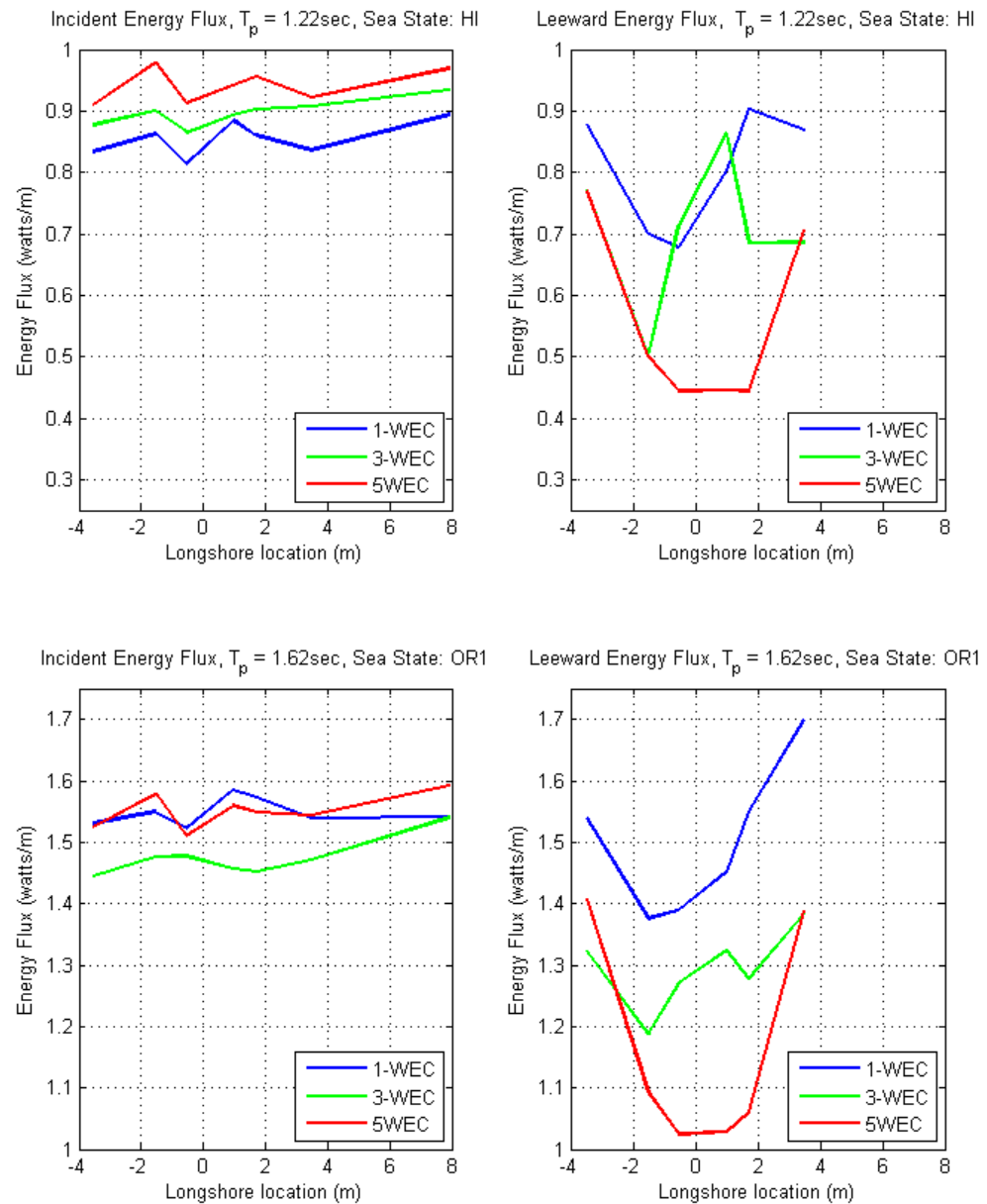


Figure 24: Longshore transects of energy flux in HI and OR1 sea states

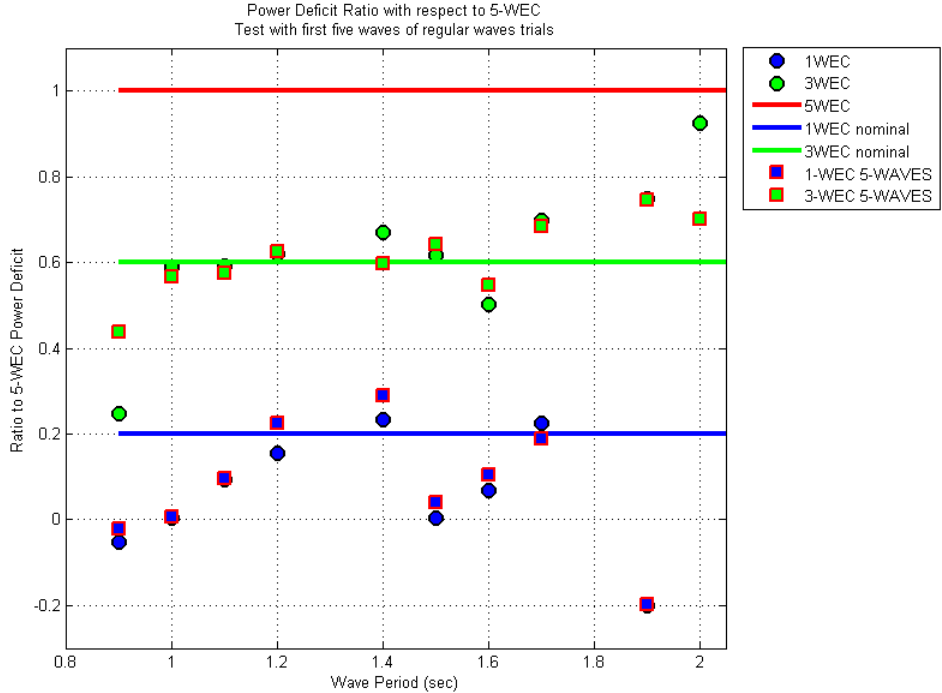


Figure 25: First Five Waves: WEC-Array Size Power Loss Ratios Compare

device arrays to that of a five WEC array in a suite of regular wave trials. The circles represent wave data from an entire trial, and the squares represent wave characteristics measured from only the first five waves in those respective trials. Because the differences between the circles and the squares are relatively minor, we can say that the WECs affect on the wave climate is consistent throughout the trial.

The results from an investigation of offshore wave height patterns from different WEC array sizes in numerous sea states is plotted in Figure 26. In all panels the blue colors corresponds to 1-WEC, green to 3-WEC, and red to 5-WEC arrays. These longshore transects of wave height show definite increased wave heights in 5-WEC arrays above 1-WEC arrays, and moderate increases in 3-WEC arrays above 1-WEC arrays. Effects from larger arrays on the offshore gages are pronounced, and likely would have an adverse effect on relative wave height reduction calculations.

On a spectral shape basis, the incident wave conditions also vary by array size. It has already been shown that the incident significant wave height was higher in larger arrays. Figure 27 shows that dependent on sea state, the single-WEC arrays have a peakier spectra than the three and five device arrays. Reduced peakiness in multiple-WEC arrays indicates an influence by the WECs on the shape of the incident spectra.

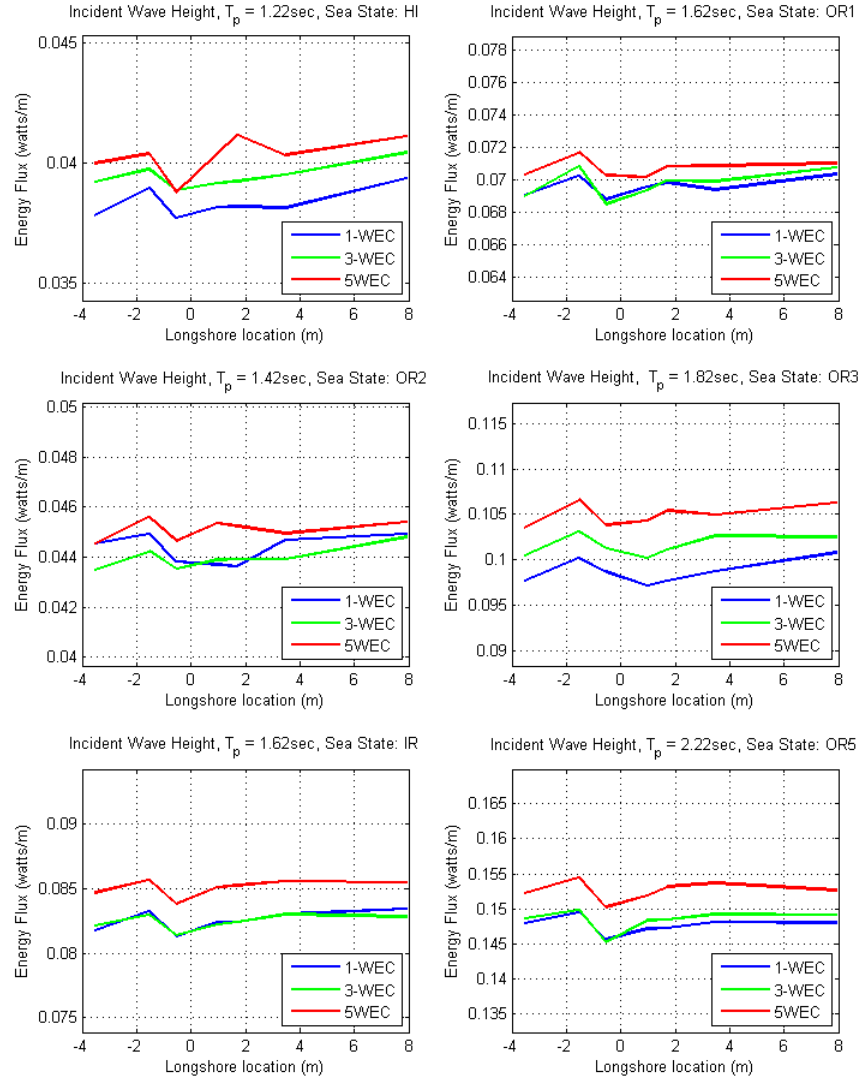


Figure 26: Offshore wave heights for six sea states in different array sizes. Blue lines represent 1-WEC arrays, green represent 3-WEC arrays, and red lines represent 5-WEC arrays. The 5-WEC arrays consistently have higher offshore wave heights.

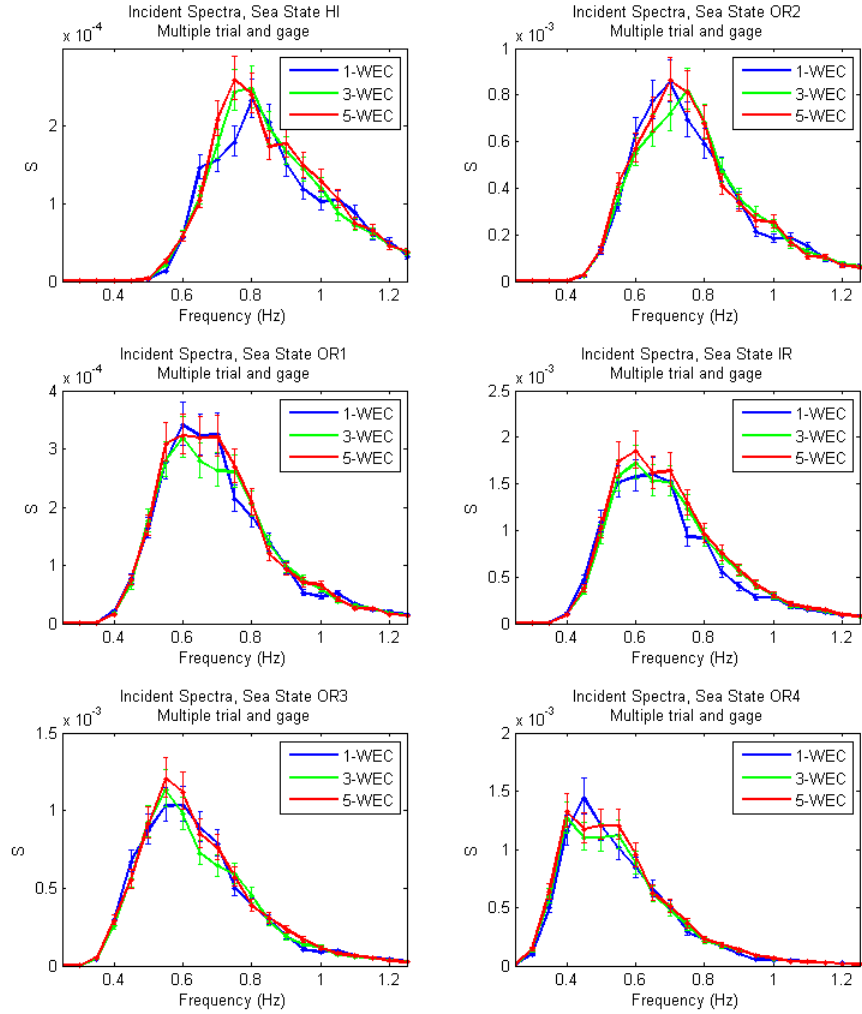


Figure 27: Measured incident wave spectra at forty-eight degrees of freedom, from one, three and five device arrays. In all panels the blue colors corresponds to 1-WEC, green to 3-WEC, and red to 5-WEC. Spectra were averaged from seven gages and two like trials. Confidence intervals were calculated from the χ^2 distribution with associated degrees of freedom.

3.3.2 Phase and Coherence

To average the offshore wave gage with gage ten there must be a high level of confidence that the two sets of gages are experiencing the same wave field. If they are, results from the wave gages can be combined, which increases the degrees of freedom and decreases error bar size in the data set. Testing whether or not gage ten is statistically identical to the offshore wave gage array was done by calculating the coherence spectra. for spectra with twenty four degrees of freedom, the 99.999 percent confidence level, $\gamma_{critical}^2$, is 0.6489

Coherence spectra were calculated for all unidirectional trials of the seven sea states, in the five buoy array arrangement. It was expected that the limits of coherence would be tested in the 5-WEC arrangement due to a larger array, with increased WEC influence on the offshore gages. In this process similar trials were not averaged together to limit the degrees of freedom and run a more conservative test. It was found that the coherence at frequencies in the most energetic portions of the spectra (i.e., the portion of interest) was above $\gamma_{critical}^2$. Therefore gage ten is statistically identical to the offshore gage array for the frequencies of interest.

3.4 Laboratory Effects

3.4.1 Spatial Variance

A useful tool in analyzing this wave data is understanding characteristics of the wave basin in the absence of WECs, but in the presence of in-situ instruments and sidewalls. In this way the spatial variability observed in the wave data can be better interpreted. Since the wave basin is not infinitely wide or long, it will have certain natural frequencies that may create standing waves, and this could affect the wave data. Such standing wave shapes can be complex, occur in the cross-shore and the longshore directions, and will be different for each frequency and directional spreading case. Adding to the potential of spatial variance within the tank are possible reflected waves from the gravel beach; the beach was designed to reduce reflections, but it is not a perfect energy absorber.

Only a limited amount of data is available without WECs in the water. Eleven trials that were run to calibrate the Argus video system, which had no WECs in the basin. Data from these gives a glimpse into levels of spatial variability in the tank for regular waves and real seas. The seven were regular wave trials at three wave periods ($T = 1.4s, 2.0s, 2.6s$), and four real seas tests at two different wave periods ($T = 1.42s, 2.22s$) with varying levels of directional spreading ($s = 10, 25$). Wave data from these trials were processed into wave height transects in the longshore and cross-shore.

As shown in Figures 29 and 30, wave heights generally varied between +/- 5 percent of the mean incident wave height of the individual Empty Tank trials. This mean wave height was calculated as the average of gages one through six and gage ten. Tank behavior from

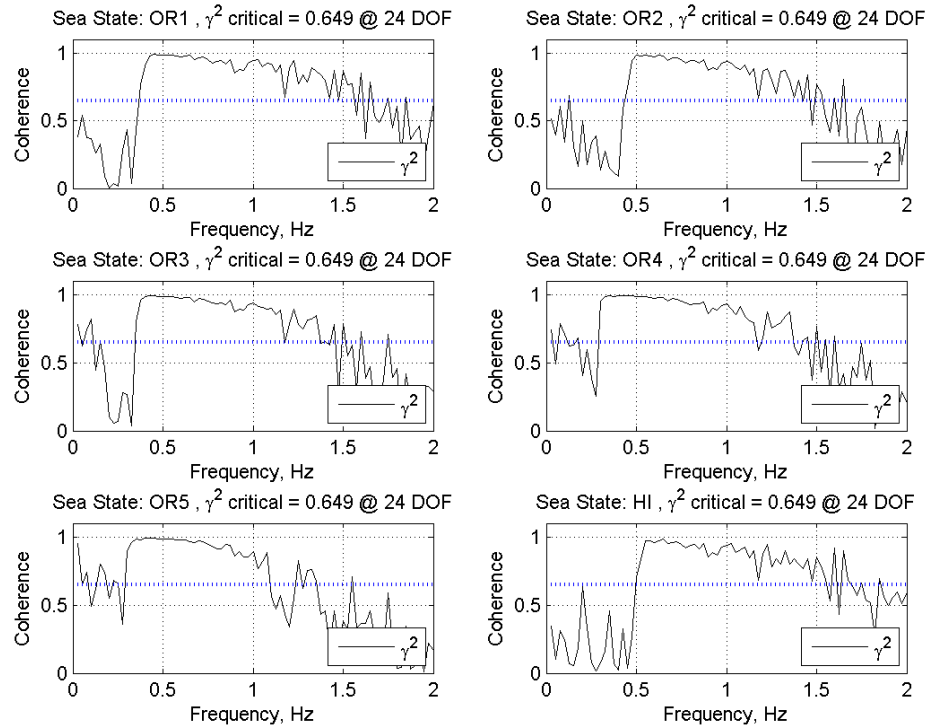


Figure 28: Coherence between gage ten and the offshore gage array. Computed during five-WEC array configurations for six sea states. The dashed line indicates the $\gamma^2_{critical}$ value, the solid black line indicates the coherence as a function of frequency.

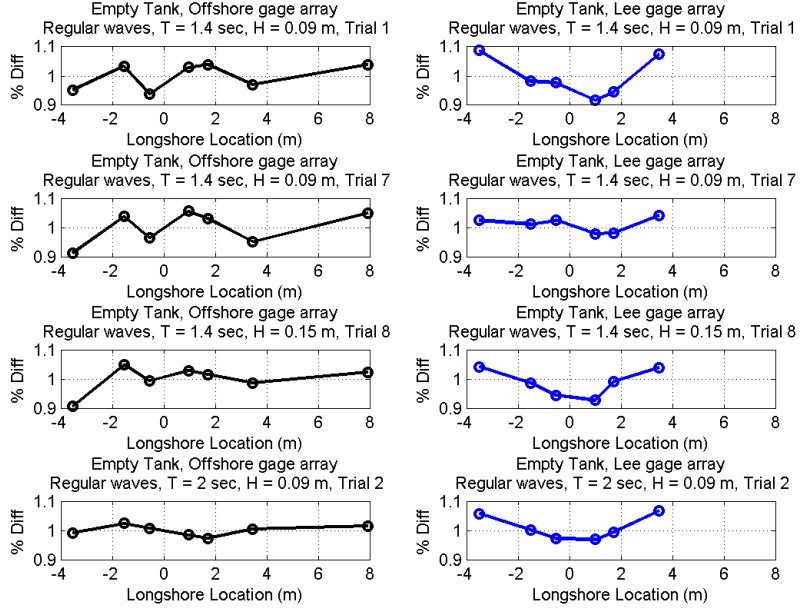


Figure 29: Empty tank analysis: regular wave longshore transects

multiple trials is shown in regular waves in Figure 29, and real seas in Figure 30.

Cross-shore wave height transects of the empty tank data were calculated from select gages near the middle of the basin except in the cases where there were many longshore gages such a cross-shore location, in which case the longshore average wave height was characteristic of that cross-shore location (i.e. offshore gages, lee gages, far-field gages).

To check cross-shore behavior in the empty tank, cross-shore transects of wave heights along the center of the basin were calculated and plotted in Figure 31. On the y-axis are the normalized wave heights with respect to the mean wave height of the offshore gages and gage ten, for each trial. This figure shows that wave heights in the offshore gage array are zero to five percent smaller than in the lee gage array ($x = 13.2\text{m}$) and far-field gage arrays ($x = 18.0\text{m}$). Although these percentages are small, there is a discernible pattern of higher wave heights closer to the beach than the wavemaker in both regular wave, and real seas wave fields. In real seas, the gage ten marker is zero to five percent less than the offshore gage array, but with no discernible pattern.

3.4.2 Cross-shore Beach Reflection

The beach installed in the wave basin during the WEC-Array Experiments was designed to dissipate energy to reduce the amount of wave energy reflected back towards the wave gages.

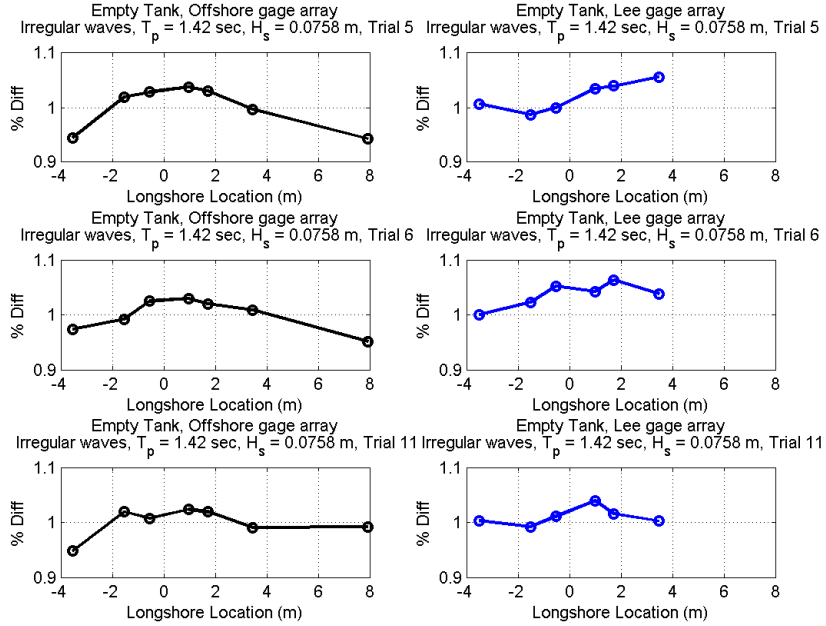


Figure 30: Empty tank analysis: real seas longshore transects

The far-field array was arranged with a closely spaced cross-shore gage transect in order to be able to resolve the incident and reflected wave components. To analyze reflection, a routine based off of Baldock's [Baldock & Simmonds, 1999] *ref_slope* code was chosen. Given two gages and their cross-shore location, depth, and sea surface time series, and collection rate, this routine will calculate the incident and reflected sea surface elevation time-series .

The best way to analyze cross-shore reflections is within an empty tank but, because of the lack of empty tank data available, 1-WEC trials were also analyzed as the best shot to understand beach reflection trends over many different sea states. Other tests such as three and five-WEC have a large signal due to the WEC-array effects and were not considered.

Regular wave trials from the *SingleBuoyCharacterization* tests was chosen as the basis for reflection analysis because it has more waves, fifty, than *SingleBuoyAmplitudeScan* or *SingleBuoyFrequencyScan*, which had twelve. Real Seas trials have a similar situation where the *SingleBuoyRealSeas* test ran a shorter sample time (313 seconds) than *SingleBuoyChar-RealSeas* (540 seconds), so the latter test was chosen for this analysis. A suite of frequencies was available for analysis, from 0.9 second waves to 2.8 second waves at an interval of one tenth of a second (except for 2.5 second waves). It is expected that longer period waves will have a higher reflection coefficient, as seen in previous experiments [Elgar et al., 1994].

At the onset of wavemaker action there should not be any reflection in the tank since

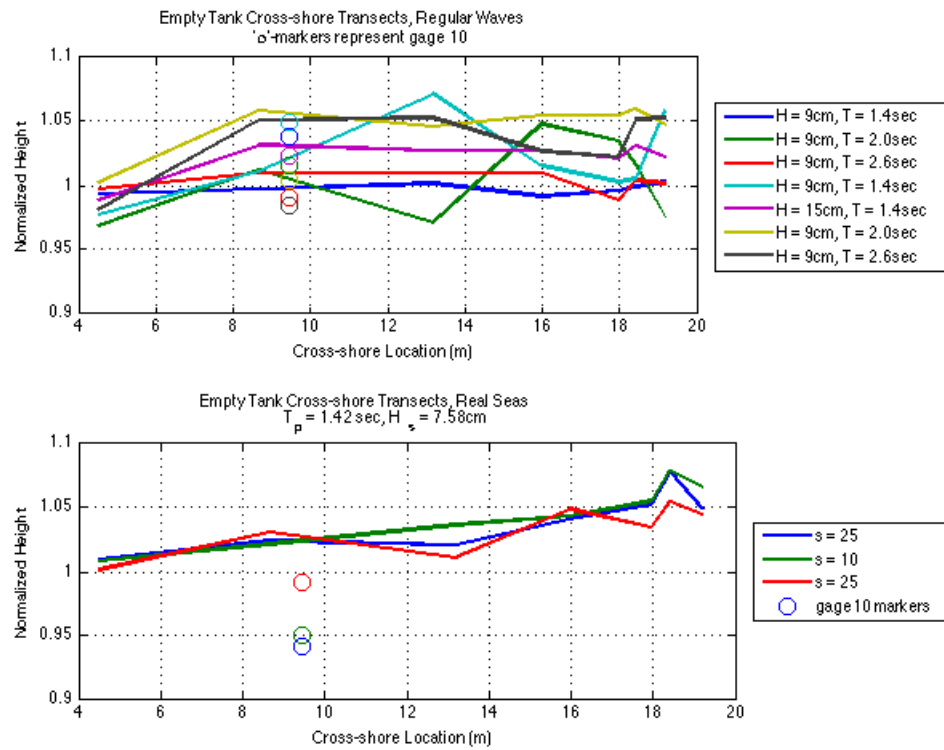


Figure 31: Wave heights from regular waves (top panel) and real seas (bottom panel) are plotted across the cross-shore extent of the empty basin. The longshore averaged wave height of each trial is indicated by a different colored line, and gage ten is plotted as a circle with the corresponding color.

the waves have not had sufficient time to reach the beach and reflect back to the gages. This analysis looks only at data that occurred in time after sufficient time had passed for the waves to reflect back to the far-field gage array. Wave speed was determined by the dispersion relationship and calculated for the peak frequency of each trial, and the time it took for that wave to reflect back to the far-field array was noted; only data past this point was considered for reflection analysis.

Reflection coefficients were calculated for regular and real seas wave conditions. The results from regular wave tests are shown in Figure 32. There appears to be a frequency dependence, however, the trend is opposite of what was expected i.e. there is increased reflection at smaller periods. The reflection coefficient is within the level of uncertainty measured by the empty tank data (+/- 5%). However, upon further analysis for trial numbers less than 130 the mean reflection coefficient was 0.052. These trials all occurred during the first fill/drain period (UTC dates 340-360, Figure 32 bottom panel) and show little dependence on wave period. Mostly the reflection coefficient is within eight percent. However, the trials performed after UTC date 390 show increased reflection levels for shorter wave periods. We suspect either that the separations algorithm is less robust for these cases (since time series including the reflection signal is shorter for shorter periods) or increased wave gage noise for these particular gages after the second fill.

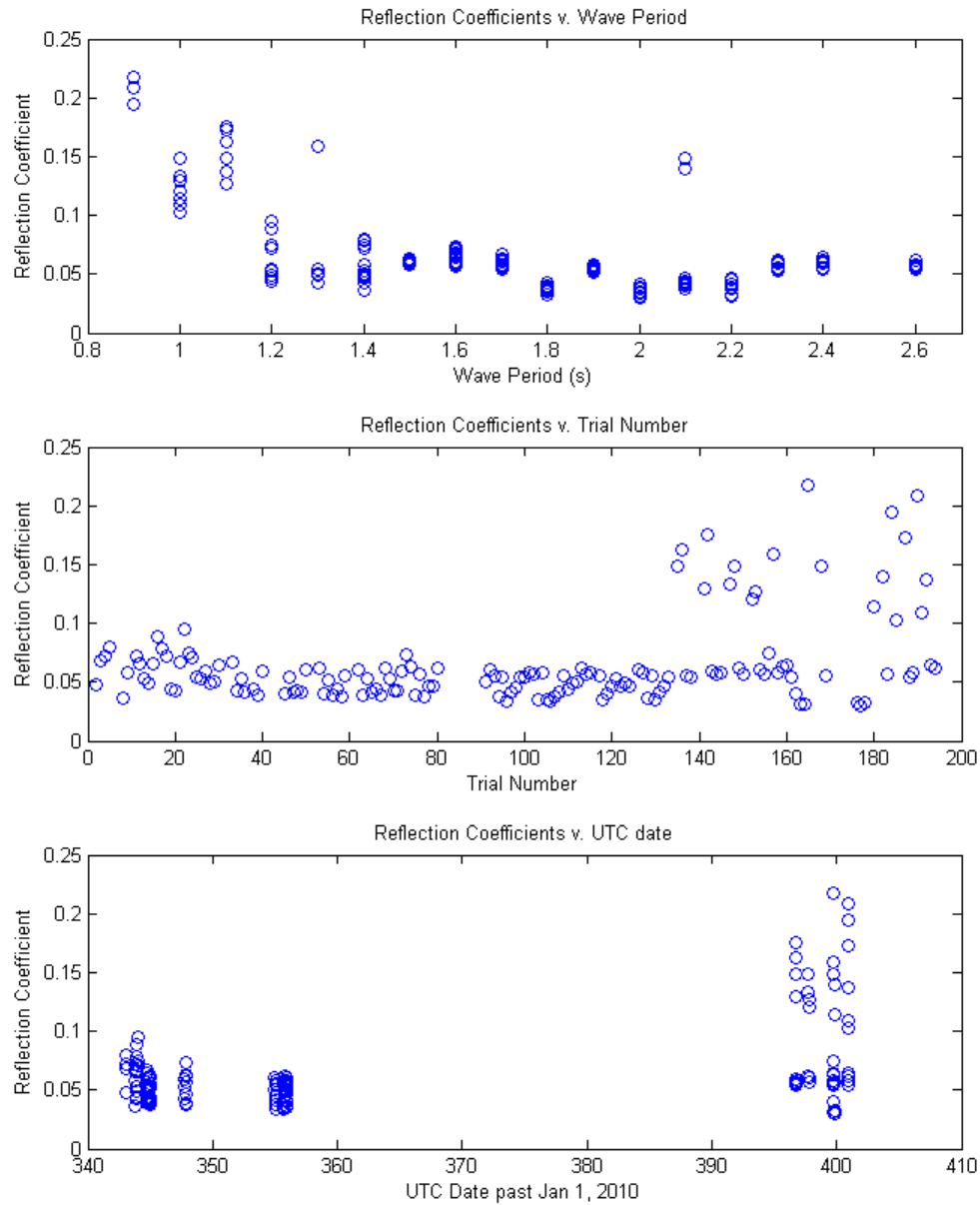


Figure 32: Reflection coefficients calculated from regular waves by Baldock's method. The top panel plots reflection coefficients as a function of wave period. The middle panel plots reflection coefficients as a function of trial number. The bottom panel plots reflection coefficients as a function of Coordinated Universal Time (UTC) date with Jan 1, 2010 as the datum.

4 Experimental Data Set Conclusions

Results from the extensive WEC-Array experiments have shown that the wave shadow is a function of wave period. Because the wave shadows is a function of wave period, and the same is true of mechanical WEC power capture, it can be concluded that a primary driver of wave shadowing is due to power absorption by the WEC. At certain small wave periods ($T = 1\text{-}1.4$ seconds) it was seen that the influence of the device on the wave field was not fully captured by absorption since the RIW curve was much higher than the RCW curve at these wave periods.

The data set is large, and has not yet been fully utilized. Future analysis should include more thorough real seas investigations since in-situ field applications will need to consider directionality. Whether this be in SWAN or some other model, the data set is extensive enough work with in almost any capacity.

Incident conditions for regular waves and real seas were best specified by wave data measured during 1-WEC trials at gages one through six and ten. Three and five device arrays showed repeated increased incident wave heights for the same conditions as in single device arrays. Measured incident spectral shapes of multiple device arrays were different than the single device array, indicating an influence by the WEC array on incident spectral shape as well. Getting the spectral shape correct is extremely important for modeling the effects of WECs on the wave field since the devices themselves modify the wave field on a frequency-wise basis.

Power deficits in the lee of the array with respect to the incident wave conditions have shown a great influence on frequency (wave period) and array size in regular waves and real seas trials. The scaling between three device and five device arrays is moderately linear for both real seas and regular waves. Shadow magnitudes calculated during single device array trials because of very low signal-to-noise ratios. Because scaling between array sizes has been shown to be moderately linear, several RCW curves measured from devices in isolation should do a fair job of representing multiple devices in a model. The relative influence of WECs measured in mechanical power (RCW) and wave power deficits (RIW) mirror each other well in regular waves and real seas, which tells us WEC power absorption is a primary driver of wave shadow behavior. Because the shadow is primarily driven by WEC absorption, the effect of the WEC array on the wave field may be able to be parametrized solely by absorption. At certain high frequencies (short wave periods) however, the RCW does not fully capture the influence of the WEC on the wave field, and it is likely that wave scattering has a significant influence on wave shadow magnitude and shape.

5 Numerical Modeling

This portion of the thesis compares WEC-array modeling results with the empirical data obtained and analyzed Section 3. Modeling was performed with the spectral model SWAN. Influences of WECs upon the wave field were parametrized by a frequency dependent sink function that was based on the behavior of mechanical power absorbed by a WEC in isolation. Three separate WEC-array sizes (1, 3, 5) were modeled, just as were tested in the WEC-Array Experiments. The analysis was limited to trial conditions with a normal incident wave direction and no directional spreading. Input wave climate boundary conditions for SWAN were taken from the empirical data collection described in Section 3.

SWAN is a third generation numerical wave model intended to compute short-crested waves based on spectral balances of wave action density [Booij et al., 1999]. In this case SWAN was implemented to imitate the WEC-array experiments in order to validate methods of WEC representation and modeling. The source code for SWAN was not altered, instead spectra at longshore transects within the domain were modified externally at several in-situ WEC locations by a transfer function that was based on WEC performance. This method involved several nested SWAN grids and mathematical manipulation external of SWAN calculations. The following section will illustrate why SWAN was chosen, the expectations of such modeling, the physics and settings in the models, explain methods of modeling WECs, and how well model results compare to experimental data.

5.1 SWAN Physics

SWAN was developed to numerically represent the effects of effects of spatial propagation, refraction, shoaling, wave generation, dissipation, and nonlinear wave-wave interactions. In order to accurately represent these effects, SWAN solves the spectral action balance equation:

$$\frac{\partial N}{\partial t} + \frac{\partial c_x N}{\partial x} + \frac{\partial c_y N}{\partial y} + \frac{\partial c_\sigma N}{\partial \sigma} + \frac{\partial c_\theta N}{\partial \theta} = \frac{S_{tot}}{\sigma} \quad (19)$$

where σ = radian frequency, N is the energy density $E(\sigma, \theta)$ distributed over radian frequencies σ and propagation directions θ . The evolution of the action density, N , is determined in space and time; it is defined as $N = E/\sigma$ and is contained wholly on the left side of the equation. The right side S_{tot} is the sum of physical processes, or the “sources and sinks”, that generate, dissipate, or redistribute wave energy. S_{tot} balances with the kinematics of the wave energy located on the left side of the equation. SWAN has six process that add to S_{tot} :

$$S_{tot} = S_{in} + S_{nl3} + S_{nl4} + S_{ds,w} + S_{ds,b} + S_{ds,br} \quad (20)$$

These terms, in order, represent: wave growth due to wind, nonlinear transfer of wave energy through three-wave and four wave interactions, wave decay due to white-capping, wave decay due to bottom friction, and wave decay due to wave breaking [SWANTeam, 2011].

5.1.1 Benefits and Limitation

As a spectral model, SWAN does not model individual wave forms, instead it tracks spectral energy in space and time as phase averaged quantities. This type of model creates both benefits and limitations. The major benefit is decreased computation time for large, management scale domains over varying bathymetry. A major limitation is that it cannot model constructive or destructive interference from multiple waves, or interactions between WECs. These limitations were kept in mind during modeling and interpretation of results. However, since SWAN is often used in field applications of coastal wave modeling, it is appropriate to use such a model herein.

5.1.2 Obstacles and WEC modeling

Typically in SWAN obstacles are modeled using the “OBSTACLE toggle in the input file, and choosing a relative significant wave height decrease, and locations of obstacle endpoints. Using this method results in energy being removed equally from all frequencies. WECs however, do not behave as such, instead the amount of power removed from the spectrum is a function of frequency. As of this thesis, the GNU SWAN releases do not have this capability. Although the source code has been modified by others to do this, such as the Wave Hub modeling group [Smith et al., 2012], we used an different method. One way to implement frequency dependent objects in SWAN is to nest SWAN at the each longshore transect of WECs in the array. Then to modify the wave field by a given transfer function outside of SWAN while it is stopped, and then run SWAN to the next cross-shore nest boundary. Whether it be it to the shore or to the next nest, it does not matter. Although reflection cannot be modeled in this way, it is not a goal of this paper to include such physics or inter-array interactions in the model since it is not expected that SWAN would be able to accurately resolve such near field physics.

5.1.3 Lateral Energy Spreading

Diffraction is the process of energy spreading laterally perpendicular to the direction of wave propagation [Dean & Dalrymple, 1998]. In this section diffraction was not enabled because we are more interested in accurately modeling downwave power of the wave field rather than the distribution of such energy. Additionally, the grid size resolution needed to resolve WEC geometry (10cm) was too fine for the diffraction calculations in SWAN to converge.

The SWAN manual suggests a wavelength to mesh size ratio of 1/5 to 1/10. Wavelength to mesh size ratios required to resolve the WECs herein was 1/40, approximately 10cm to 4 meter wavelength. Physics in SWAN do not account for diffraction, but it is approximated using the mild-slope equation. Later in this paper diffraction is toggled on during SWAN modeling for comparisons to WAMIT model results.

The Anti-Garden Sprinkler Effect (GSE) toggle in SWAN can also be used to increase lateral smoothing of the wave field to give a more realistic representation. Again though, lateral distributions of energy was not the main goal of this section. It is expected that a thorough sweep of GSE parameters could in fact eventually result in an accurate smoothing of the wave field, but not tried within this thesis.

5.1.4 Additional SWAN Physics

There are additional physics SWAN can model in addition to those listed above. SWAN has the capability to model wave breaking (BREAKING), white capping (WCAP), three and four wave interactions (TRIADS, QUAD), and bottom friction (FRICTION). Of these additional physics only wave breaking was turned on, the other physics were assumed to have minimal effect in such a small domain and in relatively deep water.

5.2 SWAN Model Simulations

Simulations of the WEC-Array experiments were done using SWAN. This section details how measured bathymetry and incident wave conditions, and WEC modification of the wave field were implemented in the computational grid. Because currently SWAN does not have the capability to internally model frequency dependent objects, and source code modifications were not attempted here, the wave field was modified externally from SWAN. Wave energy spectra at points in the longshore where WECs were located, were modified using the relative capture performance curve measured from the “Manta 3.1” WEC used in the WEC-Array Experiments. This section details the process in which spectra modification was done in conjunction with SWAN models.

5.2.1 Bathymetry

Bathymetric surveys of the beach were taken before and after the WEC-Array experiments occurred. The surveys were taken using LIDAR technology, by the OSU Geomatics unit, at a resolution of 5 cm, with a total number of points of 222,744. For the purposes of this experiment five centimeter spacing was not needed, so the original regular grid was interpolated to a 10cm regular grid. The 10cm grid was normalized by a nominal water depth of 1.365m, so that the survey is transformed from elevations to depth. Additionally,

surveys before and after show a slight change in shoreline bathymetry near the sidewalls, likely due to increased levels of positive interference in the surf-zone at these locations.

5.2.2 Incident Wave Spectra

Incident spectra for this modeling analysis come directly from wave data measured in the WEC-array experiments. The goal is replicate the incident wave data in the experiments as close as possible so that model results may be compared to experimental results. Here we model a frequency sweep of regular waves, and unidirectional wave spectra measured from the seven sea states listed in table 4. All of the incident spectra in this analysis are from unidirectional waves, so the directional spreading must be minimized. In this case the unidirectional spreading was minimized in the boundary specification line BOUND SPEC by calling the standard deviation of *DPSR* equal to one, where *DPSR* [SWANTeam, 2011] is equal to:

$$DPSR = \sqrt{\left(\frac{180}{\pi}\right) \int_0^{2\pi} \left[2 \sin\left(\frac{\theta - \theta_0}{2}\right)\right]^2 D(\theta) d\theta} \quad (21)$$

Incident wave spectra were calculated from the mean wave characteristics of gages one through six and ten, from trials with 1-WEC present only, and are identical to the data used to evaluate wave shadow in Section 3. Further discussion on this can be found in section 3.3 on page 48. Regular wave spectra were determined by a parametrized SWAN spectra that contains energy only at the frequency bin nearest the nominal frequency of the regular wave. This means that the incident spectra for regular waves is not from measured wave data, it is instead from a parametrized spectrum for a single frequency, which SWAN calls a BIN-parametrized spectra. Unidirectional real seas spectra were input as the mean of the measured spectra from gages one through six and ten; the resulting degrees of freedom for these spectra are $48 \frac{dofs}{gage} * 7 \frac{gages}{trial} * 2trials = 672dofs$.

Regular Waves Boundary conditions in SWAN simulations for regular waves use measured mean wave heights from the gages one through six and ten from data measured in trials with a single WEC only, and are identical to the data used to evaluate wave shadow in Section 3. The wave periods range from 0.9 seconds to 2.7 seconds and all have a target wave height of six centimeters. It is apparent that the 1.3 second wave period case is not listed. Waves with periods of 1.3 seconds were run in the WEC-Array Experiments, but were not included in this analysis because of an initial quality control flag that was later dismissed.

Real Seas Boundary conditions for model simulations of real seas trials consisted of a characteristic incident wave spectra for unidirectional waves of each of the seven sea states

Table 5: Regular wave boundary conditions for SWAN

Regular Wave Boundary Conditions		
Wave Height (cm)	Nominal Wave Period (sec)	SWAN Wave Period (sec)
5.70	0.9	.913
5.36	1	1.00
5.70	1.1	1.11
5.62	1.2	1.22
5.41	1.4	1.41
5.54	1.5	1.47
5.48	1.6	1.62
5.64	1.7	1.70
5.50	1.8	1.79
5.47	1.9	1.87
5.41	2.0	2.0
5.43	2.1	2.06
5.52	2.3	2.27
5.59	2.5	2.5
5.45	2.6	2.62
5.37	2.7	2.75

outlined in Table 6. As outlined in Section 3.3 the incident spectra are averaged spectra measured from gages one through six and gage ten over multiple trials from single-WEC trials in the WEC-Array Experiments. The incident spectra for the models are exactly the same as the incident spectra used to calculate power losses in the data analysis portion of this thesis (Section 3). However, the frequency resolution in SWAN is different than in the experimental data. The spectra were interpolated to the frequencies outlined in Table 7, while also forcing the significant wave height to stay constant.

5.2.3 Computational Grids

Computational grids are the framework for solving the wave action balance equation that is the basis of SWAN. The grid contained two spatial dimensions, a frequency space dimension, and a directional dimension. The resolutions of these were determined by evaluating the convergence across a range and combinations of resolutions. There were three different computational grids, one for each nest, a process which will be described in more detail in section 5.2.7. These computational grids are summarized in Table 7.

Table 6: Real seas boundary conditions for SWAN

Real Seas				
Sea State	Incident wave height	Incident peak period	Nominal wave height	Nominal peak period
	$H_{m0}(cm)$	$T_p(sec)$	$H_{m0}(cm)$	$T_p(sec)$
HI	3.83	1.25	4.5	1.22
OR1	4.43	1.67	4.5	1.62
OR2	6.96	1.43	7.6	1.42
OR3	7.80	1.67	7.6	1.82
OR4	8.25	2.22	7.6	2.22
IR	9.87	1.54	10.6	1.62
OR5	14.7	2.22	13.6	2.22

Table 7: Computational grids used in SWAN modeling. X-origin is the geographic location in the cross-shore where each of the nested grids begins. The stitched grid is an overlap of each of the nested grids, with the shoreward nest having precedence beginning at each “X-origin”.

Domain	Size	X-origin	Mesh Size	Mesh #	Directional	Frequency
	x, y	x_{low}	$\Delta x, \Delta y$	mx, my	$\Delta\theta$	$f_{low}, f_{high}, f_{num}$
	[m]	[m]	[m]	[#]	[degrees]	[Hertz]
Nest1	37, 26.5	0	0.1, 0.1	370, 265	4	0.3, 3, 48
Nest2	5, 26.5	8.2	0.1, 0.1	50, 265	4	0.3, 3, 48
Nest3	26.3, 26.5	10.7	0.1, 0.1	263, 265	4	0.3, 3, 48
Stitched	37, 26.5	0	0.1, 0.1	370, 265	4	0.3, 3, 48

5.2.4 Boundary Conditions

The Western open boundary of the domain was forced with the spectra described in section 5.2.2, while the Northern and Southern boundaries are modeled as parametric PM spectra with the same peak period and significant wave height as the measured spectra. In Nest1 the measured spectra was forced at each computational point in the western boundary, and was constant along the width. The Northern and Southern boundaries were parametrized as spectra rather than one hundred percent reflecting sidewalls to remediate previous problems seen with edge effects due to the presence of the walls. In subsequent nests the Western boundary is forced with the WEC modified spectra from the previous nest at all points in the longshore.

5.2.5 Output files

In each nested grid, wave data and spectra are output at all longshore locations along the shoreward domain. Significant wave height, peak wave period, dominant direction an are output at each point in the computational grid. In Nest1, spectra are also output at the offshore gage array location, a point it the middle of the domain, in addition to at the cross-shore boundary with of Nest2 (8.2m). In Nest2 spectra are output at the cross-shore boundary with Nest3 (10.7m). Finally, in Nest3 spectra are output at the lee and far-field gage array locations, the longshore transect of the lee gage array, and the longshore transect at the nest origin. Spectra output at the following nest's origin are then modified outside of SWAN to emulate WEC behavior, and then used as the input boundary condition in the next nest.

5.2.6 Spectra Modification

Relative Capture Width Curve The relative capture curve (RCW) is the ratio of available power in the footprint of a WEC to the power absorbed from the wave field by the WEC. It has been shown that RCW can be greater than 1.0, or more energy is removed than is available in the footprint [Budal, 1977]. Columbia Power Technologies calculated the RCW curve for both regular waves and real seas based off their calculations of power absorbed by a WEC in isolation. Power absorbed is measured by the square of relative pitch velocity multiplied by the generator damping. See Section 2.2.4 for more detail.

Regular Waves vs. Real Seas RCW curves are calculated differently for regular waves and real seas. In regular wave cases the RCW is calculated simply by the ratio of power absorbed by the WEC per unit meter divided by incident wave energy flux (power) per unit meter. An individual RCW value was calculated for trials with different wave periods; the RCW curve is the stitching together of the wave period sweep.

In real seas the RCW was determined as the element-wise ratio of two frequency spectra: power absorbed per unit width [W/m/Hz] and incident wave power [W/m/Hz]. Power absorbed is the total power spectral density of the fore and aft floats. Input conditions vary over sea state, directionality, and generator damping. An RCW was calculated for each input condition and a mean RCW was calculated from these trials. The resultant curve was still peaky, so a seven point moving filter was applied for the final (spectral) RCW.

WEC as RCW Sink Measured RCW curves are intended to parametrize the WEC's performance, and be a gage as to how much energy is removed from the wave field in a frequency dependent basis. The inverse of RCW curves should then give an estimate to how much energy is allowed to pass through the WEC on a unit basis. Additionally, the resolution of the computation grid was 0.1 meters and the nominal width of the WECs are 0.55m, so a representative WEC width of 0.6 meters is needed. This means the RCW had to be scaled accordingly by $RCW_{scale} = RCW_{nominal} * [0.55m/0.60m]$. The transfer function or transfer ratio was then $ratio = 1 - RCW_{scale}$. Energy spectra were multiplied by this frequency dependent curve to determine the amount of energy passing through the spectra to be input back into SWAN, and represent the leeward wave field.

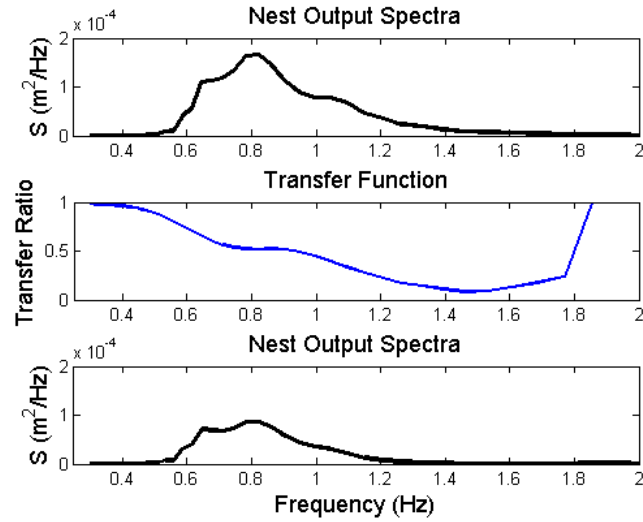
Interpolation of RCW to SWAN Frequencies The RCW curves used in this model are defined at frequencies other than computational grid frequencies, so they were interpolated to the SWAN (computational grid) frequencies. Without interpolation of the RCW to SWAN frequencies, the spectra could not be modified. Associated wave periods resolved in SWAN are described in Table 5 on page 67.

Location and footprint of WECs At each nest boundary, spectra at longshore locations associated with WEC locations for the given WEC-arrangement were modulated by the RCW-based transfer ratio. Figure 33 on the following page shows an example of spectra modification by the transfer function at locations in the domain. Sub-figure "A" shows the frequency dependent transfer function, $[1 - RCW]$, multiplied by the spectra at the Nest1/Nest2 boundary, given by the equation

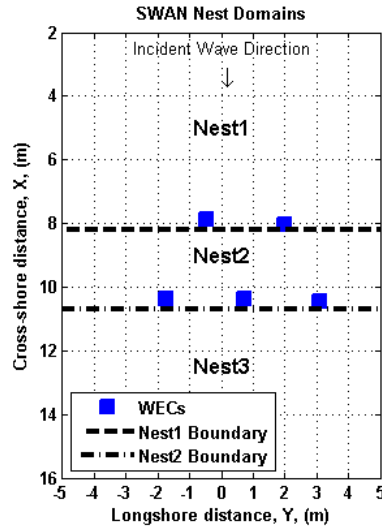
$$Spec_{WEC,i} = Spec_{Nest,i} * (1 - RCW_{scale,i}) \quad (22)$$

where i are the frequencies within $Spec$ and RCW . Sub-figure B shows the locations that the modifications took place by the blue squares on the dashed lines.

The blue squares are the locations of the WECs along each nest boundary; they are the locations in which the spectra was modified as shown in sub-figure A, at all other points in the boundary the spectra remains un-changed. The WEC locations were determined by the mean position of the WECs during select measured trials, then were placed closest as



(a) An example of frequency dependent spectra modification. This modification occurs at each point in each nest boundary where a WEC is present. Otherwise there is no spectra modification.



(b) Nests in SWAN models with locations of WECs. SWAN ran separately in each nest, with the spectra being modified by the RCW at longshore locations of the WECs at each nest boundary

Figure 33: The spectral modification process shown in sub-figure A is performed at WEC locations identified by blue squares in sub-figure B.

possible to those locations given the computational grid size resolution of SWAN.

5.2.7 Shell Script

Because currently SWAN does not have the capability to internally model frequency dependent objects, and source code modifications were not attempted here, the wave field was instead modified externally from SWAN. All of the processes listed above were included in a master shell script that ran the wrote the input files based on the incident data set for each case, ran each net within SWAN, and parametrized the WECs by transfer functions for both real seas and regular waves.

For each wave climate listed in Tables 5 and 6 on page 68 the incident wave conditions was determined by the incident data set, and then SWAN input files were written for each nest with with the current wave conditions. For regular waves the incident wave field for Nest1 was determined by BIN. In real seas simulations the incident spectra was the specified spectra of each unidirectional sea state. SWAN was then run for the Nest1, with spectra output at each location of the Nest1/Nest2 boundary (Nest1.spc). To represent the WEC influence on the wave field the WEC parametrization file “Row1PowerData” was run; it modifies the spectra (Nest1.spc) at WEC locations in row one for the current WEC arrangement. That file then wrote a new SWAN input spectra for all locations on the Nest1/Nest2 boundary (Nst2.bnd) which was used for the Nest2 SWAN simulation. After SWAN was run for Nest2, the spectra was modified by “Row2PowerData”, which represents the WEC parametrization for row two of the array. The output from the external spectra modification (Nst3.bnd) was then modeled in SWAN to the shoreline.

The results from each nest were initially separate files, so it was crucial to combine the wave-field results into a single file. This was done in the shell script by cropping and patching the domains together in a piece-wise fashion. Energy flux calculations were done for each iteration within the shell script at nest boundaries, and at the longshore transect of the lee gage array. To calculate power at the gage array longshore transects, the spatial integration of energy flux in meshes along the transect was computed. To avoid including losses due to edge effects, the integration was cropped 2 meters (20 meshes) from each edge of the longshore boundary. Power deficits in SWAN were the difference between the incident wave power measured at the offshore gage array transect, and the wave power measured at the lee gage array transect. Power loss calculations for each trial were saved in each loop iteration, along with the raw spectra, energy flux calculations at each locations, and the wave height field for model to data comparisons. Because diffraction was not viable and sea states with directional spreading have not yet been characterized in the empirical data set, replicating the exact shape of the wave shadow was not considered a goal of this section. Therefore, the best way to compare model results to empirical data was to compare power deficits, and not wave height distributions.

6 Model/Data Results

Results from the SWAN model to the empirical data set showed that parameterizing WECs solely as power absorbers in SWAN does a fair job of predicting the wave shadow magnitude. They also showed that at shorter wave periods there must be some other physics present that affect the wave shadow.

6.1 Spectral Model and Comparison to Wave Data

The SWAN model can output wave heights, energy flux, radiation stress, and many other wave characteristics; this portion of the analysis we primarily evaluate energy flux. However, to check model output for quality control purposes wave height plots were produced. Figure 34 shows the significant wave height field for a 5-WEC array with the Oregon1 incident wave spectra. Although the incident wave field is unidirectional, and diffraction is turned off, some directional leakage occurs due to coarse directional resolution. Since no lateral spreading occurs due to wave physics, the directional leakage causes GSE like patterns further in the lee of the array. While these could be significant for field application, the shape of the shadow is not what we are after; here we have looked at power only. For reference, the lee gage array is located at a cross-shore distance of 13.2 meters. At this location the distinct shadow shape structures evident, and clearly very minimal shadowing occurs outside of the region directly in the lee of the array since no lateral spreading physics have been turned on. Figure 35 takes a closer look at the lee wave gage array transect by plotting the energy flux values of the model along this transect, and comparing to empirical data from trials with the same incident wave conditions. Most noticeable are the peaks and troughs of energy flux of the SWAN results by the red line; the troughs approximately correspond to the longshore locations of WECs in the array. The green line represents the energy flux shadow measured in the empirical data; it's shape shows lateral energy spreading. Clearly the edge of the shadow from the empirical data set is not resolved by the gage array, so the power losses could be slightly underestimated.

Because incident wave conditions in SWAN are intended to match those of the incident data set it was important to check the incident wave conditions of the SWAN results. SWAN did a good job of resolving the true incident wave climate. For example, take note that the Oregon1 sea state has a target significant wave height of 0.0454 meters, and the incident significant wave height in figure 34 is very close to that. Figure 35 shows energy flux transects of the offshore and lee gage arrays for model and empirical data results of the same case shown in Figure 34 (Oregon1). Incident energy flux values were nearly the same for model and empirical results. The difference between energy flux values of empirical data and model results is likely because frequencies in SWAN are not exactly the same as in the empirical data set, which creates small changes in the group velocity of each waveform, and hence the

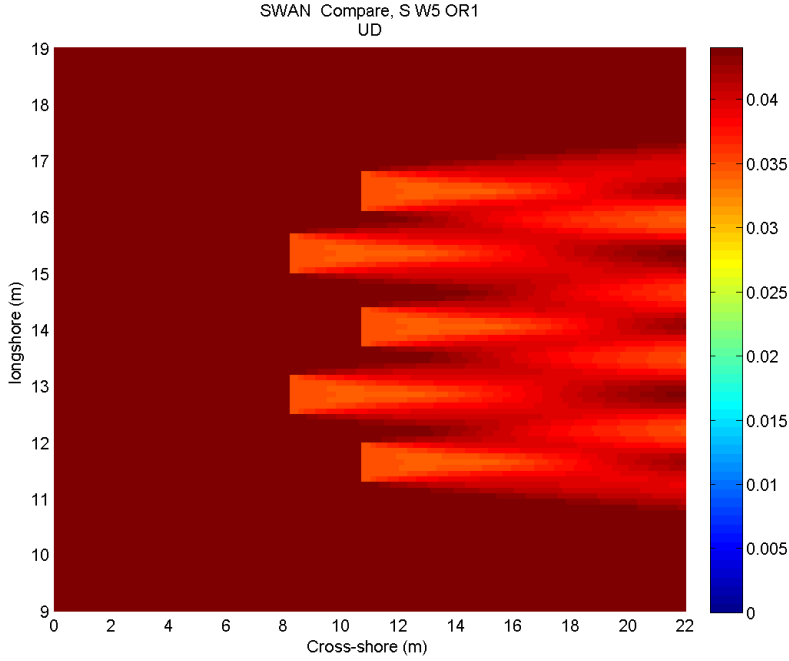


Figure 34: Typical SWAN significant wave height field result from a 5-WEC array with no directional spreading or diffraction. Units are in meters. Some directional spreading occurs due to directional mesh resolution, which also results in interference patterns in the lee. Bright colors represent more shadowing.

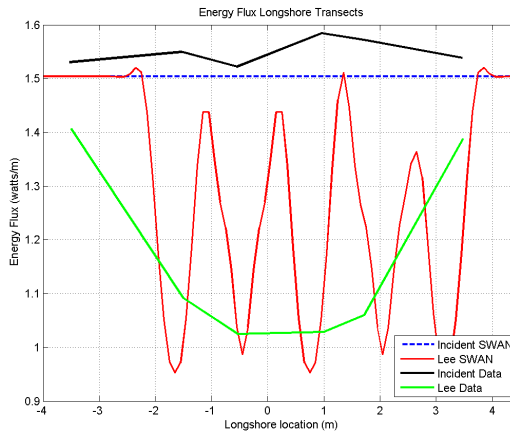


Figure 35: Typical model to data comparison of incident and lee energy flux transects. Data is from a 5-WEC array with no directional spreading or diffraction. Some directional spreading occurs due to directional mesh resolution. The blue and red lines are model results, black and green lines are empirical data results.

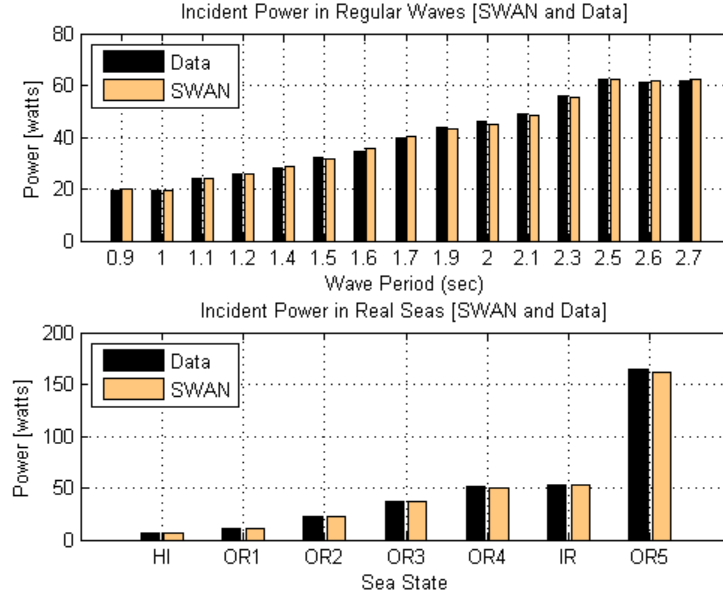


Figure 36: Incident wave power in empirical data (black) and SWAN results (copper). Because incident power in the model and the empirical data set were nearly the same, we have confidence in shadow results. Small variations occur due frequency resolution limitations in SWAN.

energy flux. These small differences occur in all wave conditions, but Figure 36 shows that such differences over all regular wave and real seas conditions tested are minimal.

Previously in this thesis, the influence of WEC-arrays on the waves was measured by the power deficit observed in the lee gage array relative to the incident wave conditions. The same method was applied to model results. Power deficits measured in the wave data from the WEC-Array Experiments were compared to deficits calculated from the model results for the same incident conditions. Figure 37 on page 77 plots this comparison from single, three, and five device arrays in regular wave, and real seas conditions. The black bars correspond to the empirical data set, and the copper bars correspond to model results. On the left side of the figure results from the regular waves tests are displayed. It is clear that in the 1-WEC case, the empirical data set is variable and that very little conclusions can be made. Power deficit calculations from the empirical data set for the single device array are variable because of small signal-to-noise ratios. The incident power in a typical regular wave case was anywhere from twenty to forty watts, while SWAN predicted power deficits of one to two watts. Resolving a change signal on the order of three percent in the lab environment would be difficult with natural variability of these experiments around +/- 5%.

Power deficits in regular waves from the three and five device WEC-arrays tell us the model does best in higher period waves. The shadow signal was much bigger in the larger arrays, 5-WEC arrays having the strongest signal; the results from 5-WEC arrays were the most trusted. In the 5-WEC array comparison, we saw that at most wave periods the model resolves power deficits reasonably well, but in several of the shorter wave periods (1.0-1.2 seconds) much larger power deficits were measured in the wave data. This was not surprising; as we saw in the RCW/RIW comparison the effective width measured in the wave data was much larger than predicted than the RCW curve (mechanical absorption) at the same regular wave periods (1.0-1.2 seconds). At these wave periods there must be physical processes present other than absorption which help to create the wave shadow.

The same wave period dependent behavior that occurs in the regular wave model-to-data comparison can help to explain the real seas simulations results. Looking at 5-WEC results, in the real seas states where the peak wave period is high (Oregon4, Oregon5) SWAN did a good job of predicting wave shadow. At sea states with shorter peak periods, the model did not do as well. This is because more energy in the spectrum is located at higher frequencies, where other physics than absorption induce a wave shadow. Recall Figure 21 on page 47 where RIW and RCW were plotted as a function of peak frequency; in the sea states with lower frequencies (high periods) the difference between RCW and RIW was very small, while at higher peak frequencies the RIW was greater (i.e., absorption did not fully predict shadow). The model exhibited the same tendencies since it was based on a parameterization of RCW behavior.

Because of this the model was built off the RCW curve behavior in both regular waves and real seas, we can approximate model results by the RCW curve. To examine how much some processes other than absorption affect the wave shadow we look at RIW results from the empirical data set, and the RCW curves. As a refresher, Relative Influence Width (RIW) is a proxy for shadow magnitude, and is calculated by the ratio of the relative power available (RPA) to measured power loss, where RPA is the incident energy flux multiplied by the nominal width of a WEC, and by the number of WECs in the water.

$$RPA = .55 * Ef * \#WECs \quad (23)$$

$$RIW = \frac{P_{deficit}[\text{watts}]}{RPA[\text{watts}]} \quad (24)$$

Sub-figure A of Figure 38 on page 79 recalls data analysis from Part 1, and plots average RIW and RCW and a function of period for regular wave and real seas. If the shadow were completely due to absorption, the RIW lines would plot directly on top of the RCW lines. It is clear in the top panel that other processes than absorption were present at periods of 1.0 seconds to 1.4 seconds since the RIW curve is higher than the RCW curve. In real seas

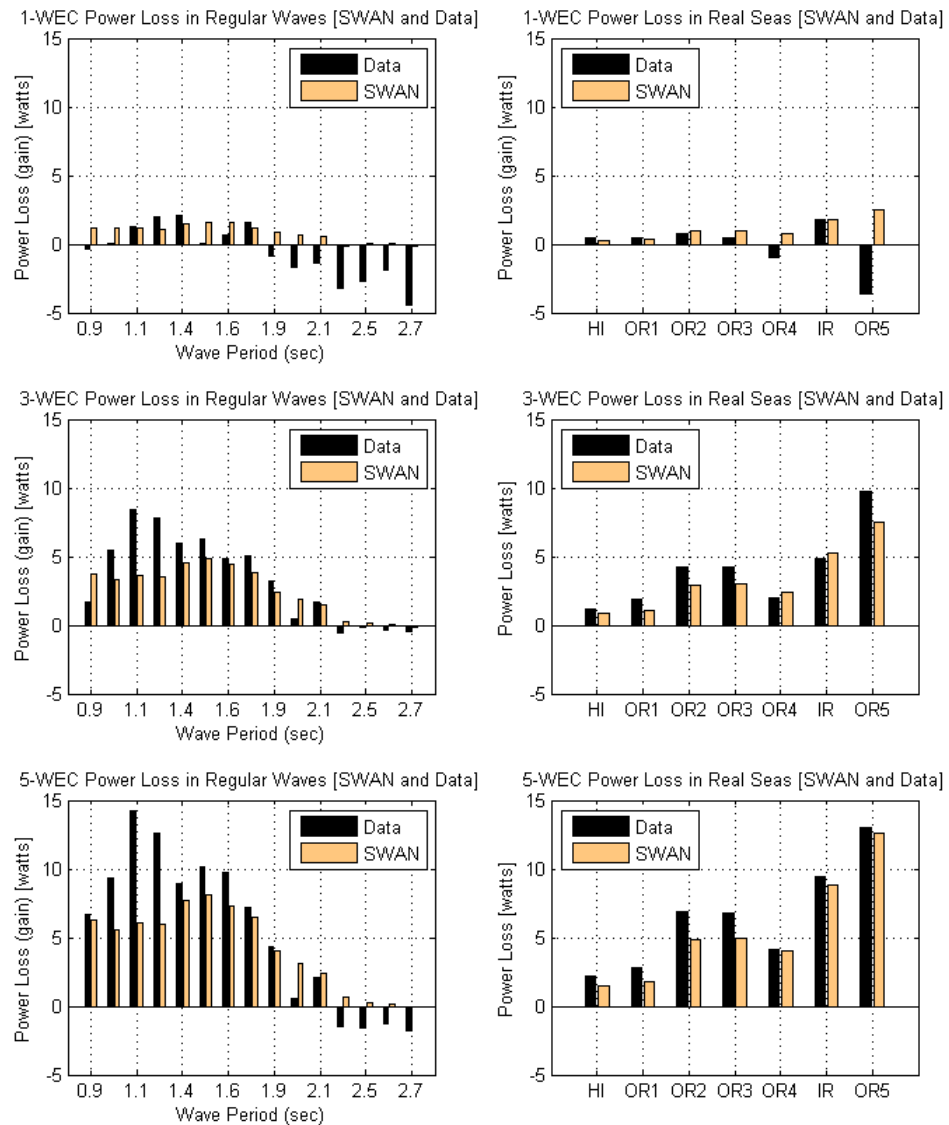


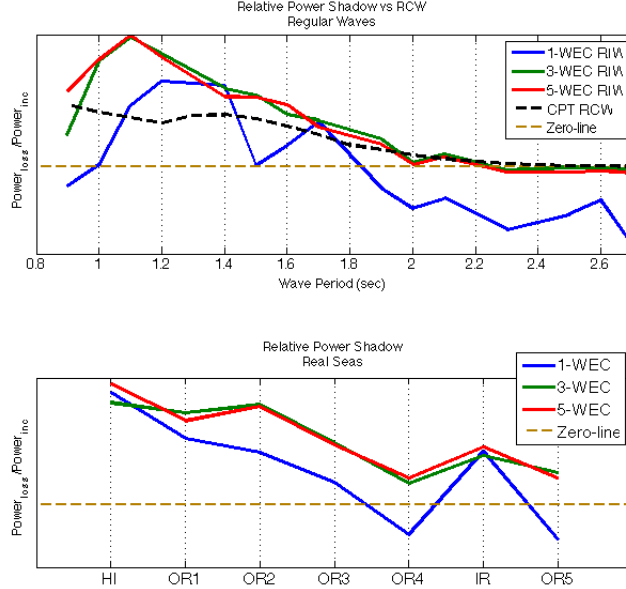
Figure 37: Comparison of model results (copper color) to empirical data (black) in regular waves, in the seven real seas sea states, for three WEC-array sizes. The mode of comparison is power lost from the wave field between upwave and downwave transects of the WEC-array.

the greatest difference between RIW and RCW curves occurs at these frequencies as well.

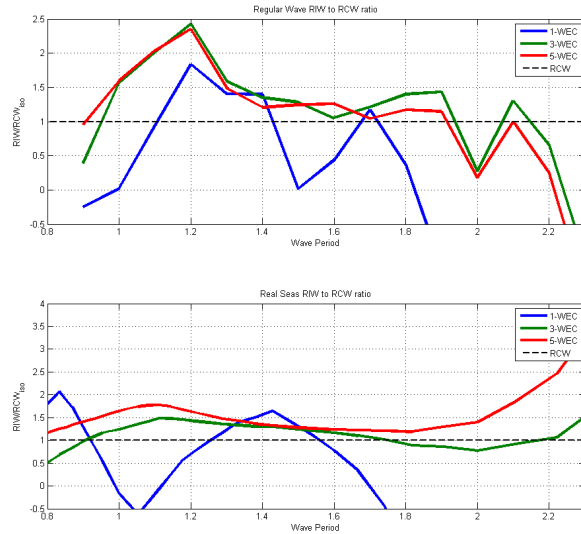
To approximate the portion of the shadow that is not accounted for by absorption, the ratio of RIW to RCW was taken. Ratio values above 1.0 indicate more shadowing occurs than predicted by absorption, and under 1.0 the opposite. Sub-figure B of Figure 38 on the next page plots this ratio as function of wave period for one, three and five device arrays. Results from single device arrays (blue) are of little use, since the wave shadow signal is so low and this plot is taking the ratio of two ratios which amplifies errors. Take note that the y-axis of this figure is the ratio of two ratios, so even in higher signals the results are very susceptible to noise. The three and five device RIW curves show that at wave periods between 1.0sec and 1.4sec some other effects must be contributing to the shadow. In the rest of the domain, however, the RIW and RCW curves show that absorption is the primary driver of the shadow. This is why the model did better in sea states that have higher peak wave periods, absorption is responsible for nearly all the shadowing and the model only accounts for absorption.

6.2 Comparison to Mechanical Power Captured

In the SWAN simulations the WECs were parametrized using data that described the mechanical power absorption behavior of a single device over a range of wave periods. Because of this, the power deficit result trends (RIW) from SWAN simulations for single device arrays should be very similar to that of the power deficit trends in mechanical power absorbed (RCW) by a single WEC. We tested this by comparing the incident wave power in SWAN to the incident wave power data that was used to calculate the mechanical RCW. Sub-figure A of Figure 39 on page 80 confirmed the incident power was the same. This validated that a comparison between mechanical RCW and the RIW in SWAN is sufficient to test mechanical power against SWAN, the results of which are shown in sub-figure B of Figure 39 on page 80. Three data sets are plotted, the reference RCW from mechanical power absorption in black, RIW calculated in SWAN as the red circles, and the RIW calculated in the external spectra modification, “RIWnest” in blue. Two curves, RCW and RIWnest are nearly identical since RIWnest is simply the RCW interpolated to SWAN frequencies. The red circles vary from the RCW curve to some degree, but the overall shape and magnitudes are similar. RIW values from SWAN results should vary slightly from RCW curve values because the RIW was calculated approximately eight WEC diameters in the lee of the device, unlike the RCW which was by definition calculated at the device. Overall, this comparison to mechanical power validates the SWAN model methods.

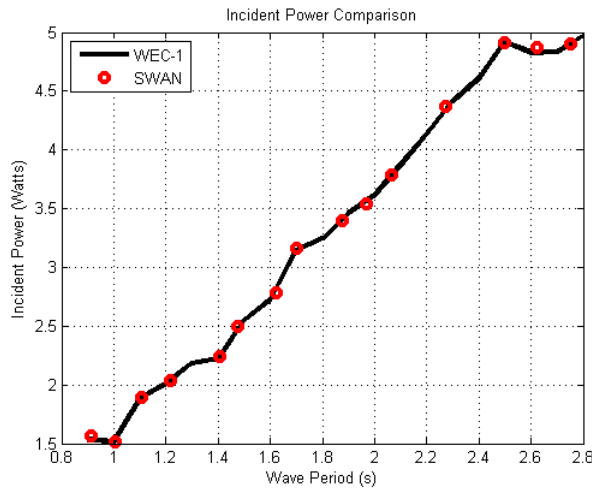


(a) Relative influence widths (RIW) measured from wave data for multiple array sizes (blue, green, red), and relative capture widths (RCW) of regular wave and real seas conditions (black). Real seas values are the mean of the seven sea states in unidirectional seas.

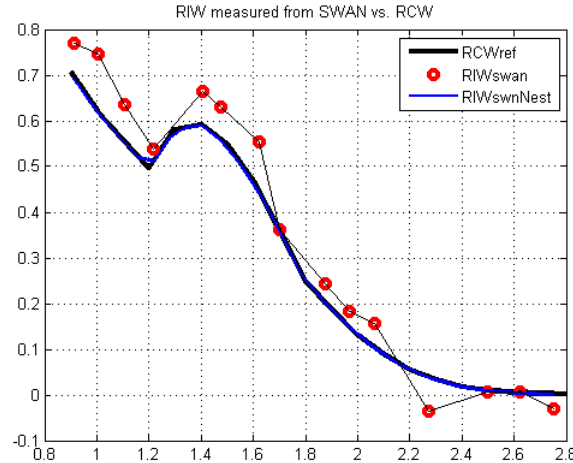


(b) Ratio of RIW to RCW as a function of wave period for regular waves and real seas. RIW values above 1.0 indicate more shadowing in wave data than predicted by WEC absorption trends (RCW).

Figure 38: These figures compare pure WEC absorption trends (RCW) used to parametrize WECs in the SWAN model to shadow magnitude trends of the empirical data set.



(a) Incident Power in SWAN and in Mechanical RCW. Red dots correspond to power measured in SWAN, and the black line is incident wave power measured in the wave data.



(b) Relative influence width measured in SWAN results (red dots), RCW of device (black line), and RIW measured in external spectral modification.

Figure 39: Relative influence and capture widths measured from SWAN results, mechanical data, and external spectra transformation

7 Numerical Model Conclusions

In conjunction with the spectral model, “SWAN”, the parametrization and modeling WECs solely as point absorbing power sinks does a fair job of accurately predicting the power of the wave field in the lee of wave energy converter array. In regular waves it does well at higher periods, but misses some shadow magnitude at shorter wave periods. In the shorter period waves there must have been physical processes present which the current model methodology does not account for; therefore there some of the power deficit is not resolved. In high period waves a greater portion of the resultant wave shadow in the empirical data set was due purely to absorption, so the model did a better job of predicting the wave field in the downwave side of the array in these conditions. The same phenomenon was observed in real seas simulations, where wave shadows from sea states with higher peak period waves were better resolved than shorter peak period waves (as in Oregon5 v. Hawaii). In sea states where a large portion of the spectral energy is located at frequencies where shadowing driven nearly completely by WEC power absorption this modeling method will do well.

8 WAMIT/SWAN WEC Model Comparison

The modeling programs SWAN and WAMIT model the waves in entirely different manners and usually serve different purposes. SWAN is generally applied to large coarse domains and varying bathymetry with the intent of short computation times, and WAMIT generally to small dense flat domains with longer computation times. Computation time of WAMIT goes up as the number of WECs squared, while SWAN computation time is only a function of domain size and computational grid resolution. It is of great interest whether SWAN can produce similar results to WAMIT for WEC-arrays because of the great gap in computation time for modeling WEC arrays and the ability of WAMIT to model the near-field. This portion of analysis compared modeling results from SWAN to modeling results from WAMIT, in order to better gage the abilities and limitations of SWAN to resolve the effects of a WEC. The extent and magnitude of wave shadows were compared in this analysis.

The effects of WECs are resolved differently in WAMIT and SWAN. WECs in SWAN were parametrized entirely as power absorbing devices and did not account for wave scattering (spatial re-distribution of wave energy) due to the presence of an object, say as like a pile will affect the wave field. Additionally, the movement of the WEC in the water causes radiated waves, which SWAN does not resolve. WAMIT however, was able to resolve these effects, so the comparison between the two models helped us to understand in which cases parameterizing WEC as power absorbers is a fair representation of the effects from the array.

Identical wave fields were fed into SWAN and WAMIT, with idealized identical WECs, and the wave fields produced in each model were compared in longshore and cross-shore transects. SWAN was ran with and without diffraction “on”, which required coarse computational grid spacing. WAMIT was fed parametric incident wave spectra exported from SWAN to ensure true apples-to-apples comparison. The WAMIT simulations come from the concurrent thesis work of McNatt [McNatt, 2012b]. Single WEC conditions were considered, and the WECs were longshore centered in a flat-bottom numerical domain.

8.1 Model Physics

SWAN and WAMIT differ in their ability to capture certain physics. WAMIT is a radiation/diffraction program developed for the linear analysis of the interaction of surface waves with various types of floating and submerged structures [WAMIT]. It has the capability to then model wave-wave interference since it is not phase-averaged like SWAN. The computation times of modeling WEC arrays for WAMIT and SWAN vary greatly

WAMIT is based on the linear and second-order potential theory for analyzing floating or submerged bodies, in the presence of ocean waves. The boundary integral equation method (BIEM), also known as the panel method, is used to solve for the velocity potential and fluid pressure on the submerged surfaces of the bodies. Separate solutions are carried out

simultaneously for the diffraction problem, giving the effects of incident waves on the body, and the radiation problems for each of the prescribed modes of motion of the bodies. These solutions are then used to obtain the relevant hydrodynamic parameters including added-mass and damping coefficients, exciting forces, response-amplitude operators (RAO's), the pressure and fluid velocity, and the mean drift forces and moments [WAMIT]

SWAN physics were described in detail in section 5.1, but the purpose of this comparison is to see whether or not SWAN physics can reasonably predict the same shadow WAMIT does. For large domains SWAN modeling is required rather than WAMIT, since WAMIT cannot model such large domains (such as the entire nearshore). It would also be computationally unfeasible to model very large arrays (50+) WECs since BEM computation time increases with the square of the number of WECs being modeled.

This portion of analysis enables diffraction in SWAN, unlike the model results shown earlier in this thesis (Section 6). Diffraction in SWAN is approximated based on the mild-slope equation for refraction-diffraction of individual waveforms, but without using any phase information. The mild-slope equation approximates linear waves propagating over a mild-sloping bottom as

$$\nabla \bullet cc_g \nabla \zeta + \kappa^2 cc_g \zeta = 0 \quad (25)$$

where c is wave velocity (celerity), c_g is group velocity, $\zeta = a \exp(i\psi)$ is the complex wave function and κ is determined by $\omega^2 = gk \tanh(\kappa d)$. Adding diffraction to the spectral energy balance involved only modifying the group velocity and the temporal rate of turning (in equation 8) [Holthuijsen et al., 2003].

8.2 Comparison Methods

8.2.1 Wave Conditions

This analysis tested two regular wave cases and two parametrized real seas cases. Trial conditions were limited by the ratio between computational grid size resolution and wavelength. SWAN can only converge on a solution if the wave length to grid size resolution is near $1/10 - 1/5$ the wavelength, any larger ratio and SWAN will not converge. After balancing the need for fine grid resolution and wave periods the following conditions were tested, and are listed in table 8, the trials center around periods of 1.0 and 2.0 seconds. The analysis was done at the same model scale as the WEC-array Experiments, one to thirty three length scale. At field scale wave periods of 1.0 and 2.0 seconds scale to 5.7 seconds and 11.5 seconds, respectively. Diffraction was turned on for the cases in which SWAN would converge at the current mesh size; regular waves with a period of two seconds did not converge, so diffraction for this case is not provided herein. Wave heights in this analysis are normalized by the incident wave height. Since WAMIT operates assuming linearity in wave

Table 8: Incident wave conditions for SWAN/WAMIT comparisons

Regular Waves		Real Seas	
T	Diffraction	T_P	s^1
[sec]	[on/off]	[sec]	[s]
1.0	On, Off	1.0	4, 10, UD ²
2.0	Off	2.0	4, 10, UD

(a) Regular Waves

Real Seas		
T_P	s^1	Diffraction
[sec]	[s]	[on/off]
1.0	4, 10, UD ²	On, Off
2.0	4, 10, UD	On, Off

¹Directional spread parameter, s , for distribution $[0.5 \cos(\theta - \theta_{mean})]^{2s}$

²Unidirectional

(b) Real Seas

heights, and there was linearity with height behavior in the data, a range of wave heights was not considered for this analysis.

8.2.2 WEC performance

In this case, the relative capture width (RCW) curve was calculated by McNatt [2012b] in WAMIT for an idealized WEC that was represented by a smooth cylinder as seen in Figure 40, which extracts power only in surge. The WEC was designed to have an RCW similar to that of the “Manta 3.1” WEC built and developed by Columbia Power Technologies, which was in use during the WEC-array Experiments. The WEC RCW curve was determined by the physical characteristics and damping of such WEC. This RCW curve was used to modify the wave field by the method outlined in section 5.2.6, and is plotted in Figure 41. The RCW values at 1.0 and 2.0 seconds are both approximately 0.3.

Unlike the previous comparison of SWAN results to experimental wave data, this analysis uses a single RCW curve for real seas, and for regular waves. This is because WAMIT operates on the assumption of linearity, and the regular wave cases in a sense build the real seas cases by the superposition of waves from all frequencies within a spectra.

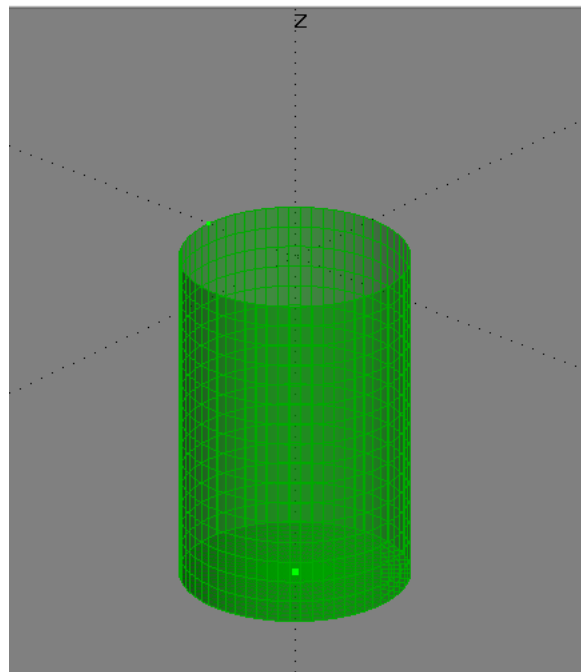


Figure 40: Idealized WEC (0.6m diameter, 0.8m draft) used to compute RCW

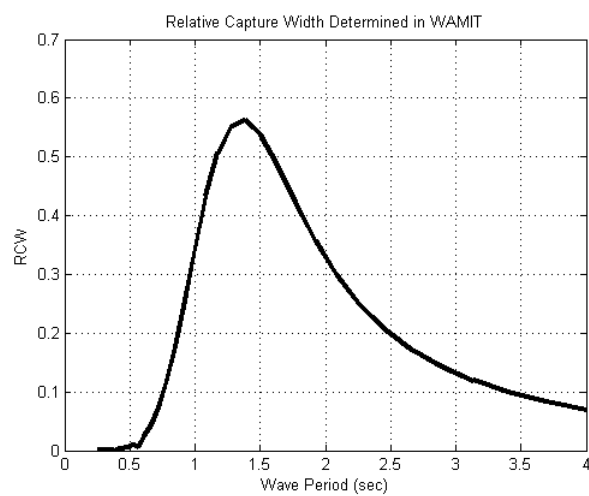


Figure 41: Relative capture width (RCW) as function of wave period for WAMIT/SWAN model comparison

9 WAMIT/SWAN Results

This section examines the model results of SWAN and WAMIT for identical incident wave conditions and idealized WEC performance for regular waves and real seas conditions. The shape and magnitude of the wave shadow of regular wave and real seas cases, and transects of wave heights in the longshore and the cross-shore directions. Unlike previous analysis in this thesis directional spreading cases results were also considered. Diffraction in SWAN is included in both unidirectional and directional seas, but one may notice that in the diffraction cases there are larger edge effects; however, materially the edge effects do not change the results.

A major difference you will notice are the differences in the offshore wave field between SWAN and WAMIT results. Since the WECs are being modeled solely as power absorbers in SWAN there is no wave reflection from the devices back to the offshore to create a standing wave pattern. Additionally, SWAN does not resolve phase, so standing waves caused by the presence of WECs are not modeled in SWAN. Standing waves created a highly variable wave field in the WAMIT results, and are best seen in the regular wave cases.

9.1 Unidirectional Waves

Wave shadow results for regular waves and unidirectional real seas simulations for WAMIT and SWAN are presented in this section. Regular wave shadow magnitudes in WAMIT results rely heavily on the incident wave period, even though the RCW value for one second and two second waves is nearly the same. WAMIT results show much more shadowing in the one second regular wave case than in the two second regular wave case. The root of this is that a significant portion of the shadow is due to scattered waves at shorter wave periods than higher wave periods. Since the RCW values are nearly the same it is not surprising that the SWAN results for one and two second waves are nearly identical, because the SWAN WEC parametrization is based only on RCW (absorption). Diffraction in SWAN made the shape of the shadow closer to that of WAMIT, but the shadow magnitude remained unchanged. These results can be seen in Figures 42 and 47, which show wave height measured throughout the domains for SWAN in the top panel, WAMIT in the middle panel and the difference between the two models in the bottom panel. The wave shadow is shown by relative wave height reduction indicated by blue colors, and the red colors indicate increased wave heights. As mentioned previously, the WAMIT results show some very interesting offshore patterns, as well as patterns to the sides of the WEC array. These standing wave patterns are due to the scattered short-wave patterns caused by WEC-wave interactions with the incident wave field. For a more detailed explanation of this physical phenomenon see McNatt [2012b].

In real seas simulations the shadow magnitudes in WAMIT rely on incident peak period much more than in SWAN, this is because the wave field in SWAN is only modulated by

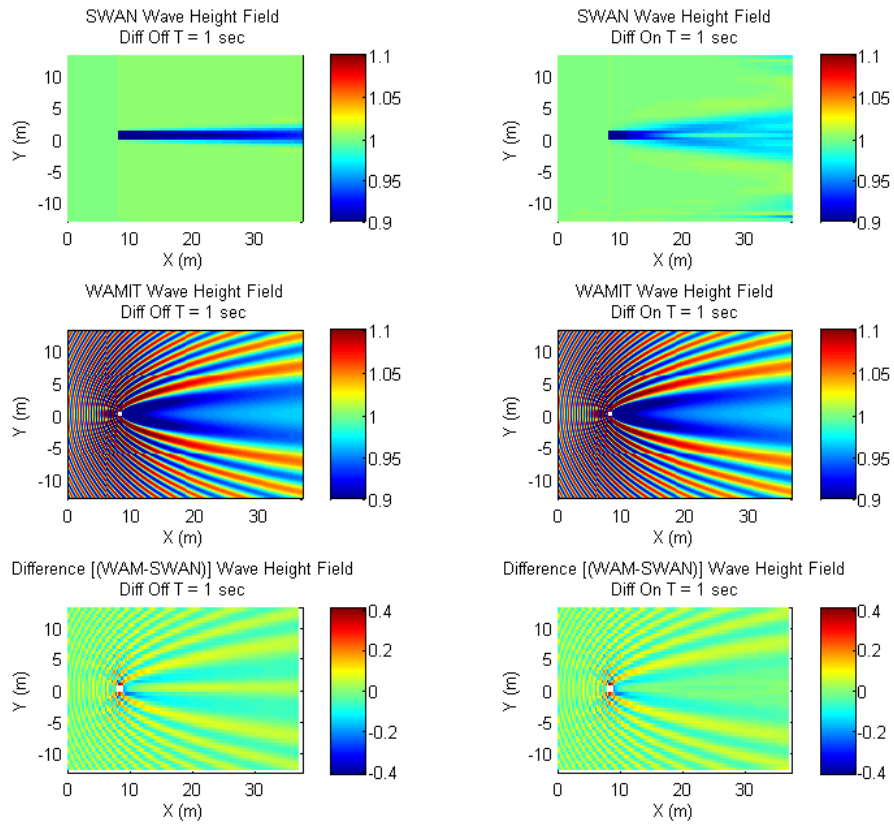


Figure 42: Regular Wave Shadowing in WAMIT and SWAN for $T = 1$ sec. Diffraction in SWAN is toggled on and off. Blue colors indicate shadowing, where red values indicate increased wave heights

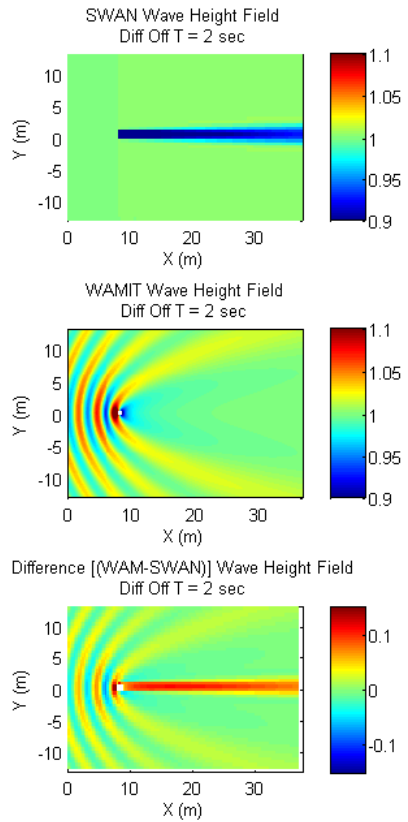


Figure 43: Regular Wave Shadowing in WAMIT and SWAN for $T = 2$ sec. Diffraction in SWAN is off since regular waves of two seconds would not converge. Blue colors indicate shadowing, where red values indicate increased wave height. WAMIT has very little shadowing in this case, but large offshore standing waves.

the RCW value, and not scattering. This can be seen in figures 44 and 45. More shadowing occurred in WAMIT results in the first set of trials' (1.0 second peak period) wave fields than the 2.0 second cases. In the 1.0 second cases WAMIT and SWAN do not mirror each other well, in both diffraction on and diffraction off cases. Increasing the peak wave period to 2.0 seconds has very different results

The second set of trials (2.0 second peak period) show good mirroring between WAMIT and SWAN results. Less short-wave scattering is present in this sea state, so a larger majority of the shadow is due to power absorption by the WEC than in the first set of trials (where more scattering was present, like in the one second regular wave case). Comparisons between SWAN and WAMIT in the second set of trials not only show similar shadow magnitudes, but also, when diffraction in SWAN is toggled “ON”, they have very similar shadow shapes (see Figure 45), which is very promising.

A measure of total shadowing is to take the average wave height across the longshore domain, this accounts for the standing wave patterns seen in the WAMIT results. The bottom panels in Figures 46 and 47 show the total shadowing in terms of longshore averaged wave height as a function of cross-shore position. There is much more total shadowing in the WAMIT tests in the first case than in the second, but the SWAN results are very similar. Since in the second figure the total shadow lines are very similar we observe that SWAN has done an fair job of representing the shadow in the lee of the array, with respect to WAMIT results. One can also see the standing wave patterns created in the offshore by the presence of the WEC in the WAMIT trials.

9.2 Directional Spreading

In this section, results from effect of directional spreading on the wave field for comparison between SWAN and WAMIT are presented. Generally, SWAN does better with directionally spread seas than unidirectional waves since it was designed to simulate real seas. Since it was shown in Section 9.1 that at short wave periods SWAN and WAMIT differ more than in longer wave periods (with similar RCW values) this section will only present results based on peak wave periods of 2.0 seconds.

With directional spreading on SWAN did a very good job of replicating the wave field in the lee of the WEC predicted by WAMIT with both diffraction on, and diffraction off. There was very little difference between SWAN wave fields with diffraction “on” or “off” in the directionally spread seas. Wave energy adequately was spread laterally without the inclusion of artificial diffraction in these cases. This can be see in figures 49 and 49 where the wave shadow shapes are nearly identical between diffraction on and off, as well as WAMIT results. Additionally, figures 50 and 51 show that in SWAN the cross-shore wave shadow magnitude directly in the lee of the WEC and the total wave shadow magnitude (estimated by longshore averaged wave height) are both very similar to the WAMIT results.

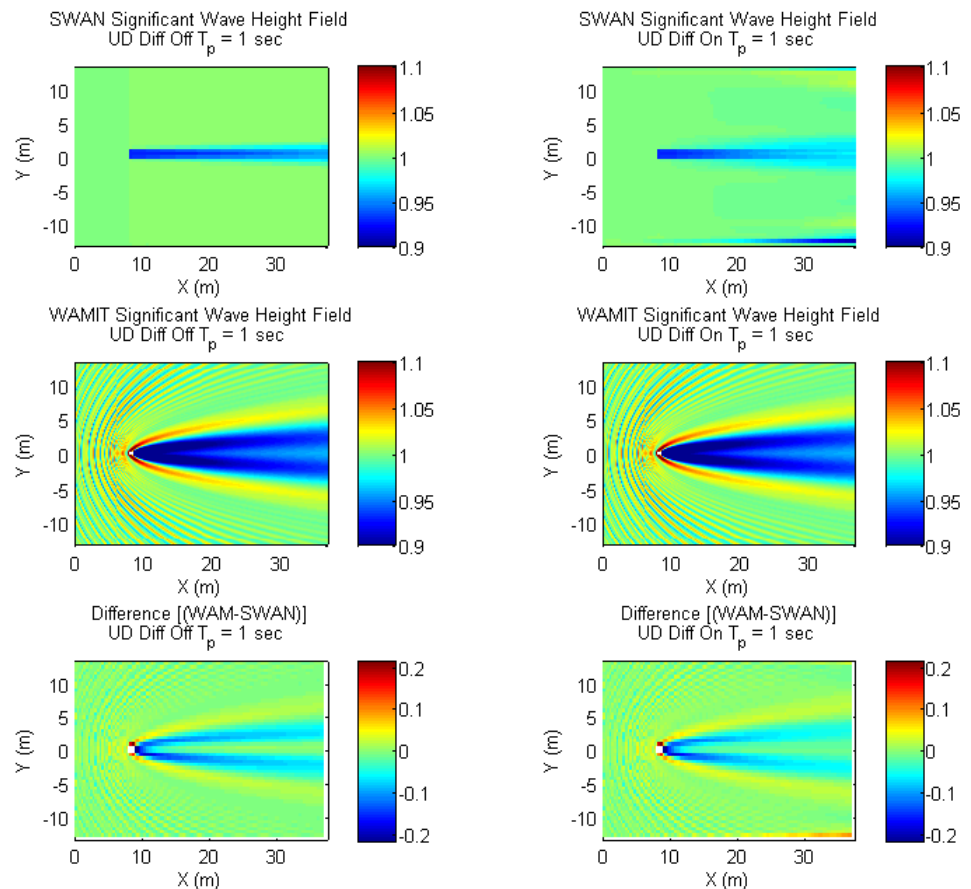


Figure 44: Wave field shadowing results from WAMIT and SWAN real seas simulations with unidirectional waves for a peak period of 1.0 seconds. Blue colors indicate relative wave reduction (shadowing), while red colors indicate increased wave heights. The bottom panel shows the difference between the two models in space

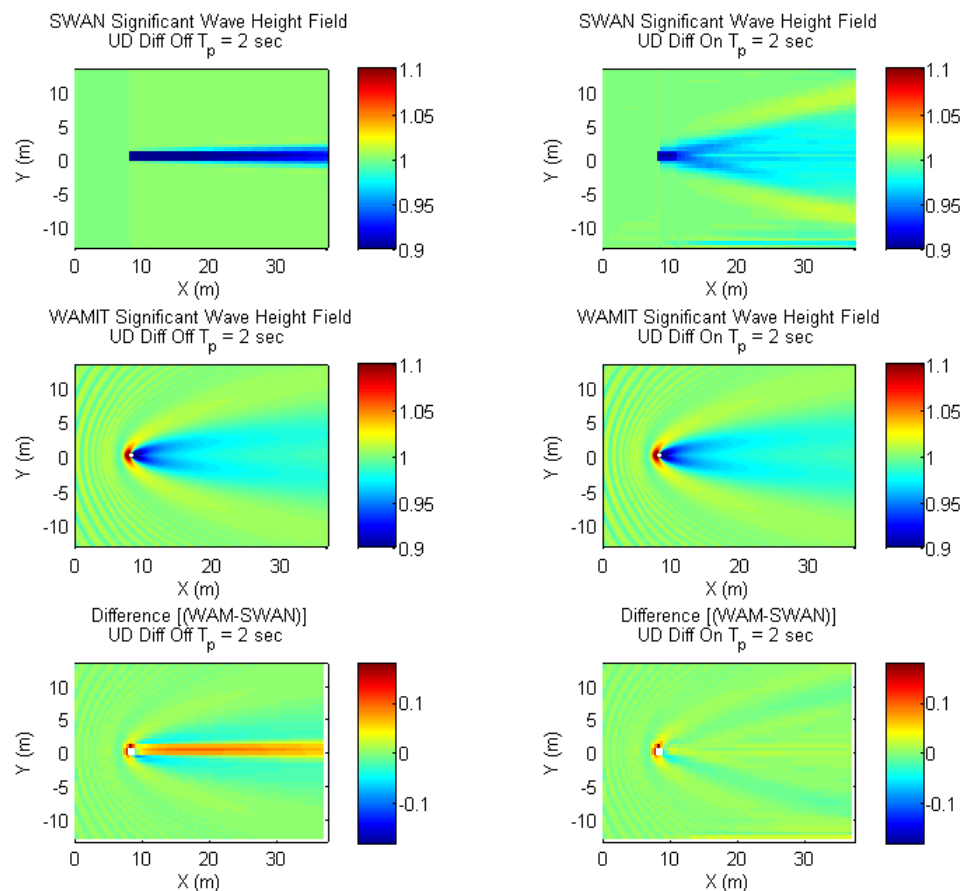


Figure 45: Wave field shadowing results from WAMIT and SWAN real seas simulations with unidirectional waves for a peak period of 2.0 seconds. Blue colors indicate relative wave reduction (shadowing), while red colors indicate increased wave heights. The bottom panel shows the difference between the two models in space

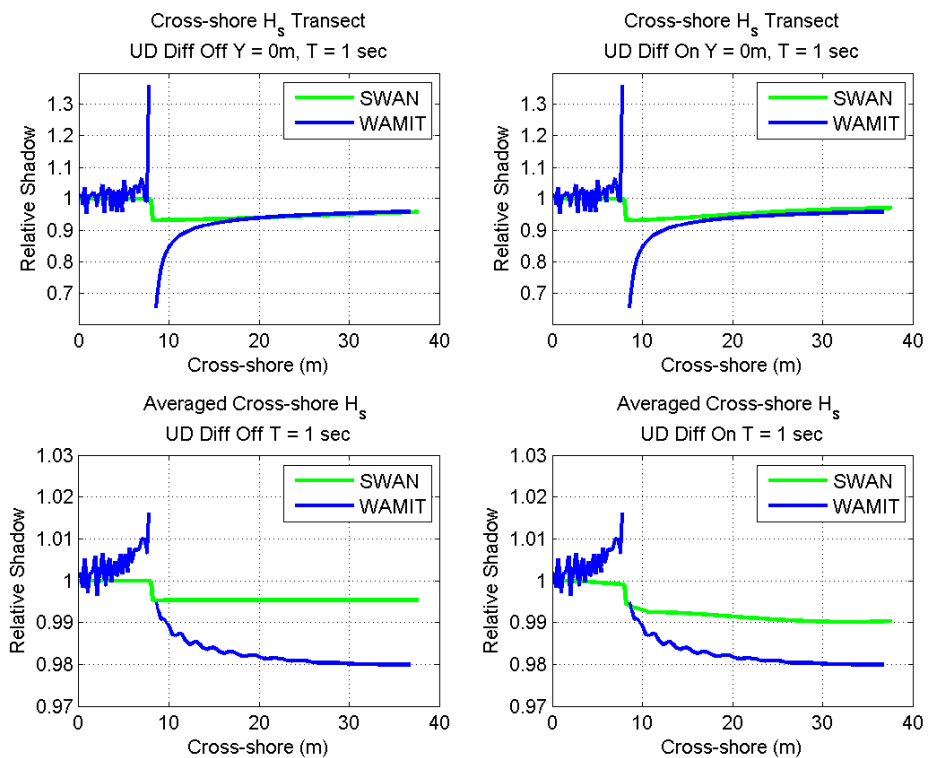


Figure 46: Cross-shore relative shadow transects of real seas simulations with unidirectional waves for a peak period of 1.0 seconds. The transects are measured at the longshore location of the WEC, and as the average wave height across the longshore domain.

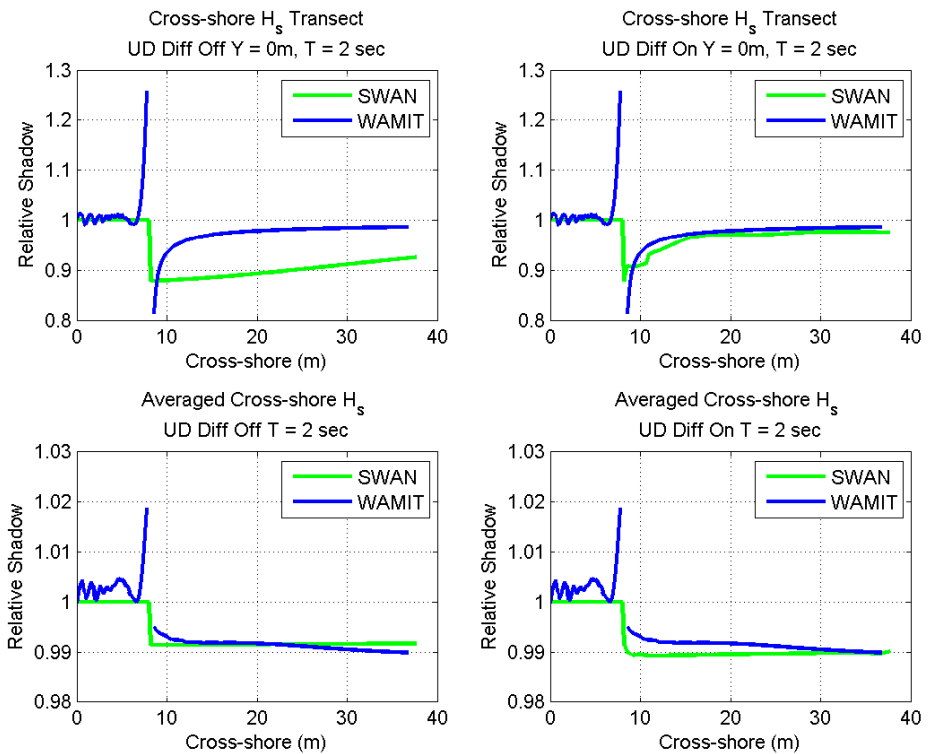


Figure 47: Cross-shore relative shadow transects of real seas simulations with unidirectional waves for a peak period of 2.0 seconds. The transects are measured at the longshore location of the WEC, and as the average wave height across the longshore domain.

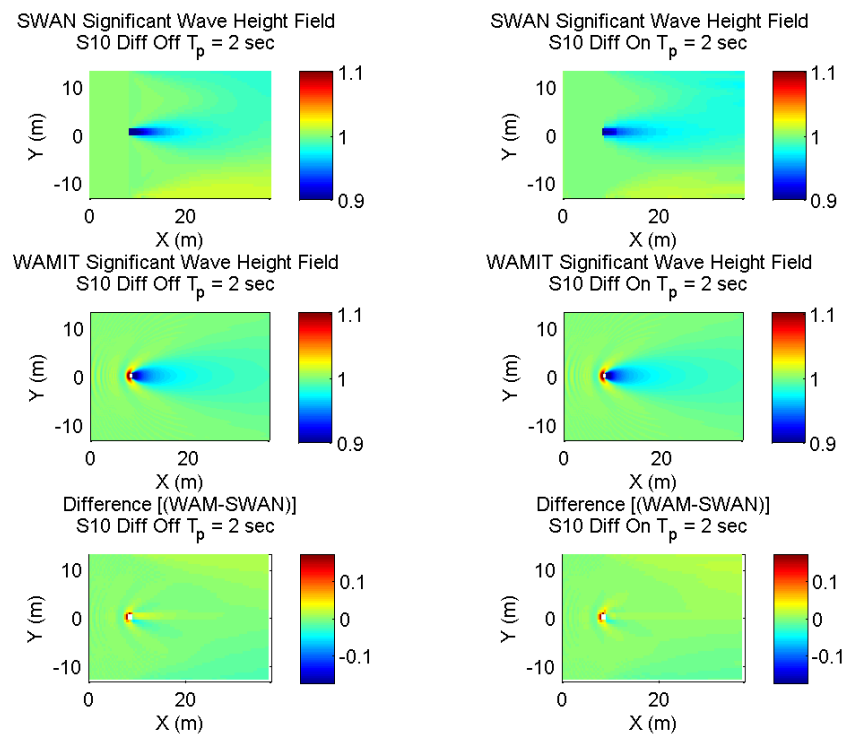


Figure 48: Wave field shadowing results from real seas simulations with a directional spreading factor of $s = 10$ with a peak period of 2.0 seconds. Blue colors indicate relative wave reduction (shadowing), while red colors indicate increased wave heights. The bottom panel shows the difference between the two models in space

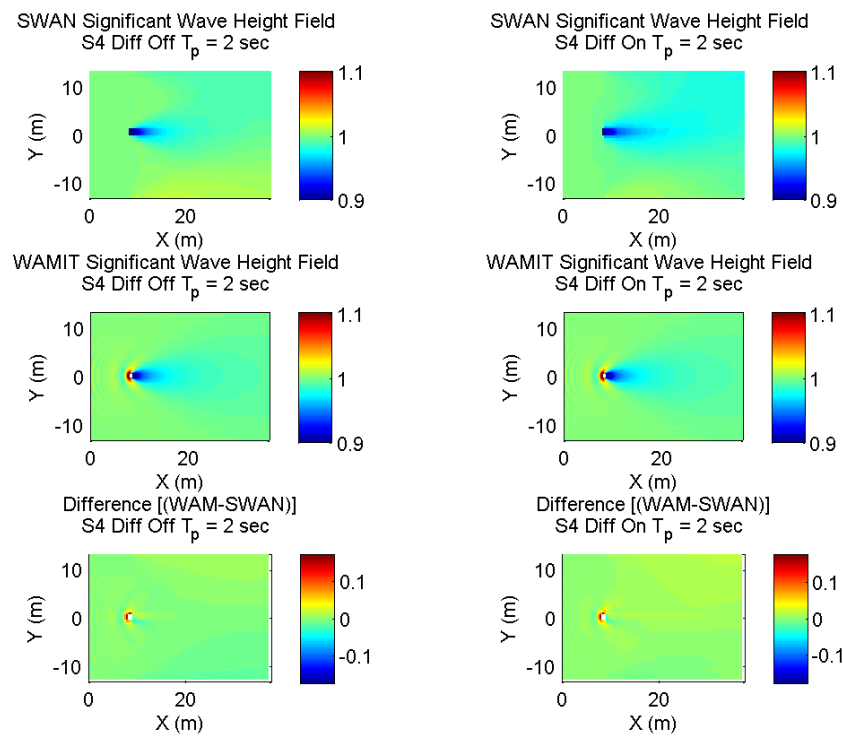


Figure 49: Wave field shadowing results from real seas simulations with a directional spreading factor of $s = 4$ with a peak period of 2.0 second. Blue colors indicate relative wave reduction (shadowing), while red colors indicate increased wave heights. The bottom panel shows the difference between the two models in space

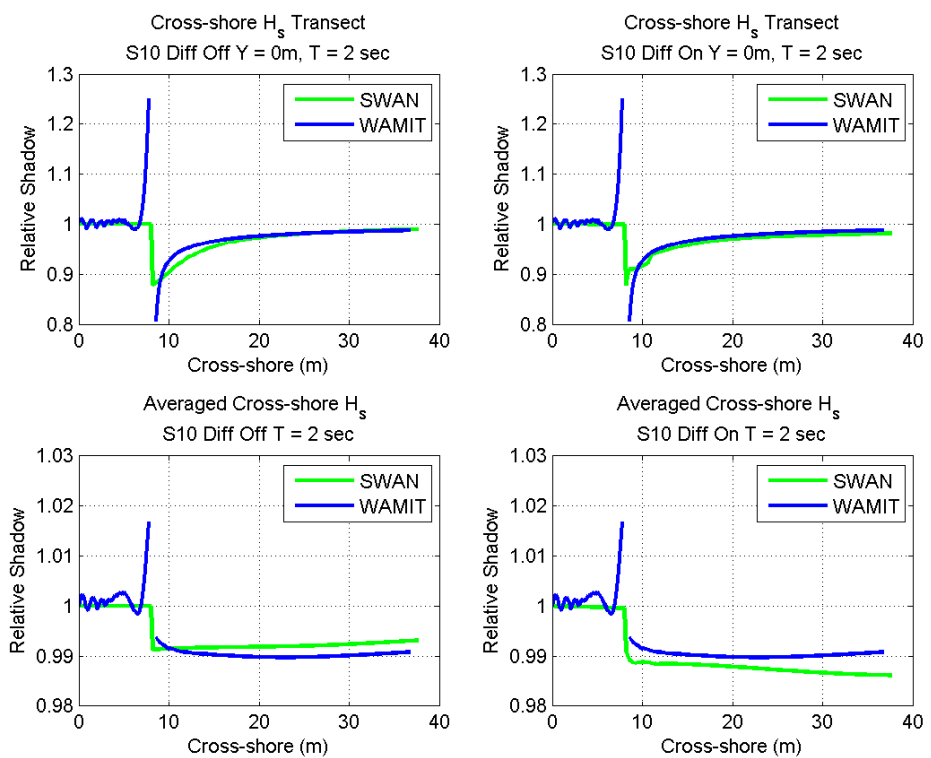


Figure 50: Cross-shore transect results from real seas simulations with a directional spreading factor of $s = 10$ with a peak period of 2.0 seconds. SWAN and WAMIT results are very similar.

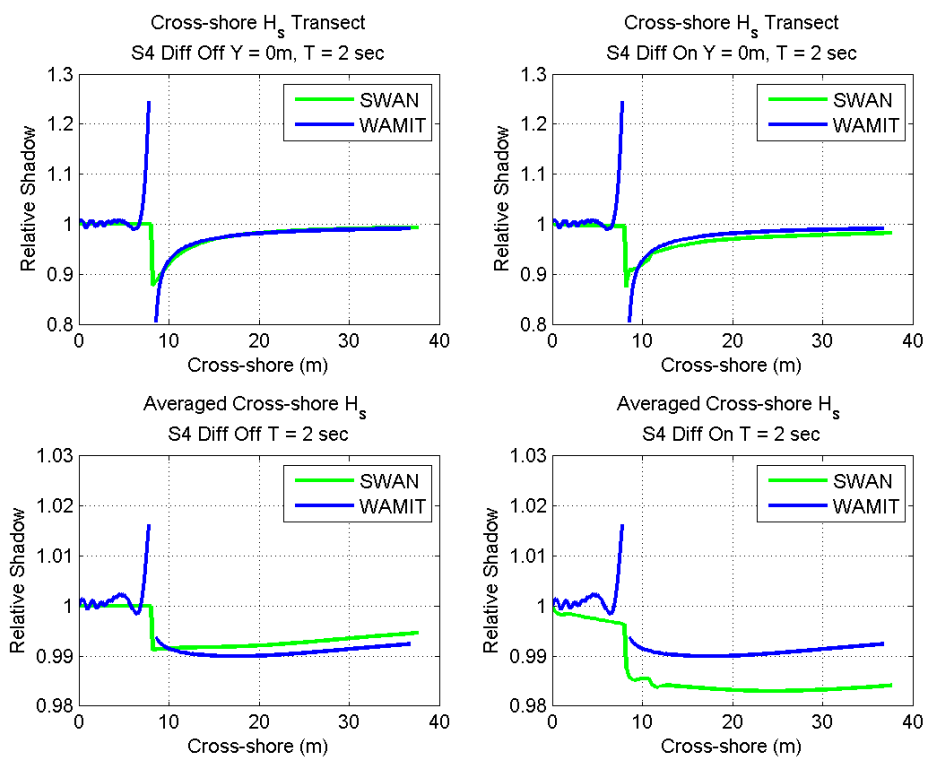


Figure 51: Wave field shadowing results from real seas simulations with a directional spreading factor of $s = 4$ with a peak period of 2.0 seconds. SWAN and WAMIT results are very similar.

10 WAMIT/SWAN Conclusions

The WAMIT to SWAN comparison proved very useful in taking a look at the physics SWAN can and cannot capture, and helps to understand exactly what is going on in the model to observational data comparisons. At very short wave periods the WEC shadow is greatly influenced by patterns created by scattered waves from hydrodynamic interaction in the array, as well as shadowing due to WEC absorption. SWAN is not able to resolve the scattered short-waves, such as $T_p = 1\text{sec}$ waves; it does not perform as well in this regime as compared to higher wave periods. At the higher wave periods, such as $T_p = 2\text{sec}$, the shadow is due almost completely to absorption. We know this since the WAMIT and SWAN models match each other well and this SWAN model only models absorption.

In regular waves SWAN did not match the wave field shape of WAMIT well in any case, but SWAN is not built for regular waves so this was not surprising. Similarly, we did not expect SWAN to provide any sort of estimation of the offshore reflected wave field as seen in the WAMIT results. Reflection was not turned on in SWAN, and it cannot model standing waves due to phase differences since it is a phase-averaged model. In this portion of the thesis of interest was solely the shape and magnitude of the shadow in the *lee* of the WEC, normalized by incident conditions, which was very promising.

In unidirectional cases when diffraction was toggled on, and lateral spreading was due to this only, the shape of the SWAN shadow matched that of the WAMIT shadow well. It can be concluded that diffraction in SWAN for unidirectional seas does a good job of replicating the actual wave field for real seas simulations. In directionally spread seas when the shadow was primarily due to wave power absorption by the WEC (i.e. $T_P = 2\text{sec}$), lateral energy spreading in SWAN without the aid of artificial diffraction did a very good job of replicating the shadow in WAMIT unlike in unidirectional cases. In the field, where directional spread seas are expected, diffraction will likely not need to be included to accurately predict the wave shadow shape.

11 Discussion

The skill of the model to predict wave shadow magnitudes was dependent on wave period, but this may not be an issue for modeling full-size wave farms. Because the WEC-parameterization in the SWAN model was based on absorption (RCW), results from the model are similar to the the comparison of RCW to measured shadow magnitude. Data to model results showed the model does reasonable well in all sea states, but as was learned from the WAMIT-SWAN comparison, it performs best where frequencies containing the most energy also have minimal diffraction and radiated wave amplitudes. It is expected that WEC-arrays will be deployed in areas where the wave power resource is large, in which case the peak wave periods of the incident wave field will be relatively high since power (energy flux) is a function of group velocity, $E_F = EC_g$. Therefore the WECs will create shadows more so from higher period waves than smaller period waves, which are better modeled by absorption behavior. This was similar to the $T_P = 2\text{sec}$ case shown in the WAMIT/SWAN comparison. It is then reasonable to say that this method can be applied to future field sites with good accuracy.

The the data set has been used to validate work from two very different models, WAMIT [McNatt, 2012b] and SWAN. Observed wave used to verify these models was from unidirectional waves only, which comprise only one quarter of all real seas simulations ran. Future work from this data set should include resolving and parameterizing the directional wave spectra. Predicting the longshore structure of the shadow is a key to field application. However, the WAMIT-SWAN comparisons showed that even without directional dependence SWAN did a fair job of predicting the wave shadow for two separate directionally spread seas cases. An application of the SWAN method to field scale should give an approximate prediction of the wave expected wave shadow.

The comparison of model results to empirical data yielded good wave shadow predictions by the model, especially since it accounts for only absorption. At the longshore extent of the shadow in the lee gage array some shadowing was still evident, that is, the lee gage array did not fully resolve the shadow width. It is possible that measurements from the empirical data set did not capture the entire magnitude of the shadow. Power loss calculations could have then been under-estimated in the empirical data set, which is why power losses from the model which are based solely on absorption are so close to empirical results. The additional power losses in the empirical data however, are likely small, and do not alter the conclusions of this report. Materially, the results and conclusions presented within this report are not affected by this, but it was worth noting.

12 Conclusions

This thesis showed that the parametrization of WEC-array effects based on WEC power capture behavior does a fair job of predicting the shadow in the lee of a WEC-array, and does a better job as wave period and directional spreading increases. Experimental results showed us that the wave shadows created by WEC-arrays were frequency dependent. Power deficits in the lee were predicted with fair accuracy by the frequency dependent WEC power absorption proxy, Relative Capture Width. This allowed us to conclude that the shadows were primarily a function of absorption by the WECs. Shadow magnitudes were well predicted in the higher wave period regimes, but under-predicted in small wave periods. Wave data showed that in regular waves with a period of 1.0-1.4 seconds the under-prediction of the magnitude was on the order of twofold. Results from the WAMIT-SWAN comparison showed us that the difference between the predicted shadow and measured shadow was due to scattered short waves caused by additional hydrodynamic interactions of the WEC with the incident wave field. At wave periods higher than this (1.5 sec +), the wave shadow magnitude was predicted by absorption (RCW) fairly well in both regular waves and the real seas frequency spectra. Scaling shadow magnitude between array sizes was shown to be moderately linear. An investigation into the ability of the spectral model SWAN to predict WEC-effects on the wave-field against a phase-resolving model, WAMIT, proved extremely useful in determining scattered waves as the sources of difference between SWAN and observations. The extensive observational data set validated not only the SWAN model, but the WAMIT model as well [McNatt, 2012b]. It provided us with great insight for investigating effects of WEC arrays on the wave-field, and the subsequent modeling. Verification at lab scale of modeling WECs based on device absorption behavior is very promising for expecting reasonable predictions at field scale.

Modeling of the WEC-Array Experiments was done with SWAN for normally incident unidirectional real seas conditions and regular waves. Only unidirectional waves were considered because relative wave reductions (wave shadow) magnitude was often characterized by the power deficit between in the incident wave field and the lee gage array, and only waves with normally incident energy flux could currently be resolved. Incident wave conditions were difficult to ascertain due to WEC-array influence on the offshore gage array. The incident wave field for data analysis and model input of all array sizes was best described by the measured incident wave conditions for like trials of the single-WEC array since offshore wave heights in these cases were the least affected (smallest).

SWAN does good job of predicting the wave shadow with WEC-array parametrization based on device absorption behavior from a single device. This modeling method was shown to predict the wave shadow in real seas more consistently than in regular waves. However, in both regular waves and real seas the shadow was predicted better in higher period sea states because short wave scattering is minimal. More scattering occurs at the shorter wave

periods because the wavelength to device size ratio is maximized. Our parameterization-by-absorption method does not account for shadowing due to scattering, so the power deficit of the shadow in the model results is sometimes underestimated. As shown in the WAMIT-SWAN comparison, at very short wave periods wave scattering can be significant. This was also evident in model-data comparisons where the power deficit was under-predicted by two-fold in small period (1.0-1.4 sec) regular waves. Larger period waves have longer wavelengths, so less scattering due to the presence of the WEC occurs. In sea states where a large portion of energy is located at frequencies whose wavelength are much longer than the characteristic device length, this modeling method should do a good job of predicting the wave shadow in the lee of a WEC-array.

In addition to the the WEC-array experiments and associated modeling, the WAMIT-SWAN model comparison showed us that with diffraction on, or in directionally spread seas, SWAN is able to make good predictions of the magnitude and shape of the wave shadow in the lee of a single device, except at small wave periods. In directionally spread seas, having diffraction “on” or “off” did not make an observable difference in results. The short wave periods tested showed that SWAN underestimates the wave shadow because of increased scattered short waves. Because of these findings the WAMIT-SWAN comparison gave great insight into what roles the different wave field physics play in wave shadows, and improved our understanding of the empirical data set.

Bibliography

Alexandre, A., Stallard, T. & Stansby, P. (2009) Transformation of wave spectra across a line of wave devices. In: Proceedings of the 8th European Wave and Tidal Energy Conference, Uppsala, Sweden.

Ashton, I., Johanning, L. & Linfoot, B. (1999) Measurement of the effect of power absorption in the lee of a wave energy converter. ASME pp. 1021–1030.

Baldock, T. & Simmonds, D. (1999) Separation of incident and reflected waves over sloping bathymetry. *Coastal Engineering* 38(3):167–176.

Beels, C., Troch, P., De Visch, K., Kofoed, J. & De Backer, G. (2010) Application of the time-dependent mild-slope equations for the simulation of wave effects in the lee of a farm of wave dragon wave energy converters. *Renewable Energy* (35):1644–1661.

Booij, N., Ris, R. C. & Holthuijsen, L. H. (1999) A third generation wave model for coastal regions 1. model description and validation. *Journal of Geophysical Research* 104(C4):7649–7666.

Borgarino, B., Babarit, A. & Ferrant, P. (2012) Impact of long separating distances on the energy production of two interacting wave energy converters. *Ocean Engineering* 41:79–88.

Boyle, L., Elsaesser, B. & Folley, M., W. T. (2011) Assessment of wave basin homogeneity for wave energy converter array studies. In: Proceedings of the 9th European Wave and Tidal Energy Conference, Southampton, UK.

Budal, K. (1977) Theory for absorption of wave power by a system of interacting bodies. *Journal of Ship Research* 21(4):248–253.

Cooley, J. & Tukey, J. (1965) An algorithm for the machine calculation of complex fourier series. *Mathematics of Computation* 19:297–301.

Cruz, J., Skykes, R., Siddorn, P. & Taylor, R. (September 2009) Wave farm design: Preliminary studies on the influence of wave climate, array layout and farm control. In: Proceedings of the 8th European Wave and Tidal Energy Conference, Uppsala, Sweden.

Dean, R. G. & Dalrymple, R. (1998) Water Wave Mechanics for Engineers & Scientists (Advanced Series on Ocean Engineering-Vol2).

Elgar, S., Herbers, T. H. C. & Guza, R. T. (1994) Reflection of ocean surface gravity waves from a natural beach. *Journal of Physical Oceanography* 24:1503–1511.

Farley, F. J. M. (2011) Far-field theory of wave power capture by oscillating systems. *Philosophical Transactions of the Royal Society A: Mathematical, Physical and Engineering Sciences* 370(1959):278–287.

Folley, M. & Whittaker, T. (2011) The adequacy of phase-averaged wave models for modelling wave farms. In: Proc. Of the ASME 2011 30th International Conference on Ocean, Offshore and Arctic Engineering.

Folley, M., Babarit, A., Child, B., Forehand, D., O'Boyle, L., Silverthorne, K., Spinneken, J., Stratigaki, V. & Troch, P. (2012) A review of numerical modelling of wave energy converter arrays. In: Proc. Of the ASME 2012 31th International Conference on Ocean, Offshore and Arctic Engineering.

Goring, G. & Nikora, V. (2002) Despiking acoustic doppler velocimeters. *Journal of Hydraulic Engineering* 128:117–126.

Haller, M., Porter, A., Lenee-Bluhm, P., Rhinefrank, K., Hammagren, E., Ozkan-Haller, H. T. & Newborn, D. (2011) Laboratory observations of waves in the vicinity of WEC-arrays. In: Proceedings of the 9th European Wave and Tidal Energy Conference, Southampton, UK.

Harris, F. J. (1978) On the use of windoes for harmonic analysis with the discrete fourier transform. In: Proceedings of the IEEE 66. pp. 51–83.

Holthuijsen, L., Herman, A. & Booij, N. (2003) Phase-decoupled refraction–diffraction for spectral wave models. *Coastal Engineering* 49(4):291–305.

Komar, P. D. (1998) Beach Processes and Sedimentation. Prentince Hall.

Lenee-Bluhm, P. (2012) Personal correspondance. E-mail.

McIver, P. (1994) Some hydrodynamic aspects of arrays of wave-energy devices. *Applied Ocean Research* 16:61–69.

McNatt, C. (2012a) Personal correspondance. E-mail.

McNatt, C. (2012b) Wave field patterns generated by wave energy converters. Master's thesis, Oregon State University.

Millar, D., Smith, H. & Reeve, D. (2007) Modelling analysis of the sensitivity of shoreline change to a wave farm. *Ocean Engineering* 34(5-6):884–901.

Monk, K., Zou, Q. & Conley, D. (2011) Numerical and analytical simulations of waver interference about a single row array of wave energy converters. *Coastal Engineering* .

Mori, N., Suzuki, T. & Kakuno, S. (2007) Noise of acoustic doopler velocimeter data in bubbly flow. *Journal of Engineering Mechanics, American Society of Civil Engineers* .

Ricci, P., Saulnier, J. B. & de O. Falcão, A. F. (2007) Point-absorber arrays: configuration study off the portuguese west coast. In: Proceedings of the 7th European Wave and Tidal Energy Conference, Porto, Portugal.

Silverthorne, K. E. & Folley, M. (2011) A new numerical representation of wave energy converters in a spectral wave model. In: Proceedings of the 9th European Wave and Tidal Energy Conference. Southampton, UK.

Smith, H., Pearce, C. & Millar, D. (2012) Further analysis of change in nearshore wave climate due to an offshore wave farm: An enhanced case study for the proposed wave hub site. *Renewable Energy* 40:51–64.

Sorensen, R. (2006) Basic Coastal Engineering. Springer.

SWANTeam (2011) SWAN Users Manual. <http://www.swan.tudelft.nl>.

The SWAN Team (2011) SWAN Technical Manual. <http://www.swan.tudelft.nl>.

Troch, P., Beels, C., De Rouck, J. & De Backer, G. (2010) Wake effects behind a farm of wave energy converters for irregular long-crested and short-crested waves. *Coastal Engineering* .

Venugopal, V. & Smith, G. (2007) Wave climate investigation for an array of wave power devices. In: Proceedings of the 7th European Wave and Tidal Energy Conference, Porto, Portugal.

WAMIT (????) Wamit user guide. Website: www.wamit.com/manual.

Weller, S., Stallard, T. & Stansby, P. (2009) Experimental measurements of irregular wave interaction factors in closely spaced arrays. In: Proceedings of 8th European Wave and Tidal Energy Conference, Uppsala , Sweeden,.

APPENDIX

A. Trial Conditions

Target trial conditions for the WEC-Array Experiments are contained in this appendix. Wave conditions are organized according to array size, real or regular wave conditions, and trial purpose. Unless otherwise noted, the trials used WEC #1.

Listed in regular waves are wave period (T), wave height (H), incident angle (Theta), trial number (Trial), and test type (Test). Test type refers to whether the trial was ran in the amplitude scan tests (A) or the frequency scan tests (F).

Listed in real seas are peak period (Tp), significant wave height (Hs), sea state (SeaState), incident angle (Theta), trial number (Trial), Test type (Test), and WEC number.

1-WEC Regular Waves

T (s)	H	Theta	Trial	Test
1.0	6	0	2	A
1.0	9	0	3	A
1.2	3	0	4	A
1.2	6	0	6	A
1.2	9	0	7	A
1.4	3	0	8	A
1.4	6	0	9	A
1.4	9	0	10	A
1.4	12	0	11	A
1.4	15	0	12	A
1.6	3	0	14	A
1.6	6	0	15	A
1.6	9	0	16	A
1.8	3	0	17	A
1.8	6	0	18	A
1.8	9	0	19	A
2.0	3	0	20	A
2.0	6	0	21	A
2.0	9	0	22	A
2.0	12	0	23	A
2.0	15	0	24	A
2.2	3	0	25	A
2.2	6	0	26	A
2.2	9	0	27	A
2.4	3	0	28	A
2.4	6	0	29	A
2.4	9	0	30	A
2.6	3	0	31	A
2.6	6	0	32	A
2.6	9	0	33	A
2.6	12	0	34	A
2.6	15	0	35	A
2.8	3	0	36	A
2.8	6	0	37	A
2.8	9	0	38	A
1.0	3	0	39	A
1.0	6	0	40	A
1.0	9	0	41	A
1.2	3	0	42	A
1.2	6	0	43	A
1.2	9	0	44	A
1.4	3	0	45	A
1.4	6	0	46	A
1.4	9	0	47	A
1.4	12	0	48	A
1.4	15	0	49	A
1.6	3	0	50	A
1.6	6	0	51	A
1.6	9	0	52	A
1.8	3	0	53	A
1.8	6	0	54	A
1.8	9	0	55	A
2.0	3	0	56	A
2.0	6	0	57	A
2.0	9	0	58	A

1-WEC Regular Waves

T (s)	H	Theta	Trial	Test
2.0	12	0	59	A
2.0	15	0	60	A
2.2	3	0	61	A
2.2	6	0	62	A
2.2	9	0	63	A
2.4	3	0	64	A
2.4	6	0	65	A
2.4	9	0	66	A
2.6	3	0	67	A
2.6	6	0	68	A
2.6	9	0	69	A
2.6	12	0	70	A
2.6	15	0	71	A
2.8	3	0	72	A
2.8	6	0	74	A
2.8	9	0	75	A
0.9	6	0	2	F
1.1	6	0	3	F
1.5	6	0	5	F
1.7	6	0	6	F
1.9	6	0	7	F
2.1	6	0	9	F
2.3	6	0	10	F
2.5	6	0	11	F
2.7	6	0	12	F
0.9	6	22.5	13	F
1.1	6	22.5	14	F
1.3	6	22.5	15	F
1.5	6	22.5	16	F
1.7	6	22.5	17	F
1.9	6	22.5	18	F
2.1	6	22.5	19	F
2.3	6	22.5	20	F
2.5	6	22.5	21	F
2.7	6	22.5	22	F
1.0	6	22.5	23	F
1.2	6	22.5	24	F
1.4	6	22.5	25	F
1.6	6	22.5	26	F
1.8	6	22.5	27	F
2.0	6	22.5	28	F
2.2	6	22.5	29	F
2.4	6	22.5	30	F
2.6	6	22.5	31	F
2.8	6	22.5	32	F
0.9	6	0	33	F
1.1	6	0	34	F
1.5	6	0	36	F
1.7	6	0	37	F
1.9	6	0	38	F
2.1	6	0	39	F
2.3	6	0	40	F
2.5	6	0	41	F
2.7	6	0	42	F
0.9	6	22.5	43	F

1-WEC Regular Waves

T (s)	H	Theta	Trial	Test
1.1	6	22.5	44	F
1.3	6	22.5	45	F
1.5	6	22.5	46	F
1.7	6	22.5	47	F
1.9	6	22.5	48	F
2.1	6	22.5	49	F
2.3	6	22.5	50	F
2.5	6	22.5	51	F
2.7	6	22.5	52	F
1.0	6	22.5	53	F
1.2	6	22.5	54	F
1.4	6	22.5	55	F
1.6	6	22.5	56	F
1.8	6	22.5	57	F
2.0	6	22.5	58	F
2.2	6	22.5	59	F
2.4	6	22.5	60	F
2.6	6	22.5	61	F
2.8	6	22.5	62	F
1.0	6	0	63	F
1.0	6	0	64	F
1.2	6	0	65	F
1.4	6	0	66	F
1.6	6	0	67	F
1.8	6	0	68	F
2.0	6	0	69	F
2.2	6	0	70	F
2.4	6	0	71	F
1.0	6	0	72	F
1.2	6	0	73	F
1.4	6	0	74	F
1.6	6	0	75	F
1.8	6	0	76	F
2.0	6	0	77	F
2.2	6	0	78	F
2.4	6	0	79	F
1.2	6	0	80	F
1.0	6	0	81	F
1.4	6	0	82	F
1.6	6	0	16	A

1-WEC Real Seas

T (s)	H	SeaState	s	Theta	Trial	Test
1.22	4.54	HI	UD	22	46	Real
1.22	4.54	HI	UD	0.0	52	Real
1.22	4.54	HI	UD	22	53	Real
1.22	4.54	HI	UD	22	60	Real
1.22	4.54	HI	UD	0.0	70	Real
1.22	4.54	HI	UD	22	71	Real
1.22	4.54	HI	UD	22	72	Real
1.42	7.58	OR2	UD	0.0	7	Real
1.42	7.58	OR2	UD	22	8	Real
1.42	7.58	OR2	UD	0.0	29	Real
1.42	7.58	OR2	UD	22	30	Real
1.42	7.58	OR2	UD	22	59	Real
1.42	7.58	OR2	UD	22	63	Real
1.62	4.54	OR1	UD	0.0	4	Real
1.62	4.54	OR1	UD	22	5	Real
1.62	4.54	OR1	UD	22	25	Real
1.62	10.6	IR	UD	22	49	Real
1.62	10.6	IR	UD	0.0	50	Real
1.62	10.6	IR	UD	22	56	Real
1.62	10.6	IR	UD	0.0	57	Real
1.62	10.6	IR	UD	22	61	Real
1.62	10.6	IR	UD	22	65	Real
1.62	10.6	IR	UD	0.0	75	Real
1.62	10.6	IR	UD	22	76	Real
1.82	7.58	OR3	UD	0.0	11	Real
1.82	7.58	OR3	UD	22	12	Real
1.82	7.58	OR3	UD	0.0	33	Real
1.82	7.58	OR3	UD	22	34	Real
2.22	7.58	OR 4	UD	0.0	15	Real
2.22	7.58	OR 4	UD	22	16	Real
2.22	13.6	OR 5	UD	0.0	19	Real
2.22	13.6	OR 5	UD	22	20	Real
2.22	7.58	OR 4	UD	0.0	37	Real
2.22	7.58	OR 4	UD	22	38	Real
2.22	13.6	OR 5	UD	0.0	40	Real
2.22	13.6	OR 5	UD	22	41	Real
2.22	13.6	OR 5	UD	0.0	66	Real
2.22	13.6	OR 5	UD	22	67	Real
1.22	4.54	HI	4.0	0.0	21	Real
1.22	4.54	HI	4.0	0.0	43	Real
1.22	4.54	HI	4.0	0.0	68	Real
1.42	7.58	OR2	4.0	0.0	6	Real
1.42	7.58	OR2	4.0	0.0	27	Real

1-WEC Real Seas

T (s)	H	SeaState	s	Theta	Trial	Test
1.42	7.58	OR2	4.0	0.0	58	Real
1.42	7.58	OR2	4.0	0.0	62	Real
1.62	4.54	OR1	4.0	0.0	1	Real
1.62	4.54	OR1	4.0	0.0	22	Real
1.62	10.6	IR	4.0	0.0	47	Real
1.62	10.6	IR	4.0	0.0	54	Real
1.62	10.6	IR	4.0	0.0	64	Real
1.62	10.6	IR	4.0	0.0	73	Real
1.82	7.58	OR3	4.0	0.0	9	Real
1.82	7.58	OR3	4.0	0.0	31	Real
2.22	7.58	OR 4	4.0	0.0	13	Real
2.22	13.6	OR 5	4.0	0.0	17	Real
2.22	7.58	OR 4	4.0	0.0	35	Real
2.22	13.6	OR 5	4.0	0.0	39	Real
1.22	4.54	HI	10.0	0.0	44	Real
1.22	4.54	HI	10.0	0.0	51	Real
1.22	4.54	HI	10.0	0.0	69	Real
1.42	7.58	OR2	10.0	0.0	2	Real
1.42	7.58	OR2	10.0	0.0	28	Real
1.62	4.54	OR1	10.0	0.0	3	Real
1.62	4.54	OR1	10.0	0.0	23	Real
1.62	10.6	IR	10.0	0.0	48	Real
1.62	10.6	IR	10.0	0.0	55	Real
1.62	10.6	IR	10.0	0.0	74	Real
1.82	7.58	OR3	10.0	0.0	10	Real
1.82	7.58	OR3	10.0	0.0	32	Real
2.22	7.58	OR 4	10.0	0.0	14	Real
2.22	13.6	OR 5	10.0	0.0	18	Real
2.22	7.58	OR 4	10.0	0.0	36	Real
1.22	4.54	HI	UD	0.0	45	Real

3-WEC Regular Waves

T (s)	H	Theta	Trial	Test
1.0	6	0	1	A
1.0	9	0	2	A
1.2	6	0	3	A
1.2	9	0	4	A
1.2	12	0	5	A
1.3	6	0	6	A
1.3	9	0	7	A
1.3	12	0	8	A
1.3	15	0	9	A
1.4	6	0	10	A
1.4	9	0	11	A
1.4	12	0	12	A
1.4	15	0	13	A
1.6	6	0	14	A
1.6	9	0	15	A
1.6	12	0	16	A
1.6	15	0	17	A
2.0	6	0	18	A
2.0	9	0	19	A
2.0	12	0	20	A
2.0	15	0	21	A
2.6	6	0	22	A
2.6	9	0	23	A
2.6	12	0	24	A
2.6	15	0	25	A
1.0	6	0	26	A
1.0	9	0	27	A
1.2	6	0	28	A
1.2	9	0	29	A
1.2	12	0	30	A
1.3	6	0	31	A
1.3	9	0	32	A
1.3	12	0	33	A
1.3	15	0	34	A
1.4	6	0	35	A
1.4	9	0	36	A
1.4	12	0	37	A
1.4	15	0	38	A
1.6	6	0	39	A
1.6	9	0	40	A
1.6	12	0	41	A
1.6	15	0	42	A
2.0	6	0	43	A
2.0	9	0	44	A

3-WEC Regular Waves

T (s)	H	Theta	Trial	Test
2.0	12	0	45	A
2.0	15	0	46	A
2.6	6	0	47	A
2.6	9	0	48	A
2.6	12	0	49	A
2.6	15	0	50	A
1.2	12	0	51	A
0.9	6	0	1	F
1.1	6	0	2	F
1.5	6	0	3	F
1.7	6	0	4	F
1.9	6	0	5	F
2.1	6	0	6	F
2.3	6	0	7	F
2.5	6	0	8	F
2.7	6	0	9	F
0.9	6	0	34	F
1.1	6	0	35	F
1.5	6	0	36	F
1.7	6	0	37	F
1.9	6	0	39	F
2.1	6	0	38	F
2.3	6	0	40	F
2.5	6	0	41	F
2.7	6	0	42	F
0.9	6	22.5	10	F
1.1	6	22.5	11	F
1.3	6	22.5	12	F
1.5	6	22.5	13	F
1.7	6	22.5	14	F
1.9	6	22.5	15	F
2.1	6	22.5	16	F
2.3	6	22.5	17	F
2.5	6	22.5	18	F
2.7	6	22.5	19	F
1.0	6	22.5	20	F
1.2	6	22.5	21	F
1.2	6	22.5	22	F
1.4	6	22.5	23	F
1.4	6	22.5	25	F
1.6	6	22.5	24	F
1.8	6	22.5	27	F
2.0	6	22.5	28	F
2.2	6	22.5	29	F

3-WEC Regular Waves

T (s)	H	Theta	Trial	Test
2.4	6	22.5	30	F
2.6	6	22.5	31	F
2.6	6	22.5	32	F
2.8	6	22.5	33	F
0.9	6	22.5	43	F
1.1	6	22.5	44	F
1.3	6	22.5	45	F
1.5	6	22.5	46	F
1.7	6	22.5	47	F
1.9	6	22.5	48	F
2.1	6	22.5	49	F
2.3	6	22.5	50	F
2.5	6	22.5	51	F
2.7	6	22.5	52	F
1.0	6	22.5	53	F
1.2	6	22.5	54	F
1.4	6	22.5	55	F
1.6	6	22.5	26	F
1.8	6	22.5	56	F
2.0	6	22.5	57	F
2.2	6	22.5	58	F
2.4	6	22.5	59	F
2.6	6	22.5	60	F
2.8	6	22.5	61	F
1.5	6	22.5	62	F

3-WEC Real Seas

Tp (s)	Hs (cm)	SeaState	s	Theta	Trial	Test
1.62	4.54	OR1	2	0.00	1	Real
1.62	4.54	OR1	4	0.00	2	Real
1.62	4.54	OR1	10	0.00	3	Real
1.62	4.54	OR1	0	0.00	4	Real
1.62	4.54	OR1	0	22.5	5	Real
1.42	7.58	OR2	2	0.00	6	Real
1.42	7.58	OR2	4	0.00	7	Real
1.42	7.58	OR2	10	0.00	8	Real
1.42	7.58	OR2	0	0.00	9	Real
1.42	7.58	OR2	0	22.5	10	Real
1.82	7.58	OR3	2	0.00	11	Real
1.82	7.58	OR3	4	0.00	12	Real
1.82	7.58	OR3	10	0.00	13	Real
1.82	7.58	OR3	0	0.00	14	Real
1.82	7.58	OR3	0	22.5	15	Real
2.22	7.58	OR4	2	0.00	16	Real
2.22	7.58	OR4	4	0.00	17	Real
2.22	7.58	OR4	10	0.00	18	Real
2.22	7.58	OR4	0	0.00	19	Real
2.22	7.58	OR4	0	22.5	20	Real
2.22	13.6	OR5	2	0.00	21	Real
2.22	13.6	OR5	4	0.00	22	Real
2.22	13.6	OR5	10	0.00	23	Real
2.22	13.6	OR5	0	0.00	24	Real
2.22	13.6	OR5	0	22.5	25	Real
1.22	4.54	HI	2	0.00	26	Real
1.22	4.54	HI	4	0.00	27	Real
1.22	4.54	HI	10	0.00	28	Real
1.22	4.54	HI	0	0.00	29	Real
1.22	4.54	HI	0	22.5	30	Real
1.62	10.6	IR	2	0.00	31	Real
1.62	10.6	IR	4	0.00	32	Real
1.62	10.6	IR	10	0.00	33	Real
1.62	10.6	IR	0	0.00	34	Real
1.62	10.6	IR	0	22.5	35	Real
1.62	4.54	OR1	2	0.00	36	Real
1.62	4.54	OR1	4	0.00	37	Real
1.62	4.54	OR1	10	0.00	38	Real
1.62	4.54	OR1	0	0.00	39	Real
1.62	4.54	OR1	0	22.5	40	Real
1.42	7.58	OR2	2	0.00	41	Real
1.42	7.58	OR2	4	0.00	42	Real
1.42	7.58	OR2	10	0.00	43	Real
1.42	7.58	OR2	0	0.00	44	Real

3-WEC Real Seas

Tp (s)	Hs (cm)	SeaState	s	Theta	Trial	Test
1.42	7.58	OR2	0	22.5	45	Real
1.82	7.58	OR3	2	0.00	46	Real
1.82	7.58	OR3	4	0.00	47	Real
1.82	7.58	OR3	10	0.00	48	Real
1.82	7.58	OR3	0	0.00	49	Real
1.82	7.58	OR3	0	22.5	50	Real
2.22	7.58	OR4	2	0.00	51	Real
2.22	7.58	OR4	4	0.00	52	Real
2.22	7.58	OR4	10	0.00	53	Real
2.22	7.58	OR4	0	0.00	54	Real
2.22	7.58	OR4	0	22.5	55	Real
2.22	13.6	OR5	2	0.00	56	Real
2.22	13.6	OR5	4	0.00	57	Real
2.22	13.6	OR5	10	0.00	58	Real
2.22	13.6	OR5	0	0.00	59	Real
2.22	13.6	OR5	0	22.5	60	Real
1.22	4.54	HI	2	0.00	61	Real
1.22	4.54	HI	4	0.00	62	Real
1.22	4.54	HI	10	0.00	63	Real
1.22	4.54	HI	0	0.00	64	Real
1.22	4.54	HI	0	22.5	65	Real
1.62	10.6	IR	2	0.00	66	Real
1.62	10.6	IR	4	0.00	67	Real
1.62	10.6	IR	10	0.00	68	Real
1.62	10.6	IR	0	0.00	69	Real
1.62	10.6	IR	0	22.5	70	Real

5-WEC Regular Waves

T (s)	H	Theta	Trial	Test
1	6	0	1	A
1	9	0	2	A
1.2	6	0	3	A
1.2	9	0	4	A
1.2	12	0	5	A
1.3	6	0	6	A
1.3	9	0	7	A
1.3	12	0	8	A
1.3	15	0	9	A
1.4	6	0	10	A
1.4	9	0	11	A
1.4	12	0	12	A
1.4	15	0	13	A
1.6	6	0	14	A
1.6	9	0	15	A
1.6	12	0	16	A
1.6	15	0	17	A
2	6	0	18	A
2	9	0	19	A
2	12	0	20	A
2	15	0	21	A
2.6	6	0	22	A
2.6	9	0	23	A
2.6	12	0	24	A
2.6	15	0	25	A
2.6	15	0	26	A
1	6	0	27	A
1	9	0	28	A
1.2	6	0	29	A
1.2	9	0	30	A
1.2	12	0	31	A
1.3	6	0	32	A
1.3	9	0	33	A
1.3	12	0	34	A
1.3	15	0	35	A
1.4	6	0	36	A
1.4	9	0	37	A
1.4	12	0	38	A
1.4	15	0	39	A
1.6	6	0	40	A
1.6	9	0	41	A
1.6	12	0	42	A
1.6	15	0	43	A
2	6	0	44	A

5-WEC Regular Waves

T (s)	H	Theta	Trial	Test
2	9	0	45	A
2	12	0	46	A
2	12	0	47	A
2	12	0	48	A
2	15	0	49	A
2.6	6	0	50	A
2.6	9	0	51	A
2.6	12	0	52	A
2.6	15	0	53	A
0.9	6	0	1	F
1.1	6	0	2	F
1.5	6	0	3	F
1.7	6	0	4	F
1.9	6	0	5	F
2.1	6	0	6	F
2.3	6	0	7	F
2.5	6	0	8	F
2.7	6	0	9	F
0.9	6	0	25	F
1.1	6	0	26	F
1.5	6	0	27	F
1.7	6	0	28	F
1.9	6	0	29	F
2.1	6	0	30	F
2.3	6	0	31	F
2.5	6	0	32	F
2.7	6	0	33	F
0.9	6	22.5	10	F
1.1	6	22.5	11	F
1.3	6	22.5	12	F
1.5	6	22.5	13	F
1.7	6	22.5	14	F
1.9	6	22.5	15	F
2.1	6	22.5	16	F
2.3	6	22.5	17	F
2.5	6	22.5	18	F
2.7	6	22.5	19	F
1.0	6	22.5	51	F
1.2	6	22.5	52	F
1.4	6	22.5	20	F
1.6	6	22.5	21	F
1.8	6	22.5	22	F
2.0	6	22.5	23	F
2.2	6	22.5	24	F

5-WEC Regular Waves

T (s)	H	Theta	Trial	Test
2.4	6	22.5	53	F
2.6	6	22.5	54	F
2.8	6	22.5	55	F
0.9	6	22.5	34	F
1.1	6	22.5	35	F
1.3	6	22.5	36	F
1.5	6	22.5	37	F
1.7	6	22.5	38	F
1.9	6	22.5	39	F
2.1	6	22.5	40	F
2.3	6	22.5	41	F
2.5	6	22.5	42	F
2.7	6	22.5	43	F
1.4	6	22.5	44	F
1.6	6	22.5	45	F
1.8	6	22.5	46	F
2	6	22.5	47	F
2.2	6	22.5	48	F
2.2	6	22.5	50	F

5-WEC Real Seas

Tp (s)	Hs (cm)	SeaState	s	Theta	Trial	Test
1.62	4.54	OR1	4	0.00	50	Real
1.62	4.54	OR1	10	0.00	2	Real
1.62	4.54	OR1	0	0.00	3	Real
1.62	4.54	OR1	0	22.5	4	Real
1.62	4.54	OR1	4	0.00	54	Real
1.62	4.54	OR1	10	0.00	23	Real
1.62	4.54	OR1	10	0.00	24	Real
1.62	4.54	OR1	0	0.00	25	Real
1.62	4.54	OR1	0	22.5	26	Real
1.42	7.58	OR2	4	0.00	47	Real
1.42	7.58	OR2	10	0.00	5	Real
1.42	7.58	OR2	0	0.00	6	Real
1.42	7.58	OR2	0	22.5	7	Real
1.42	7.58	OR2	10	0.00	27	Real
1.42	7.58	OR2	0	0.00	28	Real
1.42	7.58	OR2	0	22.5	29	Real
1.82	7.58	OR3	2	0.00	8	Real
1.82	7.58	OR3	4	0.00	9	Real
1.82	7.58	OR3	10	0.00	1	Real
1.82	7.58	OR3	0	0.00	10	Real
1.82	7.58	OR3	0	22.5	11	Real
1.82	7.58	OR3	2	0.00	30	Real
1.82	7.58	OR3	4	0.00	31	Real
1.82	7.58	OR3	10	0.00	32	Real
1.82	7.58	OR3	0	0.00	33	Real
1.82	7.58	OR3	0	22.5	34	Real
2.22	7.58	OR4	2	0.00	59	Real
2.22	7.58	OR4	4	0.00	48	Real
2.22	7.58	OR4	10	0.00	12	Real
2.22	7.58	OR4	0	0.00	13	Real
2.22	7.58	OR4	0	22.5	14	Real
2.22	7.58	OR4	4	0.00	56	Real
2.22	7.58	OR4	10	0.00	35	Real
2.22	7.58	OR4	0	0.00	36	Real
2.22	7.58	OR4	0	22.5	37	Real
2.22	13.6	OR5	0	0.00	38	Real
2.22	13.6	OR5	0	22.5	39	Real
2.22	13.6	OR5	0	0.00	15	Real
2.22	13.6	OR5	0	22.5	16	Real
1.22	4.54	HI	2	0.00	51	Real
1.22	4.54	HI	4	0.00	49	Real
1.22	4.54	HI	10	0.00	17	Real
1.22	4.54	HI	0	0.00	18	Real
1.22	4.54	HI	0	22.5	19	Real

5-WEC Real Seas

Tp (s)	Hs (cm)	SeaState	s	Theta	Trial	Test
1.22	4.54	HI	2	0.00	57	Real
1.22	4.54	HI	4	0.00	58	Real
1.22	4.54	HI	10	0.00	40	Real
1.22	4.54	HI	10	0.00	41	Real
1.22	4.54	HI	0	0.00	42	Real
1.22	4.54	HI	0	22.5	43	Real
1.62	10.6	IR	2	0.00	52	Real
1.62	10.6	IR	4	0.00	60	Real
1.62	10.6	IR	10	0.00	20	Real
1.62	10.6	IR	0	0.00	21	Real
1.62	10.6	IR	0	22.5	22	Real
1.62	10.6	IR	2	0.00	53	Real
1.62	10.6	IR	10	0.00	44	Real
1.62	10.6	IR	0	0.00	45	Real
1.62	10.6	IR	0	22.5	46	Real

Single-Buoy Characterization Regular Waves

T (s)	H	Theta	Trial	Test	WEC #
1.4	6	0	2	Normal	2
1.6	6	0	3	Normal	2
1.2	9	0	4	Normal	2
1.4	9	0	5	Normal	2
1.6	9	0	6	Normal	2
1.4	6	0	8	Normal	2
1.6	6	0	9	Normal	2
1.2	9	0	10	Normal	2
1.4	9	0	11	Normal	2
1.6	9	0	12	Normal	2
1.2	6	0	13	Normal	3
1.4	6	0	14	Normal	3
1.6	6	0	15	Normal	3
1.2	9	0	16	Normal	3
1.4	9	0	17	Normal	3
1.6	9	0	18	Normal	3
1.2	6	0	19	Normal	3
1.4	6	0	20	Normal	3
1.6	6	0	21	Normal	3
1.2	9	0	22	Normal	3
1.4	9	0	23	Normal	3
1.6	9	0	24	Normal	3
1.2	6	0	25	Normal	4
1.4	6	0	26	Normal	4
1.6	6	0	27	Normal	4
1.2	6	0	28	Normal	4
1.4	6	0	29	Normal	4
1.6	6	0	30	Normal	4
1.3	6	0	31	Normal	4
1.5	6	0	32	Normal	4
1.7	6	0	33	Normal	4
1.8	6	0	34	Normal	4
1.9	6	0	35	Normal	4
2	6	0	36	Normal	4
2.1	6	0	37	Normal	4
2.1	6	0	38	Normal	4
2.2	6	0	39	Normal	4
2.3	6	0	40	Normal	4
1.2	9	0	41	Normal	3
1.3	6	0	42	Normal	4
1.5	6	0	43	Normal	4
1.7	6	0	44	Normal	4

Single-Buoy Characterization Regular Waves

T (s)	H	Theta	Trial	Test	WEC #
1.8	6	0	45	Normal	4
1.9	6	0	46	Normal	4
2	6	0	47	Normal	4
2.1	6	0	48	Normal	4
2.1	6	0	48	Normal	4
2.2	6	0	49	Normal	4
2.3	6	0	50	Normal	4
1.3	6	0	51	Normal	3
1.5	6	0	52	Normal	3
1.7	6	0	53	Normal	3
1.8	6	0	54	Normal	3
1.9	6	0	55	Normal	3
2	6	0	56	Normal	3
2.1	6	0	57	Normal	3
2.2	6	0	58	Normal	3
2.3	6	0	59	Normal	3
1.3	6	0	60	Normal	3
1.5	6	0	61	Normal	3
1.7	6	0	62	Normal	3
1.8	6	0	63	Normal	3
1.9	6	0	64	Normal	3
2	6	0	65	Normal	3
2.1	6	0	66	Normal	3
2.2	6	0	67	Normal	3
2.3	6	0	68	Normal	3
1.2	6	0	69	Normal	5
1.3	6	0	70	Normal	5
1.4	6	0	71	Normal	5
1.5	6	0	72	Normal	5
1.6	6	0	73	Normal	5
1.7	6	0	74	Normal	5
1.8	6	0	75	Normal	5
1.9	6	0	76	Normal	5
2	6	0	77	Normal	5
2.1	6	0	78	Normal	5
2.2	6	0	79	Normal	5
2.3	6	0	80	Normal	5
1.3	6	0	81	Normal	5
1.5	6	0	82	Normal	5
1.7	6	0	83	Normal	5
1.9	6	0	84	Normal	5
2.1	6	0	85	Normal	5

Single-Buoy Characterization Regular Waves

T (s)	H	Theta	Trial	Test	WEC #
2.3	6	0	86	Normal	5
1.3	6	0	87	Normal	5
1.4	6	0	88	Normal	5
1.5	6	0	89	Normal	5
1.3	6	0	91	Normal	2
1.5	6	0	92	Normal	2
1.7	6	0	93	Normal	2
1.8	6	0	94	Normal	2
1.9	6	0	95	Normal	2
2	6	0	96	Normal	2
2.1	6	0	97	Normal	2
2.2	6	0	98	Normal	2
2.3	6	0	99	Normal	2
1.3	6	0	100	Normal	2
1.5	6	0	101	Normal	2
1.7	6	0	102	Normal	2
1.8	6	0	103	Normal	2
1.9	6	0	104	Normal	2
2	6	0	105	Normal	2
2	6	0	106	Normal	2
2.1	6	0	107	Normal	2
2.2	6	0	108	Normal	2
2.3	6	0	109	Normal	2
1.2	6	0	110	Normal	5
1.3	6	0	111	Normal	5
1.4	6	0	112	Normal	5
1.5	6	0	113	Normal	5
1.6	6	0	114	Normal	5
1.7	6	0	115	Normal	5
1.8	6	0	116	Normal	5
1.9	6	0	117	Normal	5
2	6	0	118	Normal	5
2.1	6	0	119	Normal	5
2.2	6	0	120	Normal	5
2.3	6	0	121	Normal	5
1.2	6	0	122	Normal	5
1.3	6	0	123	Normal	5
1.4	6	0	124	Normal	5
1.5	6	0	125	Normal	5
1.6	6	0	126	Normal	5
1.7	6	0	127	Normal	5
1.8	6	0	128	Normal	5

Single-Buoy Characterization Regular Waves

T (s)	H	Theta	Trial	Test	WEC #
1.9	6	0	129	Normal	5
2	6	0	130	Normal	5
2.1	6	0	131	Normal	5
2.2	6	0	132	Normal	5
2.3	6	0	133	Normal	5
0.9	6	0	134	Normal	2
1	6	0	135	Normal	2
1.1	6	0	136	Normal	2
2.4	6	0	137	Normal	2
2.6	6	0	138	Normal	2
0.9	6	0	139	Normal	2
0.9	6	0	140	Normal	2
1	6	0	141	Normal	2
1.1	6	0	142	Normal	2
2.4	6	0	143	Normal	2
2.6	6	0	144	Normal	2
2.6	6	0	145	Normal	2
0.9	6	0	146	Normal	3
1	6	0	147	Normal	3
1.1	6	0	148	Normal	3
2.4	6	0	149	Normal	3
2.6	6	0	150	Normal	3
0.9	6	0	151	Normal	3
1	6	0	152	Normal	3
1.1	6	0	153	Normal	3
2.4	6	0	154	Normal	3
2.6	6	0	155	Normal	3
1.2	6	0	156	Normal	4
1.3	6	0	157	Normal	4
1.4	6	0	158	Normal	4
1.5	6	0	159	Normal	4
1.6	6	0	160	Normal	4
1.7	6	0	161	Normal	4
1.8	6	0	162	Normal	4
2	6	0	163	Normal	4
2.2	6	0	164	Normal	4
0.9	6	0	165	Normal	4
1	6	0	166	Normal	4
1.1	6	0	167	Normal	4
2.1	6	0	168	Normal	4
2.6	6	0	169	Normal	4
1.2	6	0	170	Normal	4

Single-Buoy Characterization Regular Waves

T (s)	H	Theta	Trial	Test	WEC #
1.3	6	0	171	Normal	4
1.4	6	0	172	Normal	4
1.5	6	0	173	Normal	4
1.6	6	0	174	Normal	4
1.7	6	0	175	Normal	4
1.8	6	0	176	Normal	4
2	6	0	177	Normal	4
2.2	6	0	178	Normal	4
0.9	6	0	179	Normal	4
1	6	0	180	Normal	4
1.1	6	0	181	Normal	4
2.1	6	0	182	Normal	4
2.6	6	0	183	Normal	4
0.9	6	0	184	Normal	5
1	6	0	185	Normal	5
1.1	6	0	187	Normal	5
2.4	6	0	188	Normal	5
2.6	6	0	189	Normal	5
0.9	6	0	190	Normal	5
1	6	0	191	Normal	5
1.1	6	0	192	Normal	5
2.4	6	0	193	Normal	5
2.6	6	0	194	Normal	5
1	6	22.5	1	Off-Angle	2
1.1	6	22.5	2	Off-Angle	2
1.2	6	22.5	3	Off-Angle	2
1.3	6	22.5	4	Off-Angle	2
1.4	6	22.5	5	Off-Angle	2
1.5	6	22.5	6	Off-Angle	2
1.6	6	22.5	7	Off-Angle	2
1.7	6	22.5	8	Off-Angle	2
1.8	6	22.5	9	Off-Angle	2
1.9	6	22.5	10	Off-Angle	2
2	6	22.5	11	Off-Angle	2
2.1	6	22.5	12	Off-Angle	2
2.3	6	22.5	13	Off-Angle	2
2.5	6	22.5	14	Off-Angle	2
1	6	22.5	15	Off-Angle	2
1.1	6	22.5	16	Off-Angle	2
1.2	6	22.5	17	Off-Angle	2
1.3	6	22.5	18	Off-Angle	2
1.4	6	22.5	19	Off-Angle	2

Single-Buoy Characterization Regular Waves

T (s)	H	Theta	Trial	Test	WEC #
1.5	6	22.5	20	Off-Angle	2
1.6	6	22.5	21	Off-Angle	2
1.7	6	22.5	22	Off-Angle	2
1.8	6	22.5	23	Off-Angle	2
1.9	6	22.5	26	Off-Angle	2
2	6	22.5	27	Off-Angle	2
2.1	6	22.5	28	Off-Angle	2
2.3	6	22.5	29	Off-Angle	2
2.5	6	22.5	30	Off-Angle	2
1.0	6	22.5	31	Off-Angle	3
1.1	6	22.5	32	Off-Angle	3
1.2	6	22.5	33	Off-Angle	3
1.3	6	22.5	34	Off-Angle	3
1.4	6	22.5	35	Off-Angle	3
1.5	6	22.5	36	Off-Angle	3
1.6	6	22.5	37	Off-Angle	3
1.7	6	22.5	38	Off-Angle	3
1.8	6	22.5	39	Off-Angle	3
1.9	6	22.5	40	Off-Angle	3
2.0	6	22.5	41	Off-Angle	3
2.1	6	22.5	42	Off-Angle	3
2.2	6	22.5	43	Off-Angle	3
2.3	6	22.5	44	Off-Angle	3
1.0	6	22.5	45	Off-Angle	3
1.1	6	22.5	46	Off-Angle	3
1.2	6	22.5	47	Off-Angle	3
1.3	6	22.5	48	Off-Angle	3
1.4	6	22.5	50	Off-Angle	3
1.5	6	22.5	51	Off-Angle	3
1.6	6	22.5	52	Off-Angle	3
1.7	6	22.5	53	Off-Angle	3
1.8	6	22.5	54	Off-Angle	3
1.9	6	22.5	55	Off-Angle	3
2.0	6	22.5	56	Off-Angle	3
2.1	6	22.5	57	Off-Angle	3
2.2	6	22.5	58	Off-Angle	3
2.3	6	22.5	59	Off-Angle	3
1	6	22.5	60	Off-Angle	4
1.1	6	22.5	61	Off-Angle	4
1.2	6	22.5	62	Off-Angle	4
1.3	6	22.5	63	Off-Angle	4
1.4	6	22.5	64	Off-Angle	4

Single-Buoy Characterization Regular Waves

T (s)	H	Theta	Trial	Test	WEC #
1.5	6	22.5	65	Off-Angle	4
1.6	6	22.5	66	Off-Angle	4
1.7	6	22.5	67	Off-Angle	4
1.8	6	22.5	68	Off-Angle	4
1.9	6	22.5	69	Off-Angle	4
2	6	22.5	70	Off-Angle	4
2.1	6	22.5	71	Off-Angle	4
2.3	6	22.5	72	Off-Angle	4
2.5	6	22.5	73	Off-Angle	4
1	6	22.5	74	Off-Angle	4
1.1	6	22.5	75	Off-Angle	4
1.2	6	22.5	76	Off-Angle	4
1.3	6	22.5	77	Off-Angle	4
1.4	6	22.5	78	Off-Angle	4
1.5	6	22.5	79	Off-Angle	4
1.6	6	22.5	80	Off-Angle	4
1.7	6	22.5	81	Off-Angle	4
1.8	6	22.5	82	Off-Angle	4
1.9	6	22.5	83	Off-Angle	4
2	6	22.5	84	Off-Angle	4
2.1	6	22.5	85	Off-Angle	4
2.3	6	22.5	86	Off-Angle	4
2.5	6	22.5	87	Off-Angle	4
1.0	6	22.5	88	Off-Angle	5
1.1	6	22.5	89	Off-Angle	5
1.2	6	22.5	90	Off-Angle	5
1.3	6	22.5	91	Off-Angle	5
1.4	6	22.5	92	Off-Angle	5
1.5	6	22.5	93	Off-Angle	5
1.6	6	22.5	94	Off-Angle	5
1.7	6	22.5	95	Off-Angle	5
1.8	6	22.5	96	Off-Angle	5
1.9	6	22.5	97	Off-Angle	5
2.0	6	22.5	98	Off-Angle	5
2.1	6	22.5	99	Off-Angle	5
2.2	6	22.5	100	Off-Angle	5
2.3	6	22.5	101	Off-Angle	5
1.0	6	22.5	102	Off-Angle	5
1.1	6	22.5	103	Off-Angle	5
1.2	6	22.5	104	Off-Angle	5
1.3	6	22.5	105	Off-Angle	5
1.4	6	22.5	106	Off-Angle	5

Single-Buoy Characterization Regular Waves

T (s)	H	Theta	Trial	Test	WEC #
1.5	6	22.5	107	Off-Angle	5
1.6	6	22.5	108	Off-Angle	5
1.7	6	22.5	109	Off-Angle	5
1.8	6	22.5	110	Off-Angle	5
1.9	6	22.5	111	Off-Angle	5
2.0	6	22.5	112	Off-Angle	5
2.1	6	22.5	113	Off-Angle	5
2.2	6	22.5	114	Off-Angle	5
2.3	6	22.5	115	Off-Angle	5

Single-Buoy Characterization Real Seas

Tp (s)	Hs (cm)	SeaState	s	Theta	Trial	Test	WEC #
1.82	7.58	OR3	UD	0.00	1	Real	5
1.62	10.6	IR	UD	0.00	2	Real	5
1.62	4.54	OR1	UD	0.00	3	Real	5
1.82	7.58	OR3	UD	0.00	4	Real	5
1.62	10.6	IR	UD	0.00	5	Real	5
1.62	4.54	OR1	UD	0.0	6	Real	5
1.62	4.54	OR1	10	0.00	7	Real	3
1.62	4.54	OR1	10	0.00	8	Real	3
1.62	4.54	OR1	UD	0.00	9	Real	3
1.62	4.54	OR1	UD	22.5	10	Real	3
1.82	7.58	OR3	10	0.00	11	Real	3
1.82	7.58	OR3	UD	0.00	12	Real	3
1.82	7.58	OR3	UD	22.5	13	Real	3
1.62	10.6	IR	10	0.00	14	Real	3
1.62	10.6	IR	UD	0.00	15	Real	3
1.62	4.54	OR1	10	0.00	17	Real	3
1.62	4.54	OR1	UD	0.00	18	Real	3
1.62	4.54	OR1	UD	22.5	19	Real	3
1.82	7.58	OR3	10	0.00	20	Real	3
1.82	7.58	OR3	UD	0.00	22	Real	3
1.82	7.58	OR3	UD	22.5	23	Real	3
1.62	10.6	IR	10	0.00	24	Real	3
1.62	10.6	IR	UD	0.00	25	Real	3
1.62	10.6	IR	UD	22.5	26	Real	3
1.62	4.54	OR1	10	0.0	27	Real	5
1.62	4.54	OR1	UD	22.5	28	Real	5
1.82	7.58	OR3	10	0.00	29	Real	5
1.82	7.58	OR3	UD	22.5	30	Real	5
1.62	10.6	IR	10	0.00	31	Real	5
1.62	10.6	IR	10	0.00	32	Real	5
1.62	10.6	IR	UD	22.5	33	Real	5
1.62	4.54	OR1	10	0.00	34	Real	5
1.62	4.54	OR1	UD	22.5	35	Real	5
1.82	7.58	OR3	10	0.00	36	Real	5
1.82	7.58	OR3	UD	22.5	37	Real	5
1.62	10.6	IR	10	0.00	38	Real	5
1.62	10.6	IR	UD	22.5	39	Real	5

AN ABSTRACT OF THE THESIS OF

J. Cameron McNatt for the degree of Master of Ocean Engineering in Civil Engineering presented on August 1, 2012

Title: Wave Field Patterns Generated by Wave Energy Converters

Abstract approved:

H. Tuba Özkan-Haller

The eventual deployment of wave energy converters (WECs) on a commercial scale will necessitate the grouping of devices into arrays or “wave farms,” in order to minimize overhead costs of mooring, maintenance, installation, and electrical cabling for shoreward power delivery. Closely spaced WECs will interact hydrodynamically through diffracted and radiated waves. Recent research has focused on the WEC wave field and used its structures to design constructive WEC arrays as well as to describe the means of WEC energy absorption. In this study, the WEC wave field is investigated for a single WEC and a five WEC array with linear wave theory and experimental results. Both regular waves and spectral seas are considered. Computational results are produced with the linear boundary-element-method (BEM) hydrodynamic software WAMIT for a simple WEC geometry. Experimental data comes from WEC array tests that took place at Oregon State University over the winter of 2010-11 [1]. The experimental measurements help validate the computational modeling, and the computational models serve as an aid to interpreting the experimental data.

Results reveal two universal WEC wave field features - partially standing waves and a wave shadow, both of which are the result of the coherent interaction of the planar incident wave with the circular generated wave, composed of the diffracted and radiated waves. The partial standing waves in the offshore are seen qualitatively in experimental data but could not be exactly reproduced computationally, because the computational model is only a simple representation of the physical model. In the lee of the WEC, the measured longshore structure of the wave shadow is in good agreement with theoretical expectations as well as computational results. It is believed that the agreement is

because the formation of the wave shadow is dominated by energy extraction, which was approximately the same for both the computational and physical models.

A study of the linear WEC wave field in regular waves and spectral seas reveals patterns such as the wave shadow that have also been found in experimental data. The positions and magnitudes of the offshore partially standing waves are very sensitive to wavelength, and WEC geometry, motions and location, and in spectral seas, they are smoothed when considering significant wave height. All of which suggest that it may be difficult to use them advantageously in the design of WEC arrays. The wave shadow is a dominant feature of the WEC wave field for both regular waves and spectral seas. It appears to be fairly generic and to be based on power absorption. In the design of WEC arrays, rather than attempting constructive interference by using standing wave crests, perhaps the best one can do is to avoid destructive interference of the wave shadow.

© Copyright by J. Cameron McNatt

August 1, 2012

All Rights Reserved

Wave Field Patterns Generated by Wave Energy Converters

by

J. Cameron McNatt

A THESIS

submitted to

Oregon State University

in partial fulfillment of

the requirements for the

degree of

Master of Ocean Engineering

Presented August 1, 2012

Commencement June 2013

Master of Ocean Engineering thesis of J. Cameron McNatt presented on
August 1, 2012

APPROVED:

Major Professor, representing Civil Engineering

Head of the School of Civil and Construction Engineering

Dean of the Graduate School

I understand that my thesis will become part of the permanent collection of Oregon State University libraries. My signature below authorizes release of my thesis to any reader upon request.

J. Cameron McNatt, Author

ACKNOWLEDGMENTS

This research was partially funded by the U.S. Department of Energy (DE-EE0002658), Sandia National Labs, and Columbia Power Technologies under Research Subagreement NO. 2010-1698, additional support came from Oregon Wave Energy Trust through Award Number OIC-0911-109. A portion of the thesis is based upon work enabled by the National Northwest Marine Renewable Energy Center and the U.S. Department of Energy under Award Number DE-FG36-08GO18179.

Throughout the course of this project I had a great amount of assistance and support. The experimental data analysis and organization was performed by Aaron Porter. This, I know, was no small task. All I had to do was put the numbers in a plot. Aaron also conducted all of the SWAN runs. Using one computational model is hard enough, I am glad I did not have to learn two. Aaron, I could not have done it without you.

Mick Haller, Pukha Lenee-Bluhm, and Aaron suffered through numerous overtime meetings, discussing our results and planning our next moves. It was always rewarding to share the ideas and work in which I had been engrossed in the weeks previous and extremely helpful to get outside feedback. The discussions we had were impassioned and thought-provoking. The meetings served as regular check points in our progress towards a final product. Thank you all for your considerate attention, observations, and guidance.

I would like to thank Tuba Özkan-Haller, my advisor. Not only during this project, but throughout my graduate studies at Oregon State, she has been so supportive, encouraging, and interested in my endeavors. She gave me the freedom and provided the projects and tools that enabled me to follow courses of investigation about which I was passionate. Her advice and input especially on my writing was always thoughtful and insightful. Tuba, you have been a superb advisor. Thank you so much, and I wish you all the best.

And to my beautiful wife, Tess, thank you for taking on this adventure with me. It is no small deal to move across the country to a new place with new people, leave your friends and family behind, quit your well paying jobs, and live the life of students. Your love, support, and simply your company made it a pleasure. You encouraged me to follow my dreams, and were there at my side as I did. Home is wherever I'm with you. Bootie, I love you so much!

TABLE OF CONTENTS

1	Introduction	1
2	Background	5
2.1	Computation of WEC Array Performance	5
2.2	WEC Array Optimization	7
2.3	WEC Wave Field	9
3	Methods	13
3.1	Boundary Value Problem	13
3.2	Equations of Motion	17
3.3	Device Power	19
3.4	Wave Energy Flux	20
3.5	Theoretical WEC Wave Field	22
3.6	WEC and Wave Field Computation	29
4	Results	31
4.1	Generic WEC Wave Field	31
4.1.1	Regular Waves	33
4.1.2	Spectral Seas	41
4.2	Experimental Wave Field Analysis	49
4.2.1	Incident Wave Conditions	54
4.2.2	Regular Waves	55
4.2.3	Spectral Seas - Significant Wave Height	58
4.2.4	Spectral Seas - Wave Spectra	58
4.3	SWAN Wave Field Analysis	63
4.3.1	Regular waves	67
4.3.2	Unidirectional Spectral Seas	69
4.3.3	Directional Spectral Seas	71
5	Discussion	75
5.1	WEC Wave Field Patterns	75
5.2	Application of the WEC Wave Field to Array Design	78
5.3	Future Work	80
6	Conclusion	82
	Bibliography	84

LIST OF FIGURES

<u>Figure</u>	<u>Page</u>
1 Five cylinder array	2
2 Superposition of 2D waves	10
3 Theoretical WEC wave fields	27
4 Generic WEC RAO and power curves	33
5 Generic WEC real wave fields	34
6 Generic WEC wave field magnitudes	37
7 Generic WEC wave energy flux transects	40
8 Generic WEC non-directional incident wave spectrum	41
9 Generic WEC non-directional spectral wave field	43
10 Generic WEC non-direction field spectra	44
11 Generic WEC cross-shore transects	45
12 Generic WEC directional incident wave spectrum	46
13 Generic WEC directional spectral wave field	47
14 Generic WEC directional wave field spectra	48
15 Photo of the WEC array experiment	49
16 WEC array tests experimental layout	50
17 Manta geometry and cylinder for computational model	51
18 Experimental WEC RAO and RCW	52
19 Experimental WEC interpolated wave field	53
20 Experimental and computational 1 WEC regular wave transects	57
21 Experimental and computational 5 WEC regular wave transects	59
22 Experimental and computational 1 WEC spectral seas transects	60
23 Experimental and computational 5 WEC spectral seas transects	61
24 Experimental and computational field spectra for 1 WEC . . .	64
25 Experimental and computational field spectra for 5 WEC . . .	65
26 WAMIT-SWAN regular-wave wave field comparison	67
27 WAMIT-SWAN comparison cross-shore transects at $T = 1\text{ s}$. .	69
28 WAMIT-SWAN longshore transects at $T = 1\text{ s}$	70
29 WAMIT-SWAN input spectra and WEC RCW curve	71
30 WAMIT-SWAN unidirectional spectral seas comparison	72
31 WAMIT-SWAN directional input spectra	73
32 WAMIT-SWAN directional ($s = 10$) spectral seas comparison	74
33 WAMIT-SWAN directional ($s = 4$) spectral seas comparison .	74

Wave Field Patterns Generated by Wave Energy Converters

1 Introduction

Anyone who has been in a boat in a crowded river or lake has felt the effects of hydrodynamic interactions between floating bodies. Waves from one boat propagate through the water, become incident upon and create motion in other vessels. Typically, the waves are the Kelvin wake generated by the boat's steady forward motion. Wave energy converters (WECs) generally do not move at a steady speed. Instead, they oscillate about a mean position and so the hydrodynamic interactions between multiple closely spaced WECs are via two other types of waves, diffracted waves and radiated waves. When boat wakes intersect the resulting wave is the combination of each wake, which in some cases is larger and others smaller than each wake independently. Similarly, the coherent interaction of the incident, diffracted and radiated waves creates spatial variations in the wave height around a single WEC or arrays of WECs. An example of a WEC wave field is shown in Fig. 1.

A fundamental facet of WECs is that they remove energy from the waves, and so by conservation of energy, they necessarily must decrease the net wave height, which is related to wave energy. In fact, they not only remove energy but also redistribute it. In the wave field shoreward of a group of WECs, wave energy removal may affect coastal processes such as erosion and accretion, human commercial and recreational activities, environmental and biological processes, and even the efficacy of other arrays of wave energy converters. In the near WEC wave field, this has significant implications to the design of WEC arrays.

The eventual deployment of WECs on a commercial scale will necessitate the grouping of devices into arrays or “wave farms,” in order to minimize overhead costs of installation, mooring, maintenance, and electrical cabling for shoreward power delivery. Closely spaced devices are not isolated from one another, but interact hydrodynamically. Despite WEC energy removal, hydrodynamic WEC array interactions have been shown in theory under certain circumstances to be constructive; that is, by interacting the power performance of the array is greater than the sum of isolated individual performances. However, the assumptions made in these computations may not be realistic. In

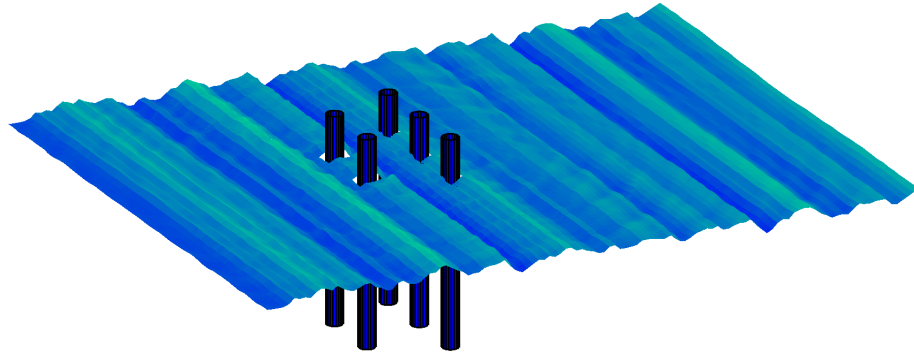


Figure 1: The picture shows the wave elevation of an array of five cylindrical WECs as computed by WAMIT. The image is stretched in the z-direction in order to magnify the size of the waves.

any case, the design of WEC arrays or array optimization is complex, but will have a significant impact on the power performance and economics of a wave farm.

In the past, array optimization has focused on performance as the only parameter to guide the spatial configuration of WEC arrays. Hydrodynamic interactions were implicit in the formulations of performance through the radiation and excitation forces, but the interaction of various waves was not explicitly examined. Only recently have researchers looked specifically at the WEC wave field, and used it to guide spatial WEC array design. For example, Child and Venugopal [2] exploited standing waves in their Parabolic Intersection method to design constructive arrays. Herein, the so-called “wave shadow” in the lee of a WEC is described.

Physically, WECs absorb wave energy when wave momentum is transferred to the mechanical motions of the device, which is converted down the line to other forms of energy. However, the process is not simple - some wave energy is reflected off the device; at times the device transfers energy back to the wave field through a momentum exchange; and within the wave field, wave energy diffuses spatially. Fortunately, linear water wave theory serves to simplify the wave-body interaction processes and computations.

Under the assumptions of potential flow, small wave height, and small body motions, linear wave theory breaks down the wave field into the superposition

of three components - the incident wave, the diffracted wave, and the radiated waves. The incident wave is the wave that exists in the absence of submerged bodies. The diffracted wave is the wave that is generated when the incident wave interacts with fixed (not moving) submerged or partially submerged bodies. One could think of the diffracted wave as similar to a reflected wave, but it includes a wave field that propagates at all directions. Radiated waves exist for each mode of motion of the device. For a given mode, the radiated wave is generated by the device motion in the absence of incident waves.

In linear wave theory, energy is removed from and redistributed within the wave field by the precise relationship in amplitude and phase of the incident wave to the combined diffracted and radiated waves. Farley [3] calls the combined diffracted and radiated waves the generated wave. Offshore, the redistribution occurs as partially standing waves. In the lee of a WEC, the energy redistribution and removal combine to create a wave shadow. These wave field patterns exist for a regular wave at a given incident wave frequency and direction. In reality, WEC arrays will operate in spectral seas, in which wave energy is spread over wave frequency and direction. Spectral seas can be approximated as multiple incident wave components at different frequency-direction pairs, and which, under linear wave theory are independent of one another. Wave fields can be computed separately for each wave component and then the results combined to produce a spectral wave field. Consideration of the spectral wave field is critical to the optimization of WEC arrays for real conditions.

In this thesis, WEC wave fields are studied explicitly with linear wave theory and through experimental data analysis in order to show fundamental patterns that could be helpful in the design of WEC arrays. Results are shown as plots of wave elevation and wave energy flux for regular waves and as plots of significant wave height and wave spectra for irregular waves. Computational results are produced by the linear boundary-element-method (BEM) hydrodynamic software WAMIT for a simple WEC geometry. Experimental data comes from WEC array tests of a device designed by Columbia Power Technologies, Inc. The experiments took place in the O.H. Hinsdale Tsunami wave basin at Oregon State University over the winter of 2010-11 [1]. The experimental results help to validate the computational model results, and the computational models serves as an invaluable aid to interpreting the experimental data.

Phase-resolving linear wave theory is one of many computational methods available with which to model the WEC wave field. And so in addition, a comparison is made of the phase-resolved wave field to that of a phase-averaged computational model, SWAN. Phase-averaged models are not able to model some of the physical wave-structure interaction processes explicitly, but can be augmented with physics-based parametric approximations. In general, they are computationally faster and can cover a broad domain with a realistic bathymetry. The goal of the comparison was the explore the adequacy of the phase-averaged model in reproducing the linear WEC wave field.

The importance of hydrodynamic interactions in the design of wave farms should not be underestimated. They will have a significant impact on the overall performance and hence the economics of the wave energy. There are numerous methods for computing WEC array interactions. Some require significant computation time and do not elucidate the means of the interactions, that is the WEC generated wave field. Recent research has studied the wave field explicitly and found it to be useful for understanding WEC energy absorption and array interactions, and for designing WEC arrays. Results discussed in this paper expand upon previous WEC wave field research and show some WEC wave field patterns experimentally. It is believed that the patterns are fundamental and apply generally to WECs of any type. WEC engineers could to apply the understanding of WEC wave field patterns as rules-of-thumb in their preliminary array designs.

2 Background

A great variety of computational methods exist for modeling wave energy converter arrays, and an excellent review and comparison is given by Folley et al. [4]. Herein, the focus is linear wave theory, which because of its relative simplicity has historically been the dominant theoretical framework for studying WEC arrays. In this section, a brief review of array computations, optimization, and wave field studies based on linear wave theory is given.

2.1 Computation of WEC Array Performance

The linear wave theory methods used in the computation of WEC array performance have developed from analytical to numerical with advances in computing power. Although numerical methods are fairly common now, some of the original analytical methods are still useful for promoting conceptual understanding, and they perform well within the range of their assumptions.

The commonly used measure of WEC array performance is the factor q .

$$q = \frac{\text{Power of Array}}{N \times (\text{Power of a Device})}$$

where N is the number of devices in the array. A q greater than 1 signifies constructive interference and is desirable. A q less than 1 indicates destructive device interaction, and a q equal to 1 means that there is no net gain from the array. Although it is not the only means of measuring WEC array hydrodynamic interaction, it is the most commonly used, has a simple and universal scale, and shall be referenced throughout this document.

The very first studies [5, 6, 7] on WEC array performance used two important assumptions: 1) the point absorber assumption and 2) optimal motions. The point absorber assumption states that the dimensions of an individual WEC are much smaller than the incident wavelength, and so the diffracted wave can be neglected. The interaction of the radiated wave with the incident wave is the only means of hydrodynamic interactions between the devices. One may wonder why, if the body is small enough to neglect the diffracted wave, should the radiated wave be significant. This is generally attributed to the assumption of optimal motions [8]. It was found by Evans [6] that if the radiation and excitation forces are known for every mode of motion of every body (all degrees of freedom), there exists an amplitude and phase of

motion for each degree of freedom that maximizes the total power absorption of the incident wave by the array.¹ Depending on incident wave frequency and the properties of the radiation interaction, the amplitudes of these motions could be very large, and in some cases unrealistically large. Because the body motions are large, the amplitude of the radiated wave is proportionally large (assumed to be much larger than the diffracted wave).

Later work improved upon these assumptions. Thomas and Evans [7] showed that for a row of five semi-submerged spheres the amplitude of optimal motions could be eight times higher than the incident wave height, which is physically unlikely. In addition to computing the performance of the array oscillating with optimal amplitude, they found the performance for motions where the amplitude was limited to two and three times the incident wave amplitude. Simon [9], developed the plane wave method to approximate the diffracted wave as well as scattering by the radiated waves in WEC arrays. The method states that if the devices are spaced far enough apart, a diffracted or radiated wave from device 1 incident on device 2 could be modeled as a plane sinusoidal wave at device 2 of an amplitude defined by the scattering properties of and distance from device 1. Kagemoto and Yue [10] devised a fully analytical method for solving hydrodynamic interactions within arrays of floating bodies that included forces due to propagating and evanescent wave modes. If the forces and wave response for each individual body is known, then the hydrodynamic problem can be formulated into a matrix and solved efficiently. Their method is exact within the context of linear wave theory.

Except for relative simple canonical cases, numerical methods are required for finding the diffracted and radiated wave fields and forces on submerged geometries. One of the more common methods is the boundary-element method (BEM), which is the method employed by WAMIT to solve linear hydrodynamic problems in the frequency domain [11]. In its most fundamental sense, the BEM is known as the integral method because a solution to the flow (Laplace's equation), is found by integrating source or dipole distributions over the surfaces in the boundary value problem. In the traditional low-order version of the BEM, wetted surfaces are discretized into quadrilateral panels containing a source or dipole. The source or dipole strength is determined so that the boundary conditions on all the panels are met [12]. The implementation of the BEM in WAMIT is described in the WAMIT User's Manual [11].

¹Section 3.3 explains the optimal motions mathematically.

Several authors have used WAMIT [13, 14, 15, 16, 17] or another BEM code [18, 19, 20] to solve for the hydrodynamic forces in WEC arrays.

Early methods in computing WEC array hydrodynamics made significant assumptions about the motion and size of the WECs. Later methods improved upon these assumptions so that the WEC array problem can now be solved completely for any number of bodies with arbitrary geometries under the assumptions of linear wave theory.

2.2 WEC Array Optimization

The primary goal of array design is to maximize the output power of the array for its intended wave conditions within the limits of cost, safety, and practicality. Such an effort is called array optimization. In general, array optimization includes the design of the spatial layout of the devices as well as individualized control and power take-off (PTO) settings. Several studies have shown that individualizing the PTO settings can have significant benefits to the array performance [18, 14, 15]. Optimization of the array would necessitate the simultaneous optimizations of both the layout and the PTO properties, which is a complex problem. In the present study on the hydrodynamic interactions, WEC array optimization is only with respect to the spatial configuration of the WECs in the wave field.

Many early studies of WEC array hydrodynamic interactions only considered a single row or a regular grid of evenly spaced devices and examined the performance as a function of the separation distance between devices [5, 6, 7, 21, 9]. They showed very high q values at certain ratios of device spacing to wavelength and q values much less than 1 at others. For a given wave frequency and direction, the spacing between the devices could be tuned to optimize the array performance. However, at that same array spacing, significant losses would occur at other wave frequencies and directions. Because real seas are spectral and vary temporally, it is clearly not possible to achieve consistent constructive hydrodynamic interference.

Recognizing this characteristic, McIver [8] stated:

...part of a practical strategy for the design of wave-power stations with large numbers of devices might be to seek to reduce destructive interference effects, perhaps by using unequal spacing, rather than attempt large increase in power absorption through constructive interference.

He computed the performance for a row of devices with unequal spacing and found that q was consistently much closer to 1 for all frequencies and directions examined. Mavrakos and Kalofonos [22] computed the performance of two irregular WEC array arrangements and compared them to a regular row of devices. For the irregular array configurations, they also found q to be more consistently near 1 over all frequencies. Neither of these studies attempted to optimize the array configuration for a given set of wave conditions.

More recent research has examined arrays in relatively simple configurations: a pair of devices [18, 19], a triangle [17], an “X” shape [23], and a square [14], in both regular and irregular waves. Borgarino et al. [20] examined triangular and regular grids of 9, 16, and 25 WECs in spectral seas and found that the triangular grid performed better than the regular grid. In several studies, the effect of device spacing on the array performance was examined, but in none was an optimization performed to find the arrangement of maximum power production.

Fitzgerald and Thomas [24] performed a constrained nonlinear optimization of the configuration of an array of five spherical WECs at a single frequency under the point absorber and optimal motions assumptions. Their optimal arrangement had a q value of 2.77, which is extremely high for such a small number of devices. In the same paper, they presented a consistency condition, which states that under the point absorber assumption at a given frequency, the average of q over all wave directions is 1. This means that for any region of constructive interference at one direction, there must be an equal amount of destructive interference at other directions. The plots of the q factor versus direction for the optimal arrangement show a large spike of 2.77 at the direction for which the array was designed, and values near or less than 1 at all other directions. Fitzgerald and Thomas’s optimization was the first of its kind but it was performed within the possibly unrealistic context of optimal motions and point absorber theory.

Folley and Whittaker [16] found optimal configurations of two, three, and four point absorbers with optimal motions for spectral seas. To find the optimal configuration, they mapped values of the average q factor (traditional q factor scaled by the incident wave energy) to values of the parameter space. In spectral seas, the average q factor of the optimal array was always close to 1. The use of spectral seas was a step forward in array design, but the optimization was still performed with point absorber and optimal motions

assumptions.

Child and Venugopal [2] used the exact analytical method of Kagemoto and Yue to solve for an array of five cylindrical WECs. To find optimal configurations, they used a genetic algorithm and a novel heuristic method, which they termed the Parabolic Intersection (PI) method. They found parabolic-like contours around a single device where the incident wave was in-phase and out-of-phase with the combined radiated and diffracted wave. The parabolic intersection method takes advantage of the parabolas formed by either the incident and diffracted wave or the incident and radiated wave to guide the placement of devices in an array. Devices placed on in-phase parabolic curves lead to higher array performance, because these intersections indicate the location of crests of partial standing waves. Although their genetic algorithm method did not explicitly guide the WEC positions towards in-phase crests, the optimal configurations found by the genetic algorithm had devices located on such crests. The optimization was performed for a single frequency and direction, but they examined the performance of the optimal arrays as a function of frequency and direction. Child and Venugopal's research was the first time that the wave field had been explicitly utilized in the design and analysis of a WEC array.

2.3 WEC Wave Field

Under linear wave theory, harmonic wave components can be superimposed to create a total wave field. If progressive wave components are of different frequencies, they travel at different speeds and pass through one another. However, if the waves are of the same frequency (coherent), their interaction is different and can lead to wave magnification, cancellation, and partially or fully standing waves depending on the relationship between the amplitude, phase and direction of the waves.

This can be most easily understood with a two-dimensional example. Consider two waves of the same frequency and traveling in the same direction with amplitudes a_1 and a_2 , respectively. When the waves are in phase, the result is a harmonic wave traveling in the same direction with an amplitude $a_1 + a_2$. When the waves are out of phase, they result in a wave of amplitude less than $a_1 + a_2$ reaching a minimum of 0 when the waves are 180° out of phase. Now, consider the wave components traveling in opposite directions.

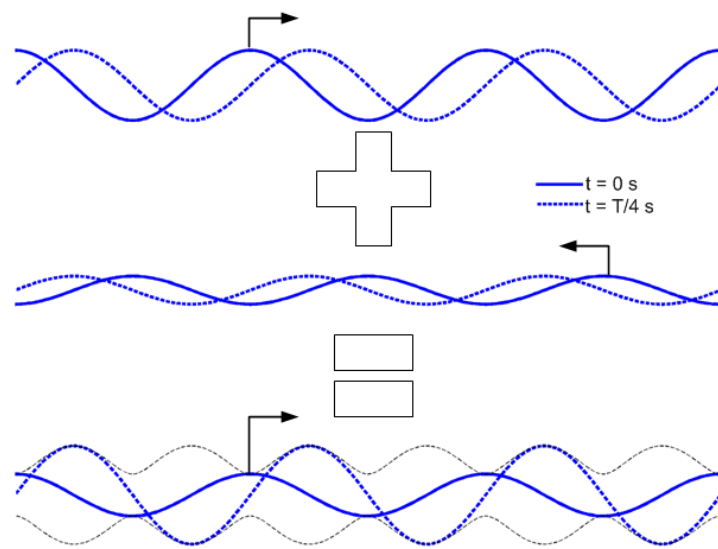


Figure 2: The figure shows the superposition of two 2D waves travelling in opposite directions. The resultant wave is a partially standing wave shown at the bottom. The solid line shows the waves at time, $t = 0 \text{ s}$, and the dashed line shows the waves at a future time, $t = T/4 \text{ s}$, where T is the wave period. The black dashed line shows the envelope of the standing wave. Note how the resultant wave increases in amplitude from $t = 0 \text{ s}$ (at a node) to $t = T/4 \text{ s}$ (at an anti-node).

When the amplitudes of the two waves are the same, the result is a fully standing (non-progressing) wave. When the amplitudes are not equal, the result is a partially standing wave progressing in the direction of the wave with the higher amplitude (see Fig. 2). The amplitude of a two-dimensional standing wave forms a simple harmonic pattern of nodes and anti-nodes. The node is the location of minimum wave height; for a fully standing wave the node has zero wave height. The anti-node is the location of maximum wave height. The positions of the nodes and anti-nodes are determined by the phasing relationship between the wave components. One can now imagine placing WECs in the two-dimensional standing wave field. It seems that a WEC placed at an anti-node would perform better than a WEC at a node.

A similar behavior occurs in three-dimensional wave fields except the patterns are more complex because there are many wave directions and because the waves do not have to be planar, but can also be circular. Modern studies have investigated the wave field to improve the understanding of WEC array hydrodynamics and guide the design of WEC configurations. Child and Venu-gopal [2] applied wave field structure to an array design method and to the analysis of their results. Newman and Mei [25] plotted the wave amplitude across a row of nine floating bodies computed with WAMIT and showed wave amplitudes four times greater than the incident amplitude due to so called “trapped” waves. Although it was not a plot of the wave field explicitly, Folley and Whittaker [16] plotted the magnitude and direction of the total radiated wave for certain array arrangements and used the plots to discuss array performance. Kalen [13] produced plots of the wave elevation for arrays of 2, 7, and 420 point absorbers and used wave elevation at each WEC as an indicator of performance. Borgarino et. al [20] plotted the wave elevation of a single WEC and three WECs in their array configurations to show that at the optimal separation distance, certain WECs were in the peak of standing waves.

It was shown early in WEC research that a WEC could absorb power from an incident wave front much wider than its physical dimensions. For instance, a heaving axisymmetric WEC of any size can theoretically absorb energy from a width of the incident wave front equal to $\lambda/2\pi$, where λ is the wavelength [26]. This may seem physically unintuitive but is similar to the way in which an electromagnetic antenna can absorb power from an area wider than its physical width. Within the context of linear wave theory, power absorption is explained mathematically by the destructive interference of the generated wave

(combined diffracted and radiated waves) with the incident wave [27]. Because the generated wave travels outward from the WEC in a circular pattern, it interacts with the incident wave outside the physical dimensions of the WEC, which explains the capture width phenomenon and has implications on the size and shape of the wave shadow.

Recent papers have explored the process of energy extraction in the wave field in more detail. Wypych et al. [28] used analytical functions for radiated waves produced by heaving and surging point sources to compute the energy flux through a cylindrical control surface. From a wave field formulation, they were able to derive classical absorption equations for point absorbers. Farley [3] defined the term “generated wave,” which he said is the sum of all waves both diffracted and radiated created by any number of power absorbing bodies. He plotted the wave field energy flux over a transect perpendicular to the direction of the incident wave propagation. He was also able to derive the classical limit of point absorber capture width. Most interestingly he showed that only the portion of generated wave that propagated in the direction of the incident wave is responsible for power capture. The wake or wave shadow of any single WEC or WEC array always has the same general form at a large enough distance from the devices, and that form is based on the power capture.

3 Methods

In this study, WEC motions and wave field properties are computed with linear water wave theory. Linear wave theory rests on two significant assumptions, first that the fluid can be described with potential flow and second that the free surface and body motions are small. The potential flow condition states that if the fluid can be considered inviscid and irrotational, the fluid velocity vector can be reduced to the gradient of the scalar velocity potential. For the free surface to be small, the wave height must be much less than the wavelength and the water depth. For body motions to be considered small, the motion must be small with respect to the length scale of the body. The linear wave theory principle of superposition justifies the decomposition of the total velocity potential into velocity potentials due to the incident wave, the diffracted wave, and radiated waves [29].

The following subsections describe the boundary value problem of linear water wave theory, the formulation of the equations of body motion, and the computation of power absorption by the body and through energy flux in the wave field. Additionally, a simple theoretical WEC wave field is devised that serves to illustrate mathematically some of its key features. In addition to describing concepts, this section introduces the notation used throughout the document.

3.1 Boundary Value Problem

Consider an arbitrary number bodies floating in an inviscid irrotational fluid. A right-handed coordinate system is defined with positive z up, and the $x - y$ plane at $z = 0$ is the calm water surface. The fluid extends to infinity in all x and y directions, and there is a flat sea floor at $z = -h$. Because the fluid is inviscid and irrotational, it can be defined by a velocity potential, $\Phi(x, y, z)$, where the velocity of the fluid is the vector, $\mathbf{V} = \nabla\Phi$. Also assume the motions of the bodies and fluid to be small and harmonic with a frequency ω , so that $\Phi = \text{Re}\{\phi e^{i\omega t}\}$,² where $i = \sqrt{-1}$ and ϕ is complex valued. The governing equation in the fluid domain (i.e. $-h \leq z \leq 0$ and external to all body boundaries) is Laplace's equation,

²Often in literature the time function is $e^{-i\omega t}$, which results in a slightly different set of equations. However, WAMIT uses $e^{i\omega t}$ and so that version shall be followed here.

$$\nabla^2 \phi = 0$$

On the sea floor ($z = -h$), the no penetration condition states

$$\frac{\partial \phi}{\partial z} = 0$$

On the linearized free surface ($z = 0$), the dynamic and kinematic boundary conditions can be combined as

$$\omega^2 \phi = g \frac{\partial \phi}{\partial z}$$

where g is the gravitational constant.

The velocity potential can be separated into components consisting of the incident wave potential, $A\phi_i$, the diffraction potential, $A\phi_d$, and radiation potentials due to motion in each degree of freedom, $\xi^j \phi_r^j$, where j is the index of the j^{th} motion. A is the complex amplitude of the incident wave. ξ^j is the complex amplitude of the j^{th} motion, and ϕ_r^j is the velocity potential due to unit amplitude, zero phase motion in mode j in otherwise calm water. ϕ_i is the velocity potential of a unit amplitude, zero phase incident wave and is equal to

$$\phi_i = i \frac{g \cosh k(h+z)}{\omega \cosh kh} e^{-ik(\cos \beta \cdot x + \sin \beta \cdot y)} \quad (1)$$

where β is the direction of wave propagation and k is the wave number. k is related to the frequency by the dispersion relation

$$\omega^2 = gk \tanh kh$$

ϕ_d is the velocity potential of the diffracted wave that results from a unit amplitude, zero phase incident wave. Define the j^{th} mode of motion response to a unit amplitude, zero phase incident wave as ζ^j so that $\xi^j = A\zeta^j$. For floating bodies with a total of N degrees of freedom, the total velocity potential is

$$\phi = A \left(\phi_i + \phi_d + \sum_{j=1}^N \zeta^j \phi_r^j \right) \quad (2)$$

The incident and the diffracted potential satisfy the boundary value problem for all bodies held fixed. Call S the wetted surface of all bodies and $\frac{\partial}{\partial n}$

indicates the partial derivative in the direction of the body surface normal. By the no-penetration condition, on S the diffraction potential must satisfy

$$\frac{\partial \phi_d}{\partial n} = -\frac{\partial \phi_i}{\partial n}$$

Each radiation potential, ϕ_r^j , is found for the unit amplitude, zero phase motion j , which moves at a velocity $i\omega$ in an otherwise undisturbed fluid. On the wetted surface, S , motion j has a generalized normal \mathbf{n}^j , where \mathbf{n}^j is a unit normal in the direction of the motion for translational modes and is the cross-product of the unit normal and vector about the point of rotation for rotational modes. On S , the radiation potential of the j^{th} motion satisfies the boundary condition

$$\frac{\partial \phi_r^j}{\partial n} = i\omega \mathbf{n}^j$$

Far from the bodies, the wave field should appear as the undisturbed or incident wave field, which means that the diffraction and radiation potentials must decay as the distance from the bodies increases. By energy conservation, the magnitude of the potential should decrease with inverse of the square-root of the distance. This is called the radiation boundary condition, and it is stated as

$$\phi_d, \phi_r^j \propto (kr)^{-1/2} e^{-ikr} \text{ as } r \rightarrow \infty \quad (3)$$

where r is the radial distance from the body.

The velocity potential provides a complete description of the wave field. The complex fluid velocity amplitude is

$$\mathbf{v} = \nabla \phi \quad (4)$$

From the Bernoulli equation, the complex dynamic fluid pressure is

$$p = -i\omega \rho \phi \quad (5)$$

where ρ is the fluid density. And the complex wave elevation is

$$\eta = -\frac{i\omega}{g} \phi|_{z=0} \quad (6)$$

$$= \frac{1}{\rho g} p|_{z=0} \quad (7)$$

Additionally, the velocity potential can be used to compute the hydrodynamic forces and moments on the floating bodies. Just as the solution to the boundary value problem was divided into a diffraction problem and a radiation problem so too are the hydrodynamic forces. When the bodies are held fixed, the force or moment on each mode of motion, j , is the excitation force, F_{ex}^j , which is the integral over the wetted surface of the incident plus diffracted pressure in the direction of the generalized normal \mathbf{n}^j .

$$F_{ex}^j = \operatorname{Re} \{ f_{ex}^j e^{i\omega t} \}$$

$$f_{ex}^j = -i\omega \rho A \int \int_S (\phi_i + \phi_d) \mathbf{n}^j dS$$

The radiation force on mode j , F_r^j , is slightly more complicated because it is the summation of the integrals of the pressure forces generated by motion in all modes including j .

$$F_r^j = \operatorname{Re} \{ f_r^j e^{i\omega t} \}$$

$$f_r^j = \sum_{k=1}^N -i\omega \rho A \zeta^k \int \int_S \phi_r^k \mathbf{n}^j dS$$

For unit amplitude motion, the velocity of the motion j is $i\omega \mathbf{n}^j$, which means that from the radiation body boundary condition, $i\omega \mathbf{n}^j = \frac{\partial \phi_r^j}{\partial n}$. The radiation force can be rewritten as the force on mode j due to motion in k^{th} direction

$$f_r^{jk} = A \zeta^k \left[-\rho \int \int_S \frac{\partial \phi_r^j}{\partial n} \phi_r^k dS \right]$$

The quantity in the brackets is the complex radiation resistance matrix and is typically written in terms of the real added mass, \mathcal{A}^{jk} , and damping, \mathcal{B}^{jk} , coefficients.

$$-\rho \int \int_S \frac{\partial \phi_r^j}{\partial n} \phi_r^k ds = \omega^2 \mathcal{A}^{jk} - i\omega \mathcal{B}^{jk}$$

So the total force in mode j is the sum of the forces due to motions in mode k .

$$f_r^j = -A \sum_{k=1}^N (-\omega^2 \mathcal{A}^{jk} + i\omega \mathcal{B}^{jk}) \zeta^k$$

Since, $\dot{\zeta} = i\omega \zeta$ and $\ddot{\zeta} = -\omega^2 \zeta$,

$$f_r^j = -A \sum_{k=1}^N (\mathcal{A}^{jk} \ddot{\zeta}^k + \mathcal{B}^{jk} \dot{\zeta}^k)$$

\mathcal{A}^{jk} applies a force proportional to body acceleration and \mathcal{B}^{jk} applies a force proportional to velocity, which explains the respective terminology, added mass and damping.

Diffraction and radiation velocity potentials are found from the linear water wave boundary value problem for an arbitrary number of floating bodies. From the potentials, wave field properties are found including wave elevation, pressure, and velocity. Wave pressure is used to compute the excitation force and added mass and damping coefficient matrices.

3.2 Equations of Motion

In the previous section, hydrodynamic forces and moments are described for an arbitrary number of floating rigid bodies with N degrees of freedom. Generally, one wants to know the amplitude and phase of the motions of the bodies in response to waves. And to find the total elevation of the wave field, one needs to know the complex body motions (see Eqns. 2 and 6). To compute the body motions, one also needs mass and mechanical properties of the bodies. The motions are solved with a linear equation for complex amplitudes in the frequency domain.

Again consider an arbitrary number of floating rigid bodies with N degrees of freedom. In matrix form, the equation of motion is

$$\mathbf{M} \ddot{\mathbf{X}} = \mathbf{F}_{hyd} + \mathbf{F}_{hs} + \mathbf{F}_{mech}$$

where \mathbf{M} is an $N \times N$ matrix of masses or moments of inertia depending

on whether the mode of motion is translational or rotational, $\ddot{\mathbf{X}}$ is an $N \times 1$ vector of accelerations, and each \mathbf{F} is an $N \times 1$ vector of forces, where the subscript *hyd* indicates hydrodynamic, *hs* indicates hydrostatic, and *mech* indicates mechanical forces.

As described in the previous section, the hydrodynamic force is the sum of excitation force and the radiation forces which can be written in terms of real added mass and damping coefficients.

$$\mathbf{F}_{hyd} = \mathbf{F}_{ex} - \mathbf{A}\ddot{\mathbf{X}} - \mathbf{B}\dot{\mathbf{X}}$$

where \mathbf{F}_{ex} is an $N \times 1$ vector of exciting forces, \mathbf{A} is the $N \times N$ added mass matrix and \mathbf{B} is the $N \times N$ damping matrix. The hydrostatic force can be described by the product of an $N \times N$ stiffness matrix and the body displacements

$$\mathbf{F}_{hs} = -\mathbf{C}\mathbf{X}$$

The linear body forces are a damping force proportional to body velocity and a stiffness force proportional to body displacement,

$$\mathbf{F}_{mech} = -\mathbf{D}\dot{\mathbf{X}} - \mathbf{K}\mathbf{X}$$

where \mathbf{D} is an $N \times N$ body damping matrix and \mathbf{K} is an $N \times N$ body stiffness matrix. Moving all terms in \mathbf{X} to the left-hand side, the equation of motion is written as

$$(\mathbf{A} + \mathbf{M})\ddot{\mathbf{X}} + (\mathbf{B} + \mathbf{D})\dot{\mathbf{X}} + (\mathbf{C} + \mathbf{K})\mathbf{X} = \mathbf{F}_{ex}$$

Assuming the excitation force and motions to be harmonic with a frequency ω , $\mathbf{F}_{ex} = \text{Re}\{\mathbf{f}_{ex}e^{i\omega t}\}$ and $\mathbf{X} = \text{Re}\{\boldsymbol{\xi}e^{i\omega t}\}$, the equation of motion can be written as

$$[\mathbf{C} + \mathbf{K} - \omega^2(\mathbf{A} + \mathbf{M}) + i\omega(\mathbf{B} + \mathbf{D})]\boldsymbol{\xi} = \mathbf{f}_{ex} \quad (8)$$

and so the complex amplitude vector of the motion in each degree of freedom is

$$\boldsymbol{\xi} = [\mathbf{C} + \mathbf{K} - \omega^2(\mathbf{A} + \mathbf{M}) + i\omega(\mathbf{B} + \mathbf{D})]^{-1}\mathbf{f}_{ex} \quad (9)$$

3.3 Device Power

The total time-averaged power delivered by the waves to the array of WECs is the time average of the sum of the products of the hydrodynamic forces and the body velocities.

$$P = \frac{\omega}{2\pi} \int_0^{\frac{2\pi}{\omega}} \mathbf{F}_{hyd}^T \dot{\mathbf{X}} dt$$

where T indicates the transpose. In complex form this can be written as

$$P = \frac{1}{2} \operatorname{Re} \{ i\omega \mathbf{f}_{ex}^* \boldsymbol{\xi} \} - \frac{1}{2} \omega^2 \boldsymbol{\xi}^* \mathbf{B} \boldsymbol{\xi} \quad (10)$$

where $*$ indicates the complex conjugate transpose. The first term in the power equation is the power absorbed by the bodies from the wave excitation force and the second term is the power radiated back into the wave field by waves generated by the bodies. When the excitation force (Eqn. 8) equation is substituted into Eqn. 10, the result is

$$P = \frac{1}{2} \omega^2 \boldsymbol{\xi}^* \mathbf{D} \boldsymbol{\xi} \quad (11)$$

For this reason, the mechanical body damping matrix, \mathbf{D} , is typically called the power-take-off (PTO) damping. The PTO damping determines how much power is absorbed by the floating bodies from the wave field.

Rather than computing the power for motions specified by equation 9, one can specify the motions and determine how it affects the power absorbed. Evans [6] showed that equation 10 can be rewritten as

$$P = \frac{1}{8} \mathbf{f}_{ex}^* \mathbf{B}^{-1} \mathbf{f}_{ex} - \frac{1}{2} \left(i\omega \boldsymbol{\xi} - \frac{1}{2} \mathbf{B}^{-1} \mathbf{f}_{ex} \right)^* \mathbf{B} \left(i\omega \boldsymbol{\xi} - \frac{1}{2} \mathbf{B}^{-1} \mathbf{f}_{ex} \right)$$

In this form, the body motions are part of an independent term. The power clearly reaches a maximum of (the first term)

$$P = \frac{1}{8} \mathbf{f}_x^* \mathbf{B}^{-1} \mathbf{f}_x$$

when body motions are defined by

$$\boldsymbol{\xi} = -\frac{i}{2\omega} \mathbf{B}^{-1} \mathbf{f}_x \quad (12)$$

because it results in the second term being zero. Motions found by the above

equation are the optimal motions that have been used frequently in WEC array studies. They can be computed for any array of WECs where the excitation force and radiation damping matrix are known.

3.4 Wave Energy Flux

Just as the power absorbed by the floating bodies can be computed from the body motions, it can also be computed from the wave field. Instantaneous power in a fluid is the product of pressure and a volumetric flow rate, where the volumetric flow rate can be formulated as the flux of the fluid through a control surface. If the pressure and velocity are harmonic with a frequency ω , the instantaneous power in the fluid or the wave energy flux is

$$\mathcal{F}_{inst} = \int_{CS} \operatorname{Re} \{pe^{i\omega t}\} \cdot \operatorname{Re} \{\mathbf{v}e^{i\omega t} \cdot \mathbf{n}\} ds$$

where p and \mathbf{v} are the complex pressure and velocity amplitudes as before, and \mathbf{n} is the unit normal of the control surface, CS . In the wave field, p , \mathbf{v} , and CS are functions of three dimensional space $\{x, y, z\}$ for $z \leq 0$. The time-averaged wave energy flux is

$$\mathcal{F} = \frac{\omega}{2\pi} \int_0^{\frac{2\pi}{\omega}} \int_{CS} \operatorname{Re} \{pe^{i\omega t}\} \cdot \operatorname{Re} \{\mathbf{v}e^{i\omega t} \cdot \mathbf{n}\} ds dt$$

which can be rewritten as

$$\mathcal{F} = \frac{1}{4} \int_{CS} (p\mathbf{v}^* \cdot \mathbf{n} + p^*\mathbf{v} \cdot \mathbf{n}) ds \quad (13)$$

where $*$ indicates the complex conjugate. Eqn. 13 computes the flux through some arbitrary three-dimensional wetted control surface of a harmonically oscillating fluid with only the complex pressure and velocity amplitudes.

The wave energy flux of regular waves is computed by integrating the product of the pressure and velocity values along a vertical control surface that extends from the sea floor ($z = -h$) to the linearized free-surface ($z = 0$) [30]. Here, make the assumption that the vertical profiles of the pressure and velocity are of known forms $g_p(z)$ and $\mathbf{g}_v(z)$ respectively, which can be separated functions of horizontal space, (x, y) . The separation into functions of the vertical and horizontal variables can be performed for regular waves in the absence of submerged bodies. It also seems reasonable in the region outside of where the fluid is constrained in the z direction by a submerged body, in

other words, in the region with a free surface. The pressure can be written as the product of the surface pressure, $p_s(x, y)$ at $z = 0$ and the vertical pressure function, $g_p(z)$. Likewise, the velocity can be written as a function of the velocity at the surface, $\mathbf{v}_s(x, y)$ and a vertical function, which in this case is a vector, $\mathbf{g}_v(z)$.

$$p(x, y, z) = p_s(x, y) g_p(z)$$

$$\mathbf{v}(x, y, z) = \mathbf{v}_s(x, y) \mathbf{g}_v(z)$$

Now, define the control surface, CS , to be everywhere perpendicular to planes of constant z , and to extend from the bottom, $z = -h$, to the linearized free surface, $z = 0$. Its projection onto the plane $z = 0$ would be an open or closed curve, which shall be called the control loop, CL . Just as the pressure and velocity functions were defined as the product of their values at the surface and a function of z , so too can the control surface, where at $z = 0$ it is defined by the control loop CL and its depth function is $g_{CS}(z) = 1$. CS is the constant CL at all water depths. Because CS does not change in the z direction, the normal in the z direction is zero over the entire surface, $n_z = 0$, and the normals in x and y are constants with respect to depth. The dot product of the control surface normal and the velocity in Eqn. 13 is then

$$\mathbf{v} \cdot \mathbf{n} = u_s(x, y) g_u(z) n_x(x, y) + v_s(x, y) g_v(z) n_y(x, y)$$

where u_s is the velocity in the x direction at the surface $z = 0$, v_s is the surface velocity in the y direction, g_u is the depth dependence of the x velocity and g_v is the depth dependence of the y velocity. Based off the equations for regular waves (see Eqn. 1, 4, and 5), the depth functions for pressure and velocity are all the same ($g_p(z) = g_u(z) = g_v(z) = g(z)$) and are all equal to

$$g(z) = \frac{\cosh k(h+z)}{\cosh kh} \tag{14}$$

Eqn. 13 can then be separated into the product of a depth integral and a integral around the control loop.

$$\mathcal{F} = \frac{1}{4} \int_{CL} (p_s \mathbf{v}_s^* \cdot \mathbf{n}_s + p_s^* \mathbf{v}_s \cdot \mathbf{n}_s) dl \int_{-h}^0 g(z)^2 dz$$

The depth integral is

$$\begin{aligned}\int_{-h}^0 g(z)^2 dz &= \frac{1}{\cosh^2 kh} \int_{-h}^0 \cosh^2 k(h+z) dz \\ &= \frac{c}{g} c_g\end{aligned}$$

where c is the phase speed of the wave, $c = \omega/k$, and c_g is the group velocity and is equal to

$$c_g = \frac{1}{2} \left(1 + \frac{2kh}{\sinh 2kh} \right) \cdot c$$

Assuming the pressure and velocity have a depth dependence as defined by Eqn. 14, and that the control surface is uniform in z and defined by a control loop, CL , the average wave energy flux computed with complex pressure and velocity amplitudes at the linearized free surface is

$$\mathcal{F} = \frac{cc_g}{4g} \int_{CL} (p_s \mathbf{v}_s^* \cdot \mathbf{n}_s + p_s^* \mathbf{v}_s \cdot \mathbf{n}_s) dl \quad (15)$$

If the control loop is closed, encircles a group of floating bodies, and the normals point inwards, and the surface pressure and velocity values are found with Eqn. 2, 4, and 5, then the wave energy flux given by Eqn. 15 will equal the power absorbed by the bodies given by Eqn. 10.

For a regular harmonic wave propagating through an open-ended unit-width control surface, the dimensional energy flux is

$$\mathcal{F}_{reg} = \frac{1}{2} \rho g |A|^2 c_g \quad (16)$$

which can be found by combining Eqns. 1, 4, 5, and 15 for a wave of complex amplitude, A .

3.5 Theoretical WEC Wave Field

In order to illustrate the features of the WEC wave field and provide a mathematical background, a simple theoretical WEC wave field is devised. It consists of an incident regular wave and a circular wave that represents the combined diffracted and radiated waves. Although it may be simplified, it is a reasonable approximation of the linear WEC wave field.

In general, the total wave elevation is

$$\eta_t = \eta_i + \eta_d + \sum \xi^j \eta_r^j$$

First, consider just the diffracted and radiated waves, which propagate outwards from the WEC. Define the cylindrical coordinates $\{r, \theta, z\}$, where

$$x = r \cos \theta$$

$$y = r \sin \theta$$

$$z = z$$

In cylindrical coordinates, the boundary value problem of a circular wave can be solved with a separation of variables. Waves propagating radially outward have magnitudes in the radial direction defined by the Hankel function of kr [28]. Within a few wavelengths of the source, the Hankel function can be approximated as $(kr)^{-1/2} e^{ikr}$. The approximation represents circular waves whose magnitude decays at a rate that preserves the wave energy flux through ever increasing circumferences (i.e. it satisfies the radiation condition). Additionally, a complex directional dependence function, $f(\theta)$, is defined. A general circular wave can then be approximated as

$$\eta = \frac{f(\theta)}{(kr)^{1/2}} e^{-ikr} \quad (17)$$

The $f(\theta)$ function has been used frequently to describe the angular variation of the radiated as well as the diffracted wave field in WEC literature (e.g. [5, 7, 8]). It is often called the far-field angular dependence as it is typically only applied at large radial distances, but may be valid near the device. $f(\theta)$ is a function of the geometry of the device and the mode of motion that produces the radiated wave field. In this document it shall be called the generated wave function, because it describes the angular variation of a wave generated by the device. The wave may be due to device motions (radiation), diffraction, or the combination of radiation and diffraction.

Consider the diffracted and all radiated waves to be of the form of Eqn. 17, so that the wave field is then

$$\eta_t = \eta_i + \frac{f_d(\theta)}{(kr)^{1/2}} e^{-ikr} + \sum \xi^j \frac{f_r^j(\theta)}{(kr)^{1/2}} e^{-ikr}$$

All the circular waves can be combined into a single circular wave, modified by a single generated wave function,

$$\eta_t = \eta_i + \frac{f(\theta)}{(kr)^{1/2}} e^{-ikr}$$

where

$$f(\theta) = f_d(\theta) + \sum \xi^j f_r^j(\theta)$$

The WEC wave field for a single device can be considered as the superposition of a planar incident wave and circular wave. The wave field of a WEC array could also be approximated as such in the far-field if all waves radiated from the group come from approximately the same origin. Farley [3] claims that $f(\theta)$ is a universal function for any group of WECs, and can be used to determine the WEC wave field and the power capture.

As an example, take the incident wave field as the unit amplitude, zero phase case, propagating at an angle $\beta = 0$. The complex generated wave function, $f(\theta)$ is the sum of the complex responses of the diffracted wave and the various radiated waves due to the unit amplitude, zero phase, incident wave propagating in the direction $\beta = 0$. The total wave is then

$$\eta_t = e^{-ikr \cos \theta} + \frac{f(\theta)}{(kr)^{1/2}} e^{-ikr} \quad (18)$$

Of primary interest in this paper is the spatial variation of the magnitude of the total wave field. The magnitude of Eqn. 18 is

$$|\eta_t| = \sqrt{1 + \frac{|f(\theta)|^2}{kr} + \frac{2|f(\theta)|}{(kr)^{1/2}} \cos(kr(\cos \theta - 1) + \epsilon_f(\theta))} \quad (19)$$

where $|f(\theta)|$ and $\epsilon_f(\theta)$ are the magnitude and phase of $f(\theta)$, respectively. What wave field patterns can be deduced from Eqn. 19? How does magnitude of the wave elevation vary spatially? First, as the distance from the origin increases ($kr \rightarrow \infty$), the magnitude of the wave field goes to 1 (the magnitude of the incident wave) as it should. Second, in the region near the WEC, there are peaks in the wave field when the argument of the cosine term is equal to

an integer multiple of 2π . That is, there are standing wave peaks when

$$kr(\cos\theta - 1) + \epsilon_f(\theta) = \pm 2\pi n \quad (20)$$

If ϵ_f is defined from $0 \leq \epsilon_f < 2\pi$, and $r > 0$ ($r = 0$ causes a singularity in Eqn. 17 and so is undefined in the domain), the left hand side of Eqn. 20 is always less than 2π , and so the positive symbol on the right-hand side is eliminated and $n = 0, 1, 2, 3, \dots$. Using Cartesian coordinates, Eqn. 20 becomes

$$y = \pm \sqrt{\frac{2}{k} (2\pi n + \epsilon_f(\theta)) x + \frac{1}{k^2} (2\pi n + \epsilon_f(\theta))^2} \quad (21)$$

Of course, the standing wave pattern also contains troughs which are found as

$$y = \pm \sqrt{\frac{2}{k} (2\pi(n - \frac{1}{2}) + \epsilon_f(\theta)) x + \frac{1}{k^2} (2\pi(n - \frac{1}{2}) + \epsilon_f(\theta))^2} \quad (22)$$

Note that the first trough ($n = 0$) is only valid when $\epsilon_f(\theta) \geq \pi$.

Farley showed that the power absorbed (or radiated) by a WEC can be computed from the value of the generated wave function at $\theta = 0$ [3], that is, in the direction that the incident wave propagates. Following his derivation, the power absorbed by the wave (and thus the WEC) described by Eqn. 18 is

$$P_{farley} = -\frac{2\sqrt{\pi}|f(0)|}{k} (\sin \epsilon_f(0) + \cos \epsilon_f(0)) - \frac{1}{k} \int_0^{2\pi} |f(\theta)|^2 d\theta \quad (23)$$

where $\epsilon_f(0)$ is the phase of the circular wave in the direction of incident wave propagation. The power absorbed reaches a maximum when $\epsilon_f(0) = \frac{5\pi}{4}$, which is the optimal phase of the wave. An interesting aspect of the value of the phase that Farley points out is that, for the two-dimensional case (i.e. when the generated wave is long-crested), the optimal phase is π , so that the generated wave cancels perfectly with the incident wave. However, for the combination of a circular wave with an incident planar wave, the phasing is offset from π by $\pi/4$ or $1/8$ of the wavelength.

As a simplification, consider the generated wave function to be a constant with respect to direction, $f(\theta) = f$, which would be the case for the radiated wave of an axisymmetric device operating in heave. Equations 21 and 22 (ϵ_f is a constant) then describe a family of parabolas symmetric about the x -axis and increasing towards positive x . These are the same set of parabolic

standing waves, that Child and Venugopal describe and exploit in the Parabolic Intersection method [2]. For the heaving WEC wave ($f(\theta) = f$) operating with the optimal wave phase, $\epsilon_f(0) = \frac{5\pi}{4}$, the absorbed power is

$$P_{farley} = \frac{2\sqrt{2\pi}}{k} |f| - \frac{2\pi}{k} |f|^2 \quad (24)$$

Equation 24 is quadratic in $|f|$ and has a maximum at $|f| = \frac{\sqrt{2\pi}}{2\pi}$, at which the power captured is $P_{farley} = \frac{\lambda}{2\pi}$. $\frac{\lambda}{2\pi}$ is the well known optimum capture width for a WEC operating in heave [26]. Another interesting facet of the optimal amplitude and phase of the generated wave is that they are constants with respect to wave frequency. The optimal motions of the device are functions of frequency, but that is because of the frequency dependence of the hydrodynamic forces. Essentially, the device motions have to change as a function of frequency so as to produce the same generated wave at all frequencies.

Figure 3 shows wave fields for the heaving WEC operating at optimal amplitude for different radiated wave phases (ϵ_f). The wave fields are plots of $|\eta_t|$ at a wavelength, $\lambda = 2$, as given by Eqn. 19. Also, superimposed on the plot are red and blue parabolas located on the crests and troughs respectively of the standing waves. The phase and power absorption are given above each figure. A negative power absorption means that power is radiated rather than absorbed. For only three of the phases shown does the WEC wave absorb power ($\epsilon_f = \pi$, $\epsilon_f = 5\pi/4$, and $\epsilon_f = 3\pi/2$). The phase $\epsilon_f = 5\pi/4$ is the optimal phase at which the power absorption is $P = 0.32 = \lambda/2\pi$. As the value of the phase increases, the parabolas widen, and shadow forms inside the aft-most parabolic crest. The aft-most parabolic trough and the region inside it constitutes what shall be referred to as the wave shadow. It is interesting to observe how the wave shadow changes with phase. Note that at $\epsilon_f = \pi$ and $\epsilon_f = 3\pi/2$, the wave absorbs the same amount of power, but the wave shadows look different. At $\epsilon_f = 3\pi/2$, the wave shadow is clearly a parabola and in between its arms the wave elevation increases back to almost the incident elevation. At $\epsilon_f = \pi$, the final parabola has been swept back until it collapsed into line and the wave shadow loses its “V” shape.

In its most simple form, the WEC wave field is formed by the interaction between a planar incident wave and a circular generated wave. The question remains though: how good of an approximation is the circular wave to the radiated and diffracted waves of a real device? The following sections attempt

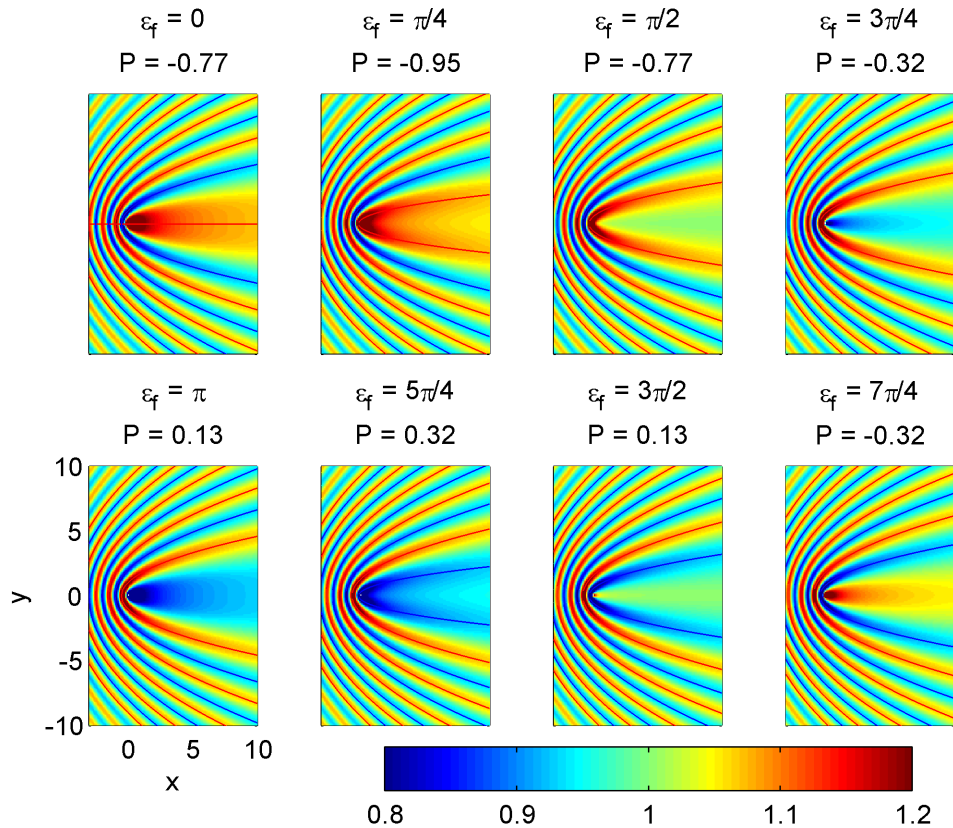


Figure 3: The figures show the magnitude of the wave elevation $|\eta_t|$ at a wavelength of $\lambda = 2$ at different phases of the generated wave. The phase and power absorption are given above each figure. A negative power absorption means that power is radiated rather than absorbed.

to answer that question by computing the radiated and diffracted wave fields for simple geometries and by comparison with experimental data.

3.6 WEC and Wave Field Computation

The linear wave BEM software WAMIT is used to solve the boundary value problem described in Sec. 3.1 for a given geometry. Hydrodynamic forces from WAMIT are combined with mechanical forces to solve for body motions as described in Sec. 3.2. WAMIT also returns separate radiation and diffraction³ pressures, and velocity vectors at user specified field points. The diffracted wave field computed by WAMIT is the wave field due to a unit amplitude, zero phase incident wave (ϕ_d from Sec. 3.1). Radiated wave fields are computed in each degree of freedom, j , for unit amplitude, zero-phase motions (ϕ_r^j from Sec. 3.1). Body motions are combined with the field quantities to produce wave fields as described in Sec. 3.1.

In addition to being functions of the wetted geometry, diffracted and radiated wave fields are functions of the radial frequency, ω . Diffracted wave fields are also functions of the incident wave direction, β , which is measured in degrees, counter-clockwise from the positive x -axis. However, because the radiated wave fields computed by WAMIT are for unit-amplitude, zero-phase body motions, they are independent of incident wave direction. Radiated wave fields become functions of direction when they are multiplied by directionally dependent body motions. Body motions can also be computed for unit-amplitude, zero-phase incident waves, and then the sum of the incident, diffracted, and radiated waves in each degree of freedom can be scaled by the complex incident wave amplitude, A (see Eqn. 2).

For regular waves, the wave field is typically represented by the wave elevation, η , as a function of space. Because wave elevation is complex valued, it can be plotted in a color map as either the real part, which represents the wave at an instant in time, or as the magnitude, which shows the size of the wave. Magnitude plots are typically used for visualizing standing wave patterns and the wave shadow. Two wave fields are of significant interest: the incident plus diffracted, $\eta_i + \eta_d$, and the total wave field, $\eta_t = \eta_i + \eta_d + \sum \eta_r^j$. The incident plus diffracted is the wave field of the fixed device, which does not absorb power, and the total wave field is that of power absorbing device. Unless otherwise specified, the wave fields are for unit-amplitude, zero-phase

³What WAMIT refers to as the diffracted wave field is herein referred to as the incident plus diffracted wave field. Therefore to compute the diffracted wave field defined by this document, one needs to subtract the incident (Eqn. 1) wave field from the WAMIT diffracted wave field.

incident waves.

In addition to computing the wave field for regular waves, spectral wave fields are considered by evaluating multiple wave components at different frequencies and directions and applying an amplitude to the incident wave as defined by a wave spectrum. Consider the spectral representation of the incident wave field to be $S_i(\omega, \beta)$. At a given frequency and direction, (ω, β) , the magnitude of incident wave amplitude is

$$|A(\omega, \beta)| = \sqrt{2S_i(\omega, \beta)\Delta\omega\Delta\beta} \quad (25)$$

where $\Delta\omega$ and $\Delta\beta$ are the bin widths at the given frequency and direction respectively. For the phase of the incident wave amplitude, random values can be chosen from a uniform distribution between 0 and 2π . The phase is only relevant when considering the real part of the wave. And so for a given incident wave spectrum, $S_i(\omega, \beta)$, the total wave field is created with Eqn. 2 where the magnitude of the of the wave amplitude is defined by Eqn. 25.

The incident wave amplitudes scale the resulting wave fields over the computed range of frequencies and directions. Within the wave field at each location, there is a spectral representation of the wave field over the range of frequencies and directions computed. The spectral representation of the total wave field is

$$S_t(\omega, \beta) = \frac{1}{2} \frac{|\eta_t(\omega, \beta)|^2}{\Delta\omega\Delta\beta}$$

At any given point, a spectrum can be computed and plotted. In order to visualize the entire spectral wave field simultaneously, the bulk parameter of the zeroth-moment significant wave height is plotted over the grid of field points. In order to accurately understand the wave field, it is important to study both the significant wave height as well as wave spectra.

4 Results

In this section, WEC wave fields are shown for three independent but inter-related studies. In the first, generic wave field patterns and techniques for analyzing the wave field are described using a heaving cylindrical WEC. Similar patterns are found in the second study, which is a comparison of WEC array experiment results to a computational model. The computational wave field proved quite useful for interpreting the experimental data and the data validates the existence of the modeled wave shadow. In the final set of results, the linear computational WEC wave field is compared to wave fields produced by a phase-averaged computational wave model, SWAN, which helps to frame the range of applicability of the phase-averaged model.

4.1 Generic WEC Wave Field

As an initial investigation, a generic WEC operating in a single degree of freedom is used in order to keep the results as general as possible. The WEC model is selected to be cylinder of diameter, d , and draft, l , allowed to operate only in heave. Results are shown for three regular wave cases and two spectral seas cases. Each regular wave case is for a different device diameter to wavelength ratio. The spectral seas cases are for unidirectional irregular waves and irregular waves spread over direction. Wave fields are presented as color plots of elevation or significant wave height, transects of wave elevation or energy flux, and wave spectra for irregular waves. Energy flux through the wave field is computed and the results are displayed graphically.

All motions, forces, and wave field properties are made nondimensional by ρ , g , and d . The nondimensional quantities are indicated by an apostrophe, $'$. The mechanical spring force shall be taken as zero, $K = 0$, and the nondimensional equation of motions for a cylindrical WEC operating only in heave is

$$\xi' = \frac{f'_{ex}}{\frac{\pi}{4} - \omega'^2 \left(\frac{\pi}{4} l' + \mathcal{A}' \right) + i\omega' (\mathcal{B}' + \mathcal{D}')} \quad (26)$$

where $\xi' = d^{-1}\xi$, $f'_{ex} = \rho^{-1}g^{-1}d^{-3}f_{ex}$, $l' = d^{-1}l$, $\mathcal{A}' = \rho^{-1}d^{-3}\mathcal{A}$, $\mathcal{B}' = \rho^{-1}g^{-1/2}d^{-5/2}\mathcal{B}$, $\mathcal{D}' = \rho^{-1}g^{-1/2}d^{-5/2}\mathcal{D}$, $\omega' = g^{-1/2}d^{1/2}\omega$. Also define the nondimensional coordinates, $x' = d^{-1}x$, $y' = d^{-1}y$, and $z' = d^{-1}z$.

The critical geometric parameter is the nondimensional draft $l' = l/d$.

Cylinders with large nondimensional drafts are typically referred to as spars and have very low resonant frequencies, which makes them stable in the typical range of ocean wave frequencies and they are often used for offshore structures such as oil platforms. WECs should respond actively to ocean waves, and as such a heaving cylindrical WEC should have a low nondimensional draft. In this case the nondimensional draft is taken as $l' = 1/2$.

In addition to the parameters of the equation of motion, the following nondimensional wave field parameters are defined, $\lambda' = d^{-1}\lambda$, $k' = dk$, $h' = d^{-1}h$, $A' = d^{-1}A$, $\phi' = g^{1/2}d^{-3/2}\phi$, $p' = \rho^{-1}g^{-1}d^{-1}p$, $\mathbf{v}' = g^{-1/2}d^{-1/2}\mathbf{v}$, $\eta' = d^{-1}\eta$. The nondimensional wavelength is related to the nondimensional wave number by $\lambda' = 2\pi/k'$, the nondimensional wave number is related to the nondimensional frequency by the nondimensional dispersion relation

$$\omega'^2 = k' \tanh k'h'$$

and the nondimensional group velocity is, $c'_g = g^{1/2}d^{-3/2}c_g$. For this study, a nondimensional water depth of $h' = 4$ is used because this would, for instance, represent a 10m diameter full scale WEC in 40m of water, which seems typical.

The power absorbed by the WEC and the energy flux through the wave field are nondimensionalized as $P' = \rho^{-1}g^{-3/2}d^{-7/2}P$, and $\mathcal{F}' = \rho^{-1}g^{-3/2}d^{-7/2}\mathcal{F}$ respectively. Unless otherwise specified for the remainder of Sec. 4.1, all quantities shall be the nondimensional quantities and the word “nondimensional” shall be left out. Power absorption by the WEC shall occur through a linear power take-off (PTO) damping,

$$P' = \frac{1}{2}\omega'^2 D' |\xi'_x|^2$$

For a given set of incident wave conditions, there is a D' value that maximizes the amount of power absorbed by the WEC. At and near the resonant frequency, the optimal D' can lead to motions that are very large. Just as the amplitude of optimal motions can be considered unrealistically large, so too can the motions for the optimal D' value. A heaving cylinder does not move at these predicted large amplitudes because of nonlinear effects and hydrodynamic viscous forces. In order to make the motions of the heaving WEC more realistic, a suboptimal D' value is chosen. For this study, the value of $D' = 0.15$ is used.

A plot of $|\xi'/A'|$, or the response amplitude operator (RAO), for the heaving

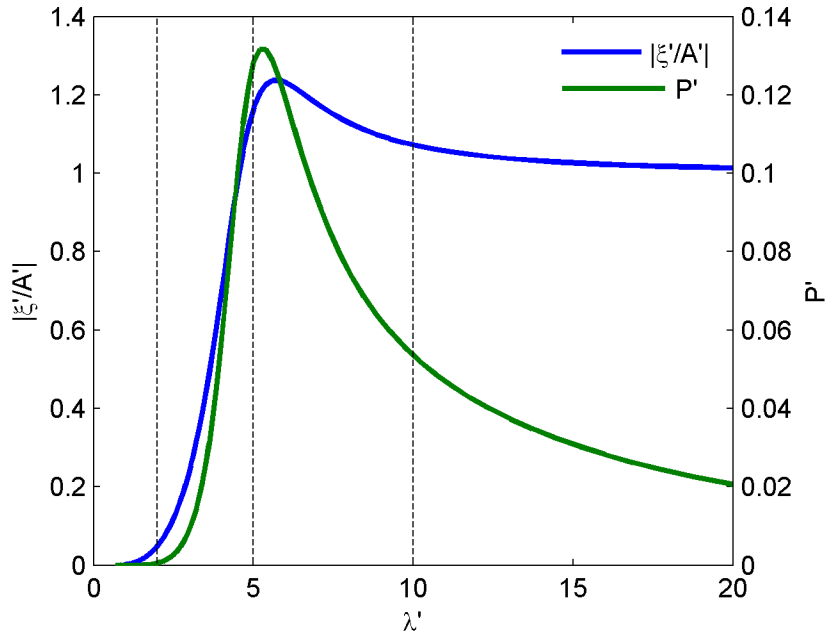


Figure 4: The RAO, $|\xi'/A'|$, is shown in blue and corresponds to the left-hand axis, and the WEC power absorption, P' , is shown in green and its axis is on the right.

WEC as a function of wavelength is shown as the blue line in Fig. 4. The RAO indicates the relative motion response of the WEC at different frequencies. For long waves, $|\xi'/A'| \approx 1$, which means the WEC mostly follows the motion of the waves. At a wavelength slight greater than $\lambda' = 5$, there is a resonant peak, and for short waves, the WEC motion goes to zero. The green line in Fig. 4 shows the power absorption of the WEC as a function of wavelength. The peak of the power absorption occurs near the resonant frequency, and power absorption decays for both longer and shorter waves. The RAO and power curves are typical of heaving WECs with linear PTO.

4.1.1 Regular Waves

Figure 5 shows the real part of four wave fields, the incident, $\text{Re}\{\eta'_i\}$, the diffracted, $\text{Re}\{\eta'_d\}$, the radiated, $\text{Re}\{\eta'_r\}$, and the total, $\text{Re}\{\eta'_t\}$ in different rows, at three different wave lengths, $\lambda' = 2$, $\lambda' = 5$, and $\lambda' = 10$ in different columns. These wavelengths are indicated by the vertical dashed lines in Fig. 4. The axes in all of the plots in Fig. 5 are the same; the x -axis is x'/λ' and the y -axis is y'/λ' , where the limits in both the x -axis and y -axis go from

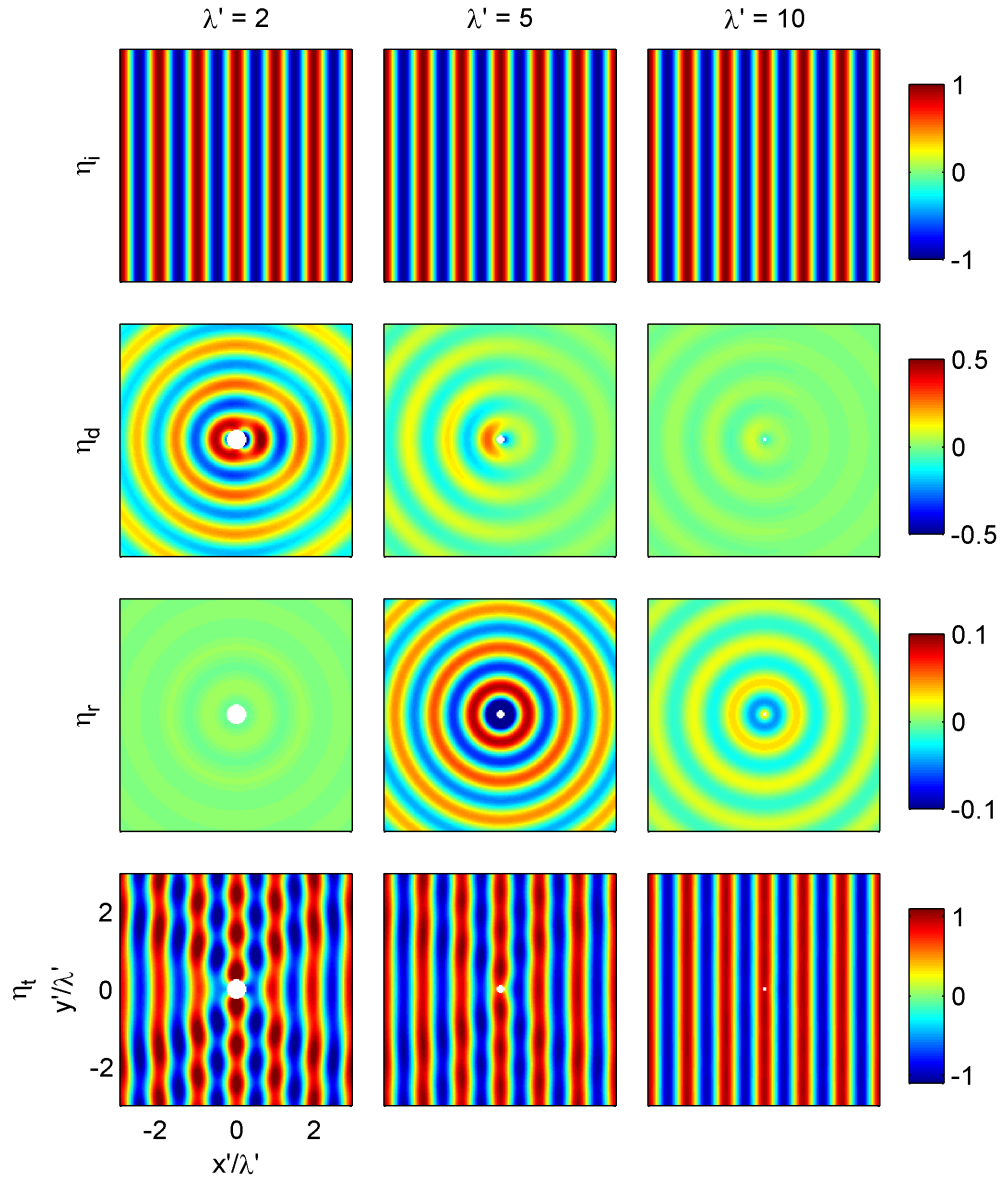


Figure 5: The figure shows real values of the incident, $\text{Re} \{ \eta_i \}$, the diffracted, $\text{Re} \{ \eta_d \}$, the radiated, $\text{Re} \{ \eta_r \}$, and the total, $\text{Re} \{ \eta_t \}$, wave fields at $\lambda' = 2$, $\lambda' = 5$, and $\lambda' = 10$. The real values are the instantaneous wave elevation at time $t = 0 \text{ s}$.

–3 to 3, and are shown in the bottom left hand figure. The axes scaling was designed so that six wavelengths fit in the wave field regardless of λ' . A result of this scaling is that the cylinder appears to shrink with increasing λ' (figures from left to right). An equally valid perspective is that the field of view is “zoomed-out” with increasing λ' .

The real part of η shows the wave elevation at time $t = 0$. In all figures, one can clearly see periodic wave patterns. The incident wave field (top row) is clearly a planar regular wave. It appears the same for all wavelengths because the incident wave is independent of the body geometry. The diffracted (second row) and radiated (third row) wave fields have an obvious circular pattern, which is periodic in the radial direction. The angular variation of the diffracted wave field is interesting. It appears as if the wave is not circular (note the asymmetry from left to right), but the wave field can still be represented by the complex generated wave function, $f(\theta)$, where the magnitude and phase changes from the front to the back of the device (left to right in the figure), because of the directionality of the incident wave. Because the device is axisymmetric and operating in heave, the radiated wave field is isotropic, which mathematically means that it has a constant generated wave function, $f(\theta) = f$, as discussed in Sec. 3.5.

Comparison of each type of wave field at different wavelengths helps to illustrate fundamental WEC concepts. The color scaling is the same across columns but varies between rows and is indicated by the color bars on the right. The diffracted wave field has the largest amplitude for the shortest wavelength, and is very weak for the longest wavelength. The point-absorber assumption states that if the wavelength is much greater than the device dimensions, the diffracted wave can be neglected, which may be reasonable in this example at the longest wavelength.

The radiated wave elevation is a function of the device geometry and the amplitude of the device motion at a given frequency. Insight into the radiated waves can be gained from Fig. 4. At $\lambda' = 2$, the relative motion and power absorption of the WEC are very small, at $\lambda' = 5$, the motion and power absorption are near the maximum, and at $\lambda' = 10$ the motion and power absorption are moderate. The radiated wave fields shown in Fig. 5 follow the same trend. It is almost nonexistent at $\lambda' = 2$ where the power absorption is very close to zero. It is maximized at $\lambda' = 5$, and slightly smaller at $\lambda' = 10$. In linear wave theory, while the phase of the wave is critical, in order to absorb

energy from the wave field, a finite amplitude radiated wave is required.

The bottom row of figures show the total wave elevation, which is the real part of the sum of the complex incident, diffracted, and radiated wave elevations. One can see waves that are nearly regular but are modulated in magnitude with respect to space, which indicates the presence of standing waves. The modulation of the waves is more discernible at the shorter wavelengths. However, it is difficult to learn a great deal from these figures. A plot of the magnitude of the wave elevation, makes the standing wave effect much more clear.

Figure 6 shows the magnitude of the combined incident and diffracted wave fields, $|\eta'_i + \eta'_d|$, and the total wave field, $|\eta'_t|$. The combined incident and diffracted wave field is significant because it is the wave field of a fixed device, for which, the wave field is modified, but no energy is removed. In Fig. 6 all plots have the same color scaling. The magnitude is centered around 1, which is the magnitude of a unit-amplitude incident wave. All plots show with varying degrees of intensity, standing waves in the form of parabolas where the crests are shown in hot colors and the troughs in cool colors. These are the parabolic formations described in Sec. 3.5 and used by Child and Venugopal [2] in the Parabolic Intersection method. The height of the standing waves decreases with increasing wavelength. The shortest wavelength produces the most intense standing waves, and in the plot of the longest wavelength, the standing waves are almost nonexistent.

It is interesting to compare the wave field of the fixed cylinder (top row of Fig. 6) to that of the energy extracting WEC (bottom row). For $\lambda' = 2$, both wave fields appear identical, which is not surprising because at this wavelength, the WEC hardly moves at all (see Fig. 4). At $\lambda' = 5$, the WEC moves a great deal and absorbs a large amount of energy. This energy absorption is clearly visible by comparing the incident and diffracted wave field to the total wave field. In the plot of the incident and diffracted wave field, most of the effect on the wave field occurs in front of the device in the form of reflection and there is little shadowing. In the plot of the total wave field, there is a distinct parabolic wave shadow in the lee of the device. For the longest wave, $\lambda' = 10$, there does not appear to be much of a shadow in either of the wave fields, but the effect of energy extraction seems to be that the standing waves in front of the WEC are smaller than those of the fixed WEC. That is, it reduces the amount of wave reflection.

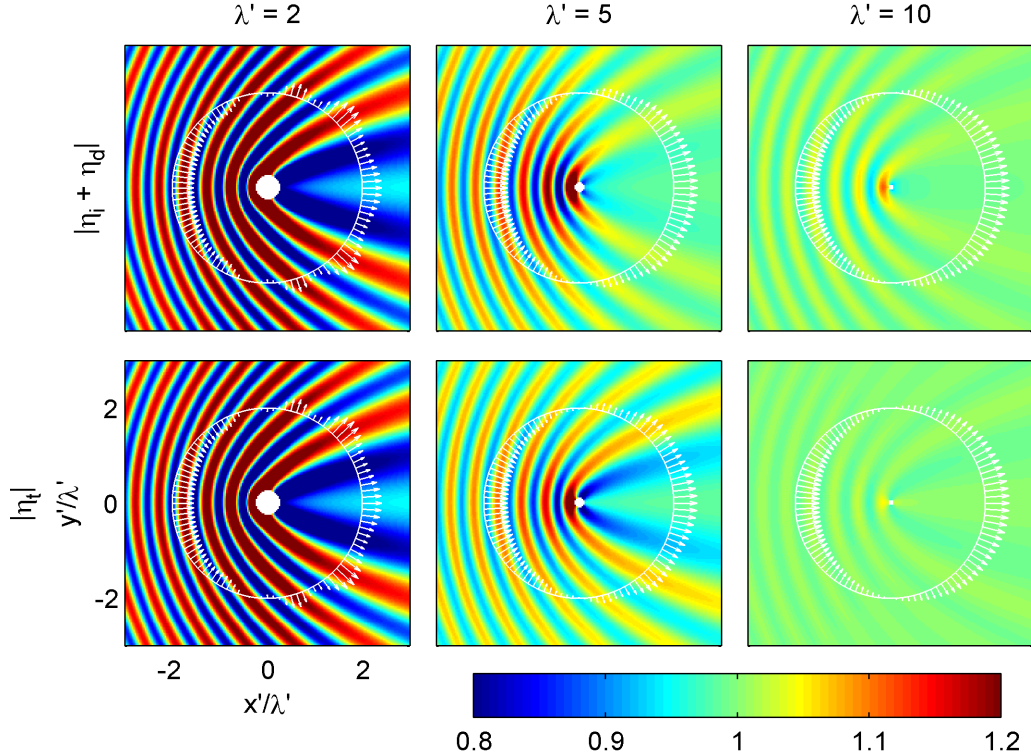


Figure 6: The figures show magnitudes of the wave elevation for a fixed cylinder, $|\eta_i + \eta_d|$, and for the heaving WEC, $|\eta_t|$, at three wavelengths, $\lambda' = 2$, $\lambda' = 5$, and $\lambda' = 10$. Parabolic standing wave patterns and a parabolic wave shadow are visible. The waves shadow is most apparent in the plot of $|\eta_t|$ at $\lambda = 5$, which is where the WEC absorbs the most energy. The white circles represent control surfaces, each has a radius equal to two wavelengths, and the white vectors are graphical representations of the wave energy flux through the control surface where the direction of the arrow is the direction of the control surface normal and the arrow length is the magnitude of the energy flux at that point.

Also shown in Fig. 6 are white circles and vectors, which are graphical representations of the wave energy flux through a cylindrical control surface surrounding the WEC. The energy flux through the wave field is computed with Eqn. 15. As mentioned at the end of Sec. 3.4, the energy flux through a control surface surrounding a WEC should be equal to the power absorbed by the WEC. The computed values of WEC power (Eqn. 11) and energy flux through the wave field (Eqn. 15) are within 0.5 % of one another. The agreement serves to verify the method of computing energy flux as well as the accuracy of the wave field. The vectors in the figures point in the directions of the control surface normals and the magnitudes of the vectors, including the signs, are the magnitudes of the flux at those points on the control surface. A vector pointing inward indicates a net energy flux into the control surface and a vector pointing outward indicates a net flux out. One can see variation in the magnitude of flux along the control surface corresponding to the magnitude of the standing wave through which the control surface passes. This is most apparent behind the WEC in the $\lambda' = 2$ plots. The differences between the magnitude of the vectors of the fixed case as compared to the power absorbing case appears quite small, but this is because the power absorption is small. At $\lambda' = 5$, the power absorption is $P' = 0.13$, which means that only 13 % of the wave power incident to the WEC is absorbed.

The $\lambda' = 2$ case is also significant because even though there is no energy extracted, the presence of the device significantly modifies the wave field including the creation of a parabolic wave shadow. There are also large standing wave ridges. Energy lost in the wave shadow is recuperated at other locations in the wave field, so that the net wave energy flux is nearly zero. The WEC modifies the wave field by reflecting and diffracting waves without extracting energy. This effect on the wave field shall be termed wave scattering, and is more prevalent at short wavelengths.

Another useful way to visualize the wave field is through transects of the wave elevation or energy flux. A longshore transect of the wave elevation is simply a plot of η' as a function of y' at a constant x' , or a slice of the wave field at a constant x' . A cross-shore wave elevation transect is a slice of the wave field at a constant y' . A longshore energy flux transect is the flux of energy through a planar control surface at a constant x' . The energy flux is related to the wave elevation, but because the flux computation includes directionality they are not linearly proportional to one another. One method

of approximating energy flux through the wave field is to assume that the waves are planar and are propagating in the direction of the incident waves, so that the energy flux can be computed by applying the complex wave elevation at field points, η' , to Eqn. 16 through a delta width in the longshore, $\Delta y'$. This is relevant because in phase-averaged wave models, such as SWAN, the waves are planar by definition and the planar wave approximation is the only means of computing energy flux. In nondimensional form, the planar wave energy flux approximation is

$$\mathcal{F}'_{pl-ap} = \frac{1}{2} |\eta'|^2 c_g' \Delta y' \quad (27)$$

Figure 7 compares the shoreward energy flux computed by Eqn. 15 to the planar wave flux approximation, Eqn. 27, across five longshore transects at $x'/\lambda' = -1, 0, 1, 2, 3$ for $\lambda' = 5$. $x'/\lambda' = -1$ is an offshore transect, $x'/\lambda' = 0$ is a transect that cuts through the WEC, and the other three transects are in the lee of the WEC. In the lee of the WEC, the planar wave flux approximation and the true flux are in reasonable agreement. However near the WEC and in front of it, the difference between the two is quite large. In all regions, the energy flux is not as large as that predicted by the planar wave approximation because the planar wave approximation assumes that all the energy is traveling toward the WEC, while in reality the radiated and diffracted energy is directed radially outwards from the WEC. The difference between the two is most significant offshore because the difference between the direction of the incident and of the radiated and diffracted waves is the greatest. Even though there may be large variation in the wave height in the longshore, the variation in the net wave energy flux relatively small. In the lee, the incident, radiated, and diffracted waves are traveling in mostly the same direction, and so the wave height is a reasonable indicator of the wave energy flux.

The pattern of the wave energy flux in the lee of the WEC is of a particular shape that appears to expand as the distance behind the WEC increases. Compare the longshore transects at $x'/\lambda' = 1, 2, 3$ in Fig. 7. The transects of $x'/\lambda' = 2$ and $x'/\lambda' = 3$ appear to be a stretched version of the transect at $x'/\lambda' = 1$. This is the same transect shape and stretching pattern is described by Farley [3] for any generic system of WECs.

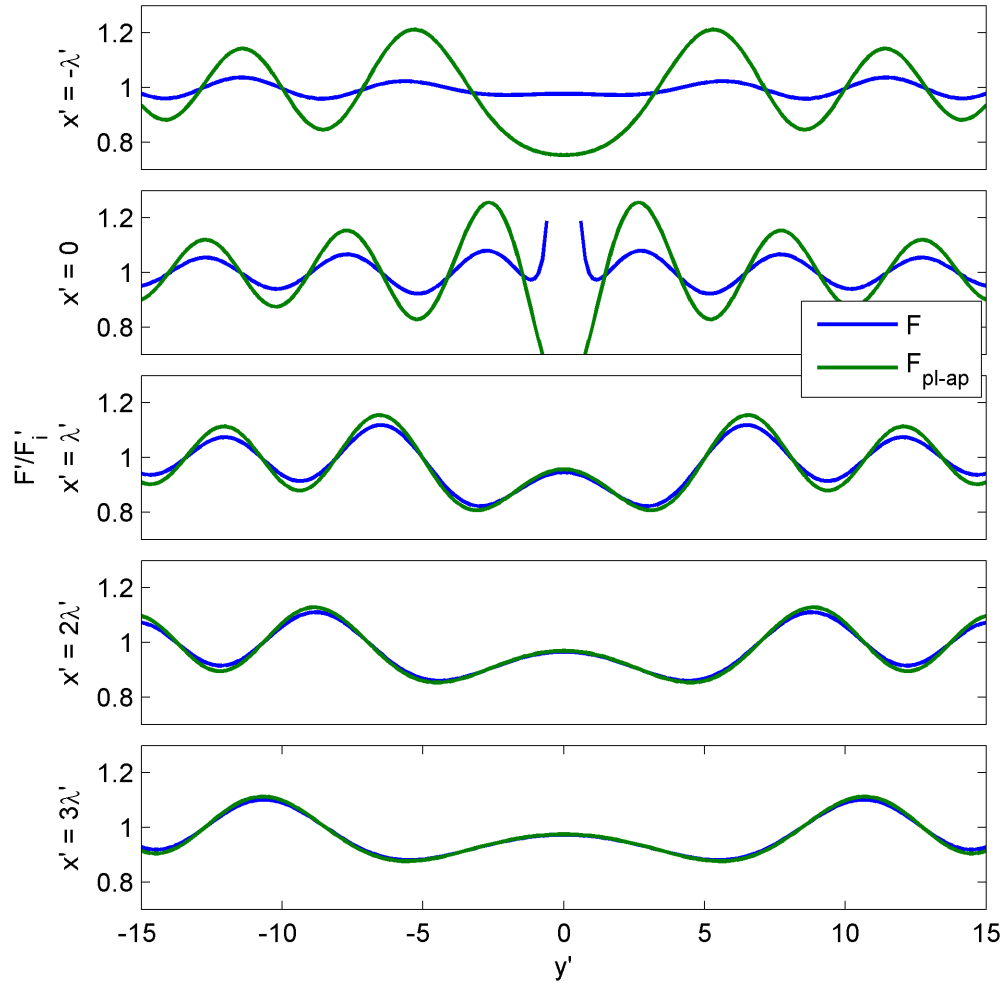


Figure 7: The figure shows longshore transects of wave energy flux computed using Eqn. 15 compared to transects of the planar wave approximation of wave energy flux computed using Eqn. 27. The wavelength is $\lambda' = 5$, and transects are shown at one wavelength in front of the device, through the device, and at one, two, and three wavelengths behind the device. The y-axis is the wave field flux normalized by the incident flux.

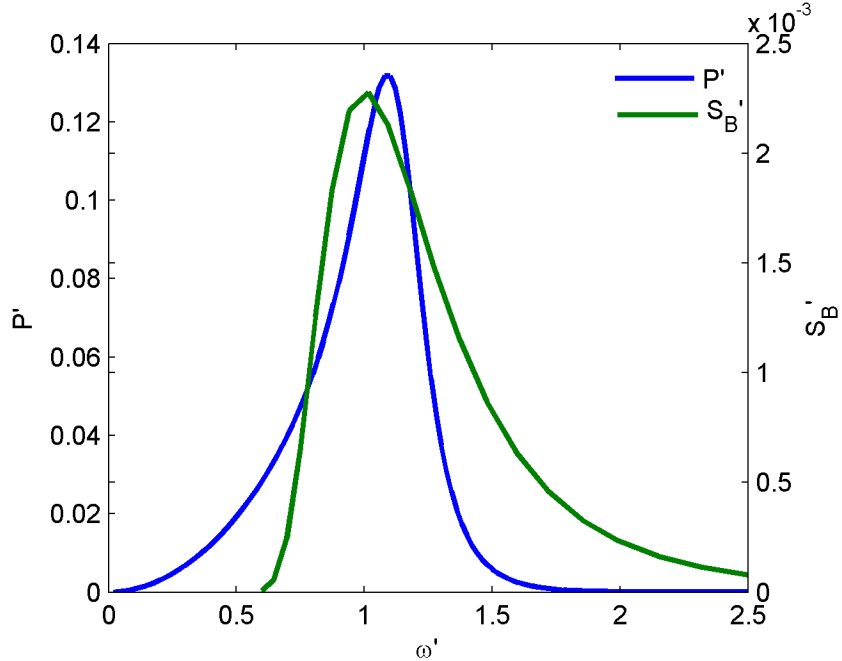


Figure 8: The figure shows the non-dimensional incident wave spectrum (S'_B) and WEC power absorption curve P' .

4.1.2 Spectral Seas

To examine the irregular wave field, a spectrum is applied to incident wave components as described in Sec. 2.1. Consider the nondimensional Bretschneider spectrum

$$S'_B(\omega) = \frac{1.25}{4} \frac{\omega'^4}{\omega'^5} H_s'^2 e^{-1.25(\omega'_m/\omega')^4}$$

where ω'_m is the nondimensional modal frequency, H_s' is the nondimensional significant wave height, and the parameters are made nondimensional as $S'_B = g^{-1/2}d^{-5/2}S_B$, $\omega'_m = g^{-1/2}d^{1/2}\omega$, and $H_s' = d^{-1}H_s$. First, consider the long-crested case, in which all wave components are traveling in the direction $\beta = 0^\circ$. The modal frequency is chosen to be near the resonant frequency of the device, $\omega'_m = 1$, and the significant wave height is chosen as $H_s' = 0.5$. The spectrum and power absorption curve as a function of frequency are shown in Fig. 8.

Figure 9 shows the significant wave height of the wave field for the fixed WEC case ($\eta'_i + \eta'_d$) and for the power absorbing WEC (η'_t). The significant wave height is normalized by the incident wave significant wave height, H_s'/H_{s-in}' , so that in regions of green, the significant wave height of the wave

field is the same as that of the incident. Although, there are still thin parabolic ridges in the offshore, the clearly defined parabolic standing wave patterns of regular wave fields are mostly smoothed out in significant wave height. There is also a clear parabolic wave shadow for both the fixed cylinder and total wave fields. Even a device not absorbing power creates a wave shadow due to wave scattering. The wave shadow of the power absorbing WEC is more intense and extends further in the lee than that of the fixed WEC. Also interesting is that the fixed WEC creates an intense peak in the wave height immediately in front of and around itself. However, this peak appears to be significantly diminished for the power absorbing WEC. By absorbing power, the WEC not only increases the wave show in its lee, but also reduces reflection in the offshore.

Examining the significant wave height wave field only tells part of the story. At each field point, there is a complete wave spectrum. In the total wave field of Fig. 9, white dots indicate points at which wave spectra are examined, three between the WEC and the wave source, or offshore, and three behind the WEC, or in the lee. Each set is numbered 1 through 3 with increasing y' . The spectra along with the original incident wave spectrum are shown in Fig. 10. First, examine the lee spectra. Spectrum “Lee 2” is taken from within the wave shadow. It shows a uniform reduction in wave energy across almost all frequencies, meaning that for most frequencies, there is a wave shadow here. In contrast, spectrum “Lee 3” shows almost no reduction in energy, because at this point, there is no wave shadow for most frequencies. “Lee 1” is quite interesting, because it shows a reduction in energy at some frequencies but a gain in energy at others. This phenomenon will become more clear in the examination of the offshore spectra.

The energy density of all offshore spectra oscillates between being less than and being greater than the incident energy as a function of frequency. This is most apparent in “Offshore 3,” which is in line with the WEC and the wave propagation. The oscillations in spectral energy are the result of spatial variations of the peaks and troughs of standing waves at different frequencies. At a given point in space, some wave frequencies will have a standing wave trough and others will have a peak. Figure 11 helps to visually explain this phenomenon. It shows cross-shore transect of the wave elevation at five frequencies for the position $y' = 0$, which cuts through the WEC, offshore spectrum 3 and lee spectrum 3. In Fig. 11, the position of the WEC is indi-

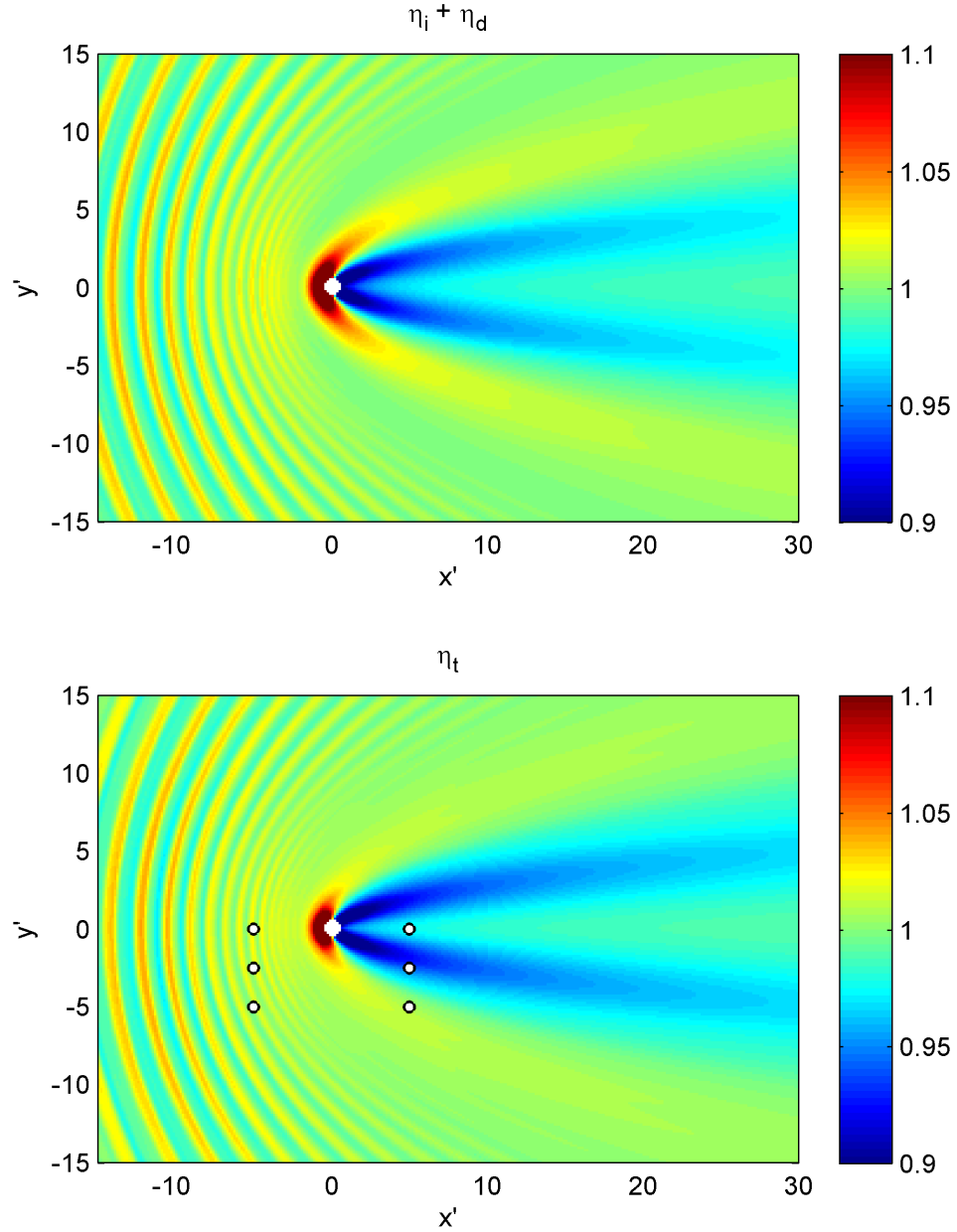


Figure 9: The figures show the normalized significant wave height (H'_s at field points divided by the incident H'_{s-in}) for the WEC held fixed ($|\eta_i + \eta_d|$) at the top and the power absorbing WEC ($|\eta_t|$) at the bottom in the non-directional spectral wave field. The incident wave spectrum is shown in Fig. 8. In the total wave field figure, the white dots indicate the locations at which wave field spectra are examined. The offshore spectra occur at $x' = -5$ and the lee spectra are at $x' = 5$. The spectra labeled 1 are located at $y' = -5$, 2 at $y' = -2.5$, and 3 at $y' = 0$.

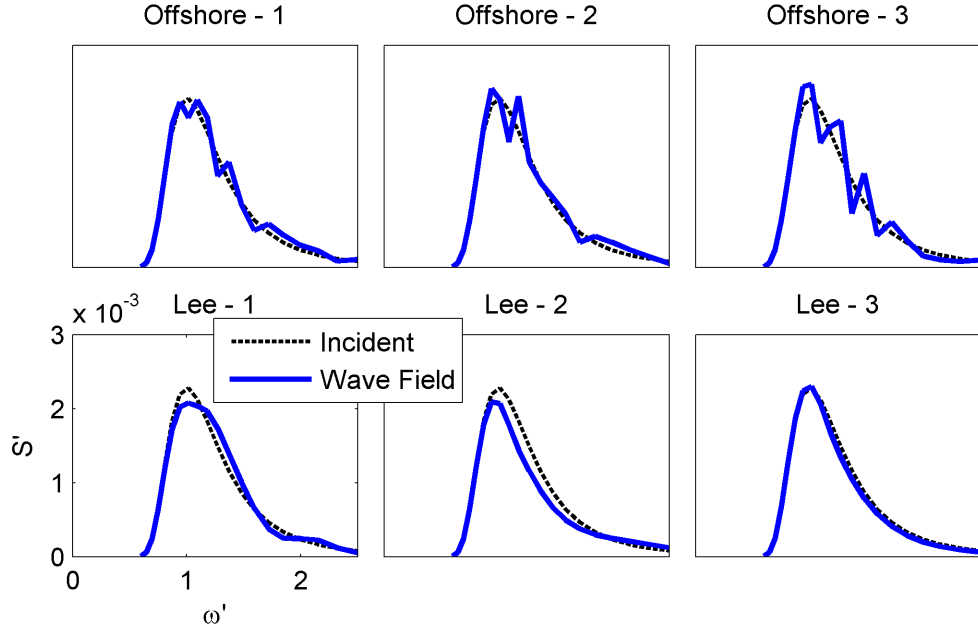


Figure 10: Figures show the field spectra for the power absorbing WEC along with the incident wave spectrum. The locations can be seen in Fig. 9. Note the spikes in the offshore spectra, while the lee spectra are smooth.

cated by a hole in the elevation, and the positions of the spectra are vertical solid lines. The horizontal dashed line shows the magnitude of the incident wave component at that given frequency. At $\omega' = 0.94$, “Offshore 3” is located at a peak of a standing wave, and the spectrum shows a corresponding peak in Fig. 10. At $\omega' = 1.09$, “Offshore 3” is located in the trough, and the spectrum shows a hole. At $\omega' = 1.18$, “Offshore 3” is near a node and the spectrum is almost the same as the incident. The pattern continues as such. The magnitudes and locations of the peaks and troughs are dependent on the generated wave function, $f(\theta)$, which depends on the WEC geometry, motions, and precise location.

Now consider a spectrum with directional spreading defined by the function

$$G(\beta) = \gamma \cos^{2s} \left(\frac{1}{2}\beta \right) \text{ for } -180^\circ < \beta \leq 180^\circ$$

$$\gamma = \frac{\Gamma(s+1)}{2\sqrt{\pi}\Gamma(s+\frac{1}{2})}$$

where the coefficient γ normalizes the area of $G(\beta)$ to 1 and Γ is the gamma function. s is a parameter that defines the width of spreading. A lower value of

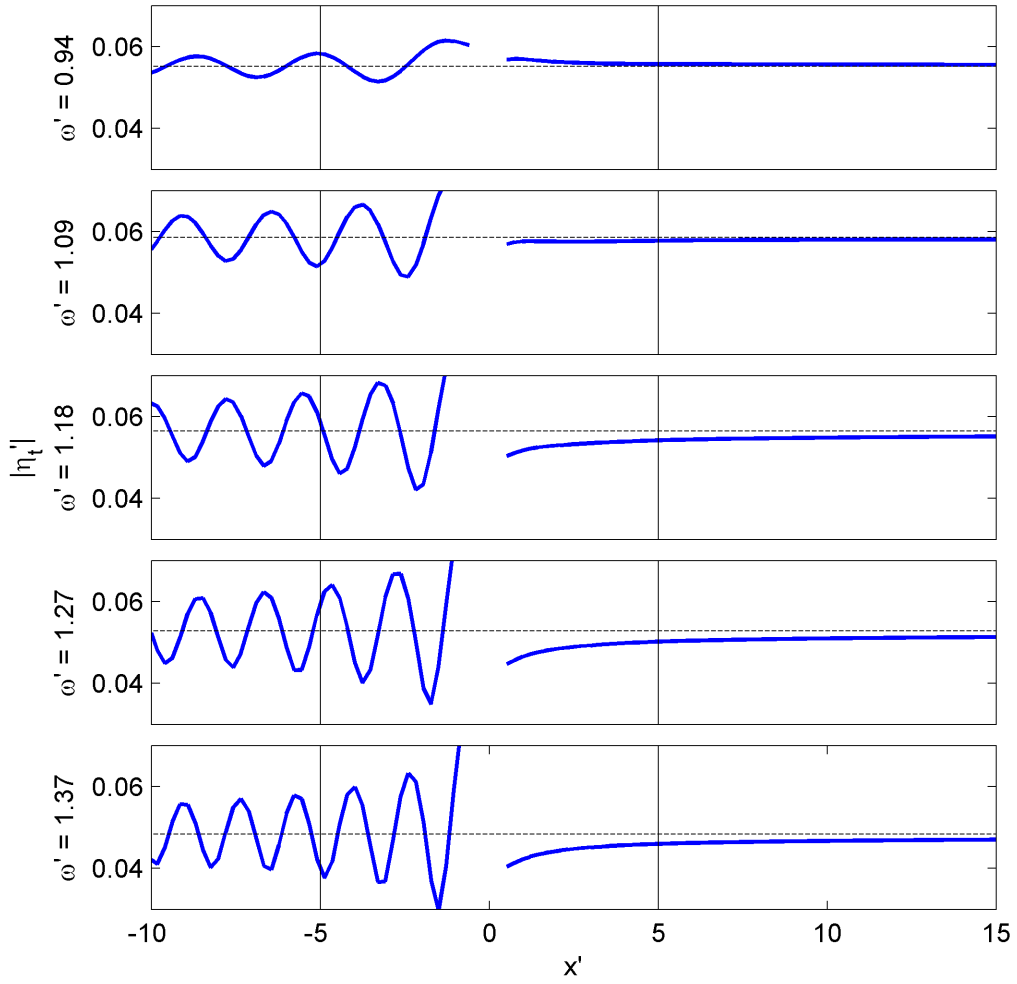


Figure 11: The figures show cross-shore transects at $x' = 0$ of the magnitude of the wave elevation of the total wave field for different frequencies. The hole in the elevation is the location of the WEC, and the vertical lines indicate the locations where spectra were examined. Note how the magnitude varies at each frequency at the location of the offshore spectrum. This causes the spikes in the offshore spectra.

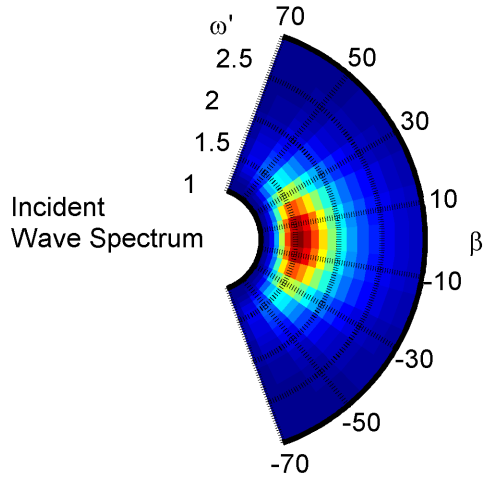


Figure 12: The figure shows the incident wave spectrum for the directional case.

s makes the directional spreading broader. As an example of spread spectrum wave field, take $s = 10$ as shown in Fig. 12. The resulting wave fields are shown in Fig. 13 as plots of the significant wave height for the fixed WEC and the power absorbing WEC. The wave fields in both figures are even more smooth than they were for the unidirectional case, and the parabolic wave shadow has become an egg shape. As with the unidirectional case, the shadow of the power absorbing WEC is greater than that of the fixed WEC and the reflection is reduced.

Figure 14 shows the directional spectra taken at field points. As with the unidirectional case, the offshore spectra are highly variable in energy density with peaks and troughs as a function of frequency and direction. The lee spectra are much more orderly in their shape. It is interesting to note that the direction of the peak of the wave energy shifts with position in the lee of the WEC. For instance, for “Lee 1” the peak is about 10° , while incident peak is at 0° . This is not too surprising; the WEC blocks wave energy from directions of 0° or less, but would do little to block energy traveling at positive directions. Perhaps if a WEC design is very directionally dependent, an array designer may want to orient WECs in the second row of an array so that they point outwards.

Wave fields around a generic heaving WEC are examined computationally. Patterns including parabolic standing waves, wave shadows, and frequency

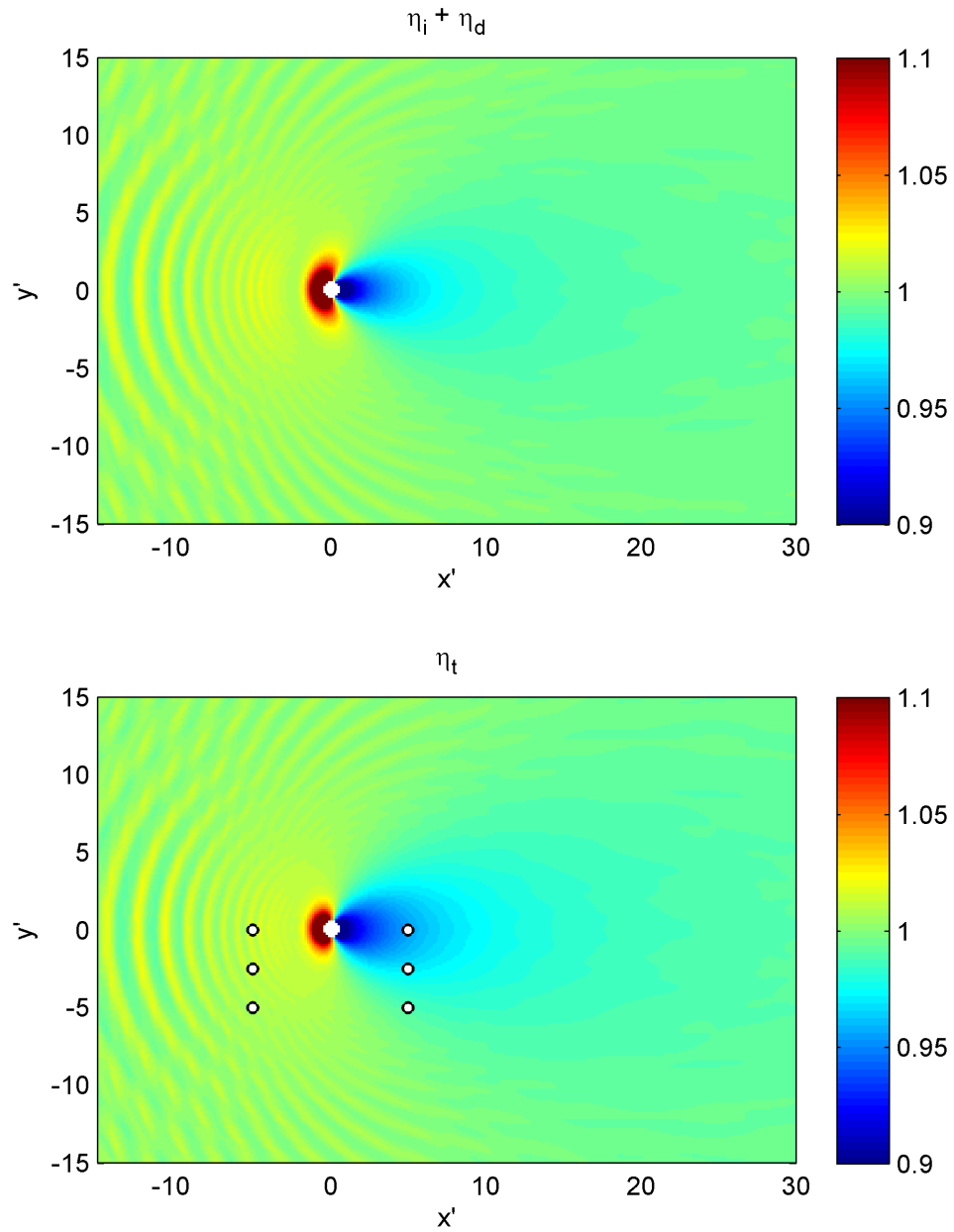


Figure 13: The figures show the normalized significant wave height (H'_s at field points divided by the incident H'_s) for the WEC held fixed (incident plus diffracted) at the top and the power absorbing WEC (total wave field) at the bottom in the directional spectral wave field. The incident wave spectrum is shown in Fig. 12. In the total wave field figure, the white dots indicate the locations at which wave field spectra are examined. The offshore spectra occur at $x' = -5$ and the lee spectra are at $x' = 5$. The spectra labeled 1 have are at $y' = -5$, 2 are at $y' = -2.5$, and 3 are at $y' = 0$.

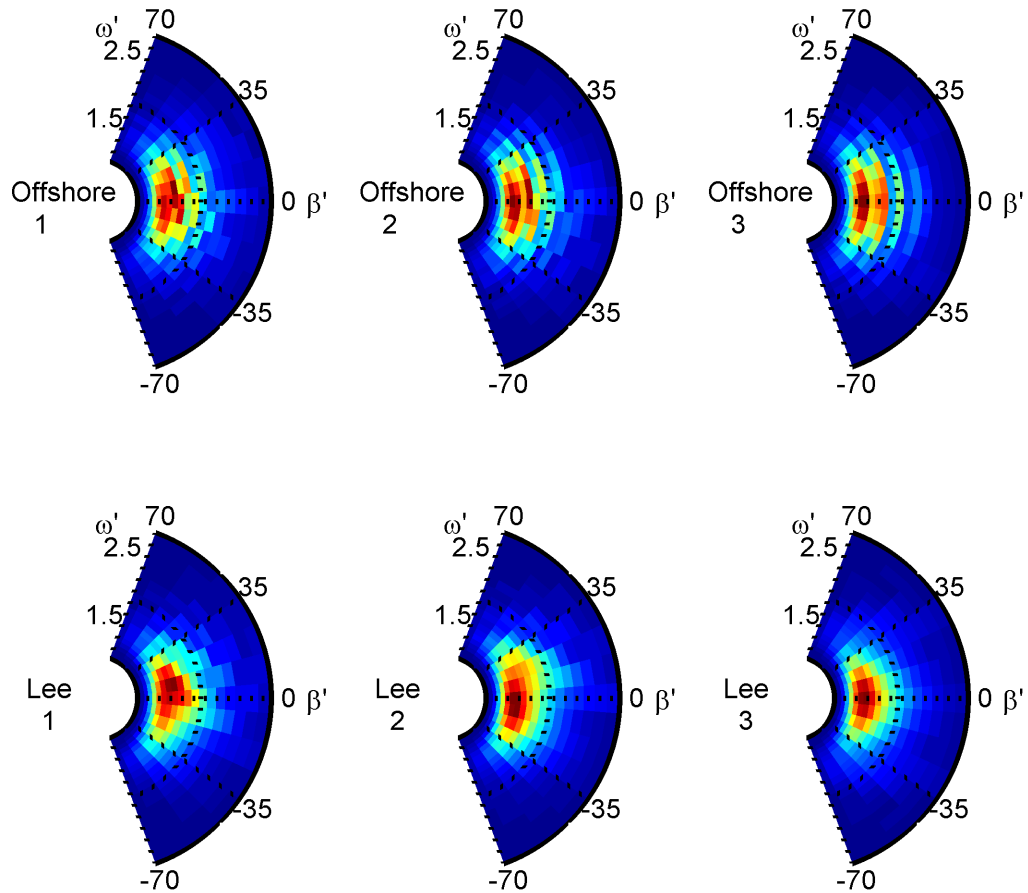


Figure 14: The figures show the wave field spectra for the directional incident wave case. The locations of the spectra can be seen in Fig. 13.



Figure 15: The photo shows the WEC array experiment for the 5 WEC case conducted in the O.H. Hinsdale Tsunami Wave Basin at Oregon State University [1].

dependent spikes in offshore spectra are described. Many of these patterns are also found in the WEC array experimental data described in the next section.

4.2 Experimental Wave Field Analysis

Over the winter of 2010-11, Oregon State University and Columbia Power Technologies, Inc. (CPT) conducted experiments on scale models of the CPT WEC design “Manta” in the O.H. Hinsdale Tsunami Wave Basin. Tests were performed on a single WEC as well as WEC arrays in a variety of wave conditions and extensive measurements were made of the wave field with a variety of instruments. A picture of the experiment is found in Fig. 15, and Fig 16 shows the experimental layout including the location of the WECs and wave gauges. The experimental wave conditions include regular waves at different frequencies and amplitudes, and irregular waves from seven sea states with and without directional spreading. A list of the regular wave conditions and the sea states of the irregular wave conditions is found in Table 1. The experiment is described by Haller et al. [1]. Experimental data presented here was provided by Porter, and details on the data analysis can be found in his Masters thesis [31]

In Sec. 4.1, modeling of the wave field around a generic WEC produced

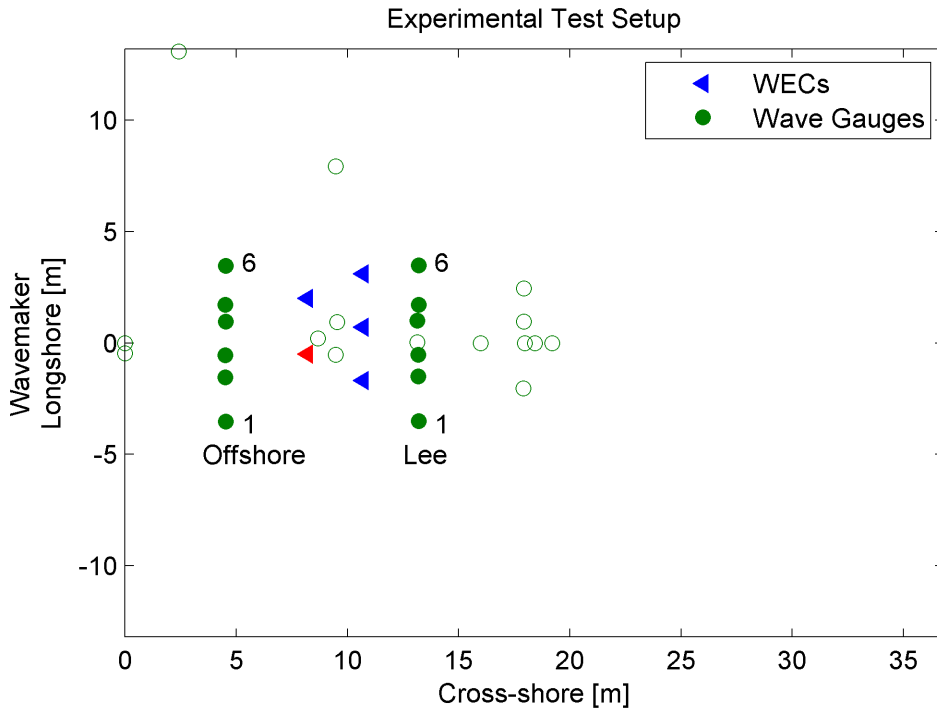


Figure 16: The figure shows tests experimental layout of the WEC array tests. The location of the WEC for the single WEC tests is shown as the red triangle. The filled-in circles indicate the offshore and lee wave gauges at which comparisons are made. Empty circles are gauges present in the experiment but not used in this analysis.

interesting information about wave field characteristics including parabolic standing wave formations, wave shadows, and modification of the offshore and lee wave spectra. The data from the WEC Array tests provides a valuable resource for validating the existence of these wave field patterns. Many of the wave field patterns are somewhat non-intuitive, and so computational modeling also aides in the interpretation and analysis of the experimental wave field data.

In order to model the WEC array experiments, a geometric model of the physical WEC under test is required. The actual physical model is described by Haller et al. [1] and is shown in Fig. 17. Because of proprietary issues and time limitations, a simple cylindrical WEC (also shown in Fig. 17) was adopted as the geometry for the computational model. Although the cylinder is a very rough approximation of the physical model, it was believed that a computational model with the cylinder could still provide useful information



Figure 17: On the left is the Manta geometry that was used in the WEC array tests [1] and on the right is the cylinder that was used as the computational model.

about the WEC wave field. In order to make the cylindrical model similar to the physical model, three things were designed into it. First, the dimensions of the cylinder were chosen to match the approximate size of the physical model. The diameter and draft of the computational model WEC were selected as $d = 0.6\text{ m}$ and $l = 0.8\text{ m}$ respectively. Secondly, the single degree-of-freedom mode of motion was chosen to be surge because surge most closely resembles the power absorbing motion of the WEC under test. The power absorption curve of the surging cylindrical WEC is closer in shape to that of the physical model than are the power curves for other modes of motion. Finally, a PTO damping was chosen for the computational model WEC so that the power absorbed was of the same approximate magnitude with a peak at approximately the same frequency as the physical model. The dimensional damping value is $D = 2000\text{kg/s}$, and the power absorption curve and RAO of the computational model WEC are shown in Fig. 18. In this case, the power absorption is plotted as the relative capture width (RCW), which is the ratio of wave power absorbed by the device to the wave power incident to the device's width.

The modeled wave field domain is the same size as the Tsunami Wave Basin. The water depth is a uniform $h = 1.4\text{ m}$. No effort was made to model the sloping beach, wave basin walls or the wave maker. Wave data from 21 wave gauges is available for comparison. Initially, interpolation of wave height between the wave gauges was explored. Figure 19 shows an interpolation of a wave field for a regular wave condition, $T = 1.5\text{ s}$, compared to the compu-

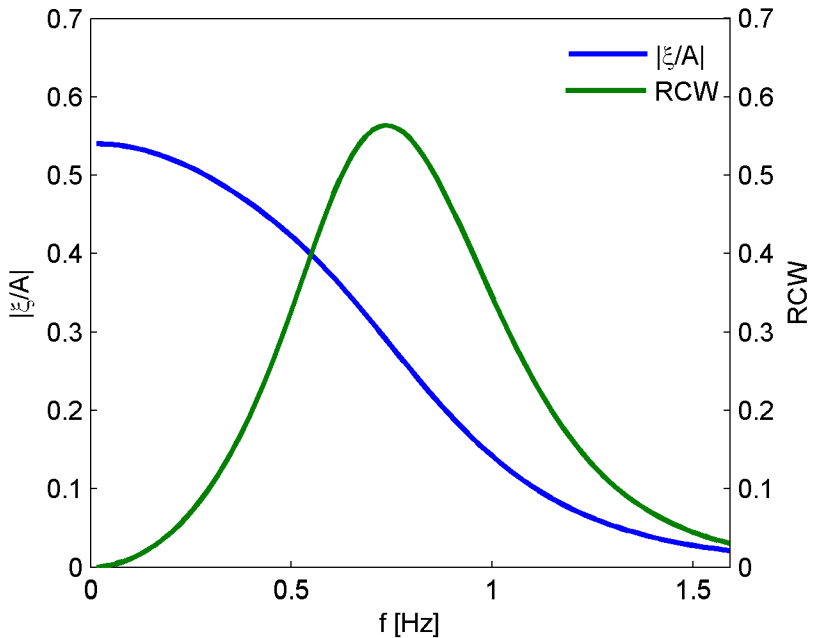


Figure 18: The plot is of the RAO ($|\xi/A|$) and relative capture width (RCW) of cylindrical computational model of the WEC under test.

tational wave field produced by WAMIT. The WEC is indicated by a white circle, and the wave gauges are marked by 'x' and '*' symbols. The experimental data interpolation can be deceiving as it misses significant wave field features and produces wave field features that may not exist. The interpolation smooths a large region of the wave field where the model predicts standing waves. For instance, consider the two gauges at the top of the figure (greatest y value), the interpolation produces a uniform high wave height between the two gauges, but the computational wave field shows that these gauges just happen to be on the crests of standing waves, and between them the wave field varies. Although it is not certain whether the predictions of the computational wave field are in fact the behavior of the real wave field, it raises strong doubts as to the validity of the interpolated wave field.

Instead of making comparisons of the interpolated wave field, comparisons are made directly at two sets of wave gauges. One, called the offshore wave gauges, is the set of six gauges indicated by 'x' symbols in Fig. 19 that is between the WEC and the wave maker (lowest x value). The other set, called the lee wave gauges, is the line of six 'x' gauges behind the WEC in Fig. 19. The offshore and lee wave gauges are numbered 1 to 6 from left to right facing the wave maker. The numbering can be seen clearly in Fig. 16.

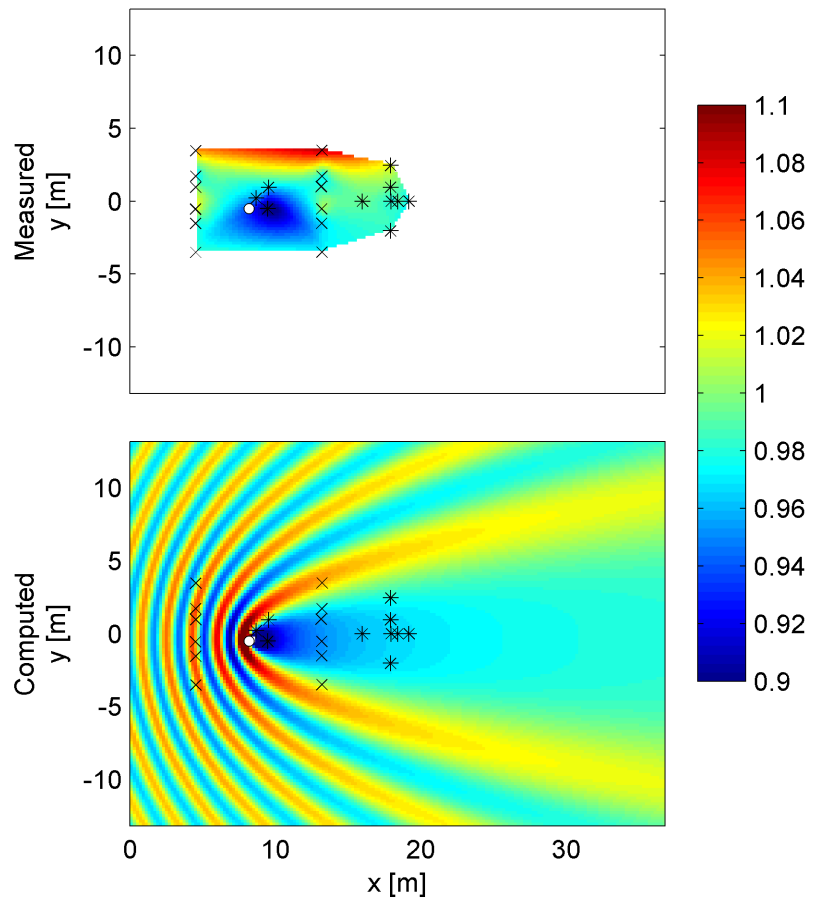


Figure 19: The top figure shows an interpolation between the values measured at the wave gauges for a regular wave with a period of $T = 1.5$ s. The bottom figure shows the WAMIT wave field for the same wave. Note how the interpolation may distort features of the wave field.

4.2.1 Incident Wave Conditions

Determining the incident wave conditions was one of the challenges of the data analysis. The incident wave conditions are critical for determining the wave power delivered to the WECs and for calibrating the computational wave fields. Wave makers are not perfect and cannot be expected to produce precisely the wave conditions entered into their setup. One should use measurements to determine the actual waves produced.

It was believed that the offshore wave gauges would be sufficient to measure the incident wave conditions. However, the offshore gauges are within the wave field region affected by the WECs. For example, in Fig. 19 the computational result predict the offshore gauges to be on the crest of a standing wave. If one were to believe these results, then the wave height measured at the offshore gauges for this wave period would be 10% higher than the incident. However, the computational predictions should not be used adjust the incident wave heights. Determining the incident wave conditions is more challenging for spectral seas where multiple frequencies exist simultaneously. The spectra at the offshore gauges show peaks and troughs from frequency to frequency as was discussed in Sec. 4.1.2 and shown in Fig. 10. Also, as the number of WECs increases, the wave conditions measured by the offshore gauges diverge more severely from the condition supplied to the wave maker, which indicates that the offshore wave data is dependent on the WECs.

In order to compare experimental data with computational data, one needs to know the incident wave conditions to scale the computational results. WAMIT computes results for a unit amplitude wave. The wave field can be scaled linearly by a dimensional incident wave height, and across frequencies by wave amplitudes determined by an incident wave spectrum (see Sec. 2.1). One way of determining incident wave conditions would have been to make wave gauge measurements for an empty tank, that is, in a wave tank without WECs. However, empty tank runs were only performed on a handful of conditions for another purpose.

It was decided that the incident wave conditions should be taken as the average of the offshore gauges and wave gauge 10 for the single WEC case. The single WEC case was selected because the influence of the WEC on the wave field would be less than the WEC influences of the 3 WEC and 5 WEC arrays. The offshore gauges were chosen because they are located in region from which the incident waves propagate, and wave gauge 10 was used because

it is far from the WECs and the WEC influence at gauge 10 should be small. By using the measurements from one particular case as the incident wave conditions for other trials, the assumption is that the wave maker produces repeatable results. The measured incident wave conditions for regular waves and spectral seas are summarized in Table 1. For the spectral seas cases, T_p is the period of the peak of the spectrum and H_{s-in} is the zeroth-moment significant wave height.

Regular Waves		Spectral Seas	
T (s)	H_{in} (cm)	T_p (s)	H_{s-in} (cm)
0.9	5.70	1.25	3.83
1.1	5.70	1.43	6.96
1.5	5.54	1.67	4.43
1.7	5.64	1.54	9.87
1.9	5.47	1.67	7.79
2.1	5.43	2.22	8.25
2.3	5.52	2.22	14.8
2.5	5.59		
2.7	5.37		

Table 1: The tables shows values of the incident wave conditions for regular waves and spectral seas as measured by average of the offshore gauges and wave gauge 10 for the single WEC trials. For the spectral seas cases, T_p is the period of the peak of the spectrum and H_{s-in} is the zeroth-moment significant wave height.

4.2.2 Regular Waves

This section compares the computational results from WAMIT to measured data from the WEC array tests for regular wave conditions. Figure 20 shows the results for the single WEC case. The left-hand column shows the offshore gauges and the right-hand shows the lee gauges. Each row shows a different wave period and the gauges are aligned as if one is facing the wave maker. The experimental data points are shown as diamond symbols. The data points are the average of two or three trials at the same condition. Repeatability between trials was excellent, and the size of the diamonds in the figure is generally greater than the one standard deviation from the average. More information on repeatability can be found in Porter [31].

For a single WEC in regular waves, there appears to be reasonable agreement between the experimental data and the computations. Two especially

exciting results are for the lee gauges at 0.9 second and 1.1 second waves. The experimental data seems to mimic the computational curve that starts with a hump on the left-hand side, decreases in the middle, has another hump to the right and then a hole. This shows the well known standing wave ridge pattern that was discussed in Secs. 3.5 and 4.1 as well as by Farley [3]. It appears that linear wave theory has some skill in modeling the wave field, and that the predicted standing waves do indeed exist for real waves. Without the linear computation model, interpreting the hills and valleys of the data transect would have been much more difficult.

For the offshore cases, the data and the model do not align as well, but as mentioned in Sec. 4.2.1, the standing wave field is very sensitive to the geometry, motions and position of the WEC, which are only crudely approximated. One would not expect to match the offshore wave field particularly well. However, it does appear that the magnitude of the variation of the data points is similar to the variation in the computational transect.

In the lee, for the periods, $T = 1.9 - 2.5$ s, there appears to be an offset between the computational measurements and the experimental data points. At $T = 2.3$ and 2.5 s, the experimental points are higher than zero, which would indicate a gain in wave height rather than a wave shadow. The offset and the gain could be the result of inaccurate assessment of the incident wave conditions. For instance, if the incident wave height as determined by measurements at the offshore gauges and gauge 10 is smaller than the actual incident wave height then such an artificial gain would be produced. The low measured incident wave height would occur if the offshore gauges happened to be in the trough of an offshore standing wave. At the period, $T = 2.7$, the data does not match computational model well in the lee, which could be due to the simplicity of the computational geometry. For longer waves, the nondimensional distance between the wave gauges and WEC is smaller, and so the wave field may be more dependent on specific geometric qualities rather than the magnitude of the power absorption.

Figure 21 shows the regular wave results for the five WEC array. Generally, the results are not quite as good as those for a single WEC. Any differences between the computational and experimental models would be exaggerated five fold in the five WEC array, including the uncertainty in the positions of the WECs, and the geometric dissimilarities. For $T = 0.9$ s, the lee experimental data may not align exactly with the computational transect, but the variation

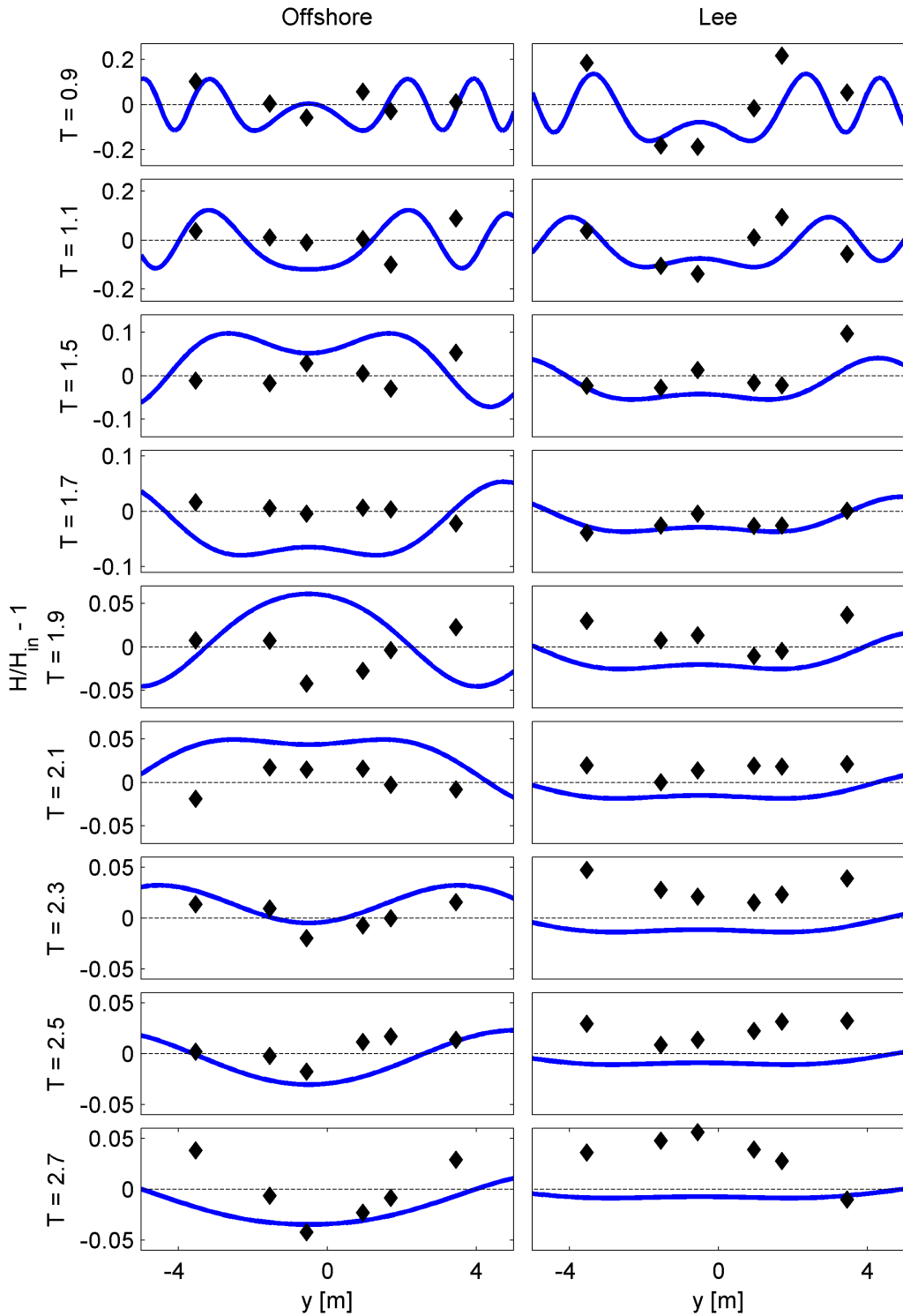


Figure 20: Figures show offshore and lee transect of the experimental results compared to the computational equivalent from WAMIT for a single WEC in regular waves.

of the data is on the same order of magnitude. The same is true for the $T = 0.9\text{ s}$ and $T = 1.1\text{ s}$ offshore transects. In the $T = 1.1\text{ s}$ lee transect, one could argue that the data points follow the hill and valley pattern predicted by the model. The lee computational transect for $T = 1.5\text{ s}$ matches the data fairly well. And the lee transects for periods, $T = 1.7 - 2.5\text{ s}$, seem reasonable. The offshore and lee transects at $T = 2.7\text{ s}$ are not great matches with the computational results, and differences are similar to the differences observed in the single WEC case, which again can be attributed to relatively close distance of the wave gauges to the WECs and the mismatch in geometry.

4.2.3 Spectral Seas - Significant Wave Height

This section compares the significant wave height from experimental data to that computed by WAMIT for unidirectional spectral seas. Both sets of significant wave heights are computed from the zeroth moment of the wave spectrum.

For both the one WEC and five WEC cases, the longshore structure of the experimental data matches well with the computational prediction. In the offshore, the significant wave height was fairly uniform. The offshore variability due to standing waves that was found in the regular wave cases is smoothed in significant wave height, because it is a bulk parameter. The wave shadow is quite clear from both the data and the model, and the model appears to accurately capture its shape and relative magnitude. A couple poorer matches occur in the single WEC case. At $H_s = 8.2\text{ cm}$, $T_p = 2.2\text{ s}$, there is an offset in the lee between the data and model, which can be attributed to inaccuracy in the estimate of the incident wave conditions. And at $H_s = 14.8\text{ cm}$, $T_p = 2.2\text{ s}$, there is an offset in the offshore transect, which could be because of the influence of wave gauge 10. In both the cases, it is important to consider that the magnitude of these differences is only about 2 – 3 %.

4.2.4 Spectral Seas - Wave Spectra

In this section, an irregular wave condition - $H_s = 7.58\text{ cm}$, $T_p = 1.42\text{ s}$ - is examined in more detail by comparing plots of the non-directional spectra at the wave gauge locations. Figure 24 shows the spectra for the single WEC case, and Fig. 25 for the five WEC case. The spectra are plotted for each gauge with the offshore spectra in the left-hand column and the lee spectra in the right. The input spectrum is the black dashed line, the computational

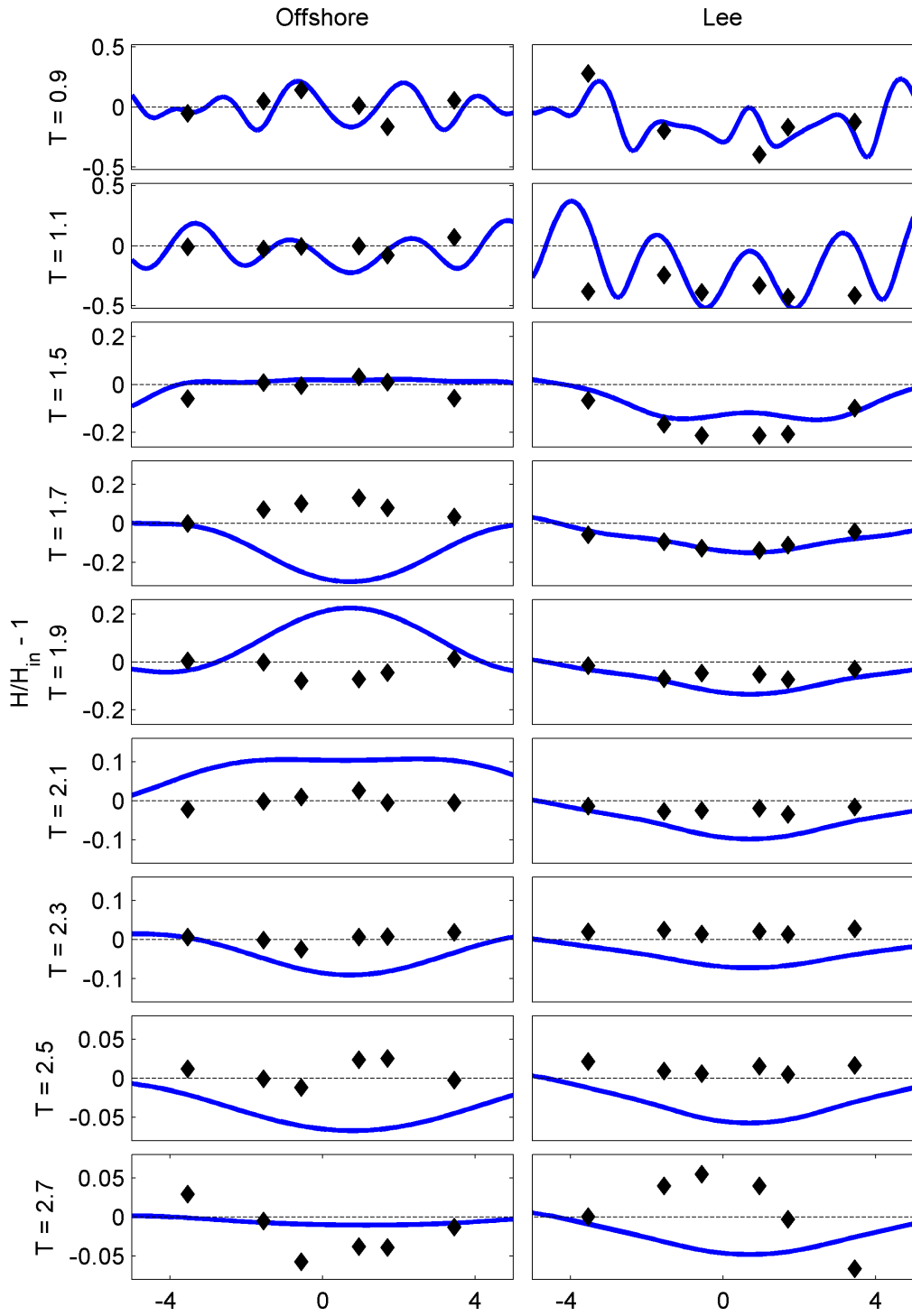


Figure 21: Figures show offshore and lee transect of the experimental results compared to the computational equivalent from WAMIT for the five WEC array in regular waves.

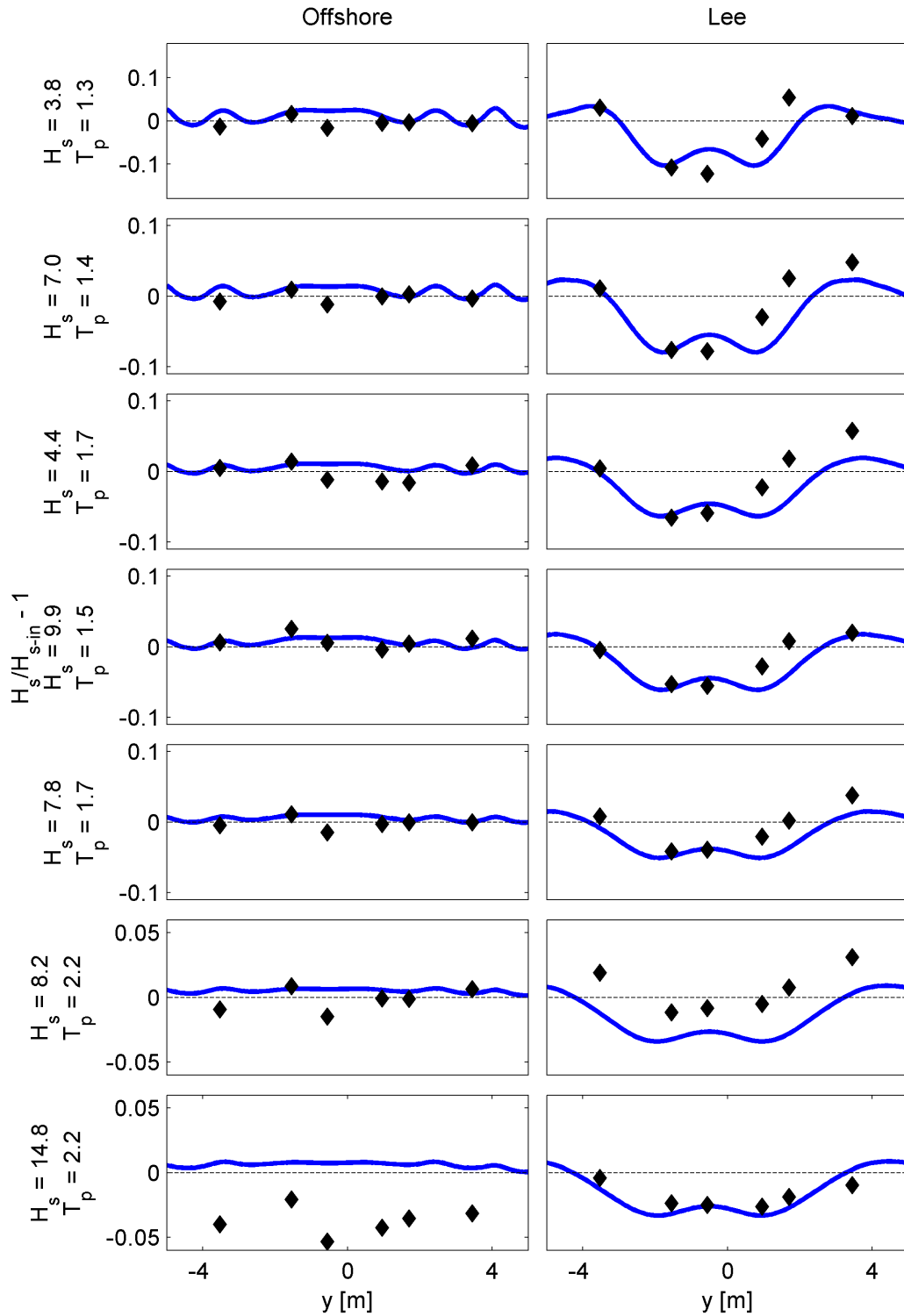


Figure 22: Figures show offshore and lee significant wave height transects of the experimental results compared to the computational equivalent from WAMIT for the single WEC in spectral seas.

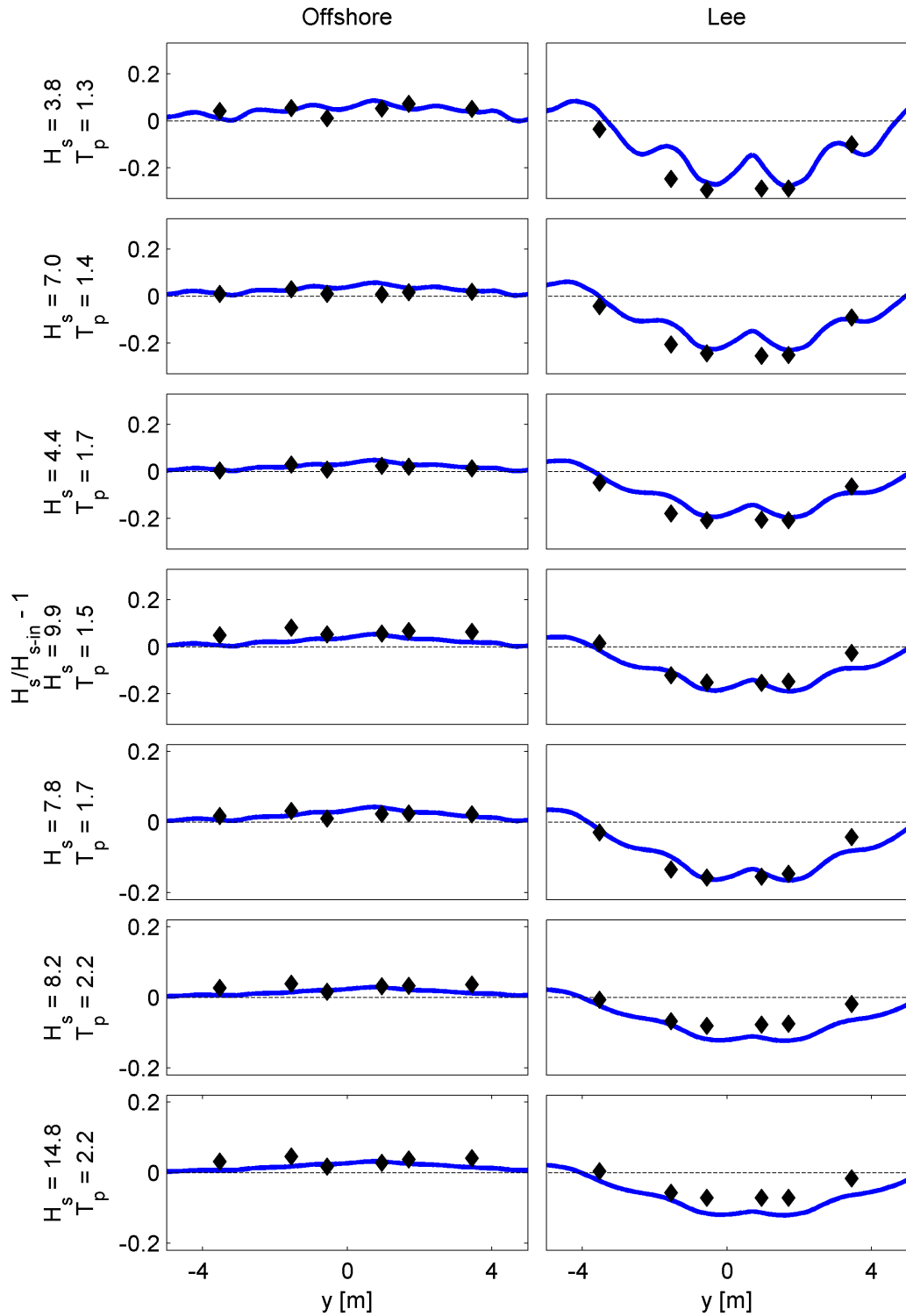


Figure 23: Figures show offshore and lee significant wave height transects of the experimental results compared to the computational equivalent from WAMIT for the five WEC array in spectral seas.

spectra are in blue and the measured spectra are in green. The green dashed lines show the 95 % confidence intervals of the measured spectra.

At first glance at the single WEC case, it is difficult to make any firm conclusions. The confidence bounds of the measured spectra are quite broad and encompass the computational spectra and the incident spectra. To understand the meaning of confidence interval, take a null hypothesis to be that the spectrum measured at a field point is the incident spectrum. If the confidence interval encloses the incident spectrum, then the null hypothesis cannot be rejected, and the field spectrum could potentially be the incident spectrum. This would mean the WECs have no effect on the wave field at those points. Now, take the null hypothesis to be that the measured spectrum is not the computational spectrum. Unless the computational result is clearly outside of the confidence intervals, the null hypothesis cannot be rejected, and the computational spectrum could be the measured spectrum. When the confidence intervals enclose the incident spectrum and the computational spectrum, then the measured spectrum could also be either the incident spectrum or the computational spectrum. To have clear results, one wants the confidence intervals to enclose the computational spectrum, but not the incident spectrum.

Despite the width of the confidence interval, the computational results do lend insight into the behavior of the experimental results. The computational results predict spikes and dips in the spectra due to frequency-dependent standing waves. The spikes and dips in the data are not extremely well resolved, which could be because of the large number of degrees-of-freedom used in the FFT that created the spectra from the time series (for details see Porter [31]). Spectral modification does appear to exist. See in particular gauge 5 offshore and lee, and gauge 2 offshore.

Because the the effect of the WECs on the wave field increases with the number of WECs, the modification of the computational and experimental spectra for the 5 WEC array is more apparent than for the single WEC case. The computation results show dramatic spikes and dips, and the experimental results show clear modification of the spectra. An interesting result is lee gauge 6, in which both computation and experiment are in good qualitative agreement. In the lee spectra, there is a clear reduction in spectral magnitude for gauges 2 through 5, which is reflected in both the experimental data and computational results. More importantly the confidence intervals of the data do not include the incident wave spectrum, which gives us confidence that this

is a real reduction in spectral energy. This is the all important region of the wave shadow

4.3 SWAN Wave Field Analysis

In phase-resolving linear water wave theory, the phase of a wave component is computed as the argument of a complex variable. For the linear wave-body interaction problem, the phasing relationship between wave components (i.e. incident, diffracted, and radiated) is critical for determining body forces, wave fields, and absorbed power. The most common method of solving the linear wave-body problem is the boundary-element method (BEM). However, BEMs have some limitations. The BEM computation time is proportional to the square of the number of panels on wetted surfaces [12], which for arrays of WECs with complicated geometries can be quite large. Computing a large number of wave field points also requires a significant amount of time, especially for spectral wave conditions. Also, BEMs are only practical for modeling a constant depth bathymetry. In general, the BEM is not appropriate for modeling spectral seas over large domains with non-uniform bathymetry.

In contrast, phase-averaged models are designed to model spectral wave propagation over large domains with variable bathymetry, which makes them attractive for modeling the effects of WECs on the far wave field. Phase-averaged models propagate wave components with a balance of wave energy in a form known as wave action density, which is a quantity that is conserved in presence of currents. In the governing equation, only information on energy is preserved, where energy is proportional to the wave height squared; the phase of wave components is lost [32]. SWAN is a well known, and well validated phase-averaged wave model [33]. Several papers [34, 35, 36, 37] have used SWAN or another phase-averaged model to model the effects of WEC arrays on the wave field. Folley and Whittaker [38] discussed the adequacy of phase-averaged models for modeling WEC arrays. They concluded that phase-averaged models may be reasonable for modeling WEC array interactions because in reality, it is not possible to achieve precise phase relationships between devices in an array and the wave field.

The purpose of this section is to further explore the adequacy of phase-averaged models for modeling the WEC wave field by comparing the phase-resolved wave fields produced by WAMIT to those of the phase-averaged

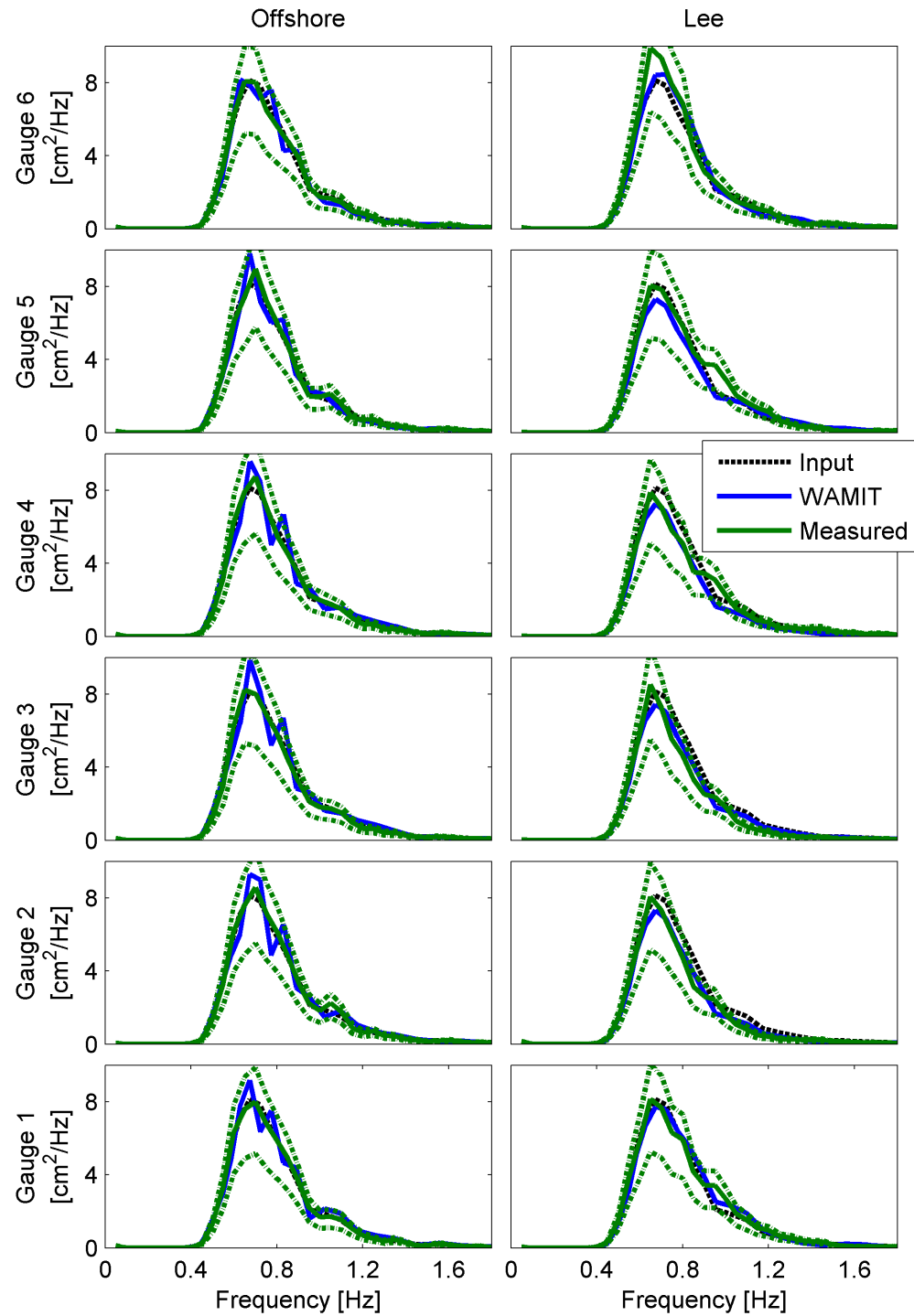


Figure 24: The figures show the measured and computational wave spectra at the wave gauges for the single WEC case.

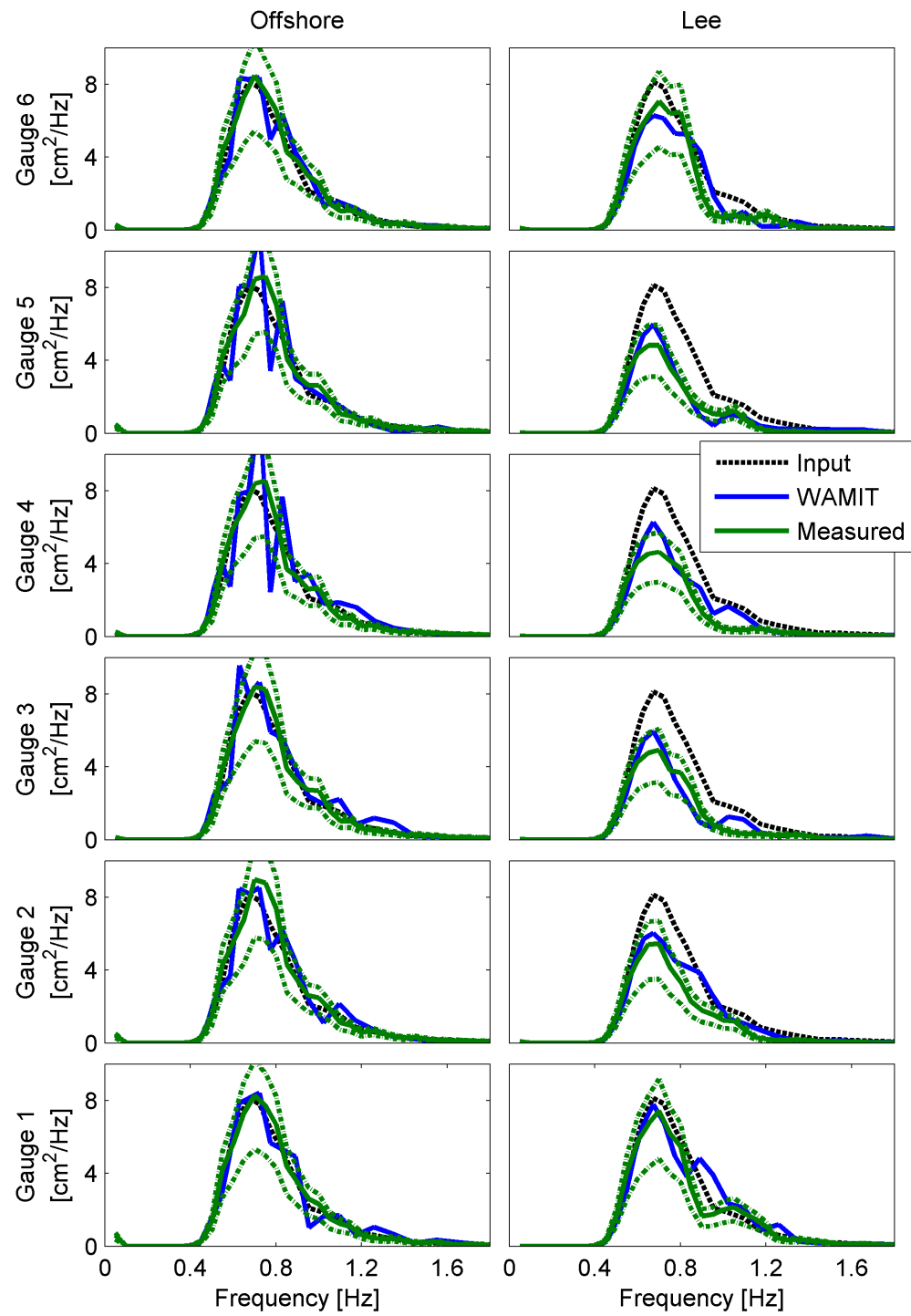


Figure 25: The figures show the measured and computational wave spectra at the wave gauges for the five WEC case.

model, SWAN. Comparisons of the wave field for regular waves and spectral seas are made in the form of plots of wave height or significant wave height respectively. In contrast to the experimental data section, incident wave conditions are known exactly, since they are inputs to the models, and wave data at all points in the wave field can be computed.

SWAN operates on a bathymetric finite element grid, propagating wave components from open boundaries throughout the domain based on the governing equations. The model domain can contain physical boundaries, which allow for partial wave reflection and transmission. Although SWAN cannot model diffraction directly, it has an option that implements a parametric approximation of diffraction that is based on the mild slope equation. The diffraction switch in SWAN changes the direction of wave energy propagation based on gradients in wave height [39].

The geometry used for the comparison is the cylindrical WEC operating in surge that is used for the WEC array experimental data study described in Sec. 4.2. To reproduce the model in SWAN, the power absorption curve is applied at an artificial boundary within the computational domain. Waves are propagated from the wave maker boundary to the location of the WEC, then over a width equal to the beam of the WEC, energy is extracted from the wave field as a function of frequency as defined by the power absorption curve, and the new waves are entered into the domain to continue propagating. The SWAN modeling was done by Porter and is described in more detail in his Masters thesis [31]. The WEC power absorption implemented in SWAN is from the power absorption curve that is determined by WAMIT. This aspect is critical to the justifying the comparison of the two models - in both models the same amount of power is absorbed at each frequency, but do the wave fields look the same?

Comparisons are made for regular waves in wave height and spectral seas with significant wave height. Plots of the wave field of the entire domain as well as transects are shown. In addition to the standard cross-shore transect, another transect in the cross-shore is introduced, the averaged cross-shore transect, which is the average in the longshore direction over the computed domain of the wave height at each cross-shore location. SWAN wave fields are shown without and with the SWAN diffraction switch set.

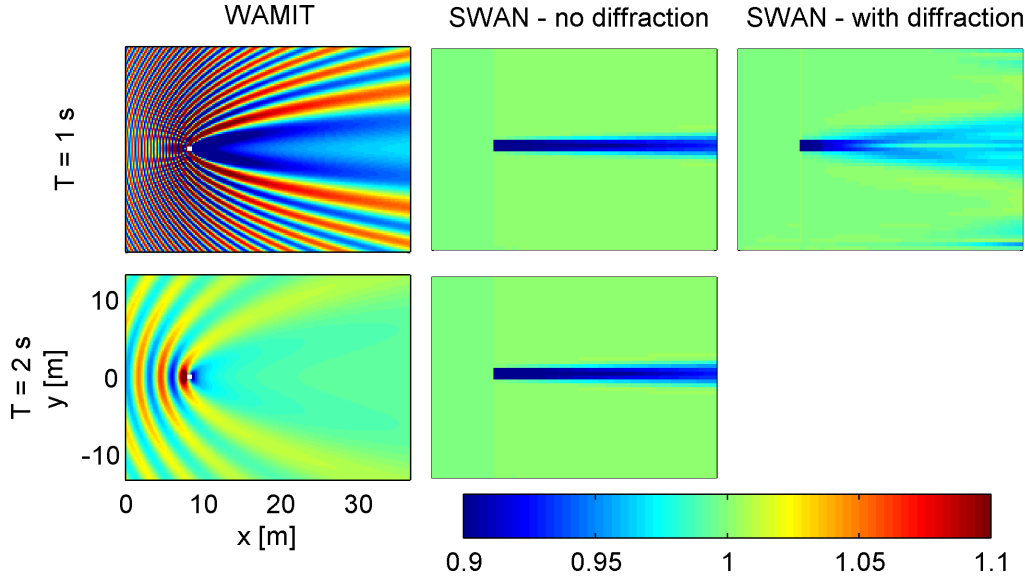


Figure 26: The figures show the wave field produced by WAMIT and SWAN for two regular wave cases. At $T = 1\text{ s}$, there is also a SWAN wave field with the diffraction switch on.

4.3.1 Regular waves

This section compares the SWAN results to those of WAMIT for two regular waves cases - a 1 second period and a 2 second period. The 1 second regular wave case was run in SWAN with and without the diffraction switch set. Unfortunately, the 2 second case did not converge to a result with SWAN diffraction turned on.

Figure 26 shows the wave fields for the two regular wave cases. The relative capture width curve in Fig. 18 shows that at both periods approximately the same amount of energy is extracted from the wave field. Because WEC modeling in SWAN is based solely on energy extraction, the diffraction-off SWAN wave fields for both periods look the same. However, the WAMIT wave fields for the two periods are quite different from one another. The 1 second WAMIT wave field is characterized by steep standing wave ridges and large wave shadow, while the 2 second wave field has smaller standing waves and a much smaller wave shadow. In the 1 second wave field, the standing waves and large wave shadow are mostly due to scattering of the shorter wavelength wave rather than energy extraction. This is the same phenomenon that is discussed for short waves in Sec. 4.1. SWAN is not able to capture wave scattering, and because its wave shadow is based only on energy extraction,

it severely underestimates the depth and breadth of the wave shadow. When the diffraction switch is turned on for SWAN, it does a better job of capturing the shape of the linear wave shadow, but still underestimates its magnitude.

The shape of the wave shadow is an important consideration in the design of WEC arrays. Because of the interaction of the planar incident waves and circular radiated and diffracted waves, phase-resolved linear wave theory produces wave shadows that are parabolically shaped and are wider than the device width. However, SWAN only extracts energy from waves that pass directly through the WEC. The wave shadow is then a streak immediately in the lee of the device. When diffraction is turned off, SWAN does not have a physical mechanism for distributing the energy loss in the wave shadow throughout the domain. A small amount spreading of the wave shadow does occur, but this is because SWAN does not allow for truly unidirectional waves and there is a tiny amount of spreading of the regular wave. When the diffraction switch is turned on in SWAN (see Fig. 26), its wave shadow much more closely resembles the phase-resolved wave shadow. The shadow spreads nicely, and actually has a longshore structure that is similar to the phase-resolved with two dips and center ridge (see Fig. 28).

Figures 27 shows cross-shore transects of wave height for the 1 second wave. Also shown are plots of the averaged cross-shore transect, which is the average of the wave height in the longshore direction as a function of the cross-shore. The averaged cross-shore transect gives an idea of how much total energy is present in the whole computational domain. Consider the 1 second wave case. In the standard cross-shore transect, the wave height immediately in the lee of the device, is quite low for WAMIT, and increases geometrically with distance from the WEC. In SWAN the wave height begins at a more moderate value in the lee of the WEC and only increases gradually. However, when considering the averaged cross-shore transects, the wave heights behind the WEC for WAMIT and both SWAN cases begin around the same value, because all three simulations extract the same energy from the wave field. The cross-shore diffraction-on SWAN transect is actually very close to the WAMIT transect. Near the WEC, it is not as close, but as the SWAN diffraction mechanism takes effect, the energy spreading produces a shape similar to the linear wave theory results.

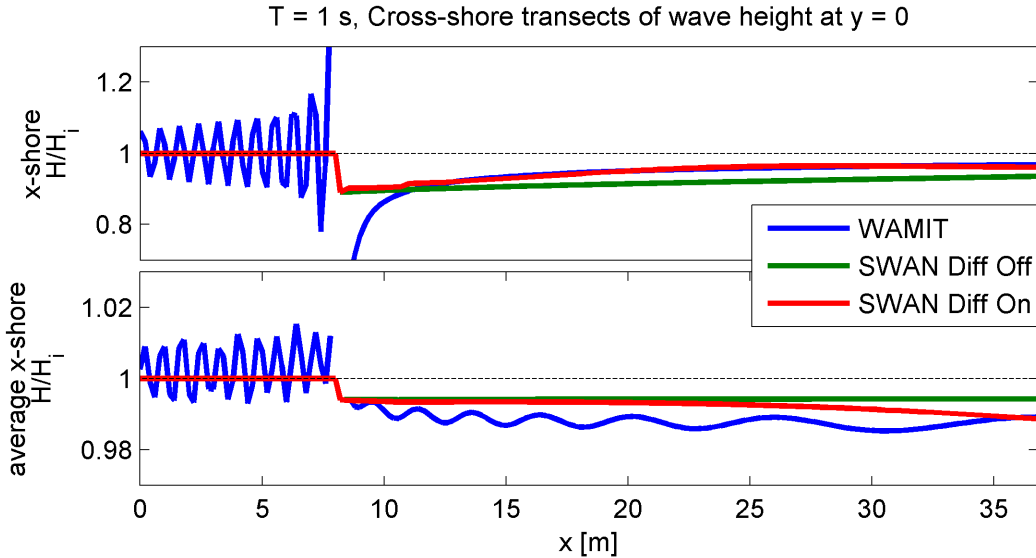


Figure 27: The figures show cross-shore transects of normalized wave height at $y = 0 \text{ m}$ (though the WEC). The top figure is a cross-section of wave height, while the bottom figure is the average of the wave height in the longshore direction at each cross-shore location.

4.3.2 Unidirectional Spectral Seas

The WAMIT and SWAN results for spectral seas are also compared. SWAN was not designed to run at a single frequency; it is generally used with a spectral distribution of wave components, and so it should perform better here. In total six spectra are considered: two peak wave periods with three levels of direction spreading. The peak wave periods are at 1 second and 2 seconds; the non-directional spectra are shown in Fig. 29 along with the RCW curve of the device. The directional spreading cases are unidirectional, and two directionally spread spectra created with cosine squared spreading functions.

First consider the unidirectional case. Wave field plots of normalized significant wave height are shown in Fig. 30. More energy is extracted by the WEC from the 2 second peak spectrum, but as before, the short wave, 1 second spectrum creates a significant scattered wave field. The results are similar to those of the regular wave case. Because of scattering of the short waves, SWAN severely underestimates the depth and width of the wave shadow even with diffraction turned on. SWAN is also not able to capture the large standing wave ridge that wraps parabolically around the device in the WAMIT 1 second case.

The SWAN results are a more similar to the WAMIT results for the 2

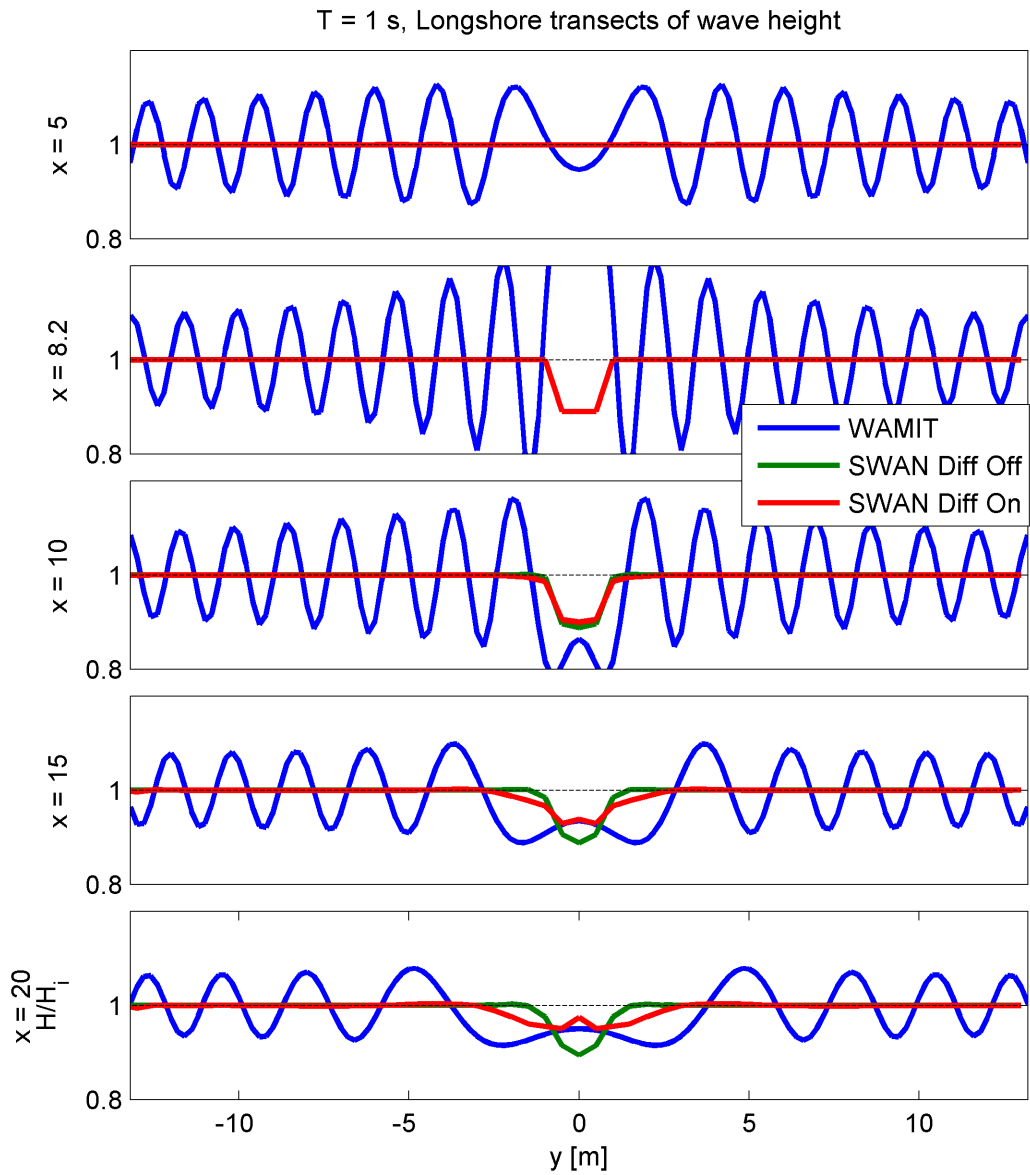


Figure 28: The figures show longshore transects at 5 locations: one offshore, one through the device, and three in the lee.

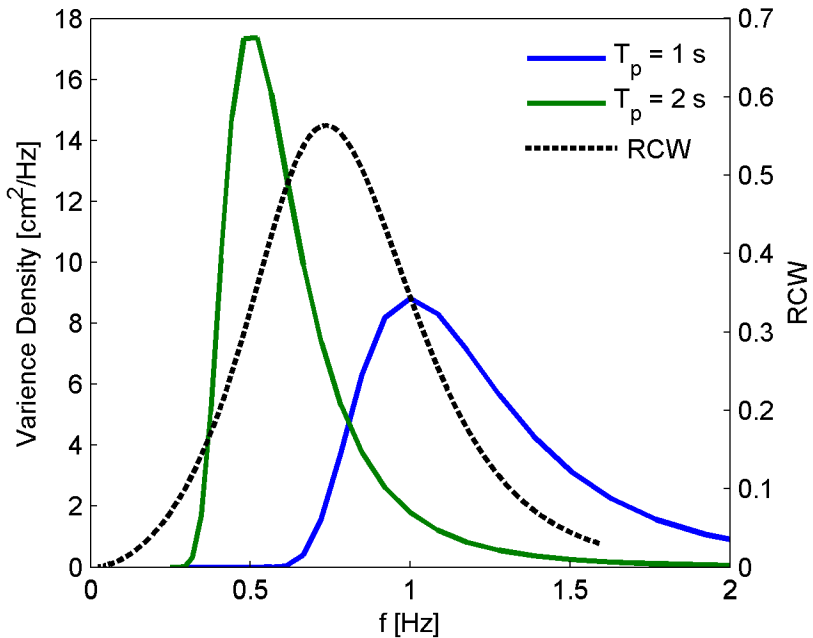


Figure 29: The figure shows the two non-directional input spectra used in the WAMIT-SWAN comparison along side the WEC RCW curve. The spectra correspond to the left y-axis and the RCW curve corresponds to the right y-axis.

second peak case, especially with diffraction turned on. For the 2 second case, the wave shadow is primarily created by energy absorption. Since SWAN only affects the wave field through energy absorption, the magnitude of the wave shadows in SWAN is similar to that of WAMIT. When diffraction is turned on, the SWAN result for the 2 second case is remarkably similar to the WAMIT result. SWAN produces the parabolic wave shadow, which has the same depth and breadth as the WAMIT shadow.

4.3.3 Directional Spectral Seas

To compare the result of directional seas, cosine squared spreading is applied to the 1 and 2 second period spectra. Two levels of spreading are used and defined by the spreading parameter, s . One case is $s = 10$, which is fairly narrow, and the second is a broader spectrum with $s = 4$. The spectra are shown in Fig. 31.

As before, in the 1 second case, the wave shadow is primarily due to wave scattering, which is not captured in SWAN. The SWAN results again underes-

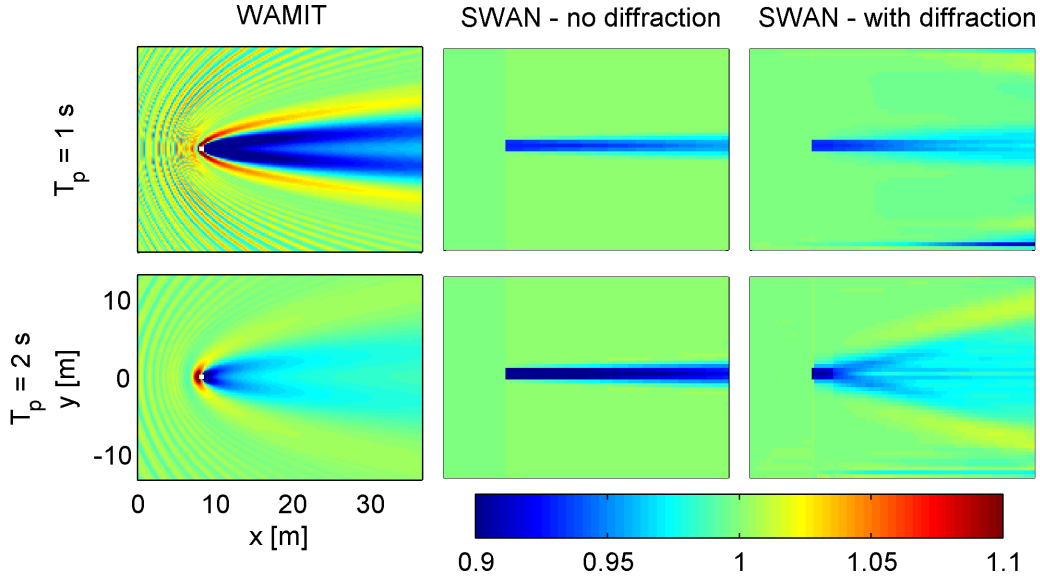


Figure 30: The figures show the wave field (H_s/H_{s-in}) produced by WAMIT and SWAN for two unidirectional spectral seas cases cases. The SWAN results include the wave field with and without the diffraction switch on. The input spectra are shown in Fig. 29.

timate the size of the wave shadow with and without diffraction at both levels of spreading. For the 2 second wave spectra, at both levels of spreading, the SWAN and WAMIT results are very similar. Both WAMIT and SWAN show egg-shaped wave shadows, due to the increase in directionality of the waves. The SWAN diffraction switch has no appreciable effect on the wave field. Directional spreading transfers the wave energy laterally and so diffraction which depends on gradients in wave height is not needed to produce a realistic wave shadow.

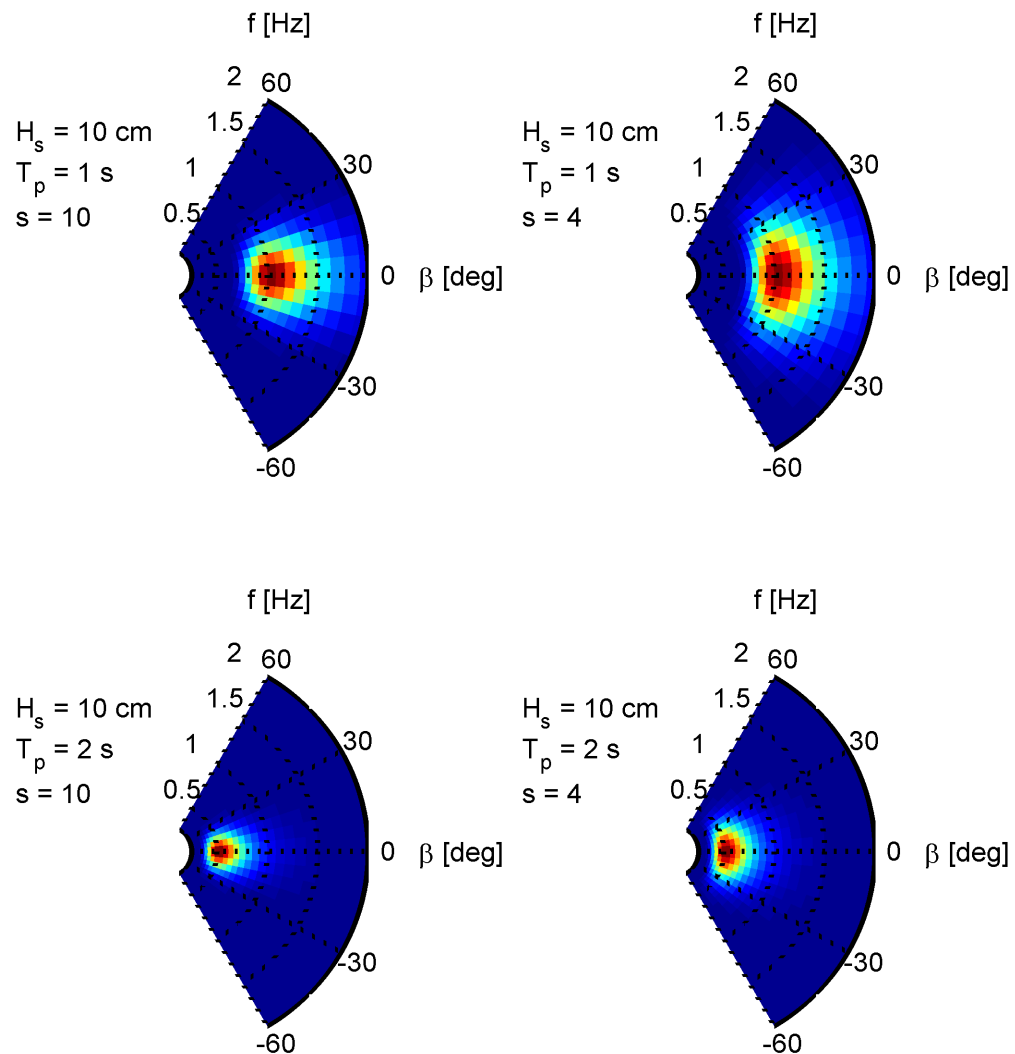


Figure 31: The figure shows the four directional input spectra (two peak periods each at two spreading widths) used in the WAMIT-SWAN comparison.

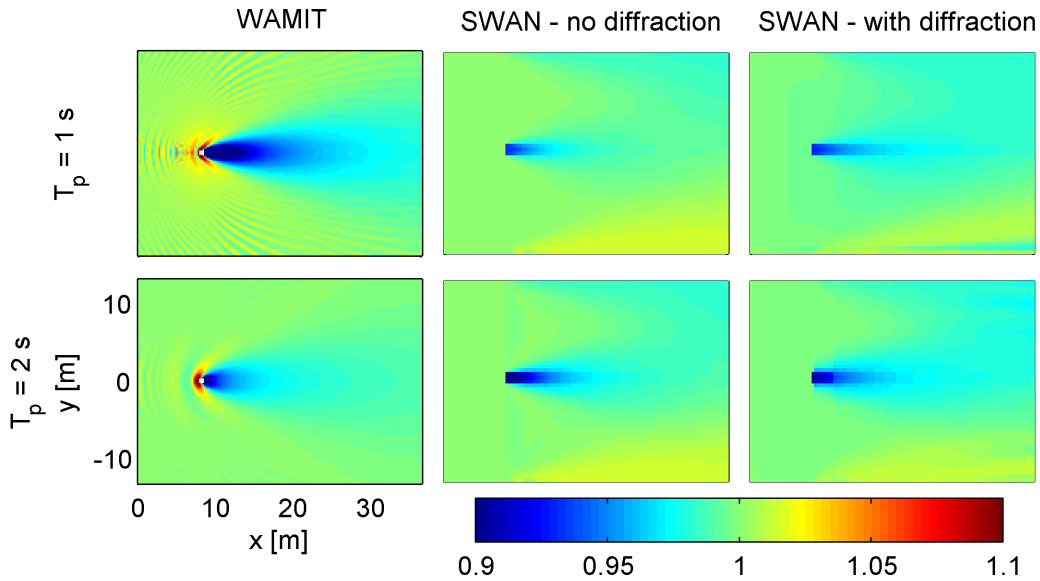


Figure 32: The figures show the wave field (H_s/H_{s-in}) produced by WAMIT and SWAN for two directional spectral seas cases, both with a spreading parameter of $s = 10$. The SWAN results include the wave field with and without the diffraction switch on. The input spectra are shown in Fig. 31

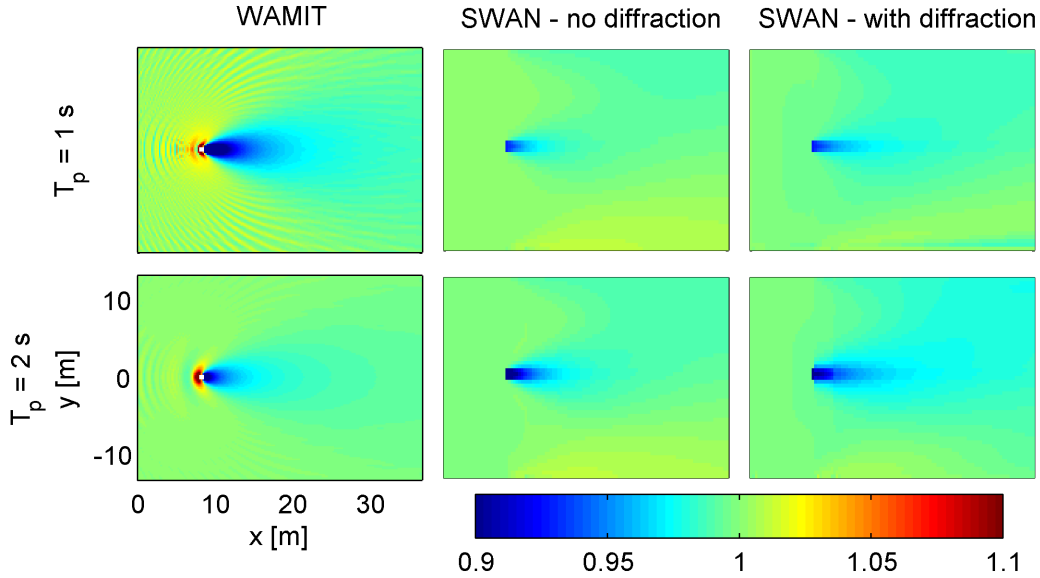


Figure 33: The figures show the wave field (H_s/H_{s-in}) produced by WAMIT and SWAN for two directional spectral seas cases, both with a spreading parameter of $s = 4$. The SWAN results include the wave field with and without the diffraction switch on. The input spectra are shown in Fig. 31

5 Discussion

5.1 WEC Wave Field Patterns

Wave energy converters affect the wave environment. The magnitude, extent and manner of the effects needs to be understood to assist in the design of WEC arrays and assess the impact of WEC arrays in the far field. The results presented here explore the near WEC wave field computationally and experimentally. A consequence of the WEC wave field effects was that in the experiment, wave gauges that were intended to measure incident wave conditions, in fact measured the WEC influenced wave field. This caused difficulty in ascertaining the incident wave conditions, which are critical for determining WEC power absorption and calibrating computational models.

The WEC wave field effects can be broken down into two related categories - standing wave ridges and the wave shadow. The standing wave ridges are partial standing waves created by the coherent interaction of the planar incident wave and the circular generated wave. In linear wave theory, they can be formulated in a straightforward manner by the superposition of a regular wave and a circular wave described by $f(\theta)(kr)^{-1/2}e^{-ikr}$. The complex generated wave function, $f(\theta)$, is responsible for the locations and magnitudes of the standing waves, while the wavelength controls the periodicity. When $f(\theta)$ is a constant the standing waves are shaped like parabolas extending to infinity in the direction of incident wave propagation. For regular waves, the standing waves are distinct.

However, in spectral seas, in terms of the bulk parameter of significant wave height, the standing wave ridges are mostly smoothed out. Although there may still be some standing waves in H_s , because the peaks and troughs occur at different locations based on the wavelength and $f(\theta)$, they appear to average towards a uniform H_s . Of course, the standing waves still exist at each frequency and can be found as spikes and holes in wave spectra taken at field points.

The standing wave phenomenon is produced by phase-resolved linear wave theory and is shown somewhat in the experimental results. From the WEC array experiment, in regular waves, there is clear variability in wave height measured across the offshore wave gauges. While in spectral seas, the significant wave height measured at the offshore wave gauges is fairly constant across the gauges. In the measured wave spectra, the magnitudes and frequency loca-

tions of the spectral spikes and dips varies across the gauges and varies between the 1 WEC and 5 WEC case. The computational results qualitatively agree. They also show variability in the offshore wave height for regular waves, which is smoothed out for spectral seas, and spikes and dips in the wave spectra. However in the offshore, the computational data does not coincide with the experimental results on a gauge by gauge and frequency by frequency basis. This can be attributed to the simplicity of the computational model and errors in the position of physical model. The standing wave field, particularly in the offshore, is very sensitive to the WEC geometry, motions, and location; none of which was captured precisely by the computational model.

In contrast, the wave field in the lee of the WEC or the wave shadow produced by linear wave theory matches the experimental data quite well. The wave shadow is the region of the wave field in the lee of the WEC where the wave height is mostly less than the incident, and which is responsible for wave energy absorption. In the context of linear wave theory, power is absorbed from the incident wave by the coherent interaction of the incident and generated wave. Farley [3] shows that only the interaction of the incident wave and the generated wave propagating in the direction of the incident wave ($\theta = \beta$) can absorb energy. The wave shadow essentially consists of the aft most parabolic standing wave trough and the region between it that converges at $\theta = \beta$.

One may think that only the generated wave at $\theta = \beta$ is needed to determine the absorbed power. However, this is a little misleading. Recall that for some fixed device cases (no power absorbed), there is a wave shadow due to wave scattering, but this is balanced by wave reflection (for example see Fig. 6 at $\lambda' = 10$, and Figs. 9, and 13). Consider Farley's equation for wave field power absorption, Eqn. 23. The power absorption occurs in the first term, which includes only the values of generated wave function in the direction of the incident wave propagation, $f(\theta) = f(0)$. The second term subtracts power based on the power radiated by the generated wave, and is the integral of $f(\theta)$ in all directions. The second term can make the power absorption zero or negative, where negative means the device radiates power. Farley gives a nice example of the Salter's Duck WEC. The Duck is asymmetric front to back and is designed *not* to radiate a wave at $\theta = \beta$. However, there is a diffracted wave at $\theta = \beta$, which is what ultimately absorbs the energy. When the device is held fixed, in addition to the wave cancellation in the lee, there

is reflected wave in the direction towards the incident wave ($\theta = -\beta$), which causes the net wave energy absorption to be zero. When the device is moving, a radiated wave propagates only at $\theta = -\beta$, which cancels the reflected wave, reduces the net radiated power (the second term in Eqn. 23), and creates power absorption.

A wave shadow must exist for a power absorbing device and may exist due to diffraction for a device that does not absorb power. Even for wave scattering, the shadow is due to generated wave in the direction of the incident wave. For a regular wave, Farley shows that the structure of the wave field in the lee of the WEC is of a certain general form (see Fig. 7). The linear wave computational results are of this form and so are some experimental results (see Fig. 20 especially $T = 0.9\text{ s}$ and $T = 1.1\text{ s}$). In the terms of the longshore structure of wave height, the computational and experimental results are in reasonable agreement of the lee transects for 1 WEC and 5 WECs in regular waves.

For unidirectional spectral seas, the wave shadow is generally found at approximately the same location for all frequencies in the spectrum. The direction of power absorption, $\theta = \beta$, is the same for all frequencies, and the aft most parabolic trough does not deviate greatly from frequency to frequency. The result is that for unidirectional waves, even though the parabolic standing wave ridges are smoothed in the offshore, the wave shadow is preserved in the lee (see Fig. 9). The computational results are in very good agreement with experiment in the lee transects of H_s for both the 1 WEC and 5 WEC cases (see Figs. 22 and 23). The comparison of the lee spectra for the 1 WEC case is inconclusive, but for the 5 WEC case, the experimental and computational spectra in the lee (gauges 2-5) conclusively show a wave shadow (see Fig. 25).

Why is the linear wave computational model able to reproduce the wave shadow that is seen in the experimental results despite the model geometry and motions being only a crude representation of the physical geometry and motions? It is likely because the wave shadow depends on the power captured by the device rather than the particulars of device geometry and motions, and the cylindrical computational model was designed to have approximately the same power capture characteristics as the physical model. It is the coherent interaction of generated wave in the direction of the incident wave that enables WEC to absorb power and create a wave shadow.

Interestingly, the wave shadow produced by the phase-averaged model

occurs at wave components traveling in the direction of the incident wave and passing through the device. However, without the parametric diffraction switch set, the phase-averaged model misses a critical element of the wave shadow. Without diffraction, the phase-averaged model produces a wave shadow that extends as a streak behind the WEC, creating a physically unrealistic canyon in wave energy. When the diffraction switch is set, the diffraction mechanism smooths the steep gradient and produces a wave shadow that can be remarkably like the phase-resolved wave shadow (see Fig. 30).

The diffraction mechanism in the phase-averaged model operates based on gradients in the wave height; it is not the solution to the linear wave-body boundary value problem. The phase-averaged model is not capable of creating standing wave fields. At short wavelengths, WECs produce a large wave shadow due to scattering even though there may be little net energy absorption. The phase-averaged model wave shadow is only created by energy absorption, and so when the wave shadow is due to scattering, the phase-averaged model underestimates it (see Figs. 26 and 30).

For directionally spread spectral seas, wave shadows due to each direction overlap and the wave shadow in H_s loses its parabolic shape. The overlapping of the streak-like wave shadows of the phase-averaged model produces a shape similar to that of linear wave theory. Because wave energy is spread laterally by the directional spreading, the phase-averaged diffraction switch has little effect on the wave field. However, again, when the wave shadow is produced by scattering, the phase-averaged model underestimates it. The phase-averaged model may produce good results when the wave shadow is produced primarily by power absorption and when diffraction is set for long-crested waves or when the seas are spread directionally.

5.2 Application of the WEC Wave Field to Array Design

How could one apply the knowledge of the wave field near a single WEC to WEC array design? Constructive interactions amongst WECs in an array are achieved theoretically for a given wave when WECs operate under precise controls of amplitude and phase (optimal motions) and are located at specific positions in the wave field. The WEC positions turn out to be the locations of the peaks of standing waves, and were found almost fortuitously by varying the spacing of arrays in regular grids or by optimization routines. Child and

Venugopal [2] explicitly examined the wave field and found that by iteratively placing WECs in an array on the parabolic standing waves of other WECs, they could produce an array that performed constructively even for non-optimal motions.

However, they and others realized that a configuration that performed well for a given wave frequency and direction would perform poorly at others. An examination of spectral seas shows that except for the wave shadow, the wave field is mostly uniform in significant wave height. Since significant wave height is proportional to wave energy, the total spectral wave energy is mostly uniform throughout the wave field except in the wave shadow where there is less energy. Also, in “The adequacy of phase-averaged wave models for modelling wave farms,” Folley and Whittaker [38] pointed out that the lack of precise knowledge about the position of the WECs and the phasing of wave and device motions would make net consistent constructive performance nearly impossible. This has implications for the design of arrays of real devices, which move about on their moorings and cannot be controlled precisely, in real wave conditions, which are spread in frequency and direction. Perhaps the goal of array design should simply be to avoid the wave shadow where there is a net reduction in wave energy.

A wave shadow could be devised for a given WEC in its expected sea state, or perhaps a generic shadow could be created for an amount of power absorption and a parametric sea spectrum. Wave shadows have been shown to exist for regular waves, unidirectional spectral seas, and spectral seas spread in direction. They have a fairly standard shapes - parabolic and in some cases with a ridge in the middle. The shape and magnitude of the wave shadow are functions of the power absorption rather than the precise geometric and motion characteristics of the WEC. It can be well produced by phase-resolving linear wave theory and in some cases by phase-averaged models. The devised wave shadow could be used to determine the placement of WECs in the array, even in as simple a manner as providing a minimum distance for the spacing between rows. By placing WECs in an array outside of the wave shadows of other WECs, the destructive losses should be minimized for real wave conditions.

5.3 Future Work

In most cases, the wave fields considered in detail in this work are for a single WEC. Individual WEC wave fields cannot necessarily be superimposed upon one another, although they can under the point absorber assumption. In the presence of multiple WECs, there is multiple scattering; that is, the diffracted and radiated waves from one WEC are diffracted off another and those waves can be diffracted off other WECs and so on. It seems prudent to see how the wave field from one WEC extends to the wave field of an array of WECs. Under what circumstances (for instance, under the point absorber assumption) can the wave field from a single WEC be used to determine the wave field of a WEC array? Will the wave shadow method of WEC array design described in the previous section work? Or is it too simple? Will it miss potentially advantageous WEC array configurations? Quite simply, can the wave field from a single WEC be used to design WEC arrays?

Another interesting aspect of the wave field is the importance of the complex generated wave function, $f(\theta)$. Wave fields produced with simple formulation of $f(\theta)$ (see Sec. 3.5) are remarkably similar to wave fields produced with a full formulation of the linear wave boundary value problem. It would be straight-forward to determine an $f(\theta)$ from computational results. Could $f(\theta)$ be determined from experimental results? If one had an $f(\theta)$ function that represented a WEC, how would the wave field produced with the simple formulation (Eqn. 18) compare to the wave field produced by the full linear wave boundary value problem? Could the $f(\theta)$ function be used to explicitly design arrays? How does the presence of other devices in an array affect the $f(\theta)$ of a single device?

There is also a good deal of work left in the experimental data comparison. Only a simple computation model of the WEC under test could be created due to time limitations and proprietary concerns. This turns out to be somewhat of a blessing in disguise, because it forces the researchers to consider why such a simple model could produce good results in the lee of the WEC, and it shows that the wave shadow is rather generic and not specific to a geometry. The question remains, could better results be obtained for a more accurate computational model, especially in the offshore? It would be nice to construct a computational geometry that was a better representation of the WEC and that operated in all modes of motion. This is not a trivial task.

The implementation of WECs in the phase-averaged model could also pos-

sibly be improved. In the current implementation, the WECs only affect the wave field by power absorption. However, for short waves, the impact of the wave scattering is significant. Perhaps the WEC in the phase-averaged model could include reflection that would redirect wave components offshore. This may be consistent in terms of conservation of energy as long as the same amount of energy that is redirected offshore is also removed from waves propagating in the lee of the WEC, which would create the wave shadow due to scattering that is missing in the current model.

6 Conclusion

The near WEC wave field is characterized by two significant patterns - 1) standing waves that are mostly parabolic and 2) a wave shadow. The standing waves can be formed through simple mathematical representations of the WEC wave field (i.e. the generated wave as $f(\theta)(kr)^{-1/2} e^{ikr}$) as well as by solving the linear wave boundary value problem. In previous theoretical work, WEC array design has taken advantage of the standing wave patterns to create arrays with constructive power production. In spectral seas, in terms of significant wave height, the standing waves are not distinct. However, they can still be found in wave field spectra as spike and dips. Because spectral seas smooth standing waves, their advantage in producing constructive arrays in real conditions is diminished.

However, in spectral seas as well as in regular waves, a significant wave shadow exists. The wave shadow is produced computationally with linear wave theory, and the linear wave results are in reasonable agreement with experimental measurements. In two single-WEC regular wave cases ($T = 0.9\text{ s}$ and $T = 1.1\text{ s}$), the lee transect shows a longshore structure including standing wave ridges that was predicted by Farley and modeled by linear wave theory. For spectral seas in terms of significant wave height, the longshore structure of wave shadow shown in experimental data is in very good agreement with computational results. The wave shadow is the necessary result of power absorption by a WEC. Farley shows that in linear wave theory, power absorption is created the destructive interference of the planar incident wave and the portion of the circular generated wave propagating in the direction of the incident wave ($\theta = \beta$). The destructive interference at $\theta = \beta$ and the aft-most standing wave trough combine to form a wave shadow that has a parabolic or triangular shape. This wave shadow shape is mostly maintained for unidirectional spectral seas and becomes more oval-like for seas spread in direction. When designing a WEC array, rather than attempting constructive interference by using standing waves patterns, perhaps the best the array designer can do is avoid the unquestionably destructive interference of the wave shadow.

Further work needs to be done to explore how the single WEC wave field extends to the wave field of multiple WECs and to devise more concrete methods of wave field based WEC array design. The WEC wave field approach to array design seems promising. The power production and economic perfor-

mance of wave energy converters will depend not just on efficient individual devises but on effective wave farm design, for which a thorough understanding of the WEC array hydrodynamics interactions is required.

Bibliography

- [1] Haller, M., Porter, A., Lenee-Bluhm, P., Rhinefrank, K., Hammagren, E., Ozkan-Haller, H. T., and Newborn, D., 2011. “Laboratory observations of waves in the vicinity of WEC-arrays”. In Proceedings of the 9th European Wave and Tidal Energy Conference, Southampton, UK.
- [2] Child, B., and Venugopal, V., 2010. “Optimal configurations of wave energy device arrays”. *Ocean Engineering*, **37**, Nov., pp. 1402–1417.
- [3] Farley, F. J. M., 2011. “Far-field theory of wave power capture by oscillating systems”. *Philosophical Transactions of the Royal Society A: Mathematical, Physical and Engineering Sciences*, **370**(1959), Dec., pp. 278–287.
- [4] Folley, M., Babarit, A., Child, B., Forehand, D., O’Boyle, L., Silverthorne, K., Spinneken, J., Stratigaki, V., and Troch, P., 2012. “A review of numerical modelling of wave energy converter arrays”. In Proc. Of the ASME 2012 31th International Conference on Ocean, Offshore and Arctic Engineering.
- [5] Budal, K., 1977. “Theory for absorption of wave power by a system of interacting bodies”. *Journal of Ship Research*, **21**(4), Dec., pp. 248–253.
- [6] Evans, D. V., 1980. “Some analytical results for two and three dimensional wave-energy absorbers”. In *Power from Sea Waves*. Academic Press, London, UK, pp. 213–249.
- [7] Thomas, G. P., and Evans, D. V., 1981. “Arrays of three-dimensional wave-energy absorbers”. *Journal of Fluid Mechanics*, **108**, pp. 67–88.
- [8] McIver, P., 1994. “Some hydrodynamic aspects of arrays of wave-energy devices”. *Applied Ocean Research*, **16**, pp. 61–69.
- [9] Simon, M. J., 1982. “Multiple scattering in arrays of axisymmetric wave-energy devices. part 1. a matrix method using a plane-wave approximation”. *Journal of Fluid Mechanics*, **120**, pp. 1–25.
- [10] Kagemoto, H., and Yue, D. P., 1986. “Interactions among multiple three-dimensional bodies in water waves: an exact algebraic method”. *Journal of Fluid Mechanics*, **166**, pp. 189–209.

- [11] WAMIT. www.wamit.com/manual.htm.
- [12] Mei, C. C., 1978. “Numerical methods in water-wave diffraction and radiation”. *Annual Review of Fluid Mechanics*, **10**, pp. 393–416.
- [13] Kalen, O., 2010. “A study of the change of the wave field due to the presence of wave energy converters”. Masters thesis, Goteborg University.
- [14] Cruz, J., Sykes, R., Siddorn, P., and Taylor, R., 2010. “Estimating the loads and energy yield of arrays of wave energy converters under realistic seas”. *IET Renewable Power Generation*, **4**, p. 488.
- [15] De Backer, G., Vantorre, M., Beels, C., De Rouck, J., and Frigaard, P., 2010. “Power absorption by closely spaced point absorbers in constrained conditions”. *IET Renewable Power Generation*, **4**, p. 579.
- [16] Folley, M., and Whittaker, T., 2009. “The effect of sub-optimal control and the spectral wave climate on the performance of wave energy converter arrays”. *Applied Ocean Research*, **31**, Oct., pp. 260–266.
- [17] Vicente, P. C., de O. Falcão, A. F., Gato, L. M., and Justino, P. A., 2009. “Dynamics of arrays of floating point-absorber wave energy converters with inter-body and bottom slack-mooring connections”. *Applied Ocean Research*, **31**, Oct., pp. 267–281.
- [18] Babarit, A., Borgarino, B., Ferrant, P., and Clement, A., 2010. “Assessment of the influence of the distance between two wave energy converters on energy production”. *IET Renewable Power Generation*, **4**, p. 592.
- [19] Babarit, A., 2010. “Impact of long separating distances on the energy production of two interacting wave energy converters”. *Ocean Engineering*, **37**, June, pp. 718–729.
- [20] Borgarino, B., Babarit, A., and Ferrant, P., 2012. “Impact of wave interactions effects on energy absorption in large arrays of wave energy converters”. *Ocean Engineering*, **41**, Feb., pp. 79–88.
- [21] Falnes, J., and Budal, K., 1982. “Wave power absorption by parallel rows of interacting oscillating bodies”. *Applied Ocean Research*, **4**(4), pp. 194–207.

- [22] Mavrakos, S. A., and Kalofonos, A., 1997. “Power absorption by arrays of interacting vertical axisymmetric wave-energy devices”. *Journal of Offshore Mechanics and Arctic Engineering*, **119**(4), Nov., pp. 244–251.
- [23] Ricci, P., Saulnier, J. B., and de O. Falcão, A. F., 2007. “Point-absorber arrays: configuration study off the potuguese west coast”. In Proceedings of the 7th European Wave and Tidal Energy Conference, Porto, Portugal.
- [24] Fitzgerald, C., and Thomas, G., 2007. “A preliminary study on the optimal formation of an array of wave power devices”. In Proceedings of the 7th European Wave and Tidal Energy Conference, Porto, Portugal.
- [25] Newman, J. N., and Lee, C.-H., 2002. “Boundary-element methods in offshore structure analysis”. *Journal of Offshore Mechanics and Arctic Engineering*, **124**, pp. 81–89.
- [26] Evans, D. V., 1976. “A theory for wave-power absorption by oscillating bodies”. *Journal of Fluid Mechanics*, **77**, pp. 1–25.
- [27] Falnes, J., 2002. *Ocean Waves and Oscillating Systems: Linear Interactions Including Wave-Energy Extraction*, 1 ed. Cambridge University Press, Apr.
- [28] Wypych, M., Le-Ngoc, L., Alexander, K., and Gardner, A., 2012. “On the application of circular–cylindrical waves to ocean wave power absorption”. *Ocean Engineering*, **40**, Feb., pp. 69–75.
- [29] Newman, J., 1977. *Marine Hydrodynamics*. MIT Press, Cambridge Mass.
- [30] Dean, R. G., and Dalrymple, R. A., 1991. *Water Wave Mechanics for Engineers & Scientists (Advanced Series on Ocean Engineering- Vol2)*. World Scientific Pub Co Inc.
- [31] Porter, A., 2012. “Laboratory observations and numerical modeling of the effects of an array of wave energy converters”. Masters thesis, Oregon State University, Aug.
- [32] Holthuijsen, L., 2007. *Waves in Oceanic and Coastal Waters*. Cambridge University Press, Cambridge.
- [33] The SWAN Team, 2011. SWAN. <http://www.swan.tudelft.nl>.

- [34] Millar, D., Smith, H., and Reeve, D., 2007. “Modelling analysis of the sensitivity of shoreline change to a wave farm”. *Ocean Engineering*, **34**(5-6), Apr., pp. 884–901.
- [35] Smith, H., Millar, D., and Reeve, D., 2007. “Generalisation of wave farm impact assessment on inshore wave climate”. In Proceedings of the 7th European Wave and Tidal Energy Conference.
- [36] Alexandre, A., Stallard, T., and Stansby, P., 2009. “Transformation of wave spectra across a line of wave devices”. In Proceedings of the 8th European Wave and Tidal Energy Conference.
- [37] Silverthorne, K. E., and Folley, M., 2011. “A new numerical representation of wave energy converters in a spectral wave model”. In Proceedings of the 9th European Wave and Tidal Energy Conference.
- [38] Folley, M., and Whittaker, T., 2011. “The adequacy of phase-averaged wave models for modelling wave farms”. In Proc. Of the ASME 2011 30th International Conference on Ocean, Offshore and Arctic Engineering.
- [39] Holthuijsen, L., Herman, A., and Booij, N., 2003. “Phase-decoupled refraction–diffraction for spectral wave models”. *Coastal Engineering*, **49**(4), Oct., pp. 291–305.